17707

NATIONAL LIBRARY
OTTAWA

BIBLIOTHÈQUE NATIONALE
OTTAWA

NAME OF AUTHOR.......RONALD PETER TETARENKO

TITLE OF THESIS.......TRANSIENT IMPEDANCE OF
IMPATT DIODES
....

UNIVERSITY.......U. of ALBERTA

DEGREE FOR WHICH THESIS WAS PRESENTED.......Ph.D.

YEAR THIS DEGREE GRANTED.......1973

Permission is hereby granted to THE NATIONAL LIBRARY OF CANADA to microfilm this thesis and to lend or sell copies of the film.

The author reserves other publication rights, and neither the thesis nor extensive extracts from it may be printed or otherwise reproduced without the author's written permission.

(Signed).......R. Tetarenko.......

PERMANENT ADDRESS:

DEPARTMENT OF ELECTRICAL
ENGINEERING
UNIVERSITY OF ALBERTA
EDMONTON, ALTA

DATED.......JUNE 13.......1973

NL-91 (10-68)

THE UNIVERSITY OF ALBERTA

TRANSIENT IMPEDANCE OF IMPATT DIODES

by

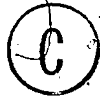

RONALD PETER TETARENKO

A THESIS

SUBMITTED TO THE FACULTY OF GRADUATE STUDIES AND RESEARCH

IN PARTIAL FULFILMENT OF THE REQUIREMENTS FOR THE DEGREE

OF DOCTOR OF PHILOSOPHY

DEPARTMENT OF ELECTRICAL ENGINEERING

EDMONTON, ALBERTA

FALL, 1973

THE UNIVERSITY OF ALBERTA

FACULTY OF GRADUATE STUDIES AND RESEARCH

The undersigned certify that they have read, and recommend to the Faculty of Graduate Studies and Research, for acceptance, a thesis entitled TRANSIENT IMPEDANCE OF IMPATT DIODES submitted by RONALD PETER TETARENKO in partial fulfilment of the requirements for the degree of Doctor of Philosophy.

Paul A. Goud
Supervisor

D. Routledge

Keith A. Stromsmoe

Ronald H. Johnston
External Examiner

Date June 11th, 1973

ABSTRACT

The work presented here is a study of the behavior of the electronic impedance under transient conditions for a type of Impatt diode. This study includes both analytical and experimental investigations and is applicable to Read model and one-sided abrupt junction Impatt diodes.

An improved analytical model of the diode has been formulated and evaluated. This model allows the inclusion of the space charge effect associated with the avalanche region as well as individual ionization rates and drift velocities for both types of carriers. The model spans the range of applicability of both small-and large-signal analysis and can be used for steady-state or transient operating conditions.

The time dependence of the Impatt diode's junction temperature is measured to within five nanoseconds of the onset of the bias pulse and a model for the transient heat flow in the diode's semiconductor junction is developed. This heat flow model gives close agreement with the experimental results and is applicable for a range of pulsed operating conditions. Also, a means of incorporating changes in the junction temperature into the analytical model is evaluated.

A method for the measurement of the diode's electronic impedance at microwave frequencies and under transient operating conditions is developed. This method employs the principle of reinserting the carrier frequency to measure the complex reflection coefficient as a function of time and is referred to here, as the Carrier Reinsertion Method. With this technique, the diode's electronic impedance is measured during the

buildup and decay of bias pulses having risetimes of five nanoseconds. There is good agreement between these measured results and those provided by the analytical model.

The analytical model of the Impatt diode and the results of the transient electronic impedance measurements are utilized to construct a computer model of the diode. This model indicates that the transient characteristics of the diode's electronic impedance have a relatively short duration and are largely confined to the real part of the electronic impedance. Also indicated is the dependence of the transient effects upon the rise times of the bias voltage pulse and on the frequency and magnitude of the R.F. voltage impressed across the diode. The significance of these transient effects with respect to Impatt diodes used in R.F. amplifiers and oscillators is discussed.

ACKNOWLEDGEMENTS

The author wishes to thank his supervising professor, Dr. P.A. Goud, for his help and encouragement throughout the course of this research.

Also gratefully acknowledged, is the assistance of the following persons during the course of this work:

Dr. J. Nigrin for many helpful discussions.

Mr. J. Fearn for his excellent technical assistance and his good humor.

Mr. K. Doerbecker and the staff of the machine shop for their help in fabricating the various components used in the experimental work.

Members of the Microwave Electronic Group for their helpful discussions and assistance.

Mrs. B. Gallaiford for her excellent work in typing this thesis.

The author wishes to express his deepest appreciation for the understanding and encouragement provided by his Wife, Peggy.

The financial assistance provided by the following organizations is gratefully acknowledged:

The Alberta Government Telephones for the provision of a Centennial Fellowship.

The University of Alberta for Graduate Teaching Assistantships.

The Communications Research Center for its support of this research under contract OGR2 - 0195.

TABLE OF CONTENTS

			Page
CHAPTER I	:	INTRODUCTION	1
CHAPTER II	:	IMPATT DIODES	7
		2.1 Basic Principles of Impatt Diode Operation	8
		2.2 Types of Impatt Diodes	11
		2.3 Fabrication of Impatt Diodes	17
CHAPTER III	:	PHYSICAL AND MATHEMATICAL MODEL	20
		3.1 Physical Model	20
		3.1.1 Carrier Recombination	20
		3.1.2 Surface Boundary Conditions	20
		3.1.3 Degeneracy	21
		3.1.4 Carrier Mobility	21
		3.1.5 Microplasmas	22
		3.2 Validity of One-Dimensional Analysis	22
		3.3 Mathematical Model	23
		3.3.1 Fundamental Mathematical Equations	23
		3.3.2 Development of Conduction Current Equations	26
		3.3.3 Constant Electric Field Model	31
		3.3.4 Simplified Conduction Current Distribution	34
		3.3.5 Validity of the Model	39
		3.3.6 Development of Electric Field Equation for the Avalanche Region	44

		Page
	3.4 Summary	49
CHAPTER IV :	COMPUTER SOLUTIONS OF THE ANALYTICAL EQUATIONS	52
	4.1 Introduction	52
	4.2 Normalization of the Analytical Equations	52
	4.3 Analog Computation	60
	4.3.1 Equations for the Analog Model	60
	4.3.2 Results of the Analog Computations	62
	4.4 Solutions by Digital Computer	65
	4.4.1 Procedure for Numerical Analysis	66
	4.4.2 Results of Computations	69
	4.4.3 Estimation of Computational Errors	77
	4.5 Summary	78
CHAPTER V :	THERMAL PROPERTIES OF IMPATT DIODES	80
	5.1 Introduction	80
	5.2 Steady-State Thermal Properties	81
	5.3 Transient Thermal Properties	85
	5.3.1 Measurement of Transient Heat Flow	86
	5.3.2 Thermal Model for Transient Heat Flow	95
	5.4 Computer Modelling of Thermal Properties	101
	5.5 Summary	103

Page

CH[illegible] : [illegible]ENT [illegible]ICROWAVE IMPEDANCE MEASUREMENTS 106

[illegible]. [illegible]ntro[illegible]ction 106

[illegible].2 T[illegible]ent Impedance by Direct Com[illegible]rison of Voltage/Current Waveforms 108

Cavity Oscillator Method 108

[illegible].2.2 Airline Tee Method 114

6.3 Transient Impedance by Carrier Re-Insertion 120

6.3.1 Biasing and Separation of Incident and Reflected Signals 123

6.3.2 R.F. Detection Sub-System 126

6.3.3 Calibration of Measuring System 129

6.4 Experimental Measurement 131

6.4.1 Derivation of the Diode Package Equivalent Circuit 133

6.4.2 Experimental Results 137

6.4.3 Accuracy of Measurement System 157

6.5 Summary 159

CHAPTER VII : DISCUSSION OF THEORETIC[illegible] [illegible]ND EXPERIMENTAL RESULTS 162

7.1 Introduction 162

7.2 Comparison of Computations and Measurements 162

Page

7.2.1 Response of the Measuring System . . . 164

7.2.2 Second Harmonic Effects . . . 165

7.2.3 Degree of Correspondence of Computed and Experimental Results . . . 169

7.3 Effects of the Bias Pulse on the Electronic Impedance . . . 171

7.3.1 Magnitude of the Bias Voltage Pulse . . . 171

7.3.2 Rise Time of the Bias Voltage Pulse . . . 172

7.4 Recovery Time from Transient to Steady-State Conditions . . . 182

7.5 Summary . . . 191

CHAPTER VIII : DISCUSSIONS AND CONCLUSIONS . . . 194

REFERENCES . . . 201

APPENDIX A: FOURIER ANALYSIS AND COMPLEX IMPEDANCE . . . 205

APPENDIX B: DE[illegible]N OF REFLECTION COEFFICIENT FROM CA[illegible]R REINSERTION . . . 208

APPENDIX C: R.F. DETECTION . . . 212

LIST OF TABLES

			Page
TABLE 3.1	:	Summary of Parameters for Constant Field Model (Silicon)	41
TABLE 4.1	:	Parameter Values for the Normalized Equations	70
TABLE 5.1	:	Characteristics of Impatt Diode Type H.P. 5082 - 0437	85
TABLE 6.1	:	Characteristics of H.P. 5082 - 0437 Impatt Diodes	142
TABLE 7.1	:	Transient and Steady-State Values of Electronic Impedance Computed and Measured at 6.0 GHz	173
TABLE 7.2	:	Transient and Steady-State Values of Electronic Impedance Computed and Measured at 7.8 GHz	174

LIST OF FIGURES

		Page
FIGURE 2.1 :	Read Diode (doping profile, electric field distribution, ionization integrand)	13
2.2 :	Voltage and Current Waveforms for Impatt Diode	14
2.3 :	One-Sided Abrupt p-n Junction (doping profile, electric field distribution, ionization integrand)	16
FIGURE 3.1 :	Boundary Conditions for Carrier Currents in the Avalanche Region of p^+n and n^+p Junctions	29
3.2 :	Distribution of Conduction Currents in an Avalanching - Reverse - Biased p^+n Junction	35
3.3 :	Constant Field Model for the Instantaneous Current Density Distributions in the Avalanche Region of p^+n and n^+p Junctions	37
3.4 :	Distribution of Electric Field for Various Models of the Impatt Diode for a Given Net Impurity Concentration	43
FIGURE 4.1 :	Analog Computer Program for an Impatt Diode Oscillator	63
4.2 :	Time Delay Circuit for Analog Computer Program	64
4.3 :	Computed Values of Electronic Impedance for an Avalanching Impatt Diode (Diode #1 at 6.0 GHz) where x_a=1.35μ, C_D=0.37 pf and K=0.0238	72

		Page
4.4 :	Computed Values of Electronic Impedance for an Avalanching Impatt Diode (Diode #1 at 6.0 GHz) where x_a=1.35μ, C_D=0.35 pf and K=0.0238	73
4.5 :	Computed Values of Electronic Impedance for an Avalanching Impatt Diode (Diode #1 at 6.0 GHz) where x_a=1.45μ, C_D=0.36 pf and K is Variable	74
4.6 :	Computed Values of Electronic Impedance for an Avalanching Impatt Diode (Diode #1 at 6.0 GHz) where x_a=1.55μ, C_D=0.35 pf and K=0.0238	75
FIGURE 5.1 :	Measuring System for Steady-State Temperature Dependence of Avalanche Diode Breakdown Voltage	82
5.2 :	Temperature Dependence of Junction Breakdown Voltage for H.P. 5082-0437 Impatt Diodes	84
5.3 :	Coaxial System for Measurement of Transient Junction Temperature	87
5.4 :	Photographs of Typical Oscilloscope Traces Observed During the Transient Junction Temperature Measurements	90
5.5 :	Relative Change in Junction Temperature with Time for an Impatt Diode	94
5.6 :	One Dimensional Model for Transient Heat Flow in an H.P. 5082-0437 Impatt Diode	96
5.7 :	Schematic of Cross Section of an H. 5082-0437 Impatt Diode	96

Page

5.8 : Relative Temperature Change with Distance in a One-Dimensional Heat Flow Model 100

FIGURE 6.1 : Circuit Arrangement for Impedance Measurements by Direct Comparison of Voltage/Current Waveforms 110

6.2 : Diode Holding Unit for Cavity-Oscillator Impedance Measurements 111

6.3 : Diode Holding Unit for Airline Tee Impedance Measurements 116

6.4 : Circuit Arrangement for Impedance Measurement by Direct Comparison of Voltage/Current Waveforms in Real Time 118

6.5 : Circuit Arrangement for Carrier Reinsertion Method of Impedance Measurement 121

6.6 : Diode Holding Unit for Carrier Reinsertion Impedance Measurements 122

6.7 : Magic Tee Portion of R.F. Detection Subsystem 127

6.8 : Cross Section of Hewlett Packard 5082-0437 Impatt Diode 132

6.9 : Equivalent Circuits for a Packaged Impatt Diode 135

6.10 : Photographs of Typical Waveforms Observed on the Oscilloscope during Electronic Impedance Measurements using the Carrier Reinsertion Method 139

		Page
6.11 :	Pulsed D.C. Current Response for Impatt Diode #1 at 6.0 GHz	144
6.12 :	Computed and Measured Electronic Impedance for Diode #1 at 6.0 GHz -4V Experimental Bias	145
6.13 :	Pulsed D.C. Current Response for Impatt Diode #1 at 6.0 GHz	146
6.14 :	Computed and Measured Electronic Impedance for Diode #1 at 6.0 GHz - 3V Experimental Bias	147
6.15 :	Pulsed D.C. Current Response for Impatt Diode #8 at 6.0 GHz	148
6.16 :	Computed and Measured Electronic Impedance for Diode #8 at 6.0 GHz - 4V Experimental Bias	149
6.17 :	Computed and Measured Electronic Impedance for Diode #8 at 6.0 GHz - 3 V Experimental Bias	150
6.18 :	Pulsed D.C. Current Response for Impatt Diode #1 at 7.8 GHz	151
6.19 :	Computed and Measured Electronic Impedance for Diode #1 at 7.8 GHz - 6 V Experimental Bias	152
6.20 :	Computed and Measured Electronic Impedance for Diode #1 at 7.8 GHz - 3 V Experimental Bias	153
6.21 :	Pulsed D.C. Current Response for Impatt Diode #8 at 7.8 GHz	154
6.22 :	Computed and Measured Electronic Impedance for Diode #8 at 7.8 GHz - 6V Experimental Bias	155

Page

Computed and Measured Electronic Impedance for Diode #8 at 7.8 GHz - 3 V Experimental Bias — 156

FIGURE 7.1 : Computed Ratio of Second Harmonic to Fundamental R.F. Component of Impatt Diode Current at 6.0 GHz — 166

7.2 : Computed Ratio of Second Harmonic to Fundamental R.F. Component of Impatt Diode Current at 7.8 GHz — 167

7.3 : Computed Steady-State Values of Electronic Impedance at 7.8 GHz and 2 V R.F. — 176

7.4 : Computed Steady-State Values of Electronic Impedance at 6.0 GHz and 2 V R.F. — 177

7.5 : Computed Steady-State Values of Electronic Impedance at 6.0 GHz and 10 V R.F. — 178

7.6 : Computed Values of Electronic Impedance for Diode #1 at 6.0 GHz for Different Bias Voltage Pulse Rise Times — 179

7 : Computed Values of Electronic Impedance for Diode #8 at 6.0 GHz for Different Bias Voltage Pulse Rise Times — 180

7.8 : Computed Current Response for Diode #1 at 6.0 GHz with 10 Volts R.F. and 4 Volts Experimental Bias — 182

7.9 : Computed Values of Electronic Impedance for Diode #1 at 6 0 GHz with 10 Volts R.F. and 4 Volts Experimental Bias — 183

Page

7.10 : Computed Current Response for Diode #1 at 6.0 GHz with 10 Volts R.F. and 3 V Experimental Bias 184

7.11 : Computed Values of Electronic Impedance for Diode #1 at 6.0 GHz and 3 Volts Experimental Bias 185

7.12 : Computed Current Response for Diode #8 at 6.0 GHz with 10 Volt R.F. and 3 Volts Experimental Bias 186

7.13 : Computed Values of Electronic Impedance for Diode #8 at 6.0 GHz and 3 Volts Experimental Bias 187

7.14 : Computed Current Response for Diode #8 at 6.0 GHz with 10 Volts R.F. and 4 Volts Experimental Bias. 188

7.15 : Computed Values of Electronic Impedance for Diode #8 at 6.0 GHz and 4 Volts Experimental Bias 189

FIGURE B.1 : Calibration Chart for R.F. Detector 211

FIGURE C.1 : Hewlett Packard Crystal Detector Model J424A 213

CHAPTER I

INTRODUCTION

In recent years, the use of semiconductor devices in microwave communications has increased significantly. Within the past several years, solid-state microwave oscillators and amplifiers have demonstrated economic and/or performance advantages over microwave tube components[1,2], and as a result are being incorporated into microwave systems. Two important semiconductor devices used for the generation and amplification of microwave frequencies are the Transferred Electron and Avalanche diodes. The Transferred Electron devices are most suited for low-noise, low-power applications, while the Avalanche devices, at the present time, are the most powerful solid-state source of microwave energy for continuous wave (CW) applications[3].

It is unlikely that the avalanche diode, or any other solid-state device, will simply replace tube devices in the near future. Rather, solid-state technology will be applied selectively to perform specific system functions which freely capitalize on the advantages of an all solid-state approach. For this reason and to ensure successful implementation in the new systems concepts, a precise knowledge of the characteristics and limitations of these solid-state devices is desirable.

This research project is concerned with studying the transient behavior of pulsed Avalanche diodes in their principal mode of operation. Avalanche diodes may operate in several modes[3], some of which are

referred to as TRAPATT, parametric and Thermal, with the principal mode being referred to as the Impatt mode (Impact ionisation Avalanche and Transit Time). Mathematical models describing the steady-state behaviour of this diode in different modes of operation have been published[4,5,6], but very little work has been carried out, so far, on the transient behavior, particularly during pulsed operation.

The buildup of oscillations in an Avalanche diode oscillator, and the operation of Avalanche diode amplifiers under varying signal conditions, are actually a study of the behavior of the diode's electronic impedance under transient conditions. The transient conditions may be those of initial turn on-off or the rapid-step changes in the level of R.F. power. The term "electronic impedance" refers only to the impedance of the active part of the semiconductor, while the term "diode impedance" refers to the combined effect of the electronic impedance, the impedance of the passive part of the semiconductor and the diode package impedance where applicable. This electronic impedance of an Impatt diode is dependent upon the d.c. bias voltage, as well as the frequency and magnitude of the R.F. voltage across the diode. Consequently, some special problems arise in the design of Impatt diode amplifiers and oscillators.

Solid-state circuits[7] capable of small-signal amplification at microwave frequencies, such as tunnel diode - and parametric amplifiers, have been in existence for many years. It has been within the last decade that semiconductor devices with potential high power

amplifying properties, such as Avalanche diodes, have become available. Several interesting circuit concepts have already been realized using Impatt diodes that promise to open up new areas of system applications[7]. Due to the negative resistance mechanism of the Impatt diode both the real and imaginary parts of the diode's impedance are strongly dependent on the d.c. bias current and R.F. signal levels. Shifts in the frequency and magnitude of the maximum gain[8] occur for different incident R.F. levels, which leads to some distortion in the amplification and injection locking characteristics of reflection amplifiers. A more thorough understanding of the transient behaviour of the diode's electronic impedance would be helpful in designing these amplifiers.

In the communications industry[9] there is a growing need for an inexpensive, short range, common carrier facility which has a high message-carrying capacity. This system would serve such purposes as intercity computer - to - computer links where the cost of laying cable would be prohibitively high. A two-level pulse code modulation (pcm) microwave repeater system with a bias modulated Impatt diode as a transmitter stage would fulfill this need. A bias modulated oscillator combines the oscillator and modulation functions into one unit. This system has significant cost advantages as well as requiring a minimum of hardware. Two ways in which two-level PCM can be produced are frequency modulation (FM), with a self-deviating oscillator, and amplitude modulation (AM) of the R.F. carrier.

In the self-deviating Impatt oscillator, the R.F. carrier is continuously produced at a constant amplitude and the bias modulation

changes the electronic impedance of the diode and hence the frequency of the R.F. oscillations. When the complex electronic impedance of the diode changes, both the real and imaginary parts change, which contributes to both amplitude and frequency changes in the R.F. oscillations. Consequently, some distortion from amplitude-frequency conversion can be expected. This, coupled with other characteristics of the FM modulation of Impatt diodes that are not fully understood[7], necessitates a better understanding of the Impatt diode's electronic impedance under transient conditions, particularly at the higher modulating frequencies.

For amplitude modulation of the R.F. carrier[10], the procedure is commonly referred to as Amplitude Shift Keying (ASK), where a binary system of either on or off can be used for the oscillator. For this ASK system, the R.F. fields have to grow in cavity,and this buildup will depend on the circuit parameters as well as on the electronic impedance of the diode. The diode's electronic impedance is a function of the modulating bias voltage and also the magnitude of the R.F. in the cavity. Therefore, a knowledge of the behaviour of the electronic impedance under transient conditions is necessary for proper circuit design. Further, the pulse lengths may be appreciable and the effects of the thermal properties of the diode junction on the performance of the oscillator will become important. Since the diode is pulse operated, the instantaneous junction temperature varies with time. This variation in temperature will cause both amplitude and frequency modulation characteristics[11] that may be detrimental to the system operation as a whole. Therefore, the transient thermal characteristics of the

diode's junction temperature should be known for design purposes.

The discussion of Impatt diodes is usually separated into small-and large-signal analysis. Small-signal results predict the range of current and frequency in which an Impatt diode will oscillate if placed in a proper resonate circuit. These results also indicate the magnitude of the maximum negative impedance which can be generated by the diode. This information is very useful during the initial stages of device evaluation for oscillator and amplifier circuits. However, small-signal analysis does not provide sufficient information(12) concerning maximum power output, efficiency, saturation and stability characteristics which are important in large-signal oscillator and amplifier designs. Thus, the requirement for and the name large-signal analysis. The analytic solutions for steady-state small-signal analysis are available in closed form due to the many approximations that can be made. While simplified analytic solutions for the steady-state large-signal case may be presented in closed form, the usual procedure is to obtain computer solutions to less simplified describing equations. A study of the transient behaviour of the electronic impedance of an Impatt diode will span the range of applicability of both small - and large-signal analysis, and incorporate the time-dependence of the d.c. bias voltage pulses, with the most probable form of solution being a computer model of the diode.

e presentation of this work is divided into several parts. Chapter II discusses the general theory of operation and the particular device structure chosen to represent the Impatt diode. Chapter III

describes the mechanisms and the assumptions made in the physical model along with the fundamental equations and boundary conditions that mathematically determine both the steady-state and transient problems. Chapter IV describes the details of the analytical formulation and computational techniques used in the solution of the time dependent equations for the Impatt diode. Chapter V presents the analytical and experimental investigation of the transient heat flow in the diode's junction. Chapter VI covers the experimental techniques developed for the measurement of the electronic impedance of the Impatt diode under transient conditions. Chapter VII provides a comparison of the computational model and the experimental results. Chapter VIII presents a discussion and conclusions drawn from the results of this study.

CHAPTER II

IMPATT DIODES

When a semiconductor p-n junction is reverse-biased, a space charge region is formed that is depleted of mobile carriers and only a small reverse saturation current flows. When the reverse bias voltage is increased until it exceeds a critical value, the junction breaks down and a large current will then flow for only a small increase in bias voltage. This large current is the result of avalanche breakdown, when internal secondary emmission causes a multiplication of electrons and holes in the depletion region of the junction. The critical level of reverse bias voltage, at which the multiplication begins, is referred to as the breakdown voltage. The p-n junction, in the avalanche breakdown condition, may exhibit a negative-resistance characteristic in the microwave frequency range. A diode (p-n junction) with negative-resistance terminal characteristics, has the capability of converting d.c. energy to R.F. energy and thus an R.F. voltage present across the diode will grow in amplitude until limited by circuit and diode losses.

Avalanche diodes can be designed and operated in various modes. The first and most important mode[13] is the IMPATT mode. (Impact ionization Avalanche and Transit Time). This mode produces its negative-resistance terminal characteristics by having the carrier density lag the applied electric field by more than 90°, which is also the phase difference between the fundamental R.F. component of the diode's external current and the R.F. voltage across the diode.

2.1 Basic Principles of Operation

The more common materials used in the fabrication of avalanche diodes are Silicon, Germanium and Gallium Arsenide. Due to the basic physical phenomena involved in the generation of the negative-resistance in this device, almost any semiconductor material can, in principle, be employed in the construction of avalanche diodes. The Impatt mode of operation involves two basic properties of carrier transport in solids at high electric fields, namely those of avalanche multiplication and transit-time delay.

The breakdown of the p-n junction is caused by an avalanche multiplication process involving both electrons and holes (as opposed to other processes such as zener breakdown and tunneling). When the electric field becomes sufficiently high, a charge carrier (electron or hole) can acquire sufficient energy from the electric field, between collisions, to dislodge a bound electron into the conduction band, during a collision, thus also creating a hole in the valence band. This action is referred to as impact ionization and occurs for magnitudes of the electric field greater than about 10^5 V/cm (for Silicon). The probability of this electron-hole pair creation, or ionization rate, is a sensitive function of the electric field strength. The ionization rate can increase as much as five orders of magnitude for an increase in the electric field strength of only two or three times[14]. When the electric field changes periodically with time around an average value, the generation rate of carriers follows the field change almost instantaneously. However, because the total generation of carriers depends upon the number of carriers present, the total number of carriers

generated does not change in unison with the electric field and keeps on increasing after the electric field has passed its peak value. The total number of carriers peaks and starts to decrease when the field has decreased from the peak to the average value. Thus, bunches of carriers are formed and the a.c. variation in the number of carriers lags the a.c. component of the electric field by 90°.

When the electric field is low, the average drift velocity of the carriers is directly proportional to the electric field and the proportionality constant is called the low field mobility. As the field strength increases, carriers interact more strongly with the lattice so that the average drift velocity falls much below that of a linear projection from the low field values. For electric field strengths above about 10^4 V/cm (for Silicon), the drift velocity approaches a limiting value and becomes independent of the electric field. This limiting value is referred to as the scattering-limited drift velocity. When a bunch of carriers is injected into a region where the electric field is such that avalanche multiplication does not occur and yet the field is sufficiently high that scattering limited drift velocities apply, the transit-time of the bunch will be directly proportional to the width of the region. This transit-time can be used to delay the collection of the bunch of carriers and thus introduce a phase shift between the fundamental R.F. component of the external current, due to the transiting bunch of carriers, and the R.F. voltage across the transit-time region.

The above discussion of avalanche multiplication and transit-time delay has been for ideal conditions. In practice, the effects of space charge and non-scattering-limited drift velocities must be taken into account. In the region where avalanche multiplication occurs, the bunch of carriers causes the electric field to be depressed. This depression of the electric field due to the space charge effect of the carriers, results in the field strength falling below the average value before it would normally do so, when affected by the R.F. voltage alone. Therefore, the phase lag of the bunch of carriers, due to the avalanche process, is decreased and will be less than the optimum 90° with respect to the R.F. voltage. This space charge effect will increase with increasing magnitude of the bunch of carriers. When the electric field in the transit-time region falls below that required to maintain scattering-limited values of drift velocity, the drift velocity becomes dependent on the magnitude of the electric field. When this occurs, dielectric relaxation tends to smooth out the carrier bunching. This "debunching" reduces the magnitude of the current external to the transit-time region and hence reduces the power output.

Generally, Impatt diodes consist of an avalanche region, where carrier multiplication occurs, appended to a transit-time (drift) region where carrier multiplication does not occur and the drift velocity of the carriers is assumed to be scattering limited. In the avalanche region holes and electrons are produced in practically equal numbers and since the multiplication is very sensitive to the magnitude of the electric field, it is here that the carrier transport

current is modulated by the R.F. field. The contribution of the avalanche process to the phase difference between the diode's external conduction current and the R.F. voltage across the diode will be something less than 90° due to the space charge effects of the bunches of carriers. As these bunches of carriers "drift" across the transit-time region, the phase difference added to that of the avalanche process is approximately equal to one-half the transit-time. The working region of the diode consists of both the avalanche and drift regions, with the total delay in the conduction current being the sum of the avalanche and transit-time processes.

2.2 Types of Impatt Diodes

The basic members of the Impatt diode family[14] are the Read diode, one-sided abrupt p-n junction, linearly-graded p-n junction and the p-i-n diode. Only the Read diode and the one-sided abrupt p-n junction are of interest for this work. The Read diode is of interest because it is a convenient structure for analytical purposes and contributes to an understanding of the dynamic operating characteristics of the Impatt diode. The one-sided abrupt p-n junction is of interest because it is the type of Impatt diode that is most commonly manufactured and also is the type which will be used in the experimental portion of this work. The linearly-graded p-n junction and the p-i-n diode are not of direct interest for this work and have only been included here for completeness.

Fig. 2.1 shows the doping profile, electric field distribution and ionization integrand, at the breakdown condition, for an idealized

Read diode ($p^+ n \nu n^+$ or its dual $n^+ p$ [illegible]). The corresponding a.c. voltage and current waveforms are shown in Fig. 2.2. For the Read model, all of the avalanche process is confined to the n region of the $p^+ n \nu n^+$ diode (in the dual model - the p region) where the actual avalanche region is defined by the ionization integrand. It is assumed that this avalanche region is sufficiently narrow that its transit time is a negligible portion of an R.F. cycle. The diode is designed such that the electric field in the drift region (the intrinsic region) is sufficiently high to ensure that the carriers travel at their scattering limited drift velocities. In Fig. 2.2, the idealized a.c. operation of the diode is depicted. The a.c. component of the electric field ($E_{a.c.}$) modulates the ionization rates for the carriers to form a pulse of carriers in the avalanche region. As this pulse of carriers is formed the space charge effect of the carriers (ΔE) also increases and, in practice, the peak of the pulse of carriers will occur before the electric field has returned from its peak to its average value. Thus, the phase shift in the avalanche region will be somewhat less than the 90° shown in Fig. 2.2. After the pulse of carriers has been formed, it travels across the transit-time region at the scattering limited drift velocity. For the duration of this transit time, of the pulse of carriers, a steady current flows in the external circuit (I_{ex}). Once the pulse of carriers reaches the collecting terminal of the drift region the electric field in the avalanche region rises above the average value and the whole process repeats itself. As shown in Fig. 2.2, the fundamental R.F. component of the external current is delayed with respect to the R.F. voltage by the phase lag

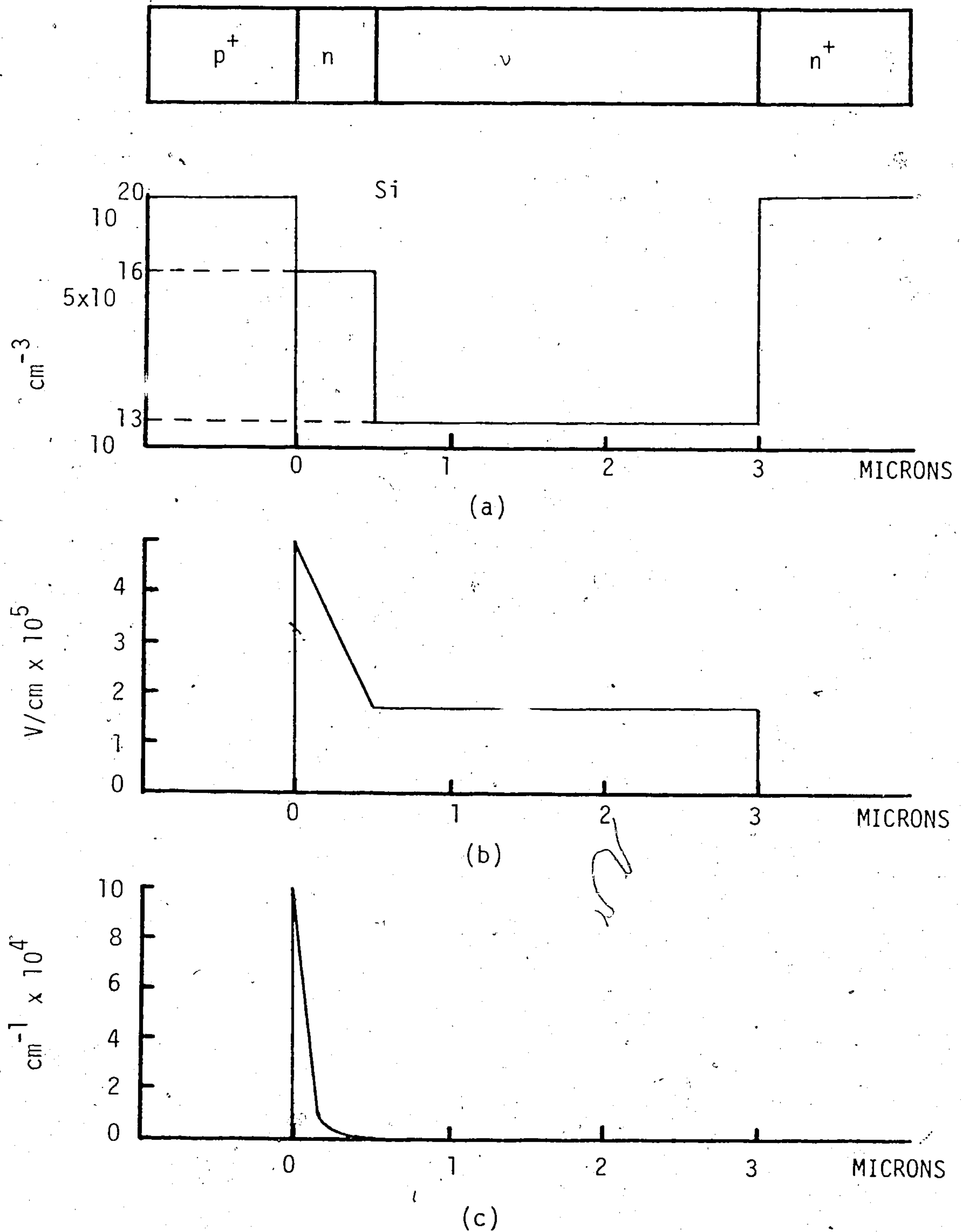

FIG. ... READ DIODE
(a) DOPING PROFILE ($p^+n\nu n^+$) NET IMPURITY CONCENTRATION
(b) ELECTRIC FIELD DISTRIBUTION
(c) IONIZATION INTEGRAND AT BREAKDOWN

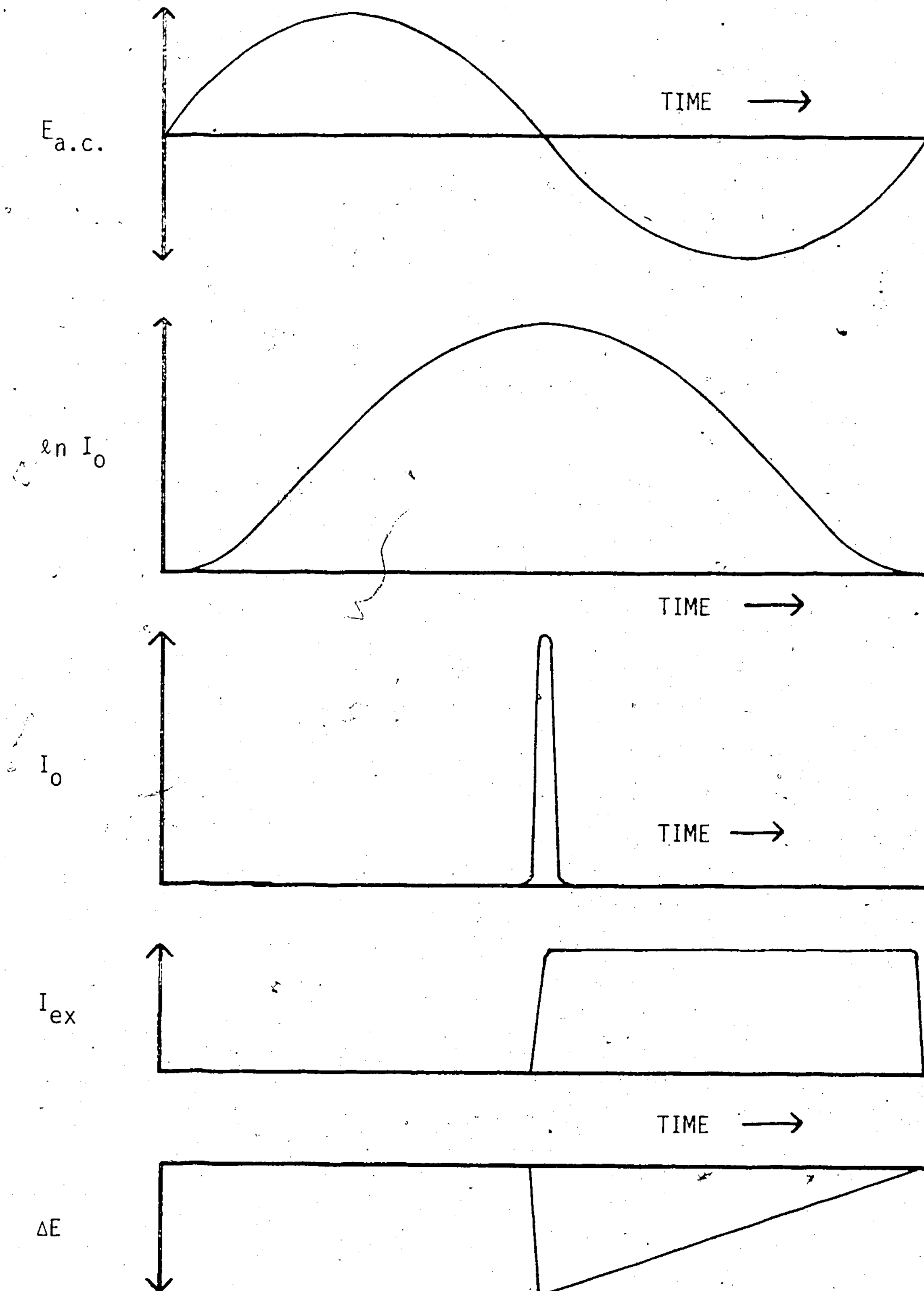

FIG. 2.2 VOLTAGE AND CURRENT WAVEFORMS FOR IMPATT DIODE
$E_{a.c.}$ -A.C. COMPONENT OF ELECTRIC FIELD IN AVALANCHE REGION
I_o -CONDUCTION CURRENT IN AVALANCHE REGION
I_{ex} -CONDUCTION CURRENT EXTERNAL TO DIODE
ΔE -REDUCTION IN ELECTRIC FIELD DUE TO SPACE CHARGE OF I_o

inherent in the avalanche process plus the phase lag of one-half the transit-time of the drift region. In this manner the negative-resistance terminal characteristics of the Read diode are formed.

In Fig. 2.3, the doping profile, electric field distribution and ionization integrand for the breakdown condition of an idealized one-sided abrupt p-n junction are given. The gradient of the electric field is sufficiently steep that the ionization integrand and hence the width of the avalanche region are localized near one end of the depletion region. Therefore, the total depletion region can be divided into separate avalanche and drift regions, with the analysis being carried out in a similar manner to that of the Read diode. A prominent distinction that occurs between these two types of Impatt diode is in the length of the drift region. For the field in the drift region to be sufficiently high to ensure that the carriers travel at their scattering limited velocities, the drift region may not be long enough to give a full 90° phase lag (at the microwave frequency in use) as in the Read model. Also, any portion of the drift region where the drift velocity falls below its scattering-limited value will contribute a debunching effect to the pulse of carriers, with a corresponding decrease in the magnitude of the external current. Therefore, the one-sided abrupt p-n junction will be less efficient than the Read diode. However, the one-sided abrupt p-n junction is more readily manufactured and therefore has a distinct practical advantage over its Read model counterpart.

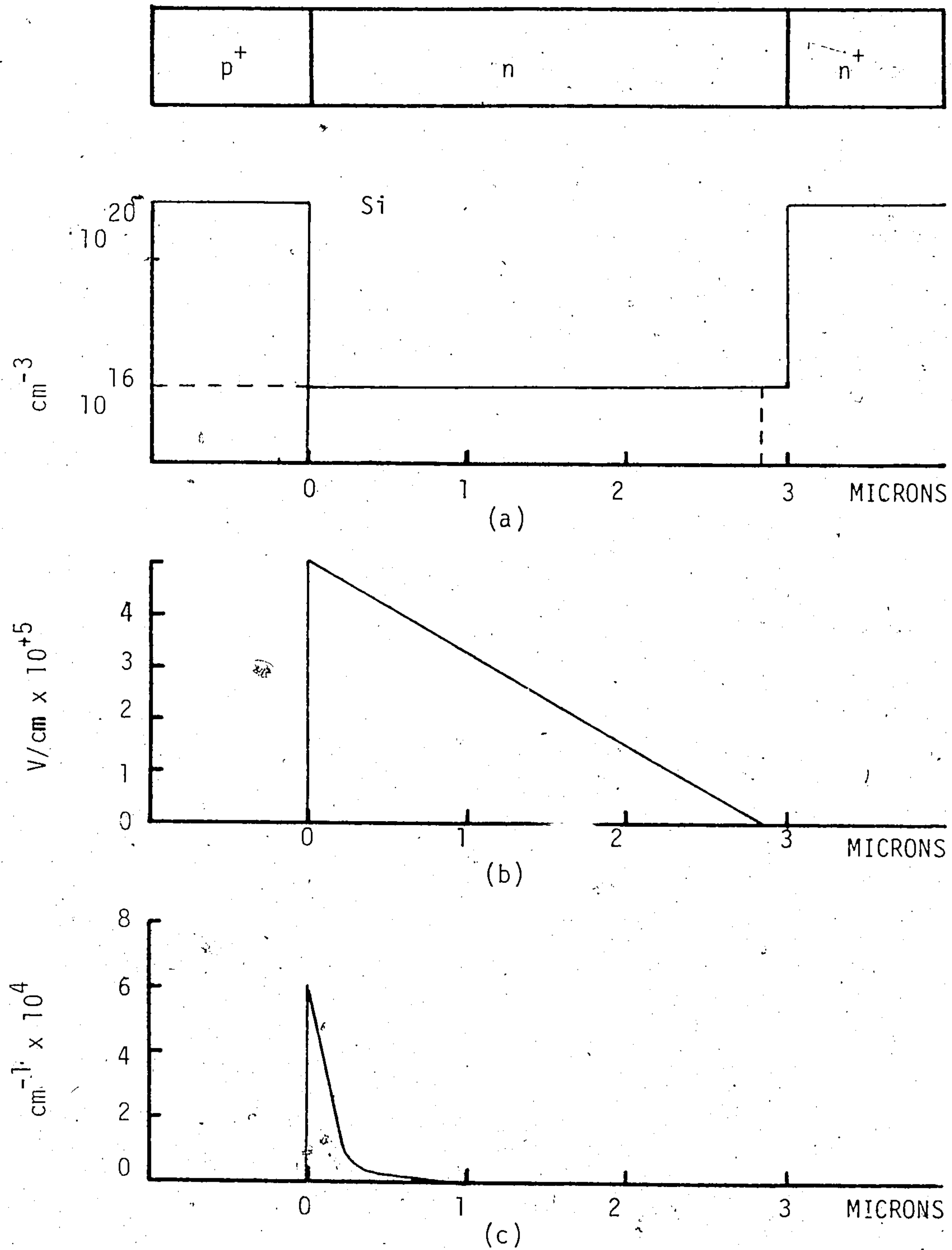

FIG. 2.3 ONE-SIDED ABRUPT P-N JUNCTION
(a) DOPING PROFILE (p^+n) NET IMPURITY CONCENTRATION
(b) ELECTRIC FIELD
(c) IONIZATION INTEGRAND AT BREAKDOWN

2.3 Fabrication of Impatt Diodes[15]

As mentioned previously in Section 2.2, the more common materials for the fabrication of Impatt diodes are Silicon, Germanium and Gallium Arsenide. The material parameters such as ionization rate, dielectric constant and thermal conductivity will alter the characteristics of the Impatt diode when constructed from different materials. Germanium has the highest ionization rate and therefore the lowest breakdown field. This is an advantage because it reduces the necessary input power for Impatt operation. The ionization rates for Gallium Arsenide and Silicon are about the same. Germanium has the largest dielectric constant and will have lower impedance levels and also higher bias currents, so this is a disadvantage. Silicon and Gallium Arsenide have similar dielectric constants. The thermal conductivity of Germanium is only about 30% that of Silicon, with Gallium Arsenide having a lower value of thermal conductivity than Germanium. Because of the relatively high values of reverse bias voltage required for Impatt diode operation, an appreciable amount of heat is generated in the p-n junction and a high value of thermal conductivity is advantageous. The technology for material preparation and processing is more highly developed for Silicon and this, along with its high thermal conductivity, make Silicon the most commonly used material for the fabrication of Impatt diodes.

Fabricating a Read model of the Impatt diode is more difficult than fabricating a one-sided abrupt p-n junction model. In the formation of the Read diode, using a $p^+ n \nu\ n^+$ as an example, a double

diffusion technique is required where a low concentration of donors is diffused deeply and then a shallow diffusion of a high concentration of acceptors is carried out. This is not the only technique for the fabrication of Read diodes but is a typical illustration of the complexities involved. In the fabrication of abrupt p-n junctions only a single diffusion is necessary, namely that of a shallow diffusion of a high concentration of acceptors. However, care must be taken that the junction depth (n region) is less than the space-charge (depletion) region for the breakdown voltage associated with the doping concentration of the n region. Otherwise, part of the high resistivity region will not be swept clear of mobile carriers when the reverse bias voltage has reached the breakdown level and also will have a magnitude of electric field that will be too low to maintain scattering limited drift velocities. In theory, the Read diode should be more efficient than the one-sided abrupt p-n junction however, according to the results reported in the literature,(15) after fabrication, the abrupt junction diodes may outperform their Read diode counterparts.

In avalanche diodes, the d.c. power which is not converted to microwave power, generates heat in the high field region near the junction. As the junction temperature increases, the breakdown voltage increases and the ionization rates decrease. Under conditions of uniform current density, the center of the junction area will be hottest and the temperature dependence of the ionization rates and breakdown voltage will tend to decrease the current density in the diode's central area. Thus, the temperature distribution across the diode junction is more uniform but the current distribution will be non

uniform and tend to concentrate near the outer regions of the junction area. It is therefore advantageous to design the diode with the junction near the semiconductor surface and to mount the diode with this semiconductor surface in contact with a low thermal resistance path to the heat sink.

CHAPTER III

PHYSICAL AND MATHEMATICAL MODEL

3.1 Physical Model

The work reported here is concerned with the behaviour of Impatt diodes. The characteristics of the semiconductor material and the formation of the p-n junction are of interest in so far as they affect the operation of the Impatt diode. Some of the physical characteristics of semiconductors that may be of interest and the assumptions made, will now be discussed.

3.1.1 Carrier Recombination[16]

Under conditions of thermal equilibrium, carrier generation is balanced by carrier recombination. When thermal equilibrium is disturbed, the mechanisms that restore equilibrium are the drift and diffusion of carriers into and out of the region, along with recombination. The lower limit of the lifetime of minority carriers in silicon[14] is of the order of 10^{-8} seconds. The transit time of the carriers in Impatt diodes is of the order of 10^{-10} seconds, for diodes designed to function below 10GHz. Therefore, although the Impatt diodes may operate with high current densities, recombination should be of small importance and will be assumed to be negligible for purposes of this study.

3.1.2 Surface Boundary Conditions[17]

In this analysis, it is assumed that thermal equilibrium prevails at the contacts, so that the carrier density at the contacts is constant and equal to its thermal equilibrium value at all voltages of interest.

Along with the condition for thermal equilibrium, it is also assumed that charge neutrality prevails at the contacts. These two assumptions are generally regarded as the basis for having ohmic contacts. Some recombination may also occur at the surfaces but this is assumed to be negligible in this study.

3.1.3 Degeneracy[16]

For purposes of this study, Boltzman's transport equation and Boltzman statistics are assumed to be valid. These assumptions simplify the mathematical analysis as changes in transport phenomena can be derived from Boltzman's transport equation and the validity of Einstein's relation can be assumed. As discussed by Shockley[18], the difference between Fermi and Boltzman's statistics is negligible when the predicted carrier concentrations are small compared to the effective number of states in the conduction and valence bands. For Silicon, Boltzman statistics are valid up to carrier densities of $10^{18} cm^{-3}$,[16] which is much higher than the normal doping levels in Impatt diodes. Therefore, the assumption of a non-degenerate semiconductor will be made.

3.1.4 Carrier Mobility[16,19]

The mobility of electrons and holes is determined by the type of dominant scattering. The two most significant forms of scattering are those caused by ionized impurities and those caused by mechanical vibrations of the crystal. Scattering by ionized impurities is coulomb scattering and is most effective at low velocities, while mechanical vibrations cause acoustic and optical phonon scattering. For high electric fields ($\sim 10^5$ v/cm),

which is the normal operating range for Impatt diodes, the carriers gain appreciable energy from the electric field. As the field increases, the average energy of the carriers also increases, and they acquire an effective temperature which is higher than the lattice temperature. These high electric fields heat the carriers at a sufficient rate that the mobility decreases in proportion to the rate of increase in the electric field, causing the carrier drift velocity to become scattering limited.

3.1.5 Microplasmas(16,20,21)

As a result of defects in the crystal structure of the semiconductor, small areas are formed that behave as a gaseous plasma. These phenomena are often referred to as microplasmas. When the Impatt diodes are reverse-biased, these microplasma areas reach the avalanche condition at an applied voltage that is a few volts lower than the remainder of the junction. The resulting avalanche breakdown starts at several locations in the junction and gradually spreads, with increasing voltage, until the whole junction avalanches. This gradual and somewhat unpredictable start of avalanche breakdown can be avoided by biasing the Impatt diode, such that a steady d.c. current of one milliampere is maintained in the diode.

3.2 Validity of One-Dimensional Analysis

In the use of more than one-dimensional analysis, all the physical parameters for a particular diode would be required and the complexity of the describing equations would be greatly increased. The Impatt diodes available for this work are not adequately characterized to warrant the greatly increased effort and expense required to carry out an analysis in more than one dimension.

Further, the physical construction of the Impatt diodes tends to accentuate one dimensional behaviour. In a typical, low power, Impatt diode, the cross-sectional area is about $10^{-4} cm^2$ and the length of the activity region is 3-5 microns (for oscillations around 7 GHz). This results in a diameter to length ratio of around 30:1. Since it is assumed that avalanche multiplication occurs uniformly over the cross-sectional area, the carriers will travel mainly directly through the diode. Only under very high current densities, where carrier mutual repulsion and non-uniformity of temperature become appreciable, will the lateral spread of carriers be significant. The Impatt diode may be operated at high current densities and some inaccuracy will be inherent in the use of one-dimensional analysis, however this should be a small effect. Therefore, one-dimensional analysis will be used throughout this work.

3.3 Mathematical Model

Having made the previous simplifying assumptions for the physical processes occurring inside the device, the next step is to obtain mathematical equations which will model the physical behaviour of the device. These mathematical equations will be written in one-dimensional form.

3.3.1 Fundamental Mathematical Equations[16]

The current equations:

These equations are sometimes referred to as charge transport equations, as they are derived from the Boltzman transport equation under the assumption of valid Boltzman statistics. The equations relate the electron and hole conduction currents to

their drift and diffusion parts and are given as:

$$J_n(x,t) = \mu_n(x,t) \cdot E(x,t)\ n(x,t)q + \mu_n(x,t)KT \frac{\partial n(x,t)}{\partial\ x} \quad (1)$$

$$J_p(x,t) = \mu_p(x,t)\ E(x,t)\ p(x,t)q - \mu_p(x,t)KT \frac{\partial p(x,t)}{\partial\ x} \quad (2)$$

$$J_c(t) = J_n(x,t) + J_p(x,t) \quad (3)$$

The current continuity equations:

The equations are statements of conservation of electric charge and for this case are written as follows:

$$\frac{\partial\ n(x,t)}{\partial t} = \frac{1}{q} \frac{\partial\ J_n(x,t)}{\partial x} + G(x,t) \quad (4)$$

$$\frac{\partial\ p(x,t)}{\partial t} = -\frac{1}{q} \frac{\partial\ J_p(x,t)}{\partial x} + G(x,t) \quad (5)$$

Where $G(x,t)$ is the net rate of generation of hole-electron pairs due to avalanche multiplication. (recombination has been assumed to be negligible)

The total current equation:

The total current is expressed as the sum of the electron and hole carrier currents plus the displacement current and is given as,

$$J_t(t) = J_n(x,t) + J_p\ (x,t) + \frac{\varepsilon\ \partial\ E(x,t)}{\partial t} \quad (6)$$

Poisson's equation:

This equation relates the divergence of the electric field to the spacial charge density and can be written in one-dimensional form as

$$\frac{\partial E(x,t)}{\partial x} = \frac{q}{\varepsilon}\left[p(x,t) - n(x,t) + N_D(x) - N_A(x)\right] \qquad (7)$$

Supplementary equations:

The carrier generation rate[14] is defined as,

$$G(x,t) = \alpha_n(E)\, v_n(x,t)\, n(x,t) + \alpha_p(E)\, v_p(x,t)\, p(x,t) \qquad (8)$$

where the ionization rates[14] have the form

$$\alpha_{n,p}(E) = A \exp\left(-\left(\frac{b}{E}\right)^m\right) \quad A,\ b,\ m \text{ are constants}$$

These equations are highly nonlinear and to arrive at an analytical solution, several simplifying assumptions have to be made, which may limit the range of applicability of the resulting solution. Even when using a digital computer to solve the equations numerically, it is advantageous to make many of these approximations, because of limitations on computer memory and to avoid excessively large amounts of computation time.

Since this study is concerned with transient response, which implies solving the equations for a time interval comprising a large number of R.F. cycles, to use a minimum number of approximations may be impractical. Therefore, a balance was reached between the amount of simplific-

ation of the equations and the cost expended, to obtain a solution sufficiently versatile to produce significant results.

3.3.2 Development of Conduction Current Equation

The basic equations given earlier, can be simplified with very little loss in accuracy by making the following assumptions:

- the drift current is many times greater than the diffusion current so that the diffusion current can be neglected.
- the electric field is sufficiently high that the carrier velocities are approximately constant, at their scattering limited values.
- carrier generation is confined to the avalanche region.

With these assumptions, the basic equations for the avalanche region become,

$$J_n(x,t) = v_n\, q\, n(x,t) \qquad J_p(x,t) = v_p\, q\, p(x,t) \tag{1}$$

$$J_c(t) = J_n(x,t) + J_p(x,t) \tag{2}$$

$$\frac{\partial\, n(x,t)}{\partial\, t} = \frac{1}{q}\,\frac{\partial\, J_n(x,t)}{\partial\, x} + \alpha_n(E)\, v_n\, n(x,t) + \alpha_p(E)\, v_p\, p(x,t) \tag{3}$$

$$\frac{\partial\, p(x,t)}{\partial\, t} = -\frac{1}{q}\,\frac{\partial\, J_p(x,t)}{\partial\, x} + \alpha_n(E)\, v_n\, n(x,t) + \alpha_p(E)\, v_p\, p(x,t) \tag{4}$$

Upon multiplying Eqs. (3) and (4) by q v_n and q v_p respectively, the result is

$$\frac{\partial J_n(x,t)}{\partial t} = v_n \frac{\partial J_n(x,t)}{\partial x} + v_n\alpha_n(E)\, J_n(x,t) + v_n\alpha_p(E)\, J_p(x,t) \qquad (5)$$

$$\frac{\partial J_p(x,t)}{\partial t} = -\, v_p \frac{\partial J_p(x,t)}{\partial x} + v_p\alpha_n(E)\, J_n(x,t) + v_p\alpha_p(E)\, J_p(x,t) \qquad (6)$$

Then, adding Eqs. (5) and (6) and using Eq. (2), the following result is obtained:

$$\frac{\partial J_c(t)}{\partial t} = v_n \frac{\partial J_n(x,t)}{\partial x} - v_p \frac{\partial J_p(x,t)}{\partial x} + (v_n+v_p)[\alpha_n(E)J_n(x,t) + \alpha_p(E)J_p(x,t)] \qquad (7)$$

A more meaning expression can be obtained by adding and subtracting the quantity $(v_n+v_p)\alpha_n(E)\, J_p(x,t)$ in Eq. (7) to give

$$\frac{\partial J_c(t)}{\partial t} = v_n \frac{\partial J_n(x,t)}{\partial x} - v_p \frac{\partial J_p(x,t)}{\partial x} + (v_n+v_p)\, [\alpha_n(E)\, J_c(t) + (\alpha_p(E) - \alpha_n(E))\, J_p(x,t)] \qquad (8)$$

Alternately, by adding and subtracting $(v_n+v_p)\, \alpha_p(E)\, J_n(x,t)$ in Eq. (7) the result is

$$\frac{\partial J_c(t)}{\partial t} = v_n \frac{\partial J_n(x,t)}{\partial x} - v_p \frac{\partial J_p(x,t)}{\partial x} + (v_n+v_p) [\alpha_p(E) J_c(t) +$$

$$(\alpha_n(E) - \alpha_p(E)) J_n(x,t)] \qquad (9)$$

The spatial dependence Eqs. (8) and (9) can be removed by integrating these equations across the avalanche region, with the following results:

$$x_a \frac{\partial J_c(t)}{\partial t} = [v_n J_n(x,t) - v_p J_p(x,t)]_0^{x_a} + (v_n+v_p) J_c(t) \int_0^{x_a} \alpha_n(E)dx +$$

$$(v_n+v_p) \int_0^{x_a} (\alpha_p(E) - \alpha_n(E)) J_p(x,t)dx \qquad (10)$$

$$x_a \frac{\partial J_c(t)}{\partial t} = [v_n J_n(x,t) - v_p J_p(x,t)]_0^{x_a} + (v_n+v_p) J_c(t) \int_0^{x_a} \alpha_p(E)dx +$$

$$(v_n+v_p) \int_0^{x_a} (\alpha_n(E) - \alpha_p(E)) J_n(x,t)dx \qquad (11)$$

Applying Eq.(10) to the p^+n junction and using the boundary conditions for the carrier currents given in Fig. 3.1, the first term on the right hand side of Eq. (10) becomes

$$[v_n J_n(x,t) - v_p J_p(x,t)]_0^{x_a} = [v_n(J_c(t) - J_{ps}) - v_p J_s] - [v_n J_{ns} - v_p(J_c(t) -$$

$$J_{ns})] = (v_n+v_p) J_c(t) - (v_n+v_p) J_s \qquad (12)$$

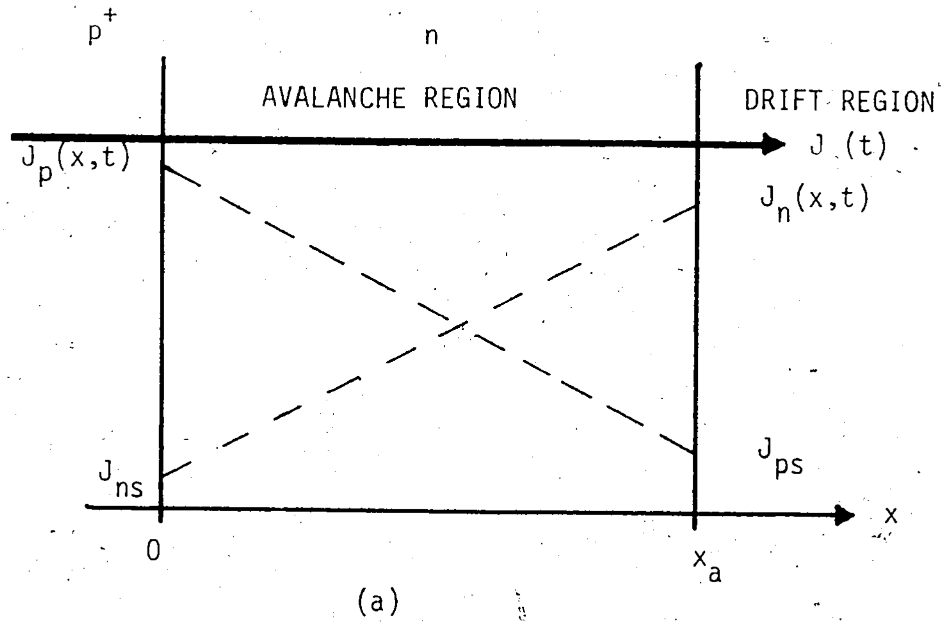

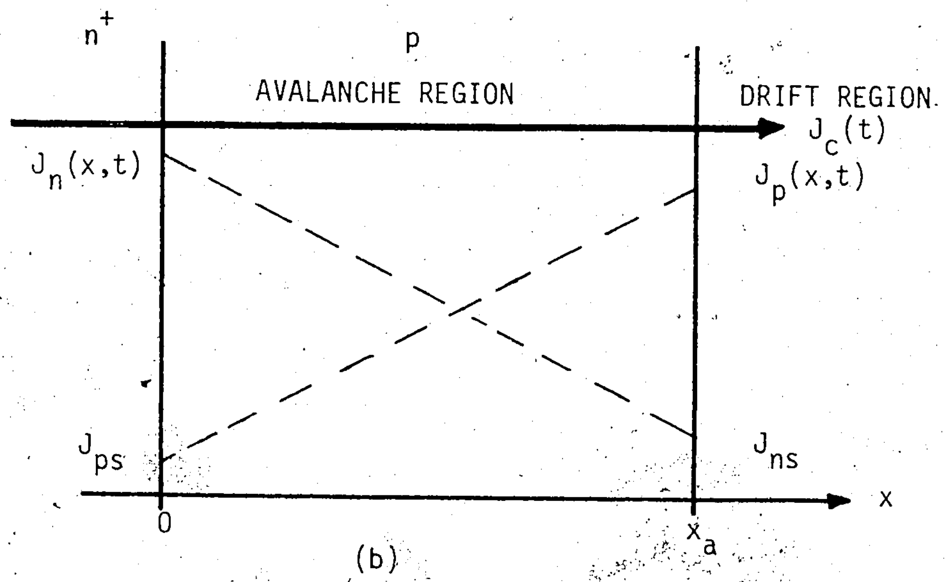

FIG. 3.1 BOUNDARY CONDITIONS FOR CARRIER CURRENTS IN THE AVALANCHE REGION OF (a) p^+n JUNCTIONS (b) n^+p JUNCTIONS

where the relation $J_s = J_{ns} + J_{ps}$ has been used.
Similarly, when Eq. (11) is applied to the n^+p junction, whose boundary conditions are also given in Fig. 3.1, the first term on the right hand side of Eq. (11) becomes the same as that expressed in Eq. (12).

Using the above results, and after some rearranging of terms, the equations become

$$\frac{\partial J_c(t)}{\partial t} = \left(\frac{v_n+v_p}{x_a}\right) J_c(t) \left(\int_0^{x_a} \alpha_n(E)\, dx - 1\right) + \left(\frac{v_n+v_p}{x_a}\right) J_s +$$
$$\left(\frac{v_n+v_p}{x_a}\right) \int_0^{x_a} (\alpha_p(E) - \alpha_n(E))\, J_p(x,t) dx \qquad (13)$$

$$\frac{\partial J_c(t)}{\partial t} = \left(\frac{v_n+v_p}{x_a}\right) J_c(t) \left(\int_0^{x_a} \alpha_p(E)\, dx - 1\right) + \left(\frac{v_n+v_p}{x_a}\right) J_s +$$
$$\left(\frac{v_n+v_p}{x_a}\right) \int_0^{x_a} (\alpha_n(E) - \alpha_p(E))\, J_n(x,t) dx \qquad (14)$$

where Eq. (13) applies to the p^+n junctions and Eq.(14) to the n^+p junctions.

These equations can be greatly simplified if the assumption is made that $\alpha_n(E) = \alpha_p(E)$. This results in both equations being identical as the last term on the right hand side of the equations vanishes. Once this assumption is made, all distinction between different types of junctions and semiconductor materials is lost. Since it has been shown that there is a significant difference between the behaviour of n^+p and p^+n junctions[22] and that in general, the ionization rates for holes and electrons are not

equal[14], this assumption will not be made and the last term on the right hand side of Eqs. (13) and (14) will be retained.

3.3.3 Constant Electric Field Model

In their present form, Eqs. (13) and (14) of the previous subsection are not readily solvable, due to the presence of terms involving the integration with respect to the spatial variable (x). One method of eliminating these spatial integration terms is to assume a constant electric field all across the avalanche region. Then, the ionization rates are constant and the spatial dependence of the current densities $J_n(x,t)$ and $J_p(x,t)$ can be taken from the d.c. analysis given by Moll[16].

From Moll, the current distributions are given as

$$\frac{J_n(x)}{J_{d.c.}} = \exp\left[\int_0^x (\alpha_n(E) - \alpha_p(E))dx'\right] \int_0^x \alpha_p(E) \exp\left[-\int_0^{x'} (\alpha_n(E) - \alpha_p(E))dx''\right]dx' \quad (1)$$

$$\frac{J_p(x)}{J_{d.c.}} = 1 - \frac{J_n(x)}{J_{d.c.}} \quad (2)$$

for a p^+n junction and as

$$\frac{J_p(x)}{J_{d.c.}} = \exp\left[\int_0^x (\alpha_p(E) - \alpha_n(E))dx'\right] \int_0^{x'} \alpha_n(E) \exp\left[-\int_0^{x'} (\alpha_p(E) - \alpha_n(E))dx''\right]dx' \quad (3)$$

$$\frac{J_n(x)}{J_{d.c.}} = 1 - \frac{J_p(x)}{J_{d.c.}} \qquad (4)$$

for the n^+p junction. The term $J_{d.c.}$ is actually the instantaneous value of the conduction current density, $J_c(t)$, for the constant electric field assumption, and using this assumption the current distribution equations reduce to

$$\frac{J_n(x)}{J_c(t)} = \frac{\alpha_p(E)}{\alpha_p(E)-\alpha_n(E)} \left[1 - \exp((\alpha_n(E) - \alpha_p(E))x)\right] \qquad (5)$$

for a p^+n junction and to

$$\frac{J_p(x)}{J_c(t)} = \frac{\alpha_n(E)}{\alpha_n(E)-\alpha_p(E)} \left[1 - \exp(-(\alpha_n(E) - \alpha_p(E))x)\right] \qquad (6)$$

for a n^+p junction. Substituting Eqs. (5) and (6) into Eqs. (2) and (4) respectively, these equations become

$$\frac{J_p(x)}{J_c(t)} = - \frac{-\alpha_n(E) + \alpha_p(E)\exp((\alpha_n(E) - \alpha_p(E))x)}{\alpha_n(E) - \alpha_p(E)} \qquad (7)$$

for a p^+n junction and

$$\frac{J_n(x)}{J_c(t)} = - \frac{\alpha_p(E) + \alpha_n(E)\exp(-(\alpha_n(E) - \alpha_p(E))x)}{\alpha_n(E) - \alpha_p(E)} \qquad (8)$$

for a n^+p junction.

When Eqs. (7) and (8) are substituted into Eqs. (13) and (14) (subsection 3.3.2) respectively, and the integration with respect to the spatial variable carried out, the differential equations which describe the conduction current in the avalanche region become:

$$\frac{\partial J_c(t)}{\partial t} = \left(\frac{v_n+v_p}{x_a}\right) \left\{ J_c(t) \left[\frac{\alpha_p(E)\{\exp[(\alpha_n(E)-\alpha_p(E))x_a]-1\}}{\alpha_n(E)-\alpha_p(E)} - 1 \right] + J_s \right\} \tag{9}$$

and

$$\frac{\partial J_c(t)}{\partial t} = \left(\frac{v_n+v_p}{x_a}\right) \left\{ J_c(t) \left[\frac{\alpha_n(E)\{1-\exp[-(\alpha_n(E)-\alpha_p(E))x_a]\}}{\alpha_n(E)-\alpha_p(E)} - 1 \right] + J_s \right\} \tag{10}$$

for p^+n and n^+p junctions, respectively.

The coefficient of the $J_c(t)$ term has to obey the criterion for breakdown in avalanche diodes, which is given as[16]

$$\int_0^W \alpha_n(E) \exp\left[- \int_x^W (\alpha_n(E) - \alpha_p(E))\, dx' \right] dx = 1 \tag{11}$$

for p^+n junctions and (W is width of depletion layer)

$$\int_0^W \alpha_p(E) \exp\left[- \int_0^x (\alpha_p(E) - \alpha_n(E))\, dx' \right] dx = 1 \tag{12}$$

for n^+p junctions. Under the constant electric field assumption both of these equations reduce to

$$\exp[(\alpha_n(E) - \alpha_p(E))x_a] = \frac{\alpha_n(E)}{\alpha_p(E)}$$

or

$$x_a = \frac{1}{\alpha_n(E)-\alpha_p(E)} \ell n \left(\frac{\alpha_n(E)}{\alpha_p(E)} \right) \tag{13}$$

where x_a is the equivalent width of the avalanche region for the constant field model. When the electric field across the avalanche region is of such magnitude and polarity that the semiconductor junction is just beginning to experience significant carrier multiplication, (i.e. the breakdown condition has been reached), the coefficient of the $J_c(t)$ term in Eqs. (9) and (10) is zero. Setting this [illegible] equal to zero results in the same relationship as given in Eq. (13) and Eqs. (9) and (10) are consistent with the criterion for breakdown in avalanche diodes.

3.3.4 Simplified conduction current distribution

Eqs. (9) and (10), of the previous sub-section, contain a large number of exponential terms, as the ionization rates are themselves exponential expressions. This makes normalization very difficult and can lead to instabilities in the numerical calculations. It would be advantagous if alternate expressions for Eqs. (7) and (8), sub-section 3.3.3, could be found, which would eliminate the exponential terms in the current density equations.

Alternate expressions for the carrier current densities can be found, which are free of exponential terms, by considering the d.c. current distribution [16] in the semiconductor junction. These distributions are shown in Fig. 3.2 along with an alternate representation that has essentially

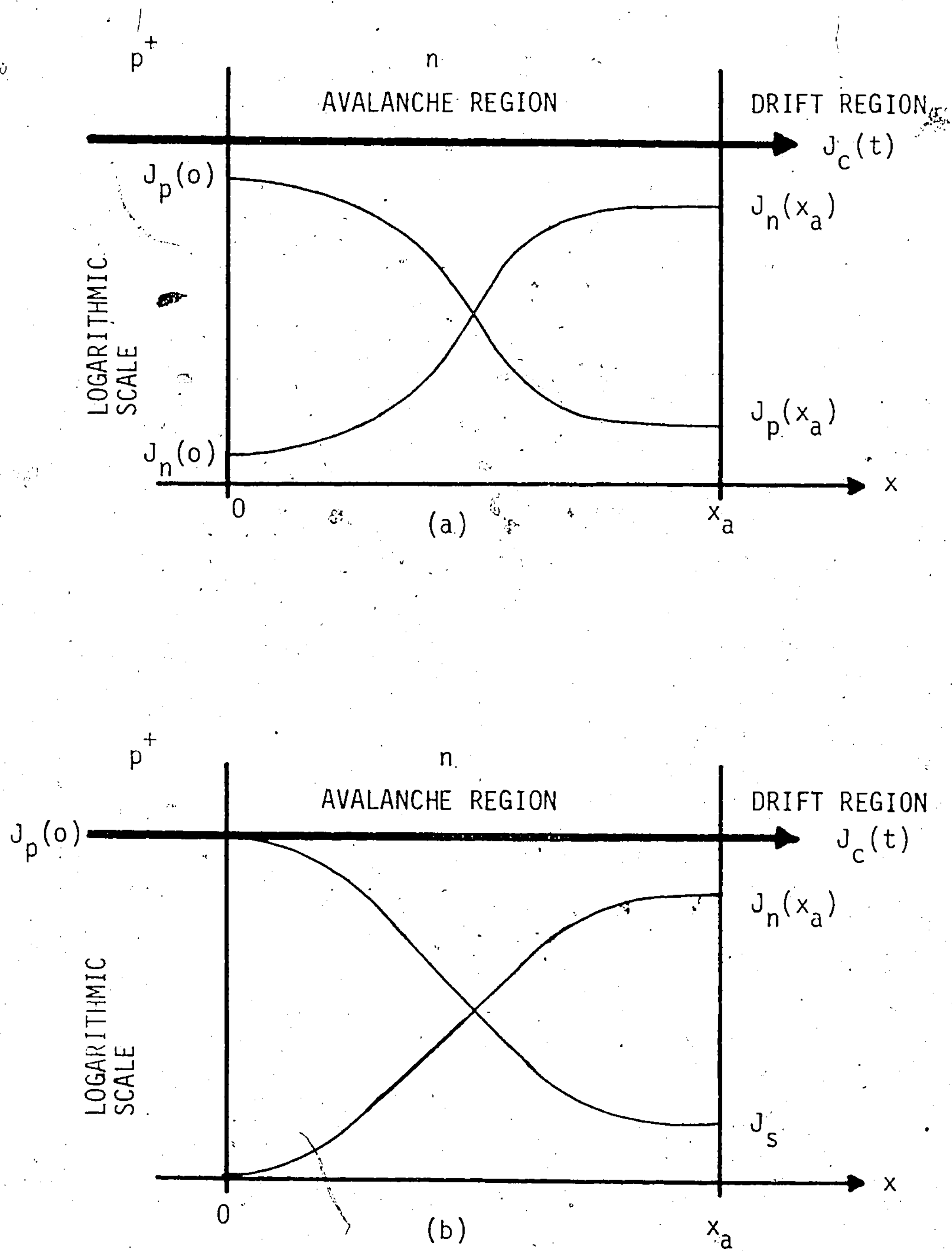

FIG. 3.2 DISTRIBUTION OF CONDUCTION CURRENTS IN AN AVALANCHING-REVERSE-BIASED p^+n JUNCTION
(a) "EXACT MODEL"
(b) ALTERNATE REPRESENTATION

the same behaviour. Since the "p^+" part of the junction has a doping level of about $10^{19} cm^{-3}$ while the "n" part of the junction has a doping level of about $10^{16}\ cm^{-3}$, the magnitude of $J_p(x_a)$ is much greater than that of $J_n(0)$. (Fig. 3.2). Thus, the relation for the reverse saturation current density (J_s) can be written as,

$$J_s = J_{ns} + J_{ps} = J_n(0) + J_p(x_a) \simeq J_p(x_a) \qquad (1)$$

and the alternate representation shown in Fig. 3.2 is valid.

A further approximation, which leads to very little error, is to let J_s be zero in the alternate representation shown in Fig. 3.2. The magnitude of J_s is of the order of $10^{-4} cm^{-2}$ for Silicon and $10^{-2}\ cm^{-2}$ for Germanium, which is much less than the typical magnitude of $10^2 cm^{-2}$ for $J_n(x_a)$[14]. Further, as will be shown in the discussion of the experiments, when the Impatt diode is operated with repetitive-pulse-type bias modulation, a d.c. current of 1 ma is required to ensure stable operation. This reduces the importance of the reverse saturation current.

The d.c. current distribution for the p^+n and n^+p junctions, under the constant field assumption, can be calculated from Eqs. (5), (6), (7) and (8) of sub-section 3.3.3. Using the previously discussed assumption of J_s equal zero, these current distributions are as shown in Fig. 3.3. By employing the boundary conditions

$$J_p(0) = J_c(t)\ ;\ J_p(x_a/\S) = J_c(t)/2\ ;\ J_p(x_a) = 0.0 \qquad (2)$$

the current distribution for the p^+n junction can be empirically expressed in the convenient form:

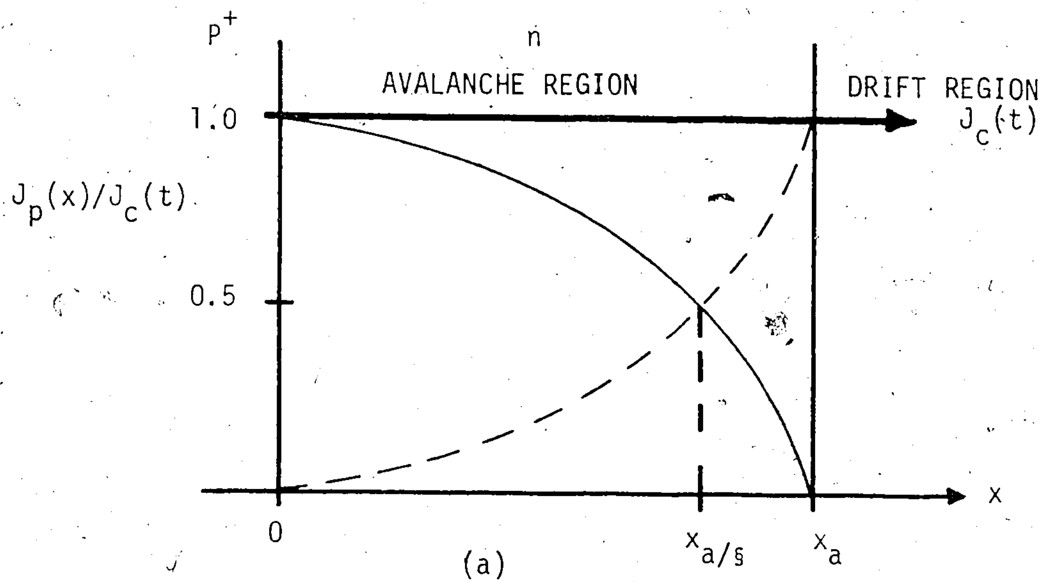

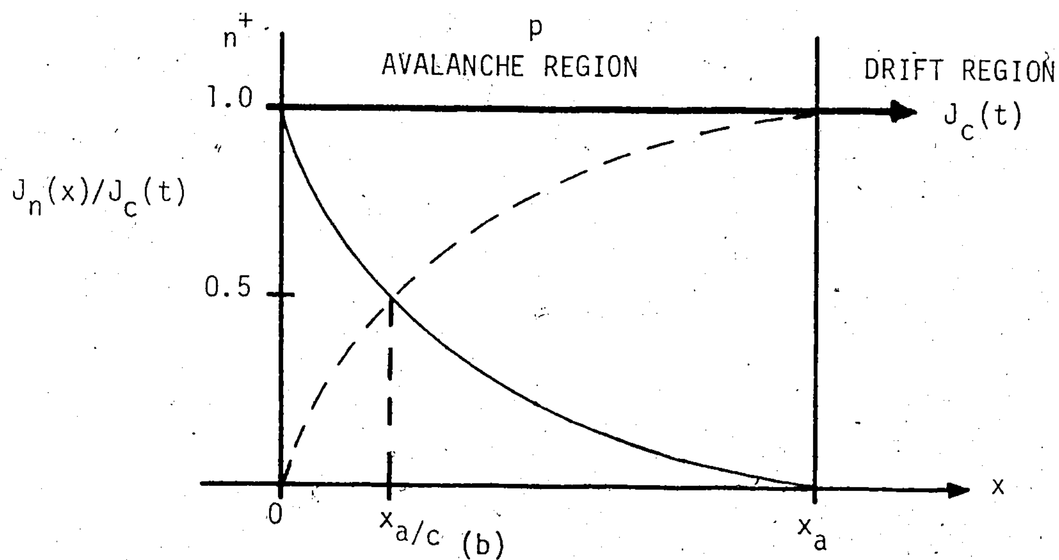

FIG. 3.3 CONSTANT FIELD MODEL FOR THE INSTANTANEOUS CURRENT DENSITY DISTRIBUTIONS IN THE AVALANCHE REGION OF (a) p^+n JUNCTION
(b) n^+p JUNCTION

$$\frac{J_p(x)}{J_c(t)} = 1 - \frac{1}{2} \left(\frac{\S\, x}{x_a} \right)^b \text{ where } \S^b = 2 \tag{3}$$

Similarly, the current distribution for the n^+p junction can be empirically expressed as

$$\frac{J_n(x)}{J_c(t)} = 1 - \frac{1}{2} \left(\frac{c\, x}{x_a} \right) \text{ where } c^d = 2 \tag{4}$$

Substituting Eqs. (3) and (4) into the conduction current relations, Eqs. (13) and (14) sub-section 3.3.2, and carrying out the spatial integration, yields the following results:

$$\frac{\partial J_c(t)}{\partial t} = \left(\frac{v_n + v_p}{x_a} \right) \{ J_c(t)\, x_a [\alpha_n(E) \left(\frac{1}{b+1} \right) + \alpha_p \left(\frac{b}{b+1} \right) - \frac{1}{x_a}] + J_s \} \tag{5}$$

for the p^+n junction and

$$\frac{\partial J_c(t)}{\partial t} = \left(\frac{v_n + v_p}{x_a} \right) \{ J_c(t)\, x_a [\alpha_n(E) \left(\frac{d}{d+1} \right) + \alpha_p(E) \left(\frac{1}{d+1} \right) - \frac{1}{x_a}] + J_s \} \tag{6}$$

for the n^+p junction.

These latest equations are much simpler than the more exact versions given earlier, Eqs. (9) and (10) sub-section 3.3.3, particularly so when the terms $x_a\, \alpha_n(E)$ and $x_a\, \alpha_p(E)$ are expanded in a Taylor series as powers of the electric field (E).

3.3.5 Validity of the Model

An appreciation of how valid the approximations leading to Eqs. (5) and (6), sub-section 3.3.4, are, can be gained by comparing the static behaviour of these equations with the more detailed analysis of Schroeder and Haddad[22]. They solved Eqs. (1), (2), (3), (4), (11) and ([illegible]) sub-section 3.3.3, to give the spatial dependence of $J_p(x)$ and $J_n(x)$ for both p^+n and n^+p abrupt junctions. In their analysis of the abrupt junction Impatt diode, they assumed a triangular representation for the electric field across the junction. This is not entirely accurate, but should give just as valid results as the constant field assumption used to arrive at the equations derived here. The more exact analysis[22] gives an avalanche region width that is about twice as large for the p^+n junction as for the n^+p junction.

Under the constant field assumption, the relation governing the equivalent width of the avalanche region, Eq. (13) sub-section 3.3.3, is the same for both p^+n and n^+p junctions. However, if Eqs. (5) and (6) sub-section 3.3.3, are solved for the position in the avalanche region where

$$\frac{J_n(x)}{J_c(t)} = \frac{1}{2} \; ; \qquad \frac{J_p(x)}{J_c(t)} = \frac{1}{2}$$

these positions ($x_{\frac{1}{2}}$) are found to be

$$x_{\frac{1}{2}} = \left(\frac{1}{\alpha_n(E)-\alpha_p(E)} \right) \ln \left(\frac{\alpha_n(E)+\alpha_p(E)}{2\,\alpha_p(E)} \right) \qquad (1)$$

for the p^+n junction and

$$x_{\frac{1}{2}} = \left(\frac{1}{\alpha_n(E)-\alpha_p(E)} \right) \ell n \left(\frac{2\alpha_n(E)}{\alpha_n(E)+\alpha_p(E)} \right) \qquad (2)$$

for n^+p junctions. With reference to Fig. 3.3 and Eq. (13) sub-section 3.3.3, the following ratios hold,

$$\frac{x_{\frac{1}{2}}}{x_a} = \frac{1}{b} = \ell n \left(\frac{\alpha_n(E)+\alpha_p(E)}{2\,\alpha_p(E)} \right) / \ell n \left(\frac{\alpha_n(E)}{\alpha_p(E)} \right) \qquad (3)$$

for p^+n junctions and

$$\frac{x_{\frac{1}{2}}}{x_a} = \frac{1}{c} = \ell n \left(\frac{2\alpha_n(E)}{\alpha_n(E)+\alpha_p(E)} \right) / \ell n \left(\frac{\alpha_n(E)}{\alpha_p(E)} \right) \qquad (4)$$

for n^+p junctions. These last relationships can be evaluated by using data given by Sze[14] for the ionization rates of Silicon where

$$\alpha_n(E) = 3.8\times10^6 \exp(-1.75\times10^6/E) \text{ and } \alpha_p(E) = 2.25\times10^7 \exp(-3.26\times10^6/E) \qquad (5)$$

Using a similar procedure to that outlined in Eqs. (1) to (4), values of $x_{3/4}/x_a$ and $x_{9/10}/x_a$ may be calculated. This information, along with other pertinant data, is summarized in Table 3.1, for the constant field model. The point at which the current levels reach 90% of their final values may be taken as the extent of the equivalent avalanche region for the model. Table 3.1 shows that the use of the constant field assumption gives an avalanche region width for p^+n junctions that is 1.54 to 1.3 times as large as that for the n^+p junctions. This is in general

TABLE 3.1

SUMMARY OF PARAMETERS FOR CONSTANT FIELD MODEL (SILICON)

PARAMETER		ELECTRIC FIELD ($\times 10^5$ V/Cm)				
		3.0	3.2	3.4	3.6	3.8
$\frac{1}{\delta}$		0.798	0.781	0.762	0.747	0.730
b		3.10	2.81	2.56	2.37	2.20
$\frac{1}{c}$		0.201	0.218	0.236	0.252	0.270
d		0.430	0.456	0.481	0.506	0.530
$\frac{x_{3/4}}{x_a}$	p^+n	0.916	0.907	0.900	0.892	0.885
	n^+p	0.398	0.422	0.452	0.478	0.505
$\frac{x_{9/10}}{x_a}$	p^+n	0.950	0.965	0.962	0.960	0.958
	n^+p	0.616	0.650	0.684	0.712	0.737
x_a (microns)		3.07	1.94	1.27	0.908	0.65
$\frac{\alpha_n}{\alpha_p}$		25.6	18.8	13.95	10.95	8.62

agreement with the previous work[22].

Previously published works[22,23] have produced many graphs showing the predicted values of the avalanche region width, depletion region width and, breakdown voltage with reference to the doping levels of the semiconductor. Unfortunately, the actual diodes do not closely obey these theoretical predictions. The actual diodes generally have a depletion region width that is less than the predicted value, while the avalanche region width and breakdown voltage are greater than the predicted value. This restricts the applicability of detailed calculations when analysing Impatt diodes.

The discrepancy between the actual diodes and the detailed calculations is due, in part, to the difference between the actual and the theoretical distribution of the electric field across the diode junctions. This can be observed by comparing the electric field, used by Scharfetter[24], which closely resembles that in an actual diode, with those used in the various theories. Fig. 3.4 shows a reproduction of the doping profile and electric field distribution used by Scharfetter[24]. The value of x_a given in Fig. 3.4 was calculated by applying the given electric field to the ionization integral of Eq. (11), sub-section 3.3.3, where the equation was evaluated to [illegible]% point. Also included in this Figure are the equivalent constant field and triangular representations for the electric field. These equivalent field distributions give the same voltage drops across the avalanche and drift regions as does the given electric field. It would appear from Fig. 3.4 that the constant field model is equally as valid as the triangular field approximation.

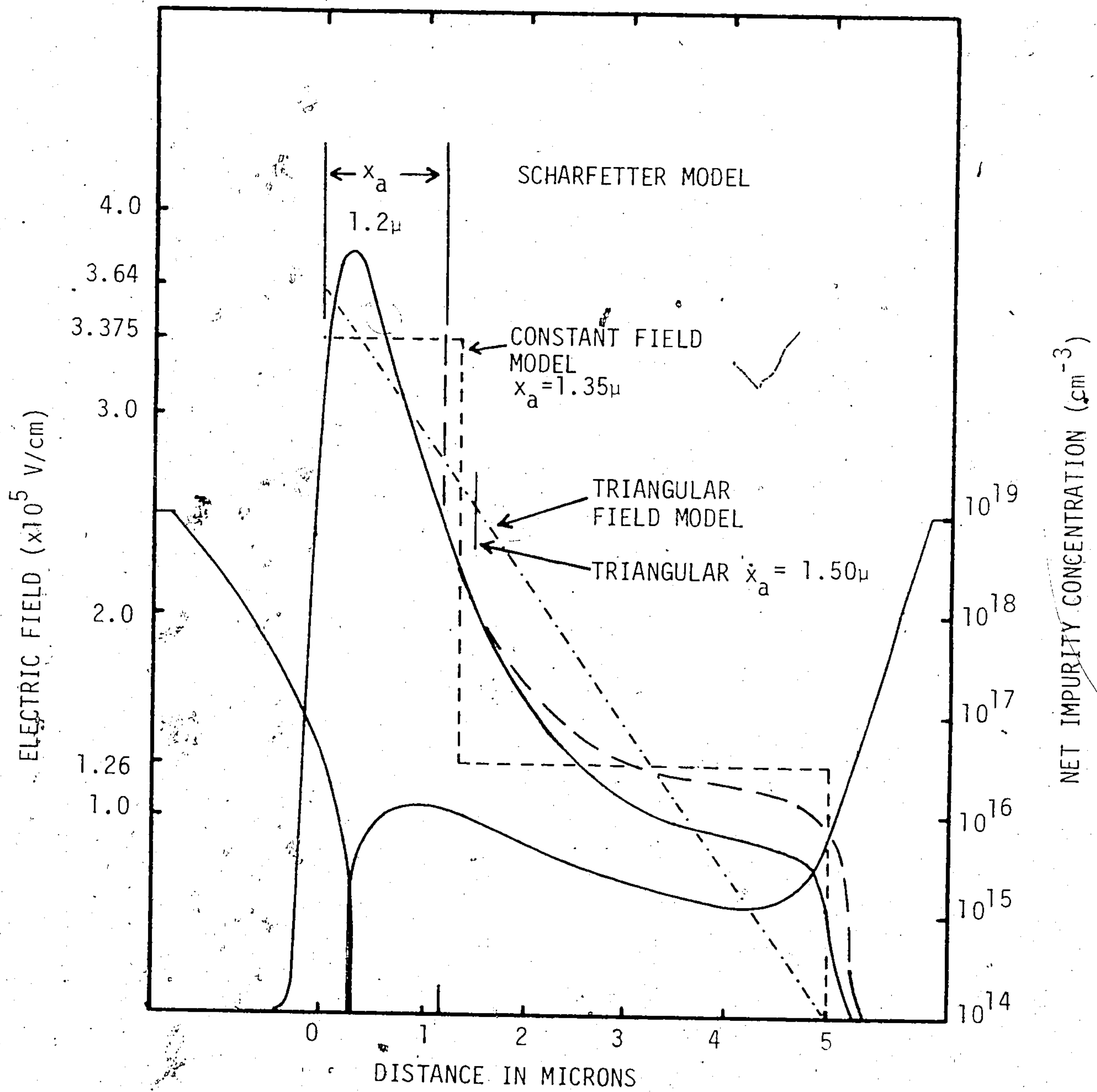

FIG. 3.4 DISTRIBUTION OF ELECTRIC FIELD FOR VARIOUS MODELS OF THE IMPATT DIODE FOR A GIVEN NET IMPURITY CONCENTRATION

From the preceeding arguments, it is seen that the use of the constant field model retains a measure of the difference between p^+n and n^+p junctions for Impatt diodes and also presents an equally valid alternative to the more commonly used triangular field representation, as shown in Fig. 3.4. Further, since detailed calculations involving doping densities etc., have some shortcomings when describing the behaviour of actual diodes, the flexibility inherent in the representation of the constant field model, shown in Fig. 3.3, is very attractive.

3.3.6 Development of Electric Field Equation for Avalanche Region

So far, an expression for the conduction current in the avalanche region has been formulated as a function of the electric field. It still remains to derive an expression for the electric field across the avalanche region. This required equation can be obtained by considering Poisson's equation [25],

$$\frac{\partial E(x,t)}{\partial x} = \frac{q}{\varepsilon_s} \left(N_D - N_A + p(x,t) - n(x,t) \right) \tag{1}$$

which, when rearranged and integrated becomes

$$E(x,t) = \frac{q}{\varepsilon_s} \int_0^x (N_D - N_A) \, dx + \frac{q}{\varepsilon_s} \int_0^x (p(x,t) - n(x,t))dx + E(o,t) \tag{2}$$

or

$$E(x,t) = E_F(x) + \text{SPACE CHARGE} + E(o,t)$$

where the zero value of the spatial variable (x) is as shown in Fig. 3.4

The term $E_F(x)$ is the electric field due to the fixed charges and is independent of time. The space charge term is the electric field due to the conduction current, while the term E(o,t) is an arbitrary constant for each interval of time. This "constant" term consists of a d.c. and an a.c. part: the d.c. part from the bias voltage applied above breakdown and the a.c. part from the R.F. voltage applied across the diode. This is more readily apparent when the Eq. (2) is rearranged and integrated to give the voltage across the diode.

Rewriting Eq. (2) as

$$E(o,t) = E(x,t) - E_F(x) - \frac{q}{\varepsilon_s}\int_0^x (p(x,t)-n(x,t))dx \qquad (3)$$

and integrating across the diode, whose depletion width is W, results in a voltage relationship:

$$E(o,t)\,W = V(x,t) - \int_0^W E_F(x) - \int_0^W \frac{q}{\varepsilon_s}\int_0^x (p(x,t)-n(x,t))dx'\,dx \qquad (4)$$

where the term, V(x,t), is the total voltage across the diode and consists of the voltage drop due to the fixed charges of the junction, the additional voltage to bias the diode above breakdown, plus the R.F. voltage across the diode junction. Taking the algebraic sum of the first two terms on the right hand side of Eq. (4) yields a d.c. and an a.c. term, with the d.c. term being essentially the bias voltage above breakdown. Keeping the above arguments in mind, Eq. (4) is rewritten as

$$E(o,t) = \frac{V_B}{W} + \frac{V_{a.c.}}{W} - \frac{1}{W}\frac{1}{\varepsilon_s}\int_o^W q \int_o^x (p(x,t) - n(x,t))dx'dx \qquad (5)$$

where V_B is the bias voltage above breakdown and $V_{a.c.}$ is the R.F. voltage across the semiconductor junction.

Eq. (5) is of the same form as that initially derived by Read[4], used in practically all discussions involving Impatt diodes. The last term on the right hand side is due to the space charge of the conduction current and is usually only applied to the drift region of the diode, as it is assumed that the avalanche region is very narrow. The assumption of an avalanche region of negligable width is not valid for most actual diodes as it has been shown,[26] that the avalanche region can occupy an appreciable portion of the total depletion region of the diode. Also, the voltage drop across the avalanche region is approximately ½ the total voltage drop across the diode[24]. Consequently, there should be a significant space charge effect from the conduction current in the avalanche region.

With the constant field assumption and using the d.c. current distributions given earlier, it is possible to apply the space charge term, independently, to both the avalanche region and the drift region. Rewriting the space charge term of Eq. (5) as a function of currents, it becomes, for the avalanche region

$$\text{SPACE CHARGE (AVAL)} = \frac{1}{W}\int_o^{x_a} \frac{1}{\varepsilon_s}\int_o^x \left(\frac{J_p(x,t)}{v_p} - \frac{J_n(x,t)}{v_n} \right) dx'dx \qquad (6)$$

Making use of the current density relations given earlier in sub-section 3.3.4, Eq. (3) and repeated here for reference purposes,

$$\frac{J_p(x,t)}{J_c(t)} = 1 - \frac{1}{2} \left(\frac{\delta x}{x_a} \right)^b \; ; \quad \frac{J_n(x,t)}{J_c(t)} = 1 - \frac{J_p(x,t)}{J_c(t)}$$

where, these relations apply to a p^+n junction. Substituting the above relations into Eq. (6), the result is

$$\text{SPACE CHARGE (AVAL)} = \frac{1}{W} \int_0^{x_a} \frac{1}{\varepsilon_s} \int_0^{x} J_c(t) \; \frac{v_n}{v_n v_p} \left[1 - \frac{1}{2} \left(\frac{v_n + v_p}{v_n} \right) \left(\frac{\delta x'}{x_a} \right)^b \right] dx' \, dx \qquad (7)$$

and after carrying out the integration

$$\text{SPACE CHARGE (AVAL)} = \frac{v_n}{W\varepsilon_s} \; \frac{x_a^2}{v_n v_p} \left[\frac{1}{2} - \left(\frac{v_n + v_p}{v_n} \right) \frac{1}{(b+1)(b+2)} \right] J_c(t) \qquad (8)$$

which is valid for a p^+n junction. For an n^+p junction simply replace "b" by "d" as defined previously in sub-section 3.3.4. Eq. (4).

In applying the space charge term to the drift region, use is made of the assumption that avalanche multiplication does not take place in the drift region. In the drift region, the conduction current consists of bunched minority carriers. For a single type of carrier in the non dispersive drift region the following relations are valid for a p^+n junction,

$$J_n(x,t) = J_n\left(t - \frac{x}{v_n}\right) = J_c\left(t - \frac{x}{v_n}\right)$$

The space charge term of Eq. (5), when applied to the drift region becomes

$$\text{SPACE CHARGE (DRIFT)} = \frac{1}{W} \int_{x_a}^{W} \frac{q}{\varepsilon_s} \int_{x}^{W} (p(x,t) - n(x,t))\,dx'\,dx \qquad (9)$$

where only one type of carrier is permitted. Continuing the derivation for a p^+n junction and carrying out the first integration gives;

$$\text{SPACE CHARGE (DRIFT)} = \frac{1}{W\varepsilon_s} \int_{0}^{W'} (W-x)\ \frac{1}{v_n}\, J_c\left(t - \frac{x}{v_n} \right) dx \qquad (10)$$

where W' is the width of the drift region and the relationship for a single type of carrier is used. This last equation can be further simplified by a change of variables, such as letting

$$t' = t - \frac{x}{v_n}$$

Using this change of variables the space charge term becomes

$$\text{SPACE CHARGE (DRIFT)} = \frac{v_n}{W\varepsilon_s} \int_{t-T_d}^{t} (T_d - t + t')\ J_c(t')\,dt' \qquad (11)$$

where T_d is the transit time for the carriers in the drift region.

Substituting Eqs. (8) and (11) into Eq. (5), the relationship for the electric field in the avalanche region becomes;

$$E(o,t) = \frac{v_B}{W} + \frac{v_{a.c.}}{W} - \frac{v_n}{W\varepsilon_s} \left\{ \frac{x_a^2}{v_n v_p} \left[\frac{1}{2} - \left(\frac{v_n + v_p}{v_n} \right) \frac{1}{(b+1)(b+2)} \right] J_c(t) + \kappa \int_{t-T_d}^{t} (T_d - t + t') J_c(t')\,dt' \right\} \qquad (12)$$

which is valid for p^+n junctions when κ is set to unity. (For n^+p junctions substitute "d" for "b" and κ is set to v_p/v_n).

It is interesting to note that the term relating to the space charge in the avalanche region varies as the square of the equivalent width of the avalanche region. Otherwise, the space charge term for the avalanche region behaves as expected, where its magnitude is directly proportional to the magnitude of the conduction current and vanishes for small values of x_a.

For n^+p junctions, the space charge associated with the avalanche region will be significantly less, approximately a factor of 4, as the value of x_a is approximately ½ that of p^+n junctions. In the constant field model, the equivalent avalanche region widths for n^+p junctions are approximately 2/3 those of the p^+n junctions. (reference Table 3.1) However, the magnitude of the "d" term for n^+p junctions is less than the magnitude of the "b" term for p^+n junctions. This further reduces the value of the avalanche region space charge term for n^+p junctions and Eq. (12) should adequately describe the difference between the two different types of semiconductor diode junctions.

3.4 Summary

The foregoing analysis has been carried out with the prerequisite that the equations developed would be used for transient analysis and would be solved on a computer. Therefore, considering the large number of R.F. cycles necessary to characterize transient response, the equations should be sufficiently simple that the solutions not take an excessive amount of computer time. The following equations that describe

the conduction current and the electric field in the Impatt diode are the results of the foregoing analysis and are summarised here for reference purposes.

The conduction current equation for the p^+n, abrupt junction, Impatt diode is

$$\frac{\partial J_c(t)}{\partial t} = \left(\frac{v_n+v_p}{x_a} \right) \{ J_c(t) x_a \left[\alpha_n(E) \left(\frac{1}{b+1} \right) + \alpha_p(E) \left(\frac{b}{b+1} \right) - \frac{1}{x_a} \right] + J_s \}$$

while the equation describing the electric field in this semiconductor junction is

$$E(o,t) = \frac{V_B}{W} + \frac{V_{a.c.}}{W} - \frac{v_n}{W\varepsilon_s} \{ \frac{x_a^2}{v_n v_p} \left[\frac{1}{2} - \left(\frac{v_n+v_p}{v_n} \right) \frac{1}{(b+1)(b+2)} \right] J_c(t) + \int_{t-T_d}^{t} (T_d - t + t') J_c(t') dt' \}$$

The equations describing the n^+p junction are identical in form but with appropriate changes in some coefficients.

These equations satisfy the preceeding criterion of simplicity and ease of solution, while at the same time using a minimum of approximations. The equations are sufficiently versatile to describe either p^+n or n^+p junctions in a wide variety of semiconductor materials. The accuracy

of the equations should be adequate, as the assumptions used in developing the current equations have been shown to be valid and the electric field equation includes an additional term to account for the space charge effect of the avalanche region.

CHAPTER IV

COMPUTER SOLUTIONS OF THE ANALYTICAL EQUATIONS

4.1 Introduction

In this chapter, the analytical equations derived previously in Chapter III, are solved. Two approaches are discussed, as both Analog and Digital computers were used. Computer usage provides a fast and accurate method of obtaining the equation solutions. Thus, a study of the results for a variety of parameter values can be readily carried out.

Obtaining solutions for a range of parameters is very important when comparing the computations to experimental results. There are parameters of the Impatt diode that cannot be determined without some trial-and-error. Although the depletion region width and doping concentrations can be estimated from capacitance - voltage measurements, the division of this depleted region into separate avalanche and drift regions is somewhat arbitrary.

Since many computer runs needed to be carried out, it was thought to be advantageous to normalize the analytical equations so that the required accuracy could be attained using the simplest computational techniques. For digital computers, this would be single-precision arithmetic, whose usage would reduce the computation time and computer memory space required for each program run.

4.2 Normalization of the Analytical Equations

Equations describing the Impatt diode that were derived in Chapter III are repeated here for reference purposes. The current equation in the avalanche region of the p^+n junction is

$$\frac{\partial J_c(t)}{\partial t} = \left(\frac{v_n + v_p}{x_a} \right) \{ J_c(t) \, x_a \left[\alpha_n(E) \left(\frac{1}{b+1} \right) + \alpha_p(E) \left(\frac{b}{b+1} \right) - \frac{1}{x_a} \right] + J_s \} \quad (1)$$

and the electric field across the avalanche region is

$$E(o,t) = \frac{V_B}{W} + \frac{V_{a.c.}}{W} - \frac{v_n}{\varepsilon_s W} \{ \frac{x_a^2}{v_n v_p} \left[\frac{1}{2} - \left(\frac{v_n + v_p}{v_n} \right) \frac{1}{(b+1)(b+2)} \right] J_c(t) + \kappa \int_{t-T_d}^{t} (T_d - t + t') \, J_c(t') \, dt' \} \quad (2)$$

where κ is unity for the p^+n junction. For n^+p junctions, the equations are the same except "b" is replaced by "d" and $\alpha_n(E)$ and $\alpha_p(E)$ in Eq. (1) are interchanged. Also, in Eq. (2), $\kappa = v_p/v_n$ for the n^+p junction.

To facilitate the use of compatible magnitudes in the computer solutions, the above equations were time-scaled and rewritten in terms of currents. The time normalization was carried out according to the relation

$$\tau = 10^{10} t \quad (3)$$

where τ is the scaled time and t is the actual time. The equations are now rewritten in terms of τ and using the relation

$$I(t) = \int_A J_c(t) \, dA \simeq J_c(t) \, A \quad (4)$$

where A is the effective cross-sectional area of the p-n junction. The time normalized equations in terms of currents are

$$\frac{\partial J_c(\tau)}{\partial \tau} = 10^{-10} \left(\frac{v_n+v_p}{x_a} \right) \{ I_c(\tau)\, x_a \left[\alpha_n(E) \left(\frac{1}{b+1} \right) + \alpha_p(E) \left(\frac{b}{b+1} \right) - \frac{1}{x_a} \right] + I_s \} \tag{5}$$

and

$$E(o,\tau) = \frac{V_B}{W} + \frac{V_{a.c.}(\tau)}{W} - \frac{v_n}{\varepsilon_s WA} \{ \frac{x_a^2}{v_n v_p} \left[\frac{1}{2} - \left(\frac{v_n+v_p}{v_n} \right) \frac{1}{(b+1)(b+2)} \right] I_c(\tau) + 10^{-20} \int_{t-T_d}^{\tau} (\tau_d-\tau+\tau')\, I_c(\tau')\, d\tau' \} \tag{6}$$

Using the values for v_n and v_p that are given in the references[27] where

$$v_n = 10^7 \text{ cm/sec and } v_p = 0.75 \times 10^7 \text{ cm/sec}$$

and also rescaling other quantities as follows:

$$\overline{I}_c(\tau) = I_c(\tau)/10^{-2} \quad ; \quad \overline{E}(o,\tau) = E(o,\tau)/10^4$$

$$\overline{x}_a = x_a/10^{-4} \quad ; \quad \overline{A} = A/10^{-4}$$

$$\overline{W} = W/10^{-4} \quad ; \quad \varepsilon_s = 11.8\ \varepsilon_o \text{ for Silicon,}$$

the electric field equation becomes

$$\overline{E}(o,\tau) = \frac{V_B}{\overline{W}} + \frac{V_{a.c.}(\tau)}{\overline{W}} - \frac{10}{1.04\ \overline{W}\ \overline{A}} \{ \frac{\overline{x}_a^2}{75} \left[\frac{1}{2} - \frac{1.75}{(b+1)(b+2)} \right] \overline{I}_c(\tau) + \int_{\tau-T_d}^{\tau} (\tau_d-\tau+\tau')\, \overline{I}_c(\tau')\, d\tau' \} \tag{7}$$

Before the current equation is further normalized, it is advantageous to expand the ionization rates in a Taylor series about the variable $(E-E_c)$, where E_c represents the value of the electric field at breakdown. The resulting relations for $\alpha_n(E)$ and $\alpha_p(E)$ will be identical except for notational differences, so only the $\alpha_n(E)$ equation will be fully developed.

The ionization rates are given by[14]

$\alpha_n(E) = F \exp(-f/E)$ and $\alpha_p(E) = G \exp(-g/E)$

where

$$F = 3.8 \times 10^6 \quad ; \quad G = 2.25 \times 10^7$$
$$f = 1.75 \times 10^6 \quad ; \quad g = 3.26 \times 10^6$$

Expanding $\alpha_n(E)$ in a Taylor series and taking only the first three terms, the relation is

$$\alpha_n(E)\Big|_{E=E_c} = \alpha_n(E_c) + (E-E_c)\frac{\partial \alpha_n(E)}{\partial E}\Big|_{E=E_c} + \frac{(E-E_c)^2}{2!}\frac{\partial^2 \alpha_n(E)}{\partial E^2}\Big|_{E=E_c} + \frac{(E-E_c)^3}{3!}\frac{\partial^3 \alpha_n(E)}{\partial E^3}\Big|_{E=E_c} + \ldots$$

$$= \alpha_n(E_c)\left\{ 1 + \frac{f}{E_c^2}(E-E_c) + \left[\frac{1}{2}\left(\frac{f}{E_c^2}\right)^2 - \frac{f}{E_c^3}\right](E-E_c)^2 + \left[\frac{1}{6}\left(\frac{f}{E_c^2}\right)^3 - \frac{f^2}{E_c^5} + \frac{f}{E_c^4}\right](E-E_c)^3 \right\} \quad (8)$$

Eq. (8) is a rapidly decreasing function of $(E-E_c)$ and the third term of the variable contributes very little to the calculation, but will be carried for completeness. Similarly, the expression for $\alpha_p(E)$ is

$$\alpha_p(E) = \alpha_p(E_c) \{ 1 + \frac{g}{E_c^2} (E-E_c) + [\frac{1}{2} (\frac{g}{E_c^2})^2 - \frac{g}{E_c^3}] (E-E_c)^2 +$$

$$[\frac{1}{6} (\frac{g}{E_c^2})^3 - \frac{g^2}{E_c^5} + \frac{g}{E_c^4}] (E-E_c)^3 \} \qquad (9)$$

When Eqs. (8) and (9) are added, with the appropriate coefficients applied, the inner bracketed term of Eq. (5) becomes,

$$x_a (\frac{1}{b+1}) \alpha_n(E) + x_a (\frac{b}{b+1}) \alpha_p(E) - 1 = [x_a (\frac{1}{b+1}) \alpha_n(E_c) +$$

$$x_a (\frac{b}{b+1}) \alpha_p(E_c) - 1] + [x_a (\frac{1}{b+1}) \alpha_n(E_c) \frac{f}{E_c^2} +$$

$$x_a (\frac{b}{b+1}) \alpha_p(E_c) \frac{g}{E_c^2}] (E-E_c) + \ldots \qquad (10)$$

The first term on the right hand side of the above equation is the break-down condition discussed in sub-section 3.3.3. Therefore, this term vanishes from the equation and Eq. (5) can be written as

$$\frac{\partial I_c(\tau)}{\partial \tau} = 10^{-10} (\frac{v_n + v_p}{x_a}) \{ I_c(\tau) [ALPHA + BETA] + I_s \} \qquad (11)$$

where

$$ALPHA = (\frac{1}{b+1}) x_a \alpha_n (E_c) \{ \frac{f}{E_c^2} (E-E_c) + [\frac{1}{2} (\frac{f}{E_c^2}) - \frac{f}{E_c^3}] (E-E_c)^2 +$$

$$[\frac{1}{6} (\frac{f}{E_c^2})^3 - \frac{f^2}{E_c^5} + \frac{f}{E_c^4}] (E-E_c)^3 \} \qquad (12)$$

and

$$\text{BETA}=\left(\frac{b}{b+1}\right) x_a\, \alpha_p(E_c) \left\{ \frac{g}{E_c^2}(E-E_c) + \left[\frac{1}{2}\left(\frac{g}{E_c^2}\right)^2 - \frac{g}{E_c^3}\right](E-E_c)^2 + \left[\frac{1}{6}\left(\frac{g}{E_c^2}\right)^3 \frac{-g^2}{E_c^5} + \frac{g}{E_c^4}\right](E-E_c)^3 \right\} \tag{13}$$

With reference to Eq. (5) of sub-section 3.3.6, the variable $(E-E_c)$ is the same as $E(o,\tau)$ defined in Eq. (6) and (7) here. By applying the normalization factors used in Eq. (7), Eq. (11) becomes

$$\frac{\partial \bar{I}_c(\tau)}{\partial\tau} = 17.5 \left\{ \bar{I}_c(\tau) \left[\overline{\text{ALPHA}} + \overline{\text{BETA}}\right] + \bar{I}_s \right\} \tag{14}$$

where upon setting

$$[\bar{E}_c, \bar{f}, \bar{g}, \overline{\alpha_n}(E_c), \overline{\alpha_p}(E_c)] = [E_c, f, g, \alpha_n(E_c), \alpha_p(E_c)]/10^4$$

respectively,

$$\overline{\text{ALPHA}} = \frac{\bar{x}_a}{b+1}\, \overline{\alpha_n}(E_c) \left\{ \frac{\bar{f}}{\bar{E}_c^2}\bar{E}(o,\tau) + \left[\frac{1}{2}\left(\frac{\bar{f}}{\bar{E}_c^2}\right)^2 - \frac{\bar{f}}{\bar{E}_c^3}\right]\bar{E}(o,\tau)^2 + \left[\frac{1}{6}\left(\frac{\bar{f}}{\bar{E}_c^2}\right)^3 - \frac{\bar{f}}{\bar{E}_c^5} + \frac{\bar{f}}{\bar{E}_c^4}\right]\bar{E}(o,\tau)^3 \right\} \tag{15}$$

and

$$\overline{\text{BETA}} = \bar{x}_a \left(\frac{b}{b+1}\right) \bar{\alpha}_p(E_c) \left\{ \frac{\bar{g}}{\bar{E}_c^2}\bar{E}(o,\tau) + \left[\frac{1}{2}\left(\frac{\bar{g}}{\bar{E}_c^2}\right)^2 - \frac{\bar{g}}{\bar{E}_c^3}\right]\bar{E}(o,\ )^2 + \left[\frac{1}{6}\left(\frac{\bar{g}}{\bar{E}_c^2}\right)^3 - \frac{\bar{g}^2}{\bar{E}_c^5} + \frac{\bar{g}}{\bar{E}_c^4}\right]\bar{E}(o,\tau)^3 \right\} \tag{16}$$

The magnitudes of E_c and X_a are related through the constant field approximation where E_c is the value of the electric field in the avalanche region, for a given value of the avalanche region width, x_a. This relationship is formulated in sub-section 3.3.3, Eq. (13) and also summarized in Table 3.1. As an indication of the magnitudes that can be expected for the coefficients of Eq. (14), when the following representative values of the variables are used

$$\overline{E}_c = 32.5,\ \overline{\alpha}_n(E_c) = 1.75,\ \overline{\alpha}_p(E_c) = 0.1,\ \overline{x}_a = 1.73$$

$$b = 2.73,\ \overline{f} = 175,\ \overline{g} = 326$$

Eq. (14) for the current in the avalanche region becomes

$$\frac{\partial \overline{I}_c(\tau)}{\partial \tau} = \frac{17.5}{\overline{x}_a} \{ \overline{I}_c(\tau) [0.173\ \overline{E(o,\tau)} + 0.012\ \overline{E(o,\tau)}^2 + 0.003\ \overline{E(o,\tau)}^3] + \overline{I}_s \}$$

Eqs. (14), (15), (16) and (7) describe the conduction current in the avalanche region of the Impatt diode in a form that is very readily computed. However, further equations are necessary to relate this avalanche current to the current flow in the circuit external to the semiconductor diode. This external conduction current (I_{ex}) can be formulated by considering that a pulse of carriers is formed in the avalanche region and then "drifts" across the drift region of the diode without dispersing. As this current pulse travels across the drift region, whose transit time is T_d, the change in the induced charge at the terminals of the junction

causes a current to flow in the external circuit. This external conduction current can be written as

$$I_{ex}(t) = \frac{1}{T_d} \int_{t-T_d}^{t} I_c(t)\, dt \quad \text{or} \quad \overline{I}'_{ex}(\tau) = \frac{1}{\tau_d} \int_{\tau-\tau_d}^{\tau} \overline{I}_c(\tau')\, d\tau' \tag{17}$$

after magnitude and time scaling.

The total current (I_T) in the external circuit of the semiconductor diode is the sum of the conduction and displacement currents, which can be written, after magnitude and time scaling, as

$$\overline{I_T}(\tau) = \overline{I}_{ex}(\tau) + \overline{C}_d \frac{\partial V(\tau)}{\partial \tau} \tag{18}$$

where $\overline{C}_d$ is the depletion region capacitance in picofarads and $V(\tau)$ is the R.F. Voltage across the diode junction.

In the computer program, the Impatt diode is completely described by Eqs. (14), (17), (18) and a relation for $V(\tau)$. $V(\tau)$ can be expressed as a simple trigonometric relation such as a cosine or sine function. The waveforms given by Eq. (18) and the relation for $V(\tau)$ are Fourier-analyzed and the complex ratio of the fundamental frequency components taken to obtain the electronic impedance (Z_e) of the semiconductor diode. The Fourier analysis procedure is explained in Appendix A.

The effects of temperature changes upon the diode junction are discussed in the following Chapter, where it is shown that this effect can be taken into account by adjusting the value of V_B in Eq. (7) as a function of time. It is also shown in Chapter V, that, for the short-

duration bias voltage pulses used here for the transient measurements, the effects of junction heating are minimal. Therefore, the effects of the junction temperature changes will be ignored in this chapter.

4.3 Analog Computation

Initially, the normalized equations were programmed on the Pace* analogue Computer. This served a two-fold purpose; (1) to gain familiarity with the behavior of the model and (2) the possibility of constructing an analog model to describe the transient behavior appeared promising, as steady-state models of the Impatt diode have been programmed on analog computers[28].

Analog computers have a limited number of amplifiers and therefore, the extent of the non-linearity that can be programmed is restricted. Hence, any representation of the Impatt diode that was modelled on the analog computer would need to be simplified. Even so, an approximate analog model of the Impatt diode would be valuable for demonstrative purposes, so work was carried out towards this goal.

4.3.1 Equations for the Analog Model

The model of the Impatt diode used for analog computation was essentially the same as that given by the equations derived in Section 4.2, Eqs. (14), (7) and (18). The simplification was mainly made in the current equation, where only the first term in $\overline{E(o,\tau)}$ was taken. Also, the model was assumed to have equal ionization rates and drift velocities for

---

* PACE - Precision Analog Computer Equipment; a general purpose d.c. analog computer, manufactured by Electronic Associates Limited (Model 231R).

both electrons and holes. The resulting equation for the current in the avalanche region was thus,

$$\frac{\partial \overline{I}_c(\tau)}{\partial \tau} = \frac{2}{\tau_a} \overline{I}_c(\tau) \overline{E}(o,\tau) + \frac{2}{\tau_a} \overline{I}_s \qquad (1)$$

where τ_a is the transit time of the avalanche region.

The equation for the electric field is the same as that given by Eq. (7) in Section 4.2, except that the space-charge term associated with the avalanche region was neglected. To facilitate programming of this equation, it was written in differential form as

$$\frac{\partial \overline{E}(o,\tau)}{\partial \tau} = \frac{1}{W} \frac{\partial V(\tau)}{\partial \tau} - \frac{1}{\varepsilon_s \tau_d A} [\tau_d \overline{I}_c(\tau) - \int_{\tau-\tau_d}^{\tau} \overline{I}_c(\tau')d\tau'] \qquad (2)$$

where the bracketed term originates from the relation

$$\frac{\partial}{\partial \tau} \int_{\tau-\tau_d}^{\tau} (\tau_d - \tau + \tau') \overline{I}_c(\tau') \, d\tau' = \tau_d \overline{I}_c(\tau) - \int_{\tau-\tau_d}^{\tau} \overline{I}_c(\tau')d\tau' \qquad (3)$$

and a d.c. initial condition simulates the constants in the original equation. Similarly, the expression for the external conduction current becomes

$$\frac{\partial \overline{I}_{ex}(\tau)}{\partial \tau} = \frac{1}{\tau_d} [\overline{I}_c(\tau) - \overline{I}_c(\tau-\tau_d)] \qquad (4)$$

The R.F. voltage across the semiconductor diode was simulated by setting

$$V(\tau) = M \cos (\bar{\omega}\,\tau) \qquad (5)$$

where M is the amplitude constant; the programmable differential equation for the R.F. voltage then becomes

$$\frac{\partial^2 V(\tau)}{\partial \tau^2} = -\bar{\omega}^2 V(\tau) \qquad (6)$$

Since the displacement current is directly proportional to the time derivative of the R.F. voltage, it was analog modelled by sampling an appropriate portion of the first derivative signal in the analog program for Eq. (6).

A schematic diagram of the program used is shown in Fig. 4.1. This program contains some extra components, such as absolute value circuits, comparators and redundant amplifiers, all of which were found necessary to improve the stability of the program. This is a fairly complex program and practically all the available amplifiers and integrators of this quite large analog computer were used.

4.3.2 Results of the Analog Computations

Steady-state operation of the model was successfully obtained. However, some difficulties were encountered in obtaining solutions to the equations and the model was found to be too unstable to produce accurate results under transient conditions. Some of the instabilities were inherent in the programming, but the main causes of the unstable results were associated with equipment limitation.

One of the inherent weaknesses of the program lay in the simulation of the time delay necessary to model Eq. (4) of sub-section 4.3.1.

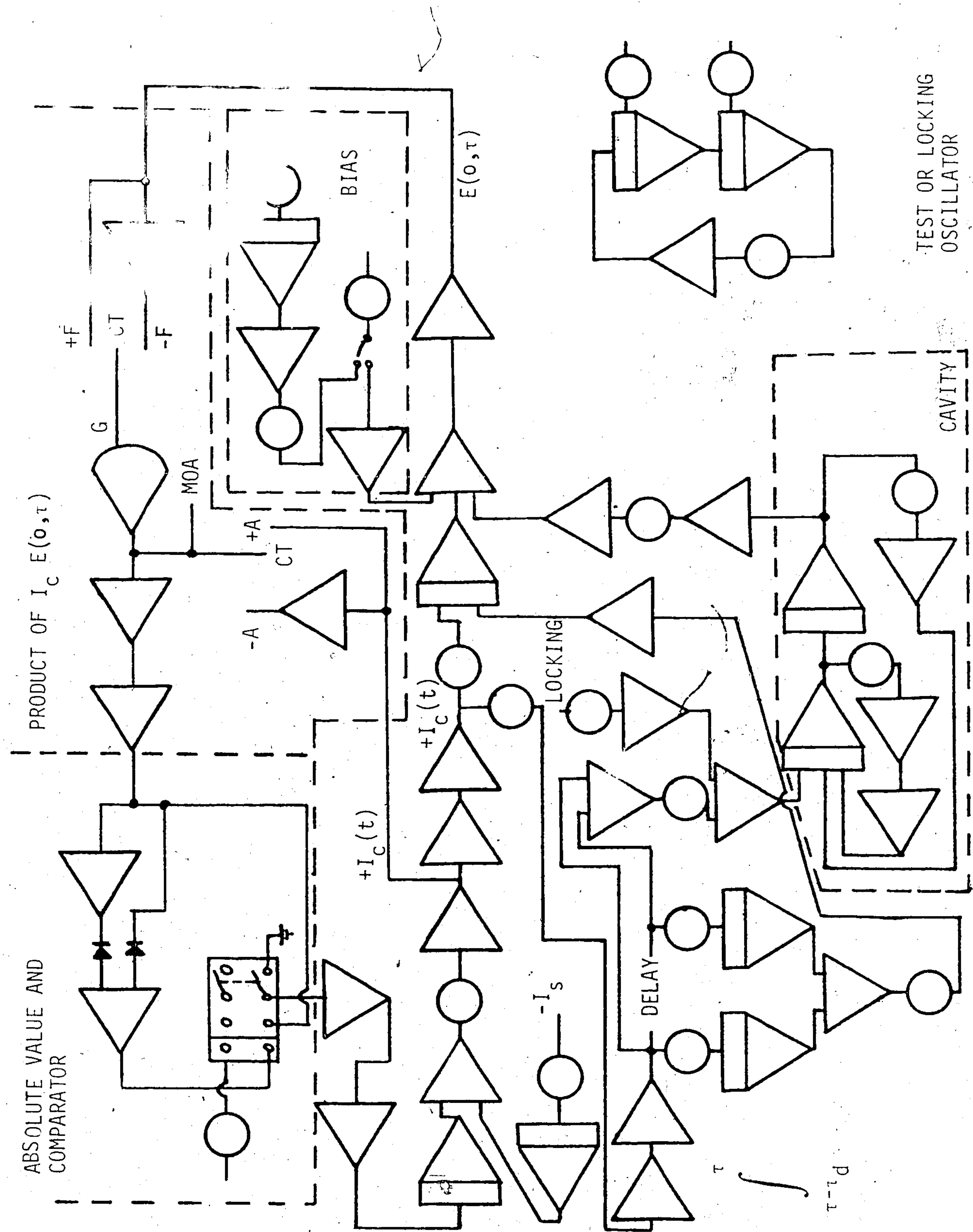

FIG. 4.1 ANALOG COMPUTER PROGRAM FOR AN IMPATT DIODE OSCILLATOR

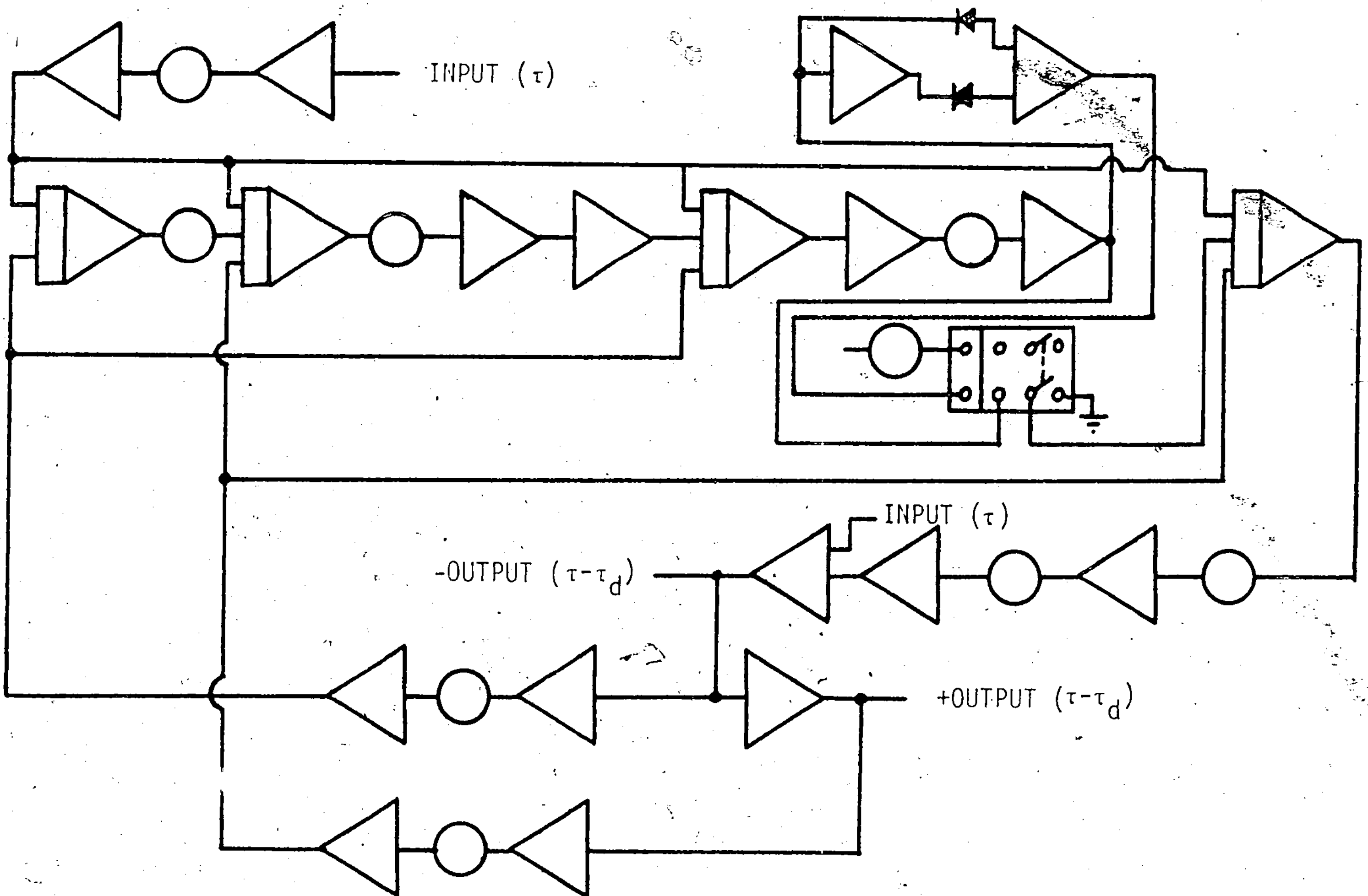

FIG. 4.2 TIME DELAY CIRCUIT FOR ANALOG COMPUTER PROGRAM

The circuit used for the time delay is shown in Fig. 4.2. This is a Padé[29] approximation of the fourth order. Although this circuit is among the most accurate approximations that can be made on the analog computer, it still suffers from d.c. drift and ringing when a sharp current pulse travels through it. One way of overcoming these problems would be by simulating time delay, by using a digital computer for storage, with analog-to-digital and digital-to-analog converter equipment. As the required converter equipment was not available, this corrective action was not taken in this study.

The major equipment limitations were the d.c. drift of the integrators as well as noise in the output of the multiplier. Absolute value circuits and comparators were placed after the multiplier and in the center of the time delay circuit. Although these extra circuits reduced these sources of error, they did not eliminate them. Consequently, the transient results were not very accurate and were difficult to reproduce.

The above - mentioned problems were not as severe when a strong R.F. voltage was applied to the Impatt model and the system operated under steady-state conditions. However, the accuracy and reproducability of the results were still somewhat limited.

4.4 Solutions by Digital Computer

An analysis of the transient behaviour of the Impatt diode requires a solution over a large number of R.F. cycles; thus, each computer run may be of appreciable length. Also, to reconcile computer behaviour

of the Impatt diode with the experimental results, some adjustment of the diode's parameters will have to be made, and this may necessitate running the program several times. It would be advantageous to use single-precision arithmetic, as this allows a reduction in the computation time and the amount of computer memory required for each program run.

By casting the equations, describing the characterization of the Impatt diode, into normalized form, it is possible to use single-precision arithmetic and still maintain sufficient accuracy.

The normalized equations derived earlier, Eqs. (7), (14) and (18) of Section 4.2, were programmed on an IBM 360/67 digital computer. A further advantage of using the normalized version of the describing equations is that the resultant solutions are very stable. Consequently, less stringent error critera and larger time intervals can be used in the solution of the equations, while still maintaining sufficient accuracy.

4.4.1 Procedure for Numerical Analysis

The set of equations to be solved include only one differential equation; however, if a coupled cavity were included in the model, there would be three first-order differential equations that would require simultaneous solutions. To ensure flexibility, a routine was used that would allow the solution of one-or-several differential equations. A specific subroutine for the solution of the differential equations was not written, as several excellent subroutines are already in existence and little would be gained by duplicating the existing programs.

A subroutine employing Hamming's modified predictor-corrector method, with a fourth-order Runga Kutta method [illegible] the starting values, was selected for the solution of the differential equations (HPCG[30]).

This subroutine is faster than the fourth-order Runga Kutta method alone and has a better error criterion. The program for the solution of the set of equations was built around this HPCG subroutine, as it had separate input and output subroutines of its own, that were supplied by the user.

In programming the normalized equations for the Impatt diode (Eqs. (7), (14), (18) of Section 4.2 plus a relation for the R.F. voltage) the equation describing the electric field in the avalanche region was rearranged slightly; the form actually used in the program was expressed as follows:

$$\overline{E}(o,\tau) = \frac{(V_B+V_B)}{\overline{W}} + \frac{V_{a.c.}(\tau)}{\overline{W}} - \frac{10}{1.04\overline{WA}} \{K\ \overline{I}_c(\tau) + \int_{\tau-\tau_d}^{\tau} (\tau_d-\tau+\tau')\ \overline{I}_c(\tau')d\tau' \tag{1}$$

Where V_B' is the d.c. bias voltage, above breakdown, needed to maintain a given steady-state current present during the experimental measurements. The term V_B still applies to the bias voltage pulse applied after the reverse breakdown voltage has been reached. A further change that is evident in Eq. (1) is that the coefficient of the space-charge term pertaining to the avalanche region has been condensed into one constant, "K". The latter change made this coefficient more readily available for variation when comparing the computed and experimental results.

The relation describing the R.F. voltage across the semiconductor diode ($V(\tau)$) was chosen as

$$V(\tau) = M \cos(\overline{\omega}\ \tau) \tag{2}$$

where M is an assigned magnitude and $\overline{\omega}$ is normalized in accordance with time scaling relationship for τ (Eq. (3) Section 4.2). Here, the R.F. voltage is assumed to be at a single frequency.

An important problem encountered in the use of this program, was in determining the most practical size of time increment for the solution of the differential equation. It was readily determined that a time increment of 0.01, for the normalized time τ, would produce practically the same results as any smaller time increment used. However, a problem developed in that the increment size would gradually change as the program time progressed. By using the time scaling of 10^{10}, the program time variable has to run to 300 to simulate 30 nanoseconds of actual time. In so doing, the change in the effective size of the time increment is sufficient to cause significant inaccuracies in the Fourier analysis results.

The solution to this problem lies in choosing a size of time increment that is convertible exactly into hexadecimal so that all the significance is in the first few digits. The computer stores all information in hexadecimal and the program increases its time variable by continually adding the increment size to the existing time. As the existing time becomes greater than 16, during the process of addition some of the significance of the time increment is lost. For values of the existing time greater than 256, even more of the significance of the time increment is lost during the addition process. Consequently, the effective size of the time increment appears to decrease as the total

scaled time increases. However, if the size of the increment is properly chosen, a value of 1/128 was found to function properly, there is no loss of significance during the progress of the program time and the effective size of the time increment remains constant.

The selection of such odd sizes of the time increment as 1/128 may necessitate some adjustment in the number of points taken for the Fourier analysis. However, any problems such as this can usually be alleviated by a judicious choice of frequency for the R.F. voltage across the diode.

4.4.2 Results of Computations

In programming the normalized equations, values need to be assigned to several parameters. These parameters are listed in Table 4.1 and the values assigned are those used in the final comparison of the computed and experimental results. The depletion width (W) was obtained from capacitance-voltage measurements taken at 1 MHz and the cross-sectional area (A) was obtained by examining a segmented diode package under a high power microscope.

During the analysis of the computer results it became evident that the equations were more sensitive to some parameters than others. The most critical parameters were τ_d, C_d, K and x_a. Small variations in W or A caused relatively small changes in the computed results. While the equations were more sensitive to variations in K and x_a, they were most sensitive to variations in τ_d and C_d.

TABLE 4.1

PARAMETER VALUES FOR THE NORMALIZED EQUATIONS

DIODE	FREQ GHz	M VOLTS	$\overline{I}_s$ AMPS	$\overline{W}$ μ	$\overline{A}$ $10^{-4}cm^2$	$\overline{x}_a$ μ	τ_d 10^{-10}	$\overline{C}_d$ pf	K
#1	6.0	2	10^{-6}	3.75	1	1.45	0.26	0.36	0.0238
	7.8	2	10^{-6}	3.75	1	1.45	0.26	0.36	0.015
#8	6.0	2	10^{-6}	4.8	1	1.65	0.327	0.30	0.050
	7.8	2	10^{-6}	4.8	1	1.65	0.327	0.28	0.035

The value of the carrier transit time for the drift region (τ_d) has a strong effect upon the computed results. It is this parameter that largely governs the d.c. current response of the equations to a given bias voltage. Increasing the value of τ_d decreases the level of d.c. current in the simulated Impatt diode, for a given value of bias voltage. Consequently, an estimate of the value of τ_d can be obtained from a comparison of the current levels in the simulated and actual diodes for a given bias voltage. A better estimate of the value of τ_d can be obtained by determining the width of the drift region and dividing this by the scattering-limited velocity of the carrier.[14] An estimate of the drift region width can be obtained from extrapolating the value of $\overline{x}_a$ used in the program, back to an actual width of the avalanche region and then taking the difference between this actual width and the value of $\overline{W}$. Once determined, the value of τ_d is held constant for a particular diode.

The depletion layer capacitance (C_d) greatly influences the magnitude of the calculated electronic impedance for the semiconductor

diode junction. This is well illustrated in Figs. 4.3 and 4.4, where the only difference is in the value of $\overline{C}_d$, which was 0.37 for Fig. 4.3 and 0.35 for Fig. 4.4. It is interesting to note that the influence of this parameter is mainly in its effect upon the magnitude of the computed results and not upon the general shape of the plotted curve. This parameter was initially set in accordance with the value found from the 1 MHz capacitance-voltage measurements and then adjusted slightly to obtain a better comparison between computed and measured results.

The main influence of the parameter K is in the slope and curvature of the computed plot of the electronic impedance, while changes in magnitudes of the plotted values are influenced to a lesser degree. This effect is illustrated in Fig. 4.5, where the only difference in the parameter values is in the magnitude of K. The time or value of d.c. current where the electronic impedance plot "changes direction" is a sensitive function of the value of K. This parameter is initially estimated from the theory and then adjusted to correlate the computed and experimental results.

A value for the equivalent width of the avalanche region (x_a) can be arrived at by considering Figs. 4.4 and 4.6. The value selected for x_a is seen to have a distinct effect upon the plotted characteristics of the electronic impedance. For the higher value of x_a (Fig. 4.6) the curvature of the impedance plot is reversed in the region of 7 nanoseconds and, also, the magnitude of the plotted values in this region are reduced somewhat. From the characterization of Scharfetter's model,

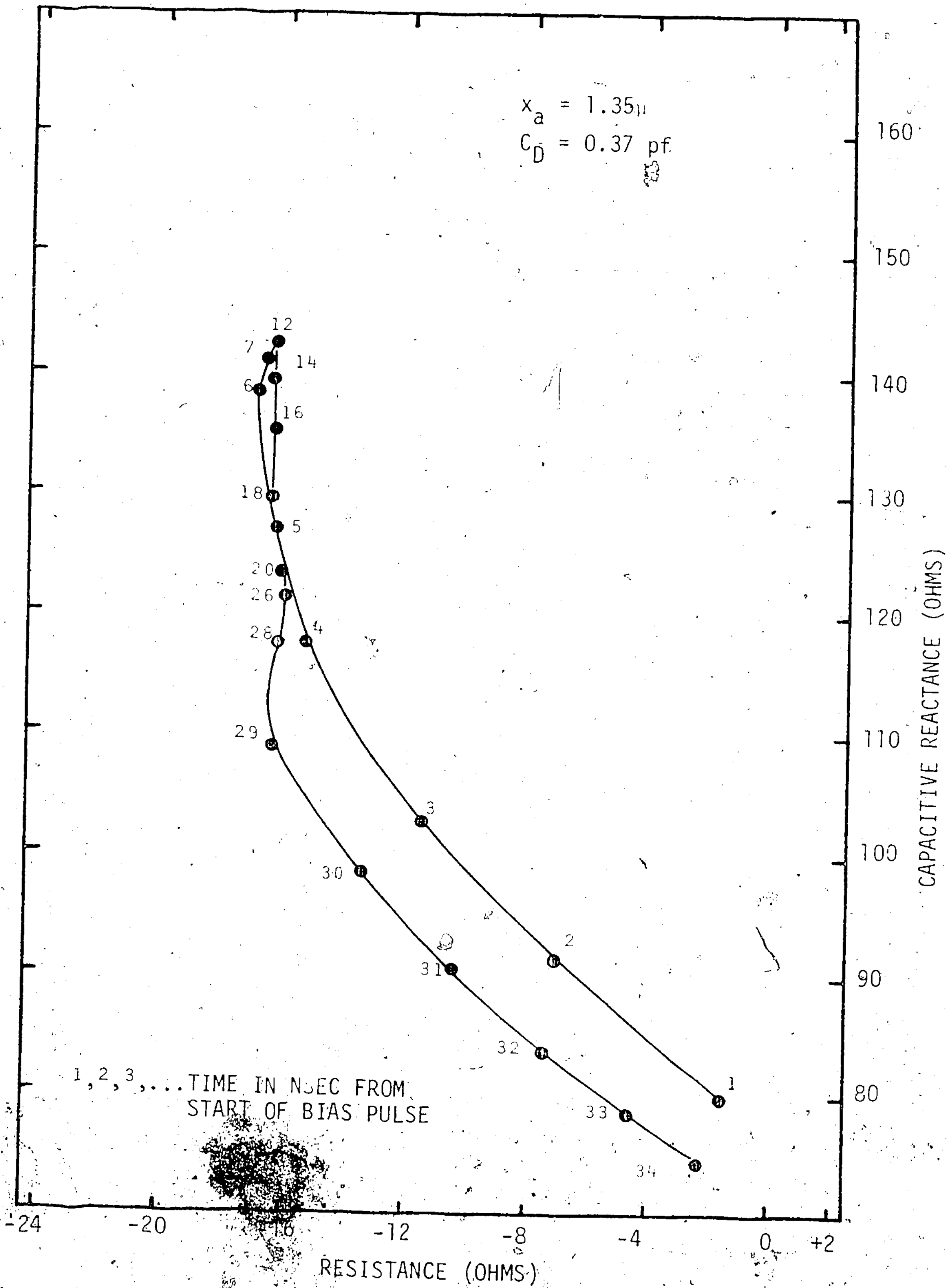

FIG. 4.3 COMPUTED VALUES OF ELECTRONIC IMPEDANCE FOR AN AVALANCHING IMPATT DIODE (DIODE #1 AT 6.0 [illegible] WHERE x_a = 1.35μ, C_D = 0.37 pf AND K = 0.[illegible]

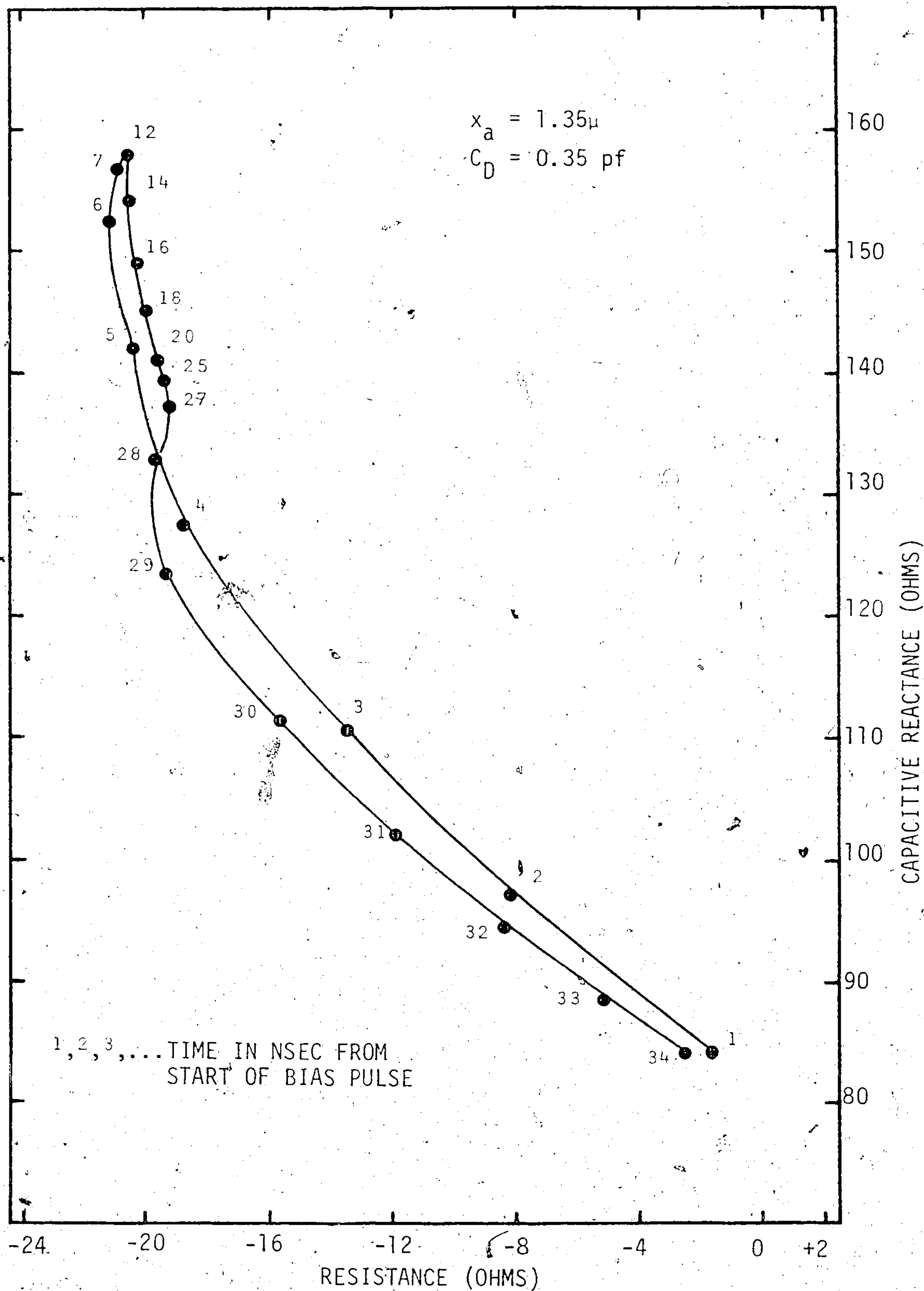

FIG. 4.4 COMPUTED VALUES OF ELECTRONIC IMPEDANCE FOR AN AVALANCHING IMPATT DIODE (DIODE #1 AT 6.0 GHz) WHERE x_a=1.35μ, C_D=0.35 pf AND K=0.0238

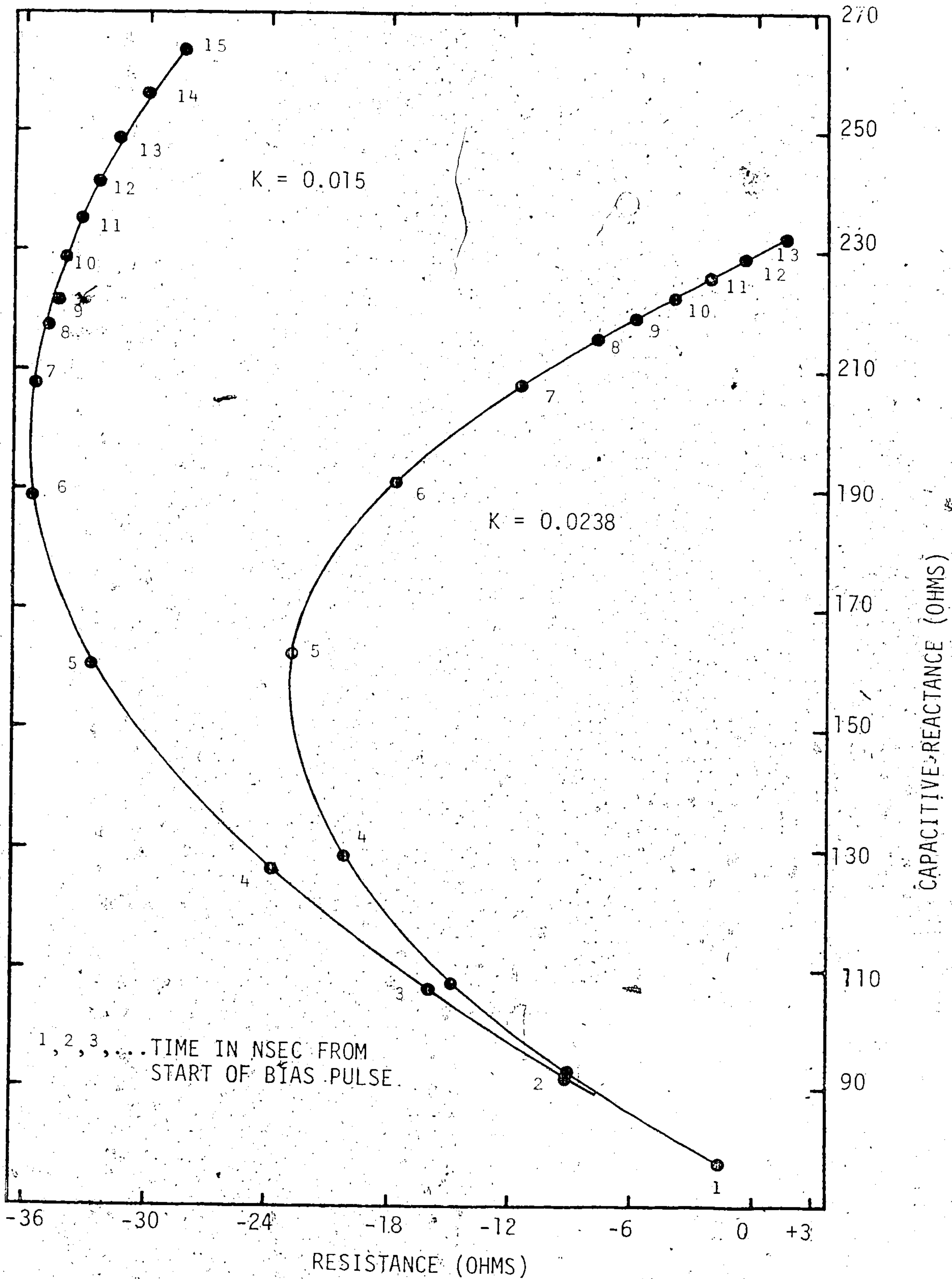

FIG. 4.5 COMPUTED VALUES OF ELECTRONIC IMPEDANCE FOR AN AVALANCHING IMPATT DIODE (DIODE #1 AT 6.0 GHz) WHERE x_a=1.45μ, C_D=0.36 pf AND K IS VARIABLE

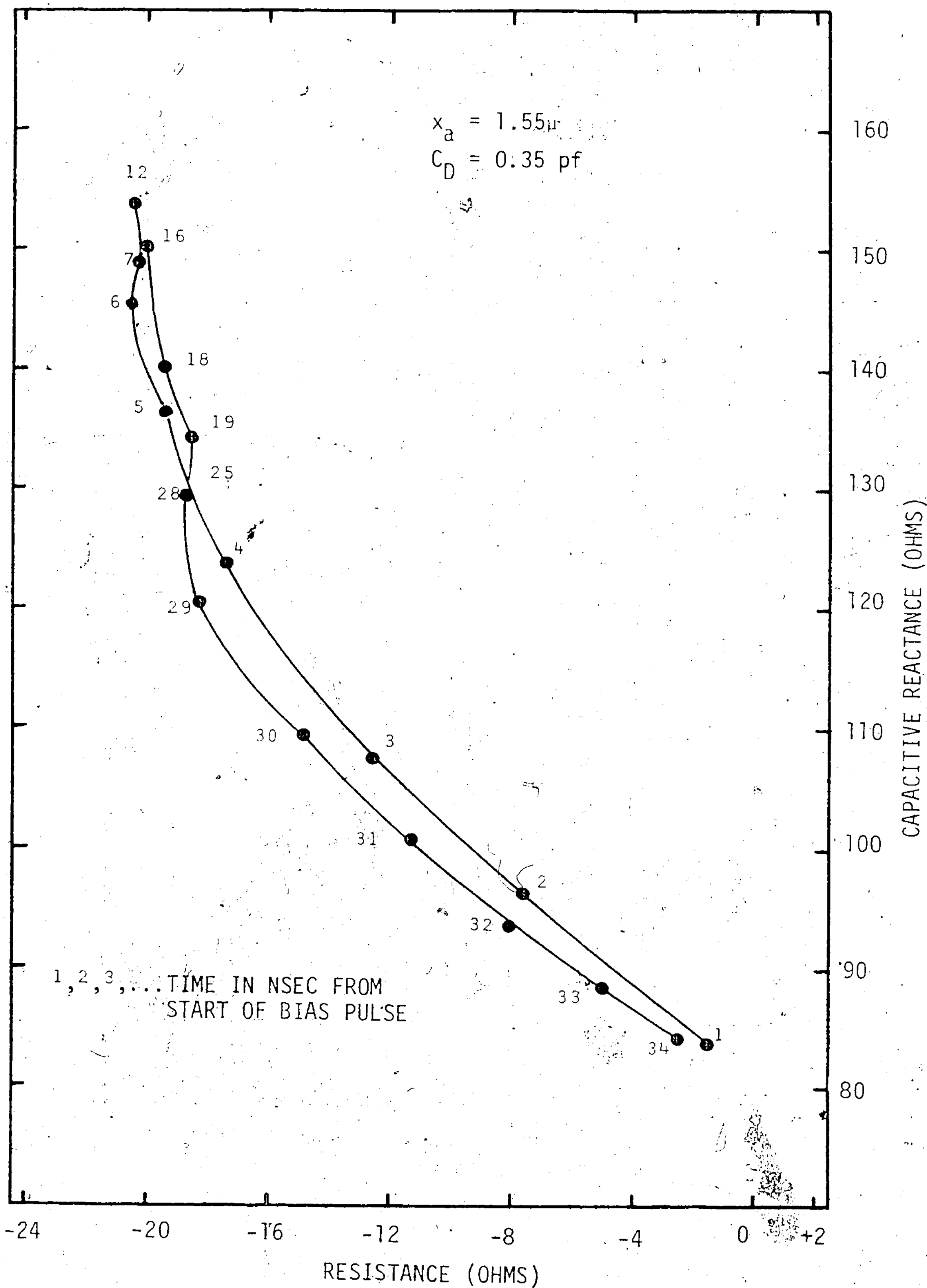

FIG. 4.6 COMPUTED VALUES OF ELECTRONIC IMPEDANCE FOR AN AVALANCHING IMPATT DIODE (DIODE #1 AT 6.0 GHz) WHERE x_a=1.55μ, C_D=0.35 pf AND K=0.0238

Fig. 3.4, the equivalent width of the avalanche region is known for a doping level of about $1.1 \times 10^{16} cm^{-3}$. An estimate for the doping levels in the diode junction can be obtained from the 1 MHz capacitance-voltage measurements and then the above information can be used in conjunction with the experimental results to determine the value of x_a.

In Figs. 4.3 to 4.6 the values of the parameters were for diode #1, driven by a R.F. voltage whose frequency was 6.0 GHz. The values of $\overline{W}$ and τ_d were fixed at 3.75 and 0.26 respectively, with the value of K set at 0.0238 unless otherwise specified. The same bias pulse was used for Figs. 4.3, 4.4 and 4.6.

During the computations, it became evident that, for a given value of bias voltage pulse, the magnitude of the d.c. current response observed in the computer model of the Impatt diode, was not quite the same as that observed in the experimental measurements. In diode #1 the computed current response had a greater magnitude than that experimentally observed for a given value of bias voltage pulse, while in diode #8 the opposite effect was found. This discrepancy could not be explained by a choice of the parameter values in the computer model and was thought to be a result of the manufacturing techniques used in fabricating the Impatt diode. Therefore, all the computed results were compared with the experiments on the basis of their d.c. current response and not on the exact magnitude of the bias voltage used.

The final computed results were plotted along with their associated experimental results given in Chapter VI. The series

resistance (R_S) due to contact losses, the resistance of the substrate and the undepleted region of the diode has not been taken into account. However, as the computations give the electronic impedance, the value of R_S can simply be added algebraically to the computed results. This action will result in a shifting of the plotted computed results along the real axis of the graphs.

4.4.3 Estimation of Computational Errors

The error in numerical calculations consists of truncation (discretization) and round-off errors. These errors are mainly controlled by the type of method used to solve the differential equation(s) and the selection of the step size. In choosing the step size, a balance must be maintained between the accuracy that is acceptable and the time required to complete a program run.

In general, the subject of round-off-error propagation is poorly understood.[31] The accumulated round-off-error is not simply the sum of the local round-off-errors because each local error is propagated and may either grow or decay as the computation proceeds. Decreasing the step size, increases the amount of calculations in the program and the accumulated round-off-error can be expected to increase. Therefore, as the step size is decreased, to reduce the truncation error, the effects of an increasing accumulated round-off-error should be considered.

The subroutine used for the solution of the differential equation(s) employed a Hamming's modified predictor-corrector method. This method gives an estimate of the local truncation error (∂) at each step in the program and thus, has the ability to automatically change

the step size. The user has to initially specify the step size (h) and the maximum allowable truncation error (e). In the subroutine, if $\partial > e$, h is halved, while if $\partial < e/50$, h is doubled. The subroutine will not allow the value of h to exceed that initially specified. When the program was initiated, it was observed that h is reduced from its initial value but, within a few steps the value of h has returned to its initial value. Therefore, at this point in the program $\partial < e/50$ for h/2. For the remainder of the program run the value of h is held constant.

The step size and the maximum truncation error were specified as 1/128 and 0.01 respectively. Computations carried out with these values gave results that were practically the same as the results obtained by using smaller values of h and e. Also, one complete program run could be carried out in less than four minutes of computer time.

4.5 Summary

A set of equations has been developed that will describe the behaviour of the electronic impedance of the Impatt diode. These equations have been cast into a form that permits them to be accurately solved by the simplest computational techniques. Solutions to these equations have been obtained using both analog and digital computers.

The solutions obtained on the analog computer were adequate to model steady-state conditions but were not sufficiently stable to yield accurate results when simulating transient conditions. Therefore,

the final solutions to the equations were obtained on an IBM 360/67 digital computer.

The structure of the equations describing the Impatt diode facilitates the correspondence between the computed and measured values of the electronic impedance. In the equations of the computer model, there are several parameters that have to be assigned values. It has been found that the more critical parameters have sufficiently independent effects upon the calculated electronic impedance, that they can be adjusted in a straight forward manner.

CHAPTER V

THERMAL PROPERTIES OF IMPATT DIODES

5.1 Introduction

In avalanche diodes, the temperature of the p-n junction influences the instantaneous magnitude of the junction breakdown voltage and hence the instantaneous magnitude of the junction current. Since the magnitude of the diode's electronic impedance is a sensitive function of the magnitude of the junction current, the characteristics of pulsed, avalanche diodes will change during the pulse on-time, as the junction temperature rises. In avalanche diode oscillators both amplitude and frequency modulation effects[11] occur as a result of these temperature fluctuations.

Previously, the junction temperature characteristics of these diodes have been reported[32] to within a few hundred nanoseconds of the initiation of the bias voltage pulse. In Digital Communications pulse durations of tens of nanoseconds may be used. Consequently, much more detailed information will be required on the time dependence of the junction temperature. The temperature-sensitive property of the semiconductor junction that is most directly related to the operation of the Impatt diode is the reverse-bias breakdown voltage. This temperature-sensitive property can be utilized to obtain a relationship between the junction temperature and the breakdown voltage. Then, if the time dependence of the breakdown voltage can be measured,

the time dependence of the junction temperature may be determined. The relationship between the junction temperature and breakdown voltage is determined with steady-state measurements, while the time dependence of the junction breakdown voltage requires measurements taken under transient conditions.

5.2 Steady-State Thermal Properties

As the junction temperature increases, the carriers interact more strongly with the crystal lattice and require a greater field strength to gain sufficient energy for impact ionization to occur. Therefore, the junction breakdown voltage increases with increasing temperature. The relationship between the diode junction temperature and the breakdown voltage was determined by measuring the breakdown voltage as the packaged diode was heated in an oven. Measurements were recorded for constant temperature levels ranging from 20°C to 150°C using the measurement system shown in Fig. 5.1. During the measurements, a constant direct current of 100 microamperes was maintained in the diode. This was necessary to ensure that microplasma effects were minimized and avalanche breakdown occurred across the entire junction area, thus ensuring that the junction was uniformly heated. This level of direct current results in only about 10 milliwatts of power dissipation within the diode junction and is small enough to have only minor effects on the measurements.

The effects of non-zero power dissipation in the junction can be accounted for if the thermal resistance between the diode junction and the heat sink is known. As shown in (32), the thermal resistance

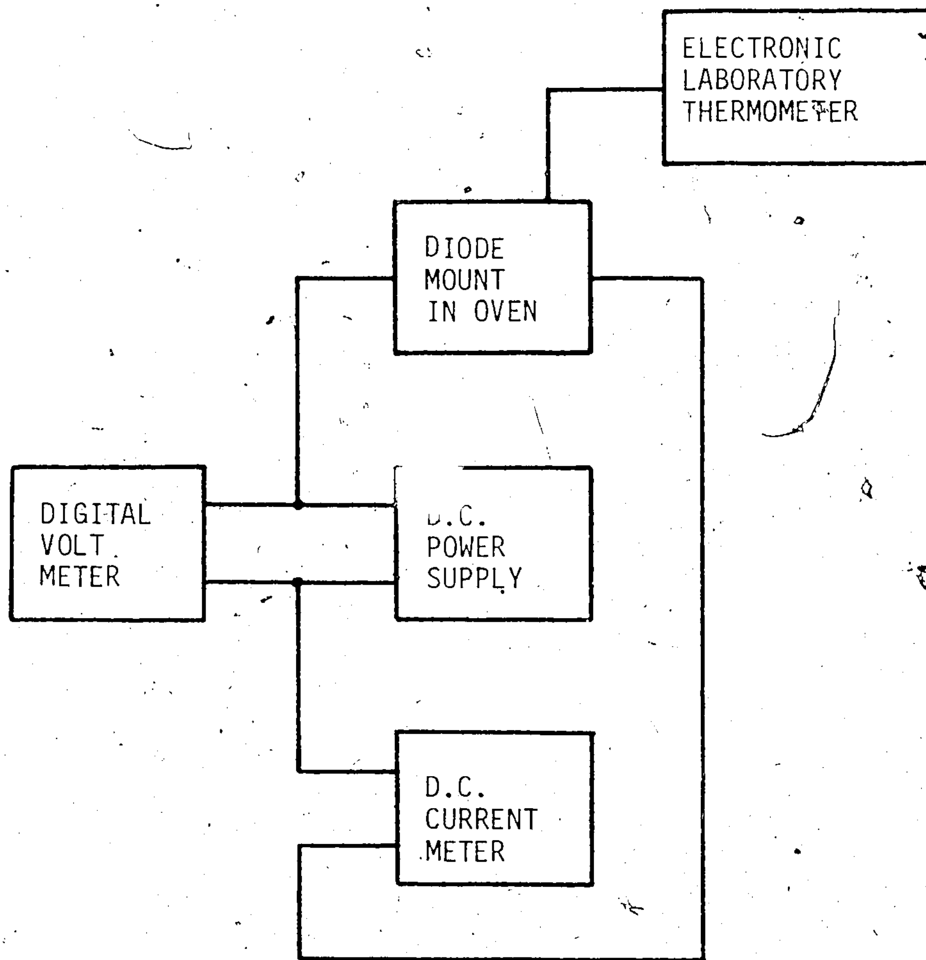

FIG. 5.1 MEASURING SYSTEM FOR STEADY-STATE TEMPERATURE DEPENDENCE OF AVALANCHE DIODE BREAKDOWN VOLTAGE

(r) is defined as

$$r = \frac{T_{j2} - T_{j1}}{V_2 I_2 - V_1 I_1} \quad (1)$$

where T_{jn} is the average junction temperature associated with the average junction power dissipation $V_n I_n$. Then the corrected junction temperature (T_{jc}) is given by

$$T_{jc} = T_j + r\, V_B(T_j) I \quad (2)$$

where $V_B(T_j)$ is the measured breakdown voltage corresponding to the heat sink temperature T_j and I is the direct current at the time of the measurement. Thu results of measurements of breakdown voltage versus temperature can be corrected for power dissipation within the junction itself.

The junction temperature-breakdown voltage measurements were carried out using commercially available Hewlett Packard 5082-0437 Impatt diodes. Results obtained for two diodes were practically identical and the typical measured temperature dependence of the breakdown voltage is shown in Fig. 5.2. From these measurements r was found to have a numerical value of 22.5°C/watt and the slope of the $V_B(T_j)$ versus T_{jc} plot was linear from 20°C to 150°C, with an average slope of 0.12 V/°C. The results obtained in these measurements are in close agreement with those of previous work[32]. The pertinent characteristics of the diodes used in these measurements are given in Table 5.1, where the values were taken at room temperature and the depletion region width and doping levels were derived from 1 MHz

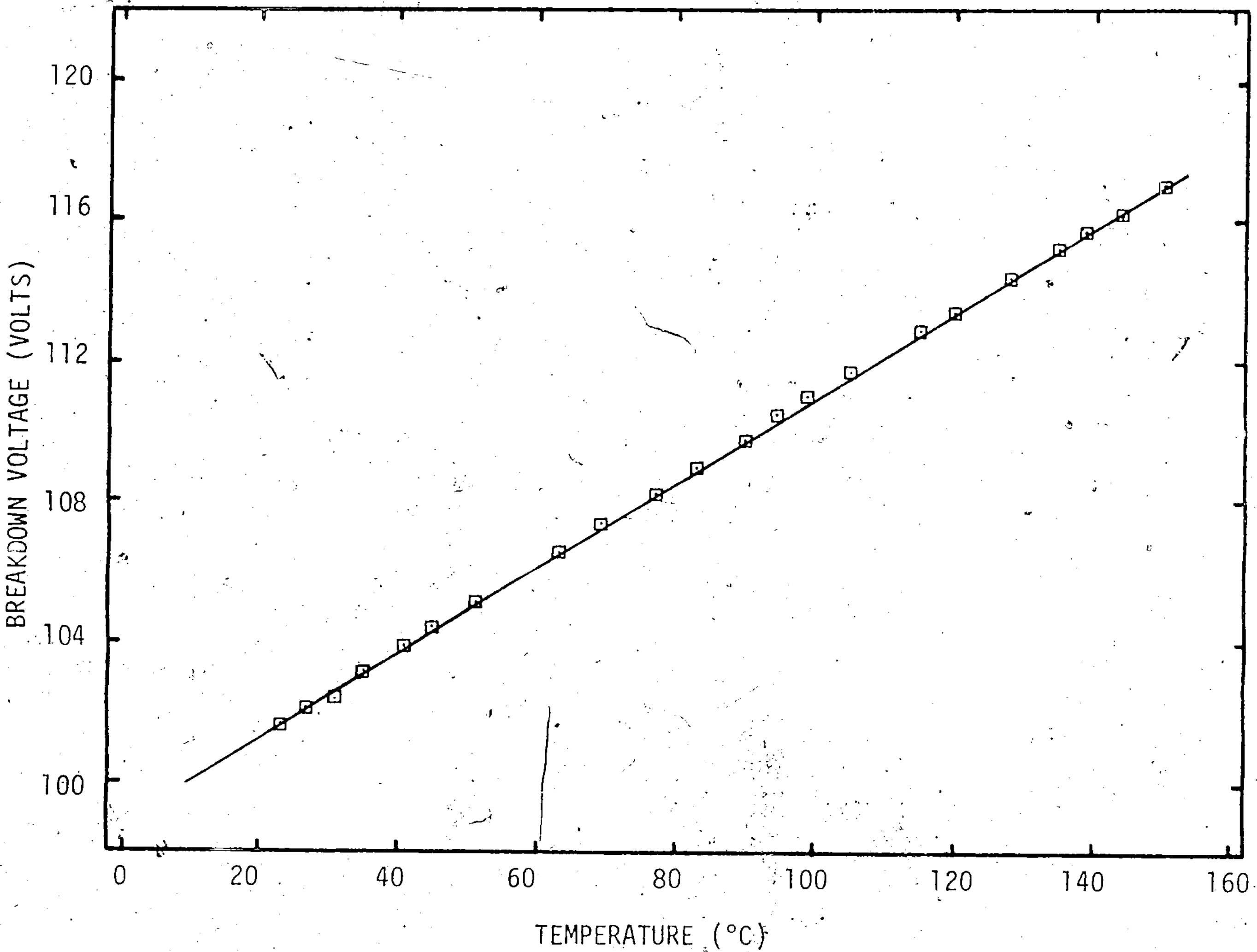

FIG. 5.2 TEMPERATURE DEPENDENCE OF JUNCTION BREAKDOWN VOLTAGE FOR H.P. 5082-0437 IMPATT DIODES

capacitance-voltage measurements. It was also noted from these measurements, that the diodes were closely approaching a punch through condition when the reverse bias voltage reached the breakdown value. Since both diodes displayed practically identical temperature dependence of the breakdown voltage, it would appear that differences in the depletion region width and doping concentrations of the range shown in Table 5.1 do not alter the steady-state thermal characteristics of these diodes.

TABLE 5.1

CHARACTERISTICS OF IMPATT DIODE

TYPE H.P 5082-0437

DIODE	BREAKDOWN VOLTAGE (100μa)	DEPLETION LAYER CAPACITANCE	DEPLETION LAYER WIDTH	AVERAGE DOPING CONCENTRATION
#1	101.7	0.28 pf	3.75 μ	9.13×10^{15}
#2	102.8	0.24 pf	4.35 μ	6.85×10^{15}

5.3 Transient Thermal Properties

Since little is known of the transient response of the junction temperature of Impatt diodes, it was deemed advisable to study its behaviour experimentally prior to developing the theoretical model of heat flow in the junction area of the diode. The philosophy of the work reported by Mosekilde *et al*[33] in their theoretical study on the thermal response of pulsed Gunn diodes, may be applicable

to Impatt diodes as well and provide an indication of the results to be expected.

5.3.1 Measurements of Transient Heat Flow

A double-pulse measurement method similar to that presented by Nigrin[32], was utilized to measure the time dependence of the junction breakdown voltage. Then, with reference to Fig. 5.2, the time dependence of the junction temperature was determined. This double pulse method utilizes a main pulse of appreciable duration to reverse bias the Impatt diode beyond breakdown and a sampling pulse of much shorter duration and opposite polarity to return the bias voltage to its breakdown level. As the junction temperature changes, so will the magnitude of the breakdown voltage and hence, the magnitude of the sampling pulse required to return the junction to its breakdown condition. In order to conduct measurements to within a few nanoseconds of the onset of the main bias pulse, the sampling pulse must have a fast rise time and be of short duration. This presents some problems in designing the circuitry so that it will accept the fast rise times and fully react within the duration of the sampling pulse. The measurement system is shown in Fig. 5.3, where the coupling of the main and sampling pulsers, plus the measurement points A and B, were incorporated into a pair of airline tees whose characteristic impedance was 50 ohms. All interconnecting leads were kept as short as possible (maximum length about 3 inches) and were constructed from heavy copper wire (12 gauge). The d.c. power supply was shunted with low parasitic inductance capacitors to enhance the system response time.

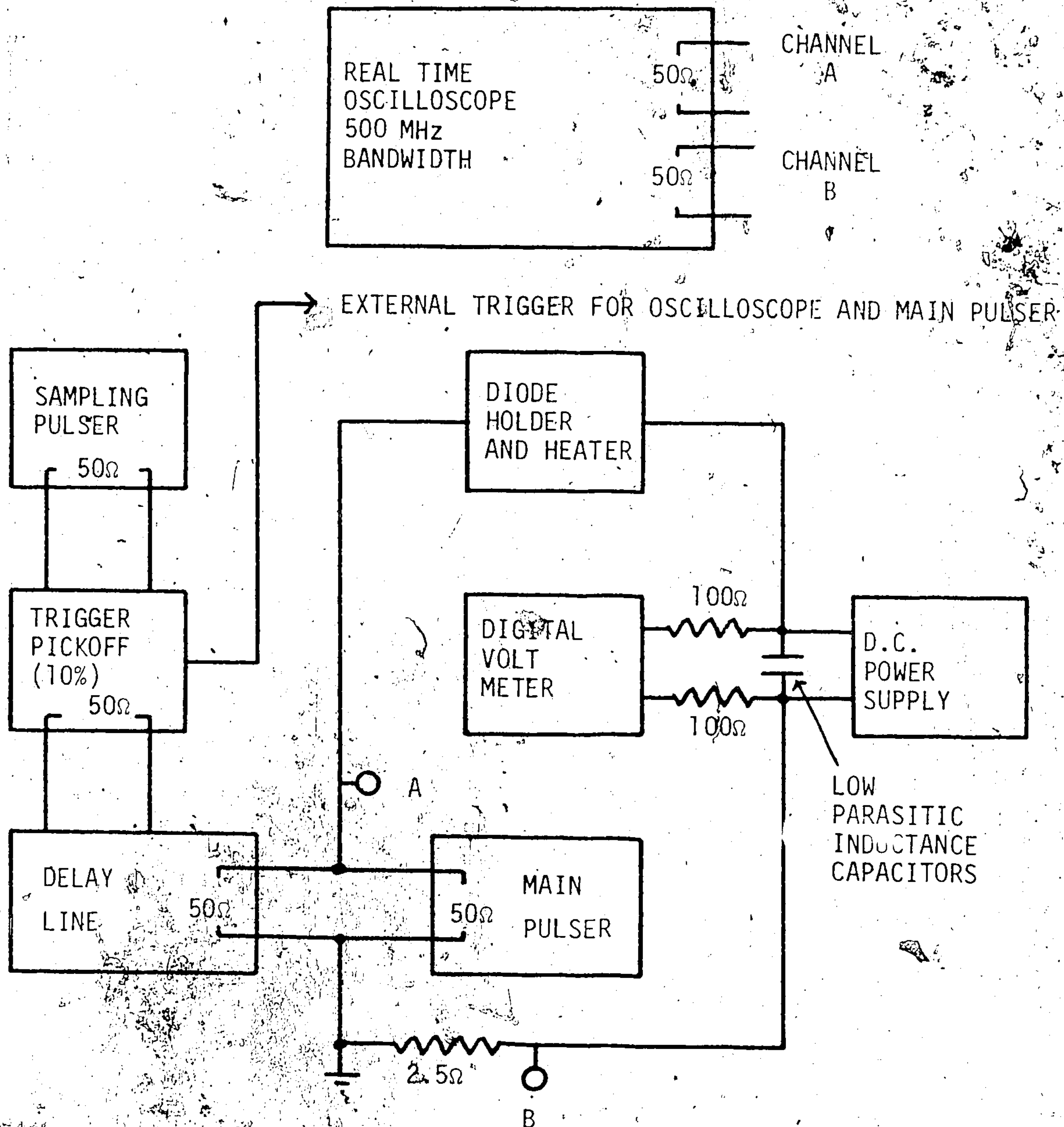

FIG. 5.3 COAXIAL SYSTEM FOR MEASUREMENT OF TRANSIENT JUNCTION TEMPERATURE

Since the double-pulse method, as used here, allows the observation of the main and sampling pulses as they are applied to the diode (measurement point A in Fig. 5.3), as well as the current through the diode (measurement point B in Fig. 5.3), the pertinent pulse shapes are known. The circuit was adjusted so that it would fully respond to the sampling pulse in less than 6 nanoseconds. Therefore, a sampling pulse with a rise time of 1 nanosecond and a duration (exclusive of rise and decay times) of 6 nanoseconds was used. The main bias pulse had a rise time of 5 nanoseconds and a duration of 200 nanoseconds. To ensure that the diode junction temperature had closely approached that of the heat sink, between main bias pulses, the pulse repetition rate was set to about 500 pulses per second.

The measurement procedure was to adjust the magnitude of the main bias voltage pulse until the diode current, during the main pulse, was at the desired level. Then, at selected time intervals following the onset of the main bias pulse, the magnitude of the sampling pulse was carefully adjusted until the net bias voltage across the diode, within the duration of the sampling pulse, had just been reduced to the breakdown value. This magnitude of the sampling pulse and the time interval were recorded and plotted as the change in the junction breakdown voltage with time, relative to the onset of the main bias pulse.

The reduction of the net bias voltage across the diode, to the breakdown value, was apparent from observing the instantaneous diode current. When bias voltage across the diode reaches the breakdown

va[illegible]ue [illegible] [illegible] [illegible]uctuations associated with microplasma b[illegible]e[illegible] cause t[illegible] [illegible]de c[illegible]urrent to vary slightly for each pulse [illegible] [illegible]titive b[illegible] voltage pulse train. The observed effect on the osc[illegible]ope tr[illegible] [illegible] a "flutter " instability in the current waveform [illegible] [illegible]sociated with the trailing edge of the sampling bias pulse [illegible] [illegible]g the experiments, the magnitude of the sampling pu[illegible]e was [illegible]eased until this instability in the current waveform became apparent. By selecting the magnitude of the sampling pulse where the flutter just becomes definite as a reference, it was possible to carry out consistent measurements at all selected sampling positions wi[illegible]hin the duration of the main bias pulse.

Typical waveforms observed during the measurements are shown in Fig. 5.4. In these photog[illegible]phs, the upper trace represents the diode current, while the lower trace shows the main and sampling bias voltage pulses. Both the diode current and the main bias pulse increase in magnitude toward the bottom of the photograph. The magnitude of the sampling bias voltage pulse increases toward the top of the photograph. Fig. 5.4(a) shows the overall relationship between the main bias voltage pulse, sampling bias voltage pulse and the diode current response to both these bia[illegible] [illegible]ulses. Fig. 5.4(b) gives an expanded view of the effect upon th[illegible] d[illegible]ode current when the sampling bias voltage pulse is applied. In Fig. 5.4(c) the magnitude of the sampling bias voltage pulse has been increased until the characteristic "flutter" in the diode current is apparent.

Fig. 5.4 PHOTOGRAPHS OF TYPICAL OSCILLOSCOPE TRACES OBSERVED DURING THE TRANSIENT JUNCTION TEMPERATURE MEASUREMENTS.

In all photographs, the upper trace represents the d.c. diode current resulting from the application of the main and sampling bias voltage pulses. These bias voltage pulses are shown in the lower trace. The upper trace has a vertical scale of 20 MV/cm and the horizontal scale is indicated in the lower right hand corner of each photograph.

Fig. 5.4(a) Overall relationship between the main and sampling bias voltage pulses and the resulting diode current.

Fig. 5.4(b) Expanded view of the sampling bias pulse and its effect on the diode current.

Fig. 5.4(c) Characteristic flutter in the diode current waveform associated with the reduction of the bias voltage to the breakdown level.

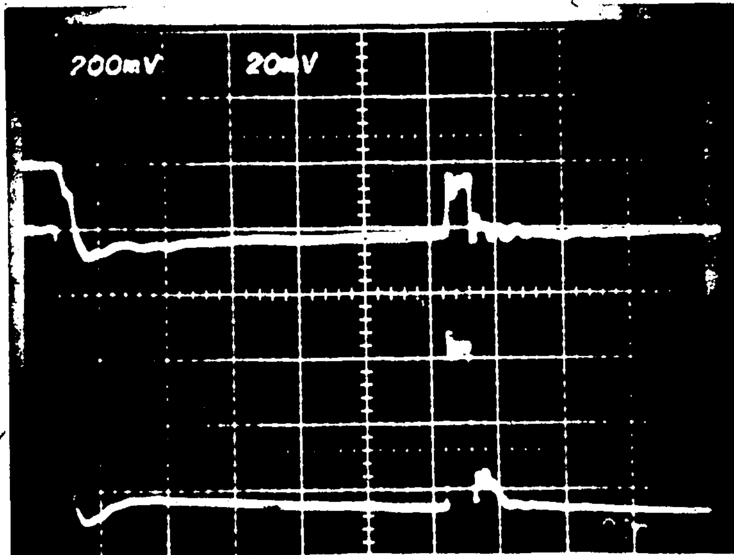

Fig. 5.4 (a)

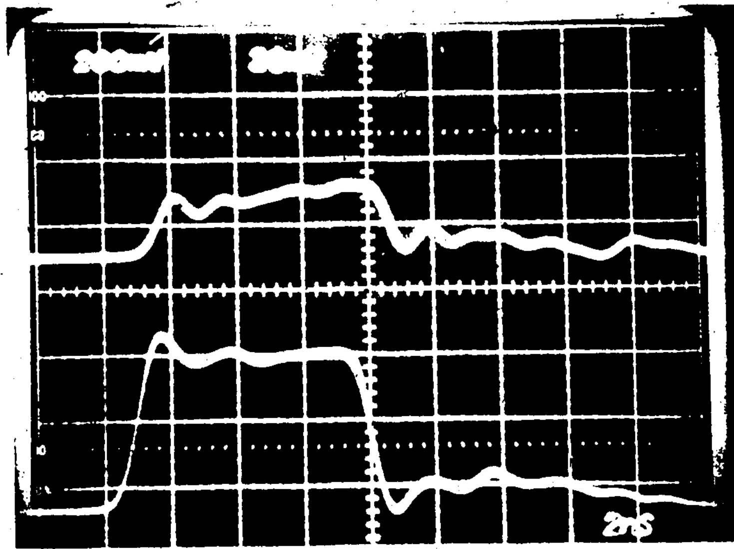

Fig. 5.4 (b)

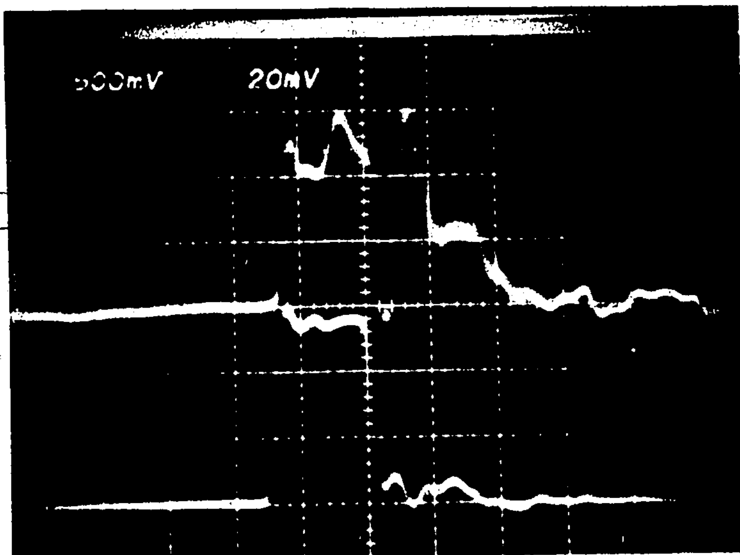

Fig. 5.4 (c)

From Fig. 5.4(a), it is observed, that, as time measured from the onset of the main bias pulse increases, that the diode current gradually decreases and the main bias pulse voltage gradually increases. This decrease in the diode current is a result of the increasing junction temperature, while the increase in the main bias pulse is a characteristic of the measuring setup. With reference to Fig. 5.3, monitor positions A and B were connected to the 50 ohm impedance oscilloscope channels A and B, respectively. Thus, the voltage applied to the diode, monitored at position A, is the fixed voltage pulse supplied by the main pulser minus the voltage drop across 3-50 ohm impedances in parallel. As the diode current decreases, so does the voltage drop across the 16.67 ohm impedance and the resultant voltage at A shows a corresponding increase. This effect may lead to some inaccuracy in the measured results; however, this effect should be very small.

The waveforms shown in Figs. 5.4 display some characteristics which are not an integral part of the measurements. The small overshoot at the leading edge of the main bias pulse is a characteristic of the circuitry and the main bias pulser, consequently part of the initial rapid decrease in the diode current shown in Fig. 5.4(a) is due to the decay of the overshoot in the buildup of the main bias pulse. Also, in Fig. 5.4(c), the initial return spike of current coinciding with the trailing edge of the sampling pulse is due to capacitive charging in the circuitry. The actual buildup of diode current after the decay of the sampling pulse is represented by the unstable portion of the waveform.

Measurements of the increase in junction breakdown voltages with time, were carried out at various heat sink temperatures in the range 25°C to 150°C. To avoid the complex current fluctuations associated with microplasma breakdown at the onset of the main bias pulse, a diode current of 1 ma was maintained before the application of the main bias pulse. Complete tests were conducted at each base temperature using two separate Impatt diodes and two magnitudes of the main bias pulse. The main bias pulse was adjusted so that average diode currents of 15 and 30 ma were maintained for the duration of the main bias pulse. Each test, within itself, was very consistent with little scatter among the plotted measurement data. The experimental results showed little change as the heat sink temperature was increased from 25°C to 150°C. While the diode current level did decrease as the heat sink temperature was raised (for a fixed magnitude of main bias pulse), the variation of the diode junction breakdown voltage stayed relatively the same. For the same reference conditions, the diodes used here produced generally similar results, with only small differences in the base levels and slopes of the plotted results.

Typical behaviour of the junction temperature with time is shown in Fig. 5.5. Also shown in this Figure are the theoretical results which are included here for comparison purposes in later discussions. The two sets of curves correspond to the two current levels used for the tests, namely 15 and 30 milliamperes. In Fig. 5.5, the zero time corresponds to the onset of the main bias pulse, which is taken as the point on the initial voltage buildup at which the magnitude of the pulse equals 90% of its maximum value, including the overshoot. Previously

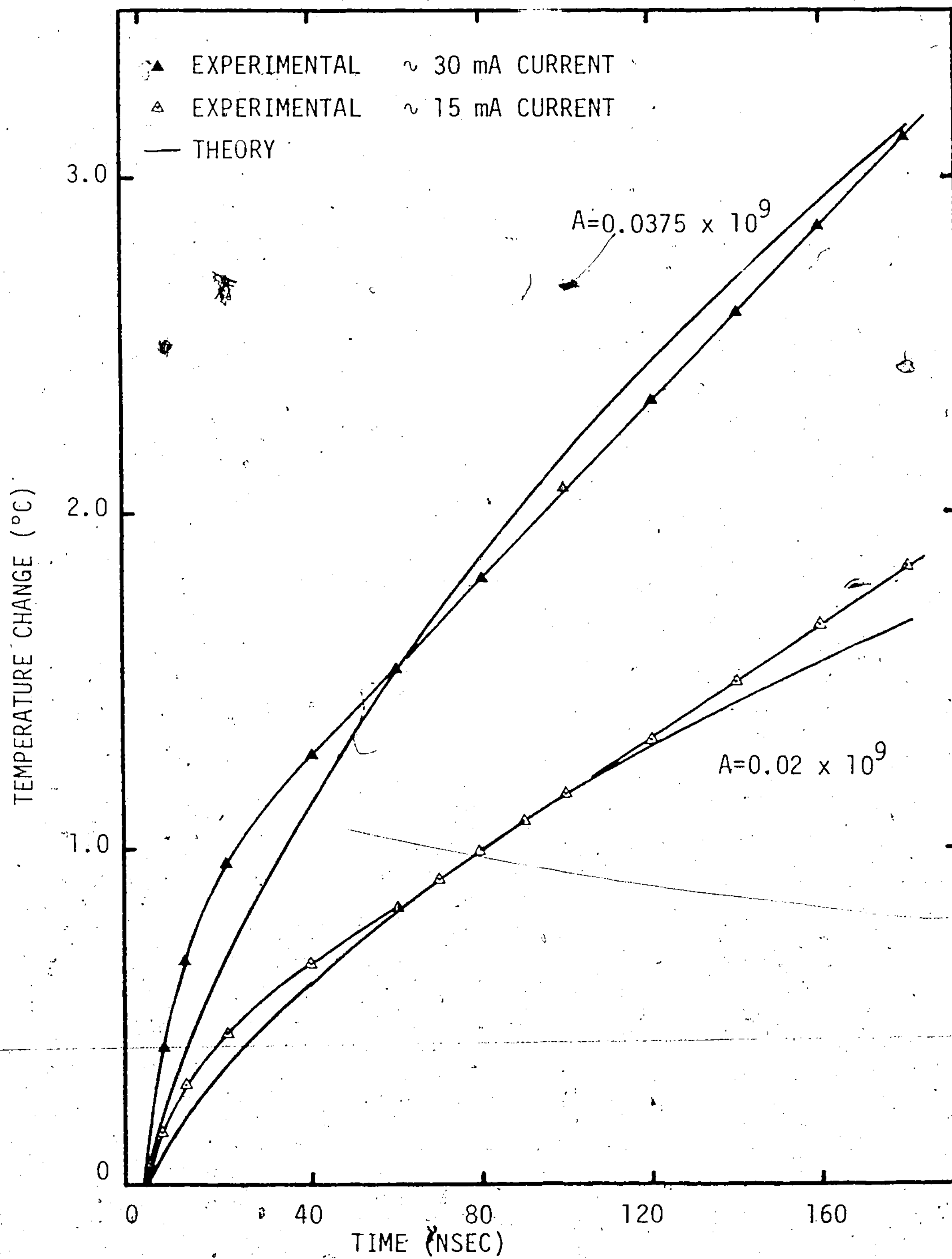

FIG. 5.5 RELATIVE CHANGE IN JUNCTION TEMPERATURE WITH TIME FOR AN IMPATT DIODE

reported[32] measurements of the temperature dependence of the diode junction can be interpreted to within 100-200 nanoseconds of the onset of the main bias pulse. These earlier measurements are consistent with the measurements reported here, in that the final slopes of the plotted measurements given in Fig. 5.5 closely agree with the initial slopes of the previous measurements.

5.3.2 Thermal Model For Transient Heat Flow

The heat generated in a p^+n Impatt diode by the direct current power dissipation is largely confined to the high resistivity region, with the major part of the heat being generated near the junction where the electric field has its largest magnitude. The argument used to justify one-dimensional analysis for the electrical properties of the Impatt diode can also be used to justify one-dimensional analysis for the thermal properties of this diode. Confining the discussion to one-dimensional analysis, the heat flow in the diode can be represented by a semi-infinite solid of length ℓ with heat generated uniformly and at a constant rate within a region at one end of the solid. This model is shown in Fig. 5.6, where the heat generation is confined to the region $o \leq x \leq y$. With reference to Fig. 5.7, which shows the physical structure of the diode[32], by taking the $x=o$ plane as the center of the heat generation region, the boundary conditions at this reference position are those of a thermally insulated plane. Far from the heat generation region the temperature will be held at some constant value, such as that of the heat sink. Under these conditions the heat conduction equation is

$$\frac{\partial T}{\partial t} = D \frac{\partial^2 T}{\partial x^2} + \frac{H}{C_V} \quad (1)$$

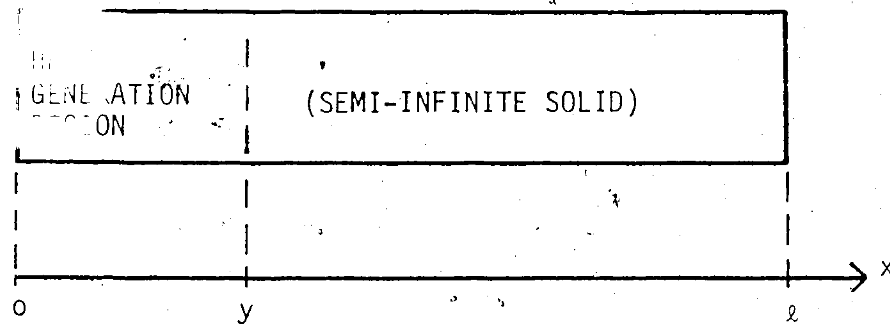

FIG. 5.6 ONE-DIMENSIONAL MODEL FOR TRANSIENT HEAT FLOW IN A H.P. 5082-0437 IMPATT DIODE

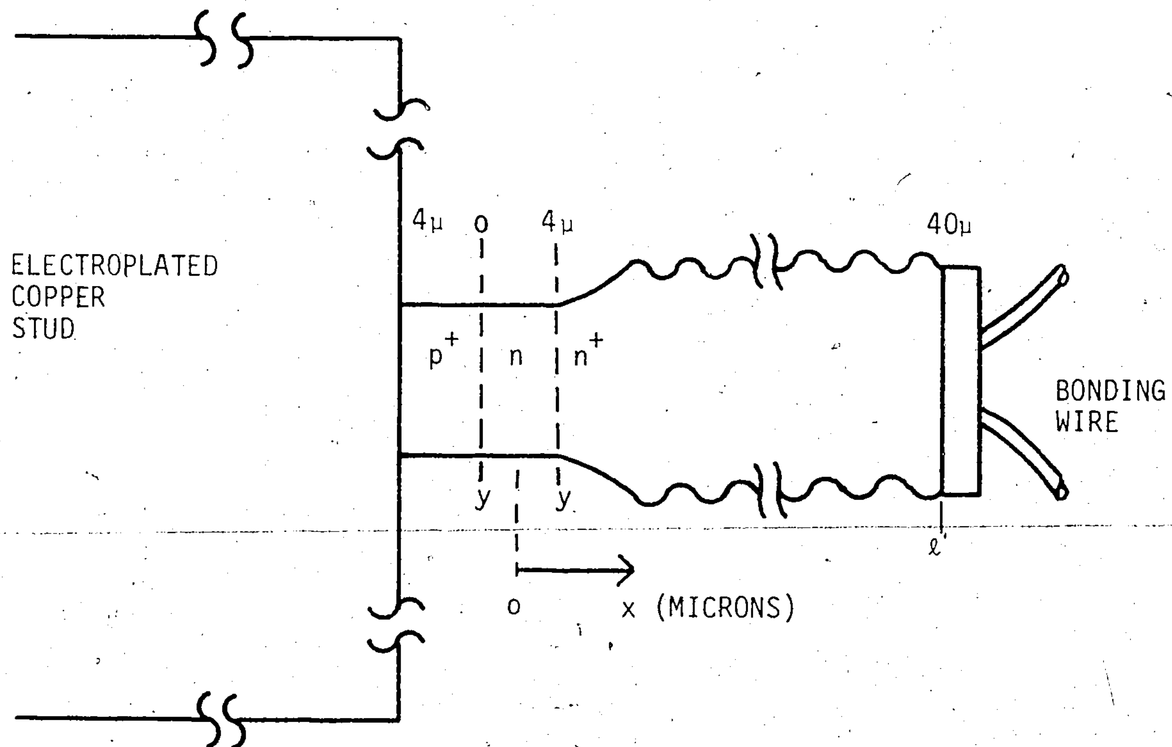

FIG. 5.7 SCHEMATIC OF CROSS SECTION OF AN H.P. 5082-0437 IMPATT DIODE

where the variation in time (t) of the temperature (T) at various positions (x) in the solid, depends upon the thermal diffusivity (D), the heat capacity (C_V) and the rate of heat generation (H) per unit volume, per unit time. The applicable boundary conditions are

$$\frac{\partial T}{\partial x} = 0 \qquad x=0 \qquad (2)$$

$$T=T_0 \qquad x=\ell$$

also, the parameters D and C_V have been assumed to be independent of temperature and constant throughout the solid. Since only the change in temperature with position and time is of interest, the initial temperature (T_0) may be taken as zero. With these boundary conditions, the solution to the heat conduction equation[35] given in Eq. (1) is

$$T = \frac{Ht}{C_V}\{ 1 - 2\, i^2 \operatorname{erfc} [\frac{(y-x)}{\sqrt{4Dt}}] - 2\, i^2 \operatorname{erfc} [\frac{(y+x)}{\sqrt{4Dt}}]\} \qquad 0 < x < y \quad (3)$$

and

$$T = \frac{2Ht}{C_V}\{ i^2 \operatorname{erfc} [\frac{(x-y)}{\sqrt{4Dt}}] - i^2 \operatorname{erfc} [\frac{(x+y)}{\sqrt{4Dt}}] \} \qquad x > y \quad (4)$$

This solution is essentially the same as that given by Mosekilde[33] *et al.* and when taken at x=o can be written as

$$T = \frac{Ht}{C_V}\{ 1 - 4\, i^2 \operatorname{erfc} [\frac{1}{2\sqrt{Dt/y^2}}]\} \qquad (5)$$

This last equation is not bounded for $t \to \infty$ and will not accurately describe the temperature for steady-state conditions; however, the transient heat flow under pulsed bias conditions should be adequately represented.

These equations will describe the heat flow in either direction in the Impatt diode (Fig. 5.7) if the diffusivity constant is similar for both directions and if there is a very low thermal resistance between the silicon and the copper. The diffusivity constant[36] for silicon and copper are given as 0.8 and 1.14 cm^2/sec, respectively, for room temperature conditions. From the steady-state temperature measurements, the value of thermal resistance between the diode junction and the heat sink was found to be low (22.2 °C/watt). This thermal resistance includes the effects of the bulk semiconductor, and the heat-sink-diode-package union plus the interface between the semiconductor chip and the copper stud. Therefore, the thermal resistance of this silicon-copper interface will be significantly less than 22.5°C/watt. Consequently, Eqs. (3), (4) and (5) should adequately describe the heat flow in the Impatt diodes used in the measurements reported here.

Since the p-n junction of the diode will be very close to the x=o plane of the heat flow model, the time-dependent temperature profile of the junction can be represented by Eq. (5), which is plotted in Fig. 5.5. In this Figure, the parameter A, which represents the quantity H/C_V, was chosen for a close correspondence of the theoretical to the experimental results. The experimentally observed initial rise of junction temperature is greater than the theory would indicate. This could be accounted for by some small delay in the initial transfer of heat away from the junction area or some inherent inadequancy in the one-dimensional approximation of the heat flow model. Otherwise,

there is generally good agreement between the experimental results and the theoretical model for the transient heat flow in the junction area of the Impatt diode used here.

When considering the heat flow through regions of the semiconductor diode which lie outside the immediate vicinity of the junction, Eqs. (3) and (4) have to be considered. These equations have been plotted in Fig. 5.8[33] as a function of the parameter Dt/y^2. Considering the physical structure of the Impatt diode given in Fig. 5.7, an appropiate value for y would be 2 microns, then using $D=0.8\ cm^2/sec$ for silicon and $t=200$ nanoseconds, the parameter Dt/y^2 is evaluated as 4.0. With reference fo Figs.5.7 and 5.8, it is observed, for durations of the main bias pulse of 200 nanoseconds or less, that heat flow from the junction area has penetrated only about half the n^+ region. Therefore, the relatively poor heat sinking at the wire bond should have little influence on the junction temperature for the low repetition rate of pulsed bias operation used here. The heat flow through the p^+ region has only a few microns distance to travel before reaching the heat sink. Hence, the heat flow through the p^+ region will be the governing factor in determining the junction temperature.

From the results given here and those reported earlier[32,33], the simplified thermal model, represented by Eqs. (3), (4) and (5) would appear to adequately describe the heat flow in the region of the semiconductor junction under pulsed bias conditions. It is likely that the thermal model only describes the heat flow during the first 30-40 nano-

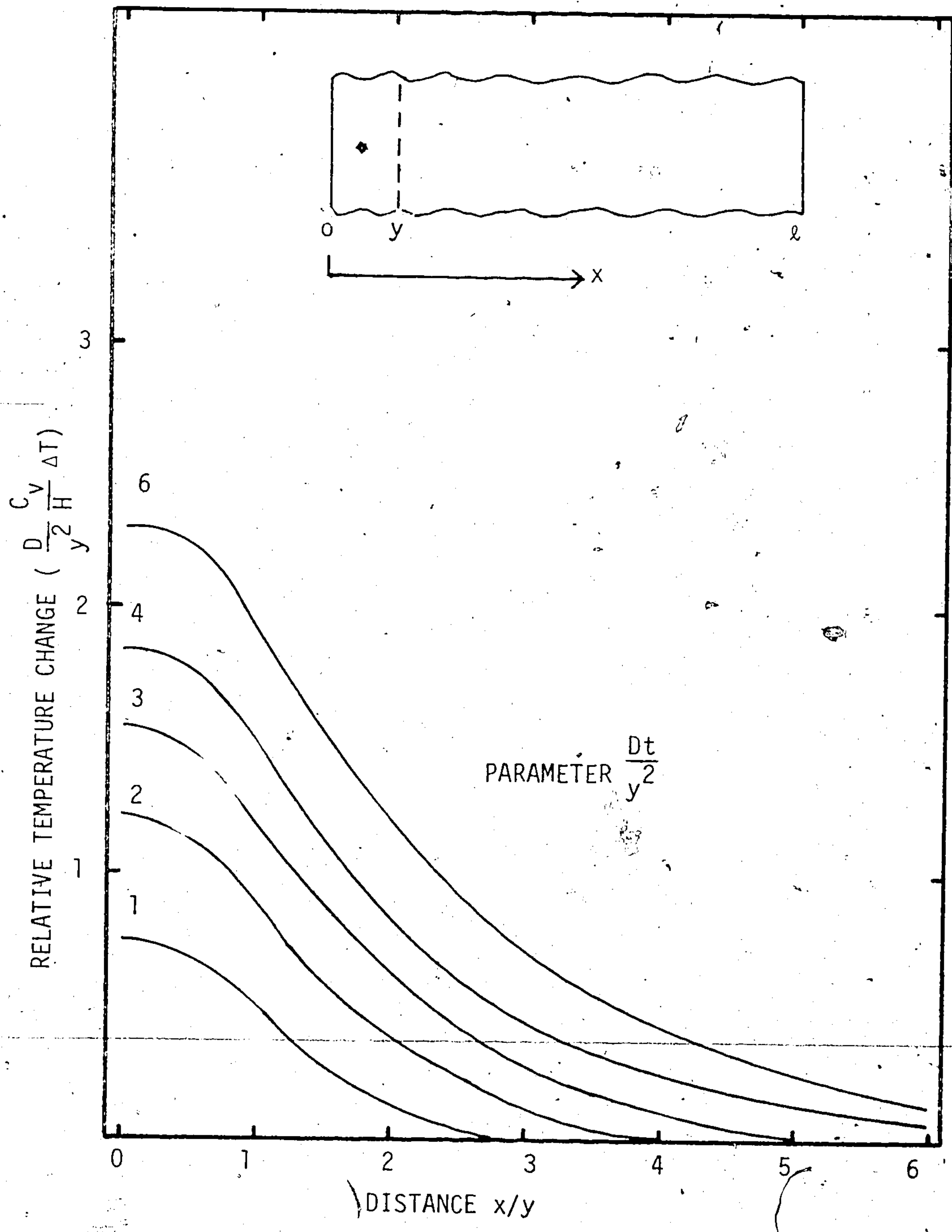

FIG. 5.8 RELATIVE TEMPERATURE CHANGE WITH DISTANCE IN A ONE-DIMENSIONAL HEAT FLOW MODEL

seconds and then the heat flow from the relatively small silicon-copper interface, to the larger copper stud, becomes increasingly important. However, this is a more complex problem where more than one-dimensional analysis may have to be used and is beyond the scope of the work being carried out here.

5.4 Computer Modelling of Thermal Properties

From the steady-state thermal properties of the Impatt diode it is known that the junction temperature is directly related to the junction breakdown voltage. Thus, for a given value of reverse bias voltage across the diode junction, an increase in the junction temperature of a certain amount is taken to correspond to a known decrease in the effective bias voltage applied to the junction, therefore, the effect of junction temperature changes can be incorporated in the equations of the computer model as a change in the d.c. bias voltage applied to the diode. With reference to the normalized equations given in the previous chapter, Eqs. (7) and (14) Section 4.2, the term V_B in the electric field equation represents the bias voltage applied to the diode and it would be this term that would be varied with time to account for the changes in the junction temperature.

To provide an accurate comparison between the computed and experimental results, both the decreasing current through the diode and the increasing main voltage pulse across the diode (reference Fig. 5.4(a)) were taken into account. In the computer model the bias voltage applied to the diode junction (V_B) consisted of three components, the

fixed bias voltage set at the main pulser (V_m), the voltage drop across the 16.67 ohm resistance, at measurement point A, due to the current flow in the circuit (V_R) and the change in the breakdown voltage due to the increasing junction temperature (V_T). The net bias voltage applied to the junction is denoted V_B and can be written as

$$V_B = V_m - V_R - V_T \qquad (1)$$

where the values of V_T are taken from the experimental results and both V_R and V_T will change with time.

In arriving at a relation that would describe the time (t) dependence of V_T, Eq. (5) sub-section 5.3.2, was replaced with a closer approximation to the experimental results by using a $\sqrt{t}$ dependence from 0 - 40 nanoseconds and a linear dependence on t from 40 - 200 nanoseconds. Following the same procedures as outlined in Chapter IV, where the scaled time (τ) was used, the following relations for V_T were obtained:

- for $o \leq t \leq 40$ nanoseconds $\qquad o \leq \tau \leq 400$

  $V_T = 0.0057 \sqrt{\tau}$ for the 15 ma current level

  $V_T = 0.0084 \sqrt{\tau}$ for the 30 ma current level

- for $t > 40$ nanoseconds $\qquad \tau > 400$

  $V_T = 0.0001\tau$ for the 15 ma current level

  $V_T = 0.00017\ \tau$ for the 30 ma current level

When these values were applied as V_T, the computed results were found to be practically identical to the experimental results in the time variation of both the diode current and the main bias pulse (reference

Fig. 5.4(a)). The computations were carried out using room temperature data for the ionization rates.

5.5 Summary

In this chapter, both the steady-state and the transient thermal properties for a type of Impatt diode have been investigated. A double-pulse method has been used which permitted measurements of the junction temperature to be carried-out to within 5 nanoseconds of the onset of the bias voltage pulse. These studies have related the experimental measurements to a theoretical model for heat flow in a semiconductor and also to the computer modelling of the Impatt diode. Good agreement has been obtained between these three aspects of this study.

A study of the time dependence of the junction temperature was carried out by measuring the time dependence of the junction breakdown voltage and the steady-state relationship between the junction temperature and breakdown voltage. These two sets of measurements were conducted over a range of temperatures from 20°C to 150°C. It was found that the relative change in junction temperature, during the application of a bias voltage pulse, was essentially the same for the entire range of heat sink temperatures used here. By extending the measurements to include the time interval of 100-200 nanoseconds after the onset of the bias pulse, it was possible to compare the results with previously published work[32]. The resulting comparison showed good agreement in the change of junction temperature with time. A temperature of 150°C was the upper limit of the measurement system as

it was used here. The main limiting factor is the method used to hold and heat the packaged diode. Electrical interconnections have to be kept short to preserve the system response to the fast rise time pulses, while at the same time, the high heat sink temperatures should not be applied to the bias voltage pulsers. Extensive design work may have to be carried out if heat sink temperatures greater than about 150°C are to be used with this method.

A theoretical model of the time dependence of the junction temperature was arrived at by considering a one-dimensional analysis of a semi-infinite semiconductor, with a well-defined location of heat generation at one end. This heat flow model gave good agreement with the experimental results but the model will be limited to representing only pulsed operation of the Impatt diode. It has been found, for the low pulse repetition frequencies used here, that the poor thermal path presented by the bonding wire in the diode package will have minimal effect on the junction temperature. However, there will be an upper limit on the pulse width and repetition rate, above which the thermal path presented by the bonding wire will affect the time dependence of the junction temperature. Then, a much more detailed analysis of the heat flow in the diode and its package would have to be carried out.

Incorporating the time dependence of the junction temperature into the computer model of the Impatt diode was readily carried out. A simple variation of the simulated d.c. bias voltage sufficed to reproduce the experimentally observed variations in diode current and bias voltage. Since the junction temperature mainly alters the diode

current, as long as the computed and experimental results are compared on the basis of similar diode currents the effects of junction temperature changes on this comparison, should be minimized.

In the following work on transient impedance studies of Impatt diodes, a knowledge of the behaviour of junction temperature as a function of the duration of the bias voltage pulse will be important. The buildup of R.F. oscillations in a diode-coupled cavity can be of the order of 100 nanoseconds, in which time the junction temperature of the diode may change appreciably, leading to changes in the electronic impedance of the diode and thus frequency changes in the R.F. If the bias pulses are of short duration (less than 40 nanoseconds) then the effects of the junction temperature change will be significantly reduced and may even be able to be ignored in certain circumstances.

CHAPTER VI

TRANSIENT MICROWAVE IMPEDANCE MEASUREMENTS

6.1 Introduction

Impedance measurements provide an important means of studying the microwave properties of Impatt diodes and are essential when designing amplifier and oscillator circuits for these diodes. Several authors(37-40,25) have published methods and/or results of microwave impedance measurements on packaged diodes. All of these measurements have been made under steady-state conditions. The usual procedure is to measure the admittance/impedance of the packaged diode at some convenient reference plane, and then transform the results through an appropiate equivalent circuit to arrive at the admittance/impedance of the semiconductor diode chip itself. The impedance measurements mentioned above are all performed by measuring the Voltage Standing Wave Ratio (VSWR) or the voltage reflection coefficient (Γ) in a transmission line. (The general relations between VSWR, Γ and impedance are given in Appendix B).

Even though a lot of work has been carried out in improving the microwave measurement techniques for Impatt diodes, they are still limited in their absolute accuracy. The magnitude of the packaged diode's negative resistance is of the order of 10 ohms, or even much less, for practical diodes. Under conditions of low d.c. currents, high R.F. voltages or maximum power output, this magnitude can be as low as 1 or 2 ohms. Van Iperen and Tjassens(41) claim that it is questionable whether the standard

VSWR or reflection coefficient measurement techniques are sensitive enough to produce highly accurate results at these low magnitudes. They advocate the use of a microwave impedance bridge technique that requires a very stable frequency source and some critically machined components.

The accuracy of the measurements is further restricted because the Impatt diode is a non-linear device and some harmonics of the fundamental frequency will be produced during the active measurements. Most measurement equipment does not possess sufficient bandwidth to handle the second harmonic component. Also, even small discontinuities in the measurement equipment and transmission lines used can cause the second harmonic component of the R.F. frequency to become significant at R.F. voltage magnitudes of only a few volts[25]. Therefore, all large-signal microwave impedance measurements were performed with R.F. voltage levels in the range of one volt (r.m.s.).

To date, a detailed comparison on the accuracy of the various applicable impedance measurement methods has not been carried out, to this writer's knowledge. However, the standard measurement methods have been used, with satisfactory accuracy, to perform similar impedance measurements to those required for the Impatt diode. Therefore, it is reasonable to expect that presently available measurement methods are sufficiently accurate to uncover the important behavioral characteristics of the diode's microwave impedance.

The previously-mentioned measurement methods are suitable only for steady-state operating conditions. Under transient conditions, the

diode impedance is a function of time, and as a result, the measurement techniques used must have the capability of displaying this time-dependent impedance over the time and impedance range of interest.

6.2 Transient Impedance by Direct Comparison of Voltage/Current Waveforms

This method[42,43] requires recording of the R.F. voltage waveform across the diode as well as the current waveform through the diode. These recorded waveforms are then Fourier analyzed and the fundamental frequency components compared to yield the desired admittance or impedance. If these waveforms can be monitored during the rise and fall times of the bias voltage pulse, the transient behavior of the diode's impedance can be visually observed. This method would be very useful for monitoring the build up of oscillations in a cavity and the effect of this build up of R.F. oscillations on the coupled Impatt diode.

In theory, this general type of impedance measurement method is very versatile. However, its usefulness is restricted by the practical difficulties that arise when the method is actually implemented. The "cavity oscillator method" and the "airline tee method" to be described below, are discussed to emphasize the practical problems of conducting transient impedance measurements and also, to illustrate the limitations of actual measurements that are made. Both of these methods have been tested and their limitations, along with suggested solutions, are presented.

6.2.1 Cavity Oscillator Method

This particular measurement method is very versatile, as it is

possible to carry out impedance measure. :nts under a variety of operating conditions. In this method the diode is placed in a cavity tuned to a specific frequency. Then, the R.F. voltage in the cavity and the R.F. current through the diode are monitored on a sampling oscilloscope alternately, an oscilloscope-driven chart recorder can be used to give an enlarged presentation of the waveforms. The waveforms are then directly compared in magnitude and phase, or Fourier analyzed, to give the admittance/ impedance measured. The use of a simple, fixed frequency, cavity enables the measurement set up to be utilized in either the R.F. driven state or the self-oscillatory state.

In the R.F. driven state, the cavity is sufficiently loaded so that the coupled diode will not self-oscillate and R.F. voltage is supplied by an external source, via the port which normally is the cavity output. When the self oscillatory state is employed, the cavity is unloaded to the extent that self-oscillations will occur. Then the loaded Q of the cavity can be varied and the build up of oscillations observed for the various conditions of the external circuitry.

Utilizing a combination of these two operating states, extensive experimental measurements can be made. The measurement system is shown in Fig. 6.1 and an expanded view of the cavity is given in Fig. 6.2. To ensure that only the TEM mode exists in the cavity, even at the second harmonic of the R.F. frequency, 7 mm airline was used for the cavity construction. These diode cavities were of the single-transformer, fixed-frequency type, so that they could be represented by a simple

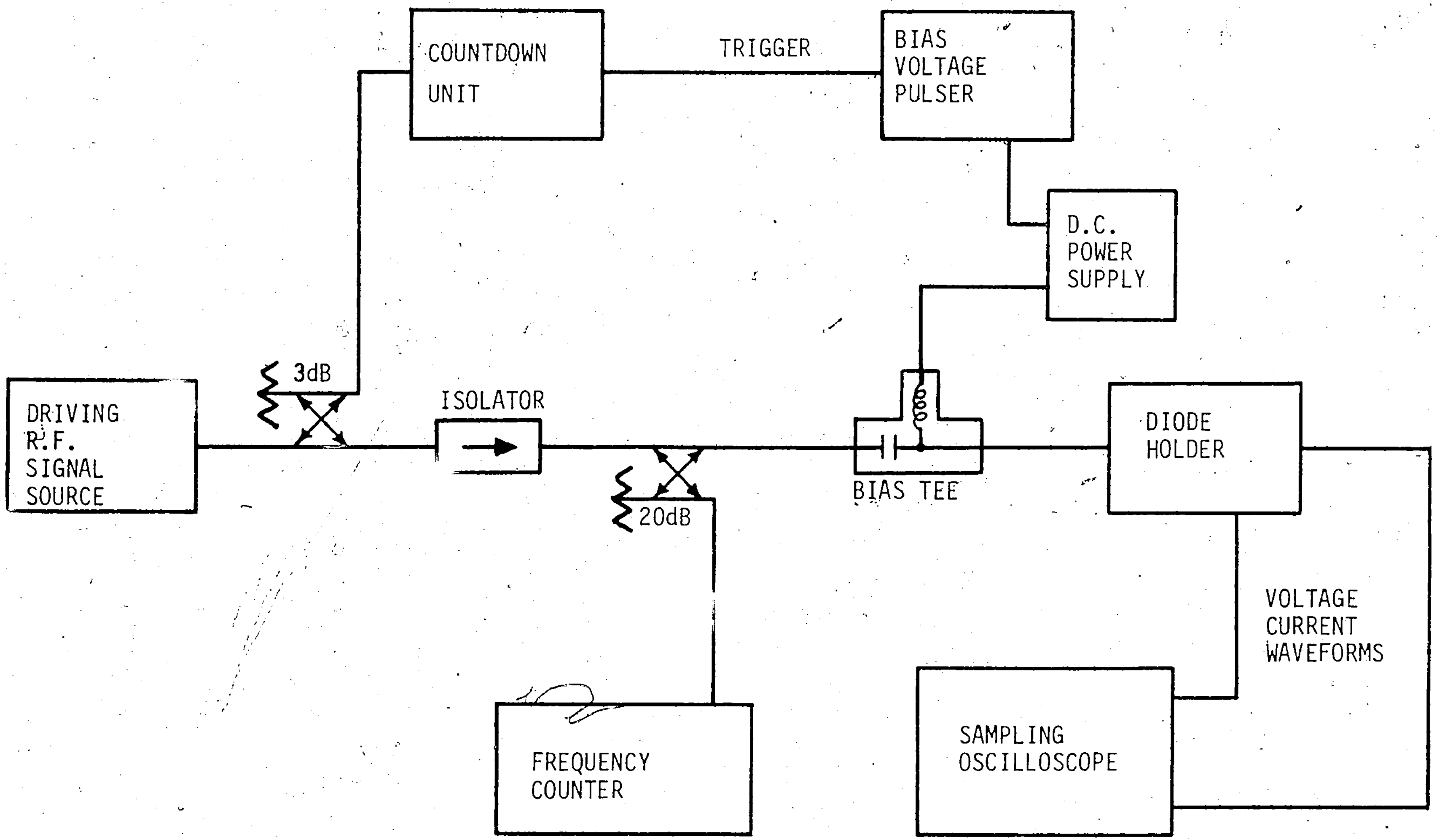

FIG. 6.1 CIRCUIT ARRANGEMENT FOR IMPEDANCE MEASUREMENTS BY DIRECT COMPARISON OF VOLTAGE/CURRENT WAVEFORMS

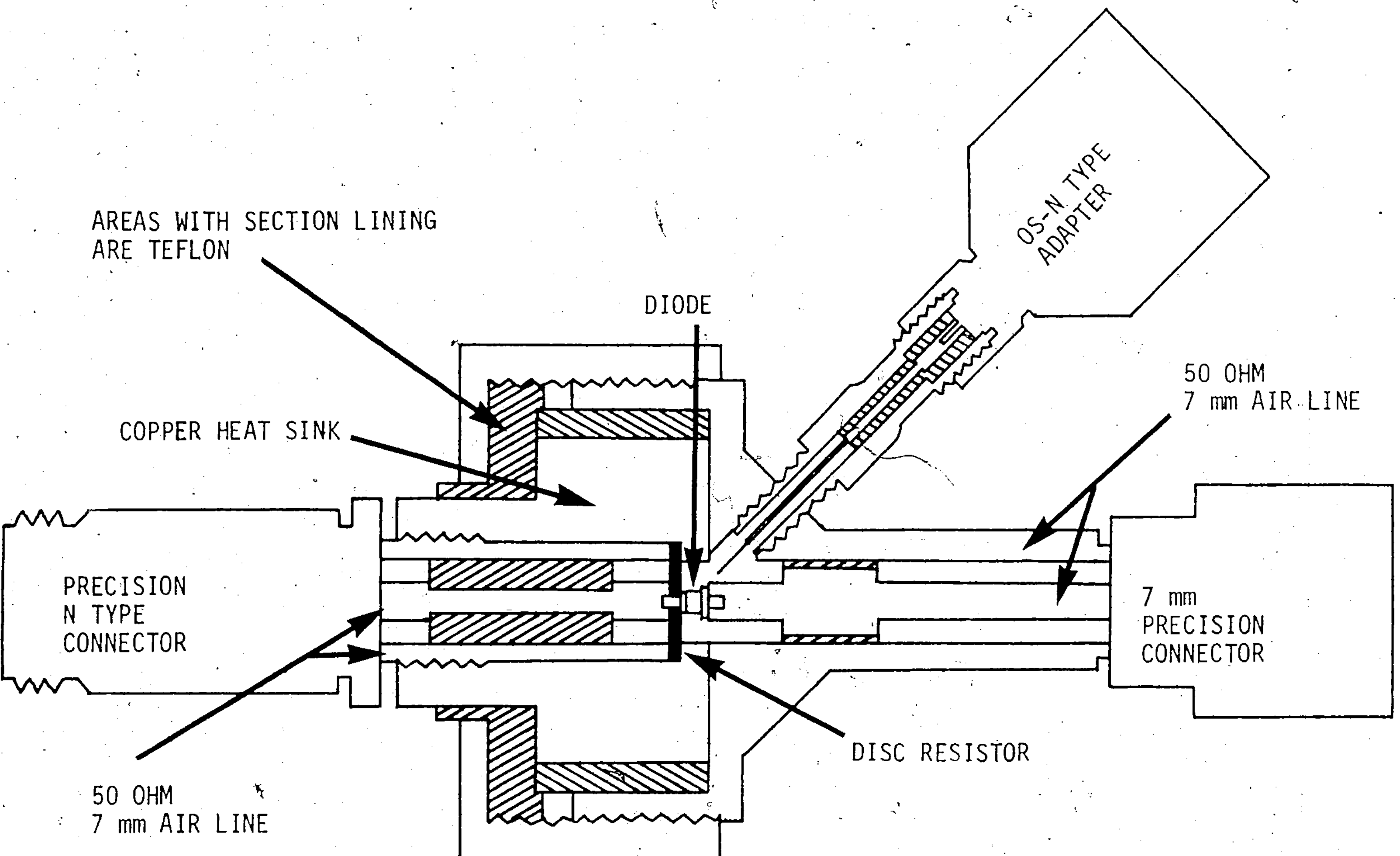

FIG. 6.2 DIODE HOLDING UNIT FOR CAVITY-OSCILLATOR IMPEDANCE MEASUREMENTS

equivalent circuit. A change of operating frequency required a change of center conductor (due to spring loading the diode contact); however this was a straight forward procedure.

The R.F. current waveform through the diode was monitored by the voltage developed across a one ohm disc resistor placed in series with the packaged diode and the copper heat sink. Monitoring of the R.F. voltage was carried out by a capacitive probe located in the vicinity of the diode. The system could be calibrated by measuring the packaged diode impedance at selected bias voltages (below and just at breakdown) in the cavity and then comparing these results with carefully made VSWR measurements of the packaged diode by itself.

Although this measurement method has a wide scope of possible uses, it suffers from practical limitations. The more restricting of these limitations are outlined below:

— For accurate measurements, it is necessary to place the current viewing resistor as close as possible to the packaged diode. However, locating the resistor between the packaged diode and the heat sink places an upper limit on the steady-state current level through the diode. This is due to the relatively high thermal resistance through the ceramic base of the disc resistor. It is not practical to reverse the diode package, as then the center conductor of the cavity would need to act as the heat sink and its thermal resistance is not satisfactory either. The

upper limit on the steady-state current flow is therefore only a few milliamperes which, for most diodes, is not sufficient for self oscillation to occur. By using special ceramic bases for the thin film resistors, such as Beryllia*, the thermal conductance can be improved, but is still lower than would be the case when the disc is not present. Thus, the d.c. bias current is limited to values sufficient to produce low-level C.W. oscillations and, in the pulsed mode, the diode is limited to low duty cycles.

— To provide sufficient sensitivity, the depth of penetration and the diameter of the voltage probe have certain minimum values. While to ensure that the entry port of the probe does not unduly disturb the electric field in the cavity, this entry port has a maximum diameter. The result is that the coaxial impedance presented to the cavity by the entry port of the voltage probe and the physical presence of the probe itself, constitute sufficient loading of the cavity that self-oscillations are not possible. Therefore, the measurement system is limited to the R.F. driven mode of operation.

---

* Al Si Mag Beryllia Ceramics (trade name) America Lava Corporation Chattanooga Tennessee.

— In the R.F. driven mode of operation, with low duty cycle bias voltage pulses applied, certain problems arise. In order to ensure that the diode will nearly return to the nominal heat sink temperature after application of each bias voltage pulse, the pulse repetition frequency has an upper limit of about 100 KHz. The frequency of the driving R.F. is about 5 GHz and this must be "counted down" to 100 KHz to synchronize the application of the bias voltage pulse and the driving R F. This synchronization is necessary so that the display of the R.F. voltage and current waveforms can be correlated to the waveshape of the bias voltage pulse. It is difficult to accomplish the frequency division, or count down, of the driving R.F. voltage, from 5 GHz to 100 KHz and still maintain a sufficiently high degree of stability to ensure proper synchronization.

This measurement system is readily set up, with a minimum of equipment, and is versatile in nature. However, the inherent practical limitations encountered in the actual implementation of the system, restrict its usefulness. The difficulty of counting down the frequency of the R.F. voltage by a factor of 5×10^4 can probably be resolved with commercially available equipment, but the loading effects of the capacitive voltage probe will require extensive design work being carried out.

6.2.2 Airline Tee Method

This method is similar in principle to the previously discussed cavity oscillator system. The R.F. voltage across the diode is compared

with the R.F. current through the packaged diode to arrive at the microwave impedance of the packaged diode. Although the airline tee is limited to the R.F. driven mode of operation, it has the advantage that the R.F. voltage across the diode is single frequency and free of second harmonics. This is accomplished by terminating the incident R.F. voltage in precision connectors and terminations that are readily available with the required frequency bandwidth.

The physical equipment layout is the same as that given in Fig. 6.1, only the diode holder has changed. An expanded view of the diode holder is given in Fig. 6.3. This diode holding unit is similar to that used by Johnston[42] in the measurement of the switching times of p-i-n diodes. In the diode holder of Fig. 6.3, the R.F. voltage at the position of the packaged diode is monitored by a capacitive probe and the R.F. current through the diode is monitored by a current viewing resistor. The current viewing resistor is commercially available and is specified to have an impedance of one ohm real part, with negligable imaginary part, to frequencies beyond 12 GHz. The use of 14 mm airline was necessitated by the physical dimensions of the packaged diode and the need for a spring-loaded contact in the center conductor of the airline. The physical size of the voltage probe and its entry port into the airline were the same as that used in the cavity oscillator method. Therefore, minimum distortion of the electric field was ensured.

Similar to the cavity oscillator system, the use of the current viewing resistor presents heat sinking problems and the airline tee

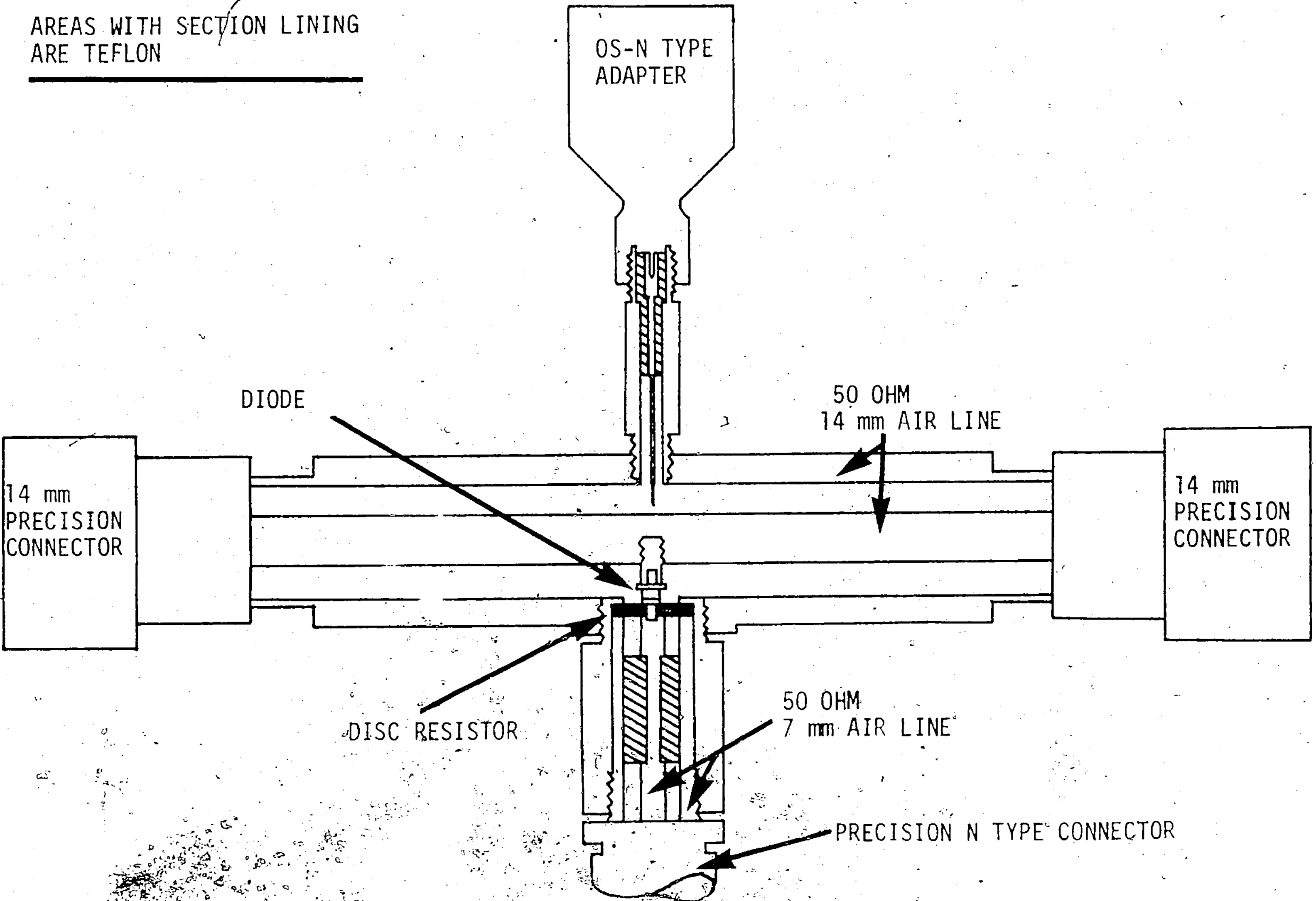

FIG. 6.3 DIODE HOLDING UNIT FOR AIR LINE TEE IMPEDANCE MEASUREMENTS

method is limited to low duty cycle, pulsed operation. However, this is not a severe restriction, as transient behaviour can still be studied. The trigger synchronizing problems inherent in this type of operation can be circumvented by using the modified equipment set up shown in Fig. 6.4. Here, the monitored R.F. voltage and current for the packaged diode are down converted to about 500 MHz and displayed on a real time oscilloscope with sufficient frequency bandwidth. The various delays in the measuring circuits can be adjusted so that a simultaneous oscilloscope display of the bias voltage pulse and the down converted voltage or current waveform is possible. One limitation inherent in the use of the down conversion of frequency, is that the second harmonic component in the current waveform may be lost.

During the calibration of the measuring system, it soon became apparent that there were serious practical limitations that restricted the accuracy of any actual impedance measurements. The more serious of these limitations were the following:

— Due to the necessity of supplying the Impatt diode with a high d.c. voltage for reverse biasing, the termination end of the diode holder has to contain a d.c. block. This means that a small, but finite, VSWR (∿1.1) is presented to the incident R.F. driving voltage and any second harmonic component generated by the diode. A similar situation exists at the driving termination due to the bias tee. Thus, there is some distortion of the electric field across the packaged diode caused by reflections and some component of the second harmonic may be

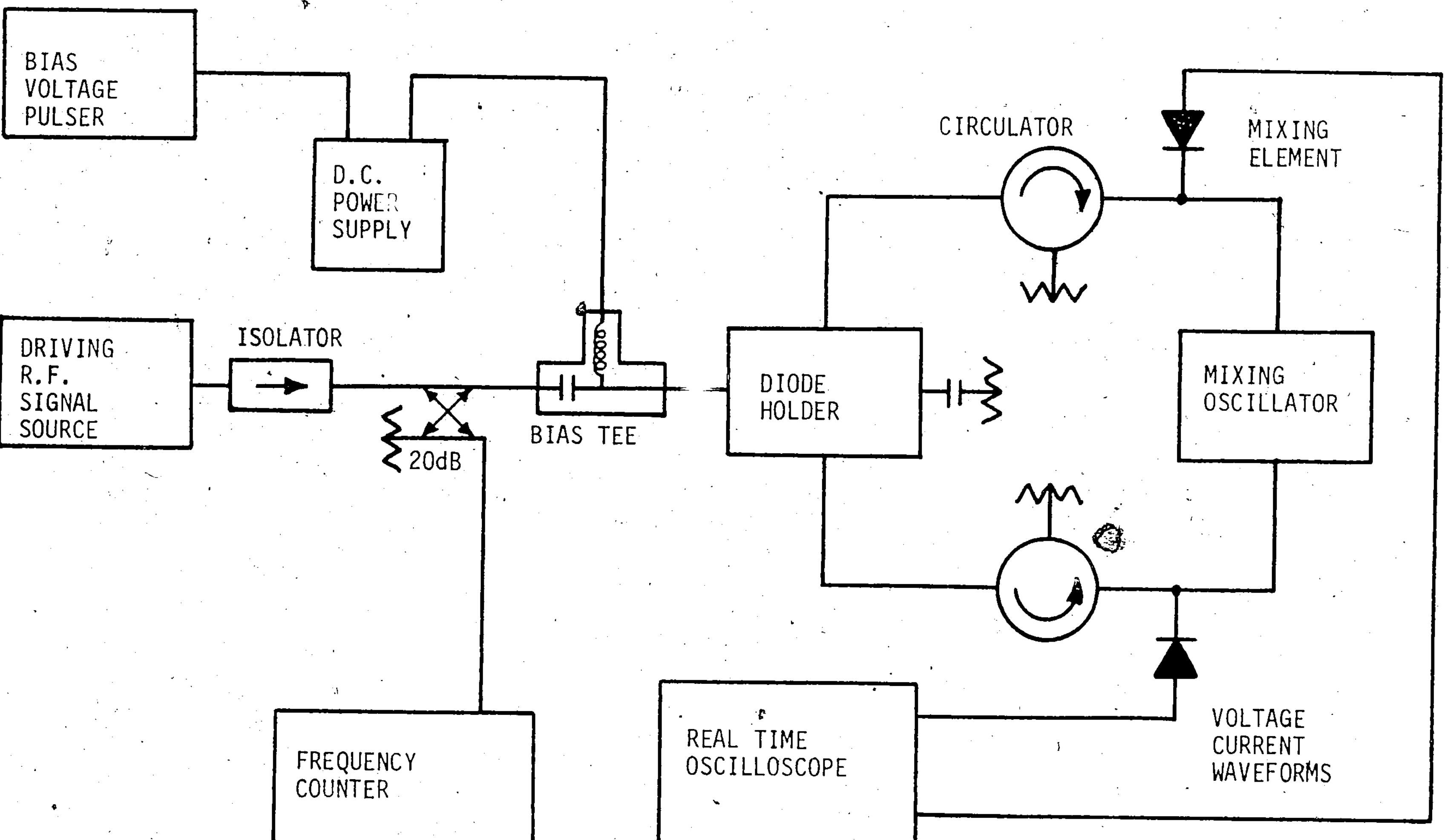

FIG. 6.4 CIRCUIT ARRANGEMENT FOR IMPEDANCE MEASUREMENT BY DIRECT COMPARISON OF VOLTAGE/CURRENT WAVEFORMS IN REAL TIME

present. This effect could be minimized by careful design of the terminating end of the diode holder unit.

— The combination of the diode holder in the airline center conductor and the physical length of the packaged diode has the electrical effect of a shunting inductive post across the coaxial airline. This post effect is so large at the fundamental frequency of interest ($\sim$ 5 GHz) that it masks the behaviour of the diode during the impedance measurements. This inductive post effect can be tuned out by placing an adjustable R.F. short at the termination end of the airline tee. After the inductive post effect was tuned out, the variations in the impedance of the packaged diode, with changing bias voltages, were readily observed in this measurement system. However, it was difficult to arrive at calibration factors that would provide a close comparison between the measured impedances and those known values for the same bias voltages. In general, attempts at calibration proved to be difficult and unreliable.

Similar to the cavity oscillator measuring system, the airline tee system is restricted in its usefulness by the practical difficulties of actually implementing the measuring system. A possible solution to the inductive post effect would be to design the center conductor of the coaxial airline in such a way that the physical separation between the

inner and outer coaxial conductors, would be equal to the height of the diode at the measurement plane of reference. This could readily be accomplished by using tapers or three-section, quarter-wave-transformers to give the necessary impedance matching over the frequency range of interest.

6.3 Transient Impedances by Carrier Reinsertion

The major advantage of this measurement method is the inherent simplicity of its operation. Although the method is restricted to the R.F. driven mode of operation, it has few other limitations. The equipment layout is given in Fig. 6.5 and an expanded view of the diode holder is shown in Fig. 6.6.

The general principle of operation is that the packaged diode is mounted in a coaxial holder which is attached to a coaxial four-port hybrid. This hybrid separates the incident and reflected R.F. voltage waves. The reflected voltage wave and a portion of the incident voltage wave are separately routed, through switches, to a waveguide four-port hybrid (magic tee). In the magic tee the R.F. voltage waveforms are applied to a crystal detector. The switching circuitry allows the reflected and incident signals to be applied to the detector either singularly or as a sum. The R.F. crystal detector gives a d.c. output voltage whose level is proportional to the R.F. signal sampled by the detector. These detected levels are displayed on a real time oscilloscope and then recorded with a polaroid camera. The resulting oscilloscope traces on the film are then analyzed to give the complex reflection coefficient.

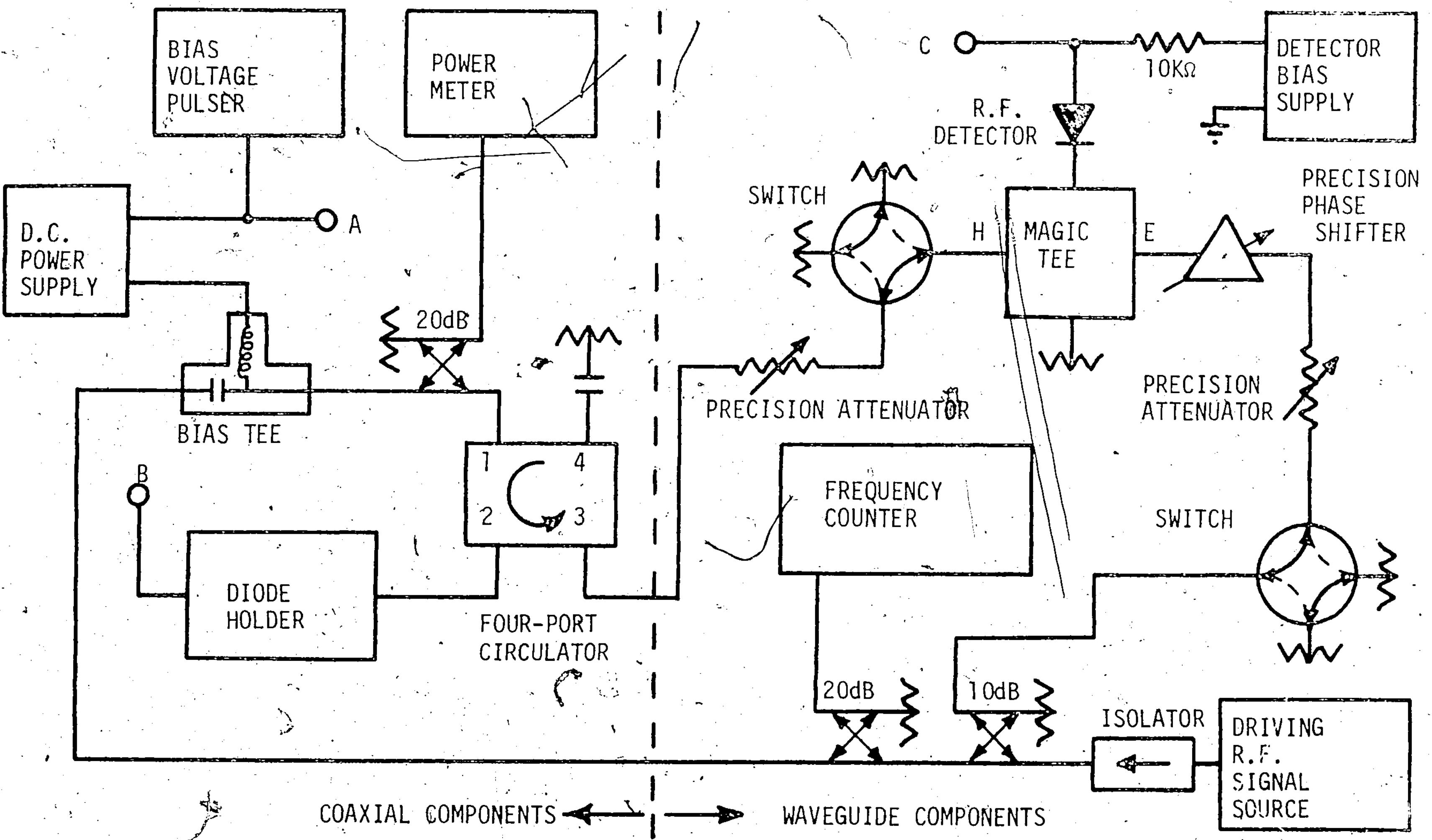

FIG. 6.5 CIRCUIT ARRANGEMENT FOR CARRIER REINSERTION METHOD OF IMPEDANCE MEASUREMENT

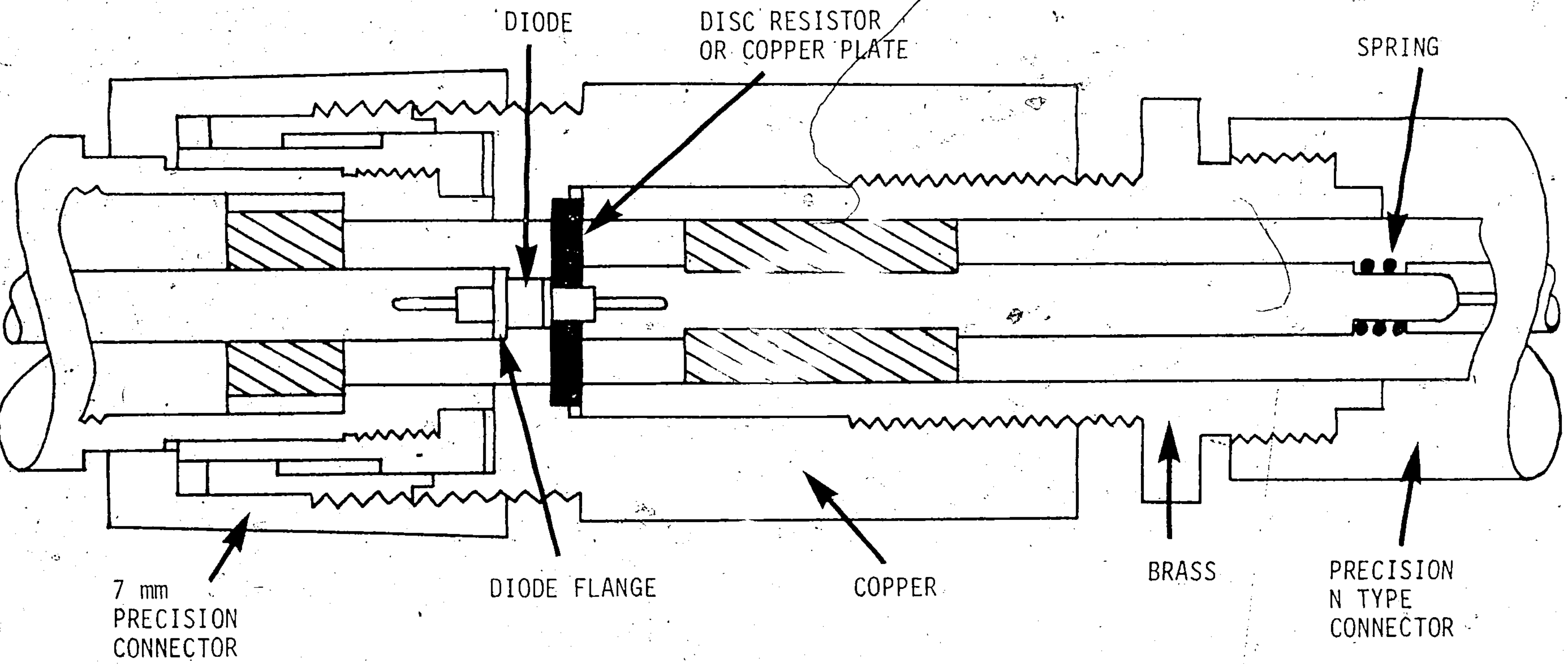

FIG. 6.6 DIODE HOLDING UNIT FOR CARRIER REINSERTION IMPEDANCE MEASUREMENTS

Thus, the major limitations of the previously discussed measurement methods are overcome. The driving R.F. voltage is supplied from a free running source so that the problems of synchronizing the driving R.F. source and the bias voltage pulser do not exist. The current viewing resistor is only used as a means of determining the current pulse through the diode to serve as a reference level for the comparison of the computed and experimental results. During the actual impedance measurements the diode package is in direct contact with the copper heat sink. Measurement sensitivity is good and the calibration procedure is straight forward and accurate. There are some restrictions on the measurement system, as it was used here, but the results obtained should have similar accuracy to those taken by VSWR/reflection coefficient measurements under steady-state operating conditions.

The practical limitations of equipment availability and the desirability of the coaxial mount for the packaged diode, necessitated the use of both coaxial and waveguide components in the measuring system. The equipment layout can be divided into two major divisions, one consisting of coaxial components and one consisting of waveguide components. The microwave aspects of the measuring system can similarly be divided along divisions of coaxial and waveguide components and will be discussed accordingly.

6.3.1 Biasing and Separation of Incident and Reflected Signals

With reference to Fig. 6.5, the biasing and separation functions are carried out in the coaxial part of the measurement system. The

incident R.F. voltage, plus the d.c. and pulse bias voltages, are supplied to the packaged diode by a bias tee. The coaxial directional coupler has very little effect upon the system operation and the d.c. open - R.F. termination on port-four of the circulator is accomplished by using a co-axial to waveguide adapter with a waveguide termination. There are two critical aspects of the equipment arrangement which will be discussed; one is the rise time of the bias voltage pulse at the diode holder and the other concerns the frequency bandwidth and R.F. isolation of the four-port hybrid.

Given a voltage pulser with sufficiently fast rise time, the rise time of the bias voltage pulse at the diode holder is governed by the rise time of the associated circuitry. Since the diode holder is mated to a conventional 50 ohm APC-7 connector, the measurement of the bias voltage pulse at the diode holder can be obtained by directly connecting the mating APC-7 connector to the 50 ohm input of the oscilloscope. By monitoring the direct output of the pulser, (position A Fig. 6.5) it was found that, placing the 50 ohm impedance of the oscilloscope channel or a conducting Impatt diode, at the diode holder, very similar loading effects were observed on the pulser output. Thus, the bias pulse voltage measured by the 50 ohm impedance of the oscilloscope was a close approximation to the actual bias pulse across the packaged diode. Normally, the rise time of the bias voltage pulse at the diode holder is about 10 nanoseconds. This rise time can be decreased to about 5 nano-seconds by a judicious choice of capacitors placed across the output

terminals of the d.c. power supply. This rise time is maintained as long as the rise time of the bias voltage pulser is greater than 5 nanoseconds. The bias voltage rise time at the diode holder can be decreased to approximately that of the pulser by redesigning the diode holder so that the heat sink is electrically insulated from the system ground. Then, the bias voltage pulser is applied between the diode and the system ground. This was not done in the measurements carried out here, but was tested during the work on the cavity oscillator measurement method.

The characteristics of the circuitry at the microwave frequencies used are mainly determined by the frequency bandwidth and R.F. isolation of the coaxial four-port circulator. As the diode holder is constructed using a precision 50 ohm connector, it has excellent characteristics (VSWR < 1.05) to frequencies beyond 18 GHz. However, the four-port circulator is limited to one octave of frequency bandwidth and outside this frequency range it presents a highly reactive impedance. Thus, any second harmonic components generated by the Impatt diode would be largely reflected from the circulator and confined within the diode mount. In this situation, the R.F. voltage incident upon the Impatt diode will have some second harmonic component present. This is a similar situation to that encountered in steady-state impedance measurements and will limit the magnitude of the incident R.F. voltage to the order of one volt so that any effect from second harmonic components will be minimized.

Another important aspect of the characteristics of the four-port circulator is the isolation between ports 1 and 3(see Fig.6.5). This

isolation describes the degree by which the incident R.F. is prevented from gaining direct access to the path of the reflected signal. The isolation of the four-port used here was greater than 20 dB between ports 1 and 3, a larger degree of isolation would be desirable however, 20 dB was found to be acceptable.

The measuring characteristics of this circuitry at microwave frequencies could be improved by increasing the frequency bandwidth and R.F. isolation of the four-port hybrid used to separate the incident and reflected R.F. signals. This will not be a simple matter, as coaxial components will give two-octaves of bandwidth but the isolation will be marginal. Waveguide components will give the high degree of isolation required but the frequency bandwidth will be narrow. A possible improvement may be to use a broad-band, 3-db, directional coupler with very high directivity, although this will result in the loss of one half of the reflected signal.

6.3.2 R.F. Detection Subsystem

With reference to Fig. 6.5, the R.F. detection takes place in the waveguide part of the measuring system. The advantages of using waveguide components are that precision components are readily available and these components have very low R.F. losses. The most important part of the waveguide portion of the measuring system is the four-port hybrid (magic-tee) R.F. detector arrangement shown in Fig. 6.7. The magic-tee was not specially compensated, but, was tested and found to have equal power division from both the "E" and "H" plane ports, while maintaining a high degree of isolation between these ports. Only one of the

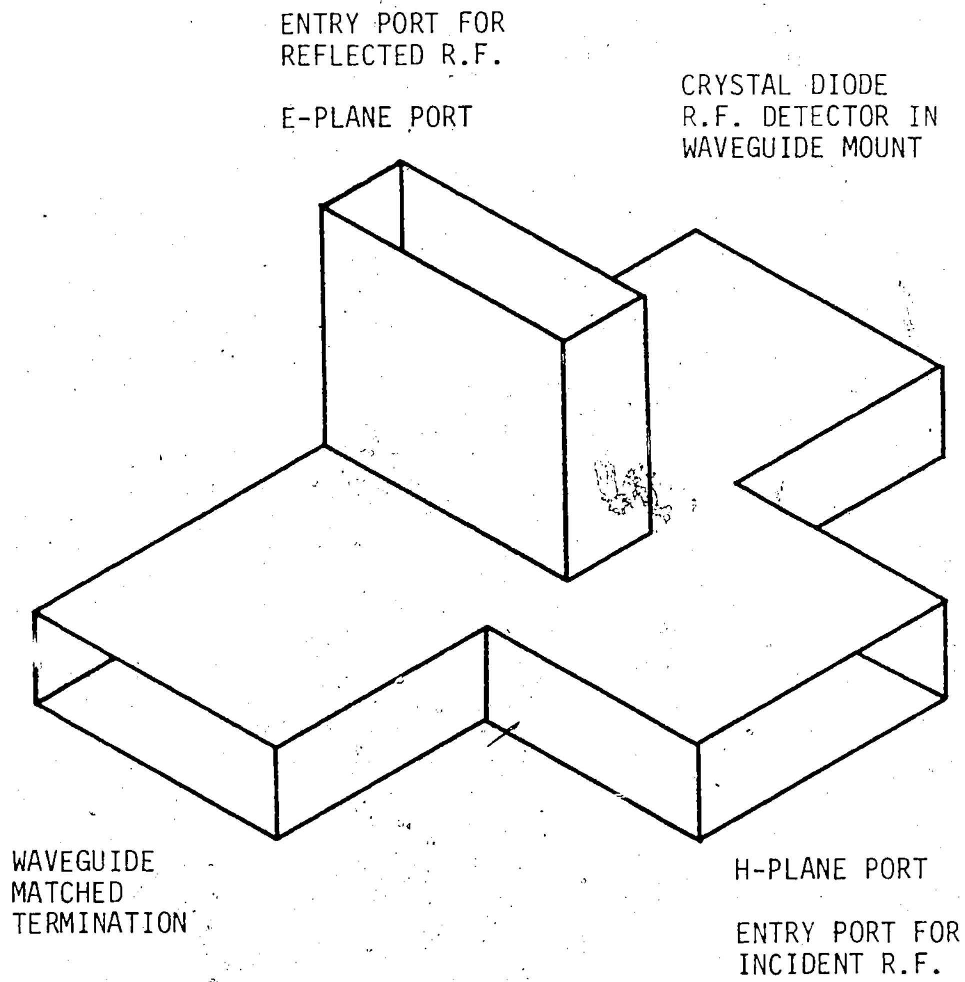

FIG. 6.7 MAGIC TEE PORTION OF R.F. DETECTION SUB-SYSTEM

sum and difference ports was used, as it was found that the outputs of these ports are very sensitive to impedance mismatches at their opposing member. Therefore, one of these ports was match terminated with a high quality waveguide load and the other was used for the R.F. detector mount.

The R.F. detector used was an integral part of a waveguide to coaxial adapter and presented a very good impedance match to the magic tee (At the measuring frequency the R.F. detector mount had a VSWR$\sim$1.05); this detector used a conventional broad-band diode. The sensitivity of the R.F. detector was increased by applying a small forward bias to the detector diode. This increased sensitivity is essentially due to improved impedance matching between the detector output and its load. The R.F. detector is designed to be loaded by a high impedance (specified as > 75 Kilohms) and if a FET probe is used (input impedance of 1 megohm shunted by a capacitance of 3 pf) high signal levels are recorded from the detector output. But the response time of the detection sub-system is $\sim$ 14 nanoseconds even with detector biasing. This slow response time is due to the high R.C. time constant of the detection system. To reduce the time constant, the detector was loaded by the 50 ohm input impedance of the oscilloscope channel and then biased for best sensitivity. With this arrangement, the response time was better than 5 nanoseconds and the sensitivity was sufficient. Detector biasing was accomplished, as shown in Appendix C, through a BNC tee to avoid any unnecessary introduction of additional capacitance.

The sensitivity of the R.F. detection part of the impedance measuring system could be enhanced by using a more sensitive detector

diode. R.F. detection over a broad frequency band is not necessary as the frequency bandwidth of the magic tee will limit the R.F. signals to their fundamental component only. Resolution of the display on the oscilloscope and the subsequent pictures was not a limiting factor here. The oscilloscope used had a frequency bandwidth of 500 MHz and the same channel was used to calibrate the measuring system, and record the reference levels for all the detector outputs. The accuracy of transferring the data from the polaroid pictures is quite good if the transfer is carried out carefully.

6.3.3 Calibration of Measuring System

Before any impedance measurements can be carried out, the system as a whole must be calibrated. This is accomplished by taking the reference plane for the measurements to be the physical location of the large flange on the Impatt diode, as shown in Fig. 6.6. This is the most convenient reference plane to take, as it can apply to any impedance measurements that are carried out on the diode package.

Placing the APC-7 electrical short in the APC-7 part of the diode holder (i.e. at the reference plane shown in Fig. 6.6) the magnitude and phase of the incident and reflected R.F. voltage waves V_i and V_r respectively, are set such that

$$|V_r| = |V_i|$$

$$|V_r + V_i| = 0.0$$

This calibration routine accounts for the electrical losses in the paths travelled by the incident and reflected signals and also is used to set the reference level of the incident R.F. voltage. Once this part of the

calibration procedure is carried out for a specific frequency, the setting of the attenuators and phase shifters is fixed.

As shown in Appendix B, to calculate the complex reflection coefficient from the information supplied by the oscilloscope traces two constants need to be evaluated. The values of these constants are arrived at by comparing the impedances measured by the reflection coefficient system with those given by carefully made VSWR measurements. Since the measurement plane of reference on the diode package is the same for both types of measurements, a direct comparison is possible. The VSWR measurements were taken on Impatt diodes that were reverse biased below breakdown. These diodes were the same ones that were used later for the transient impedance measurements. Also, these VSWR measurements were repeated to ensure that the high values of VSWR present did not lead to inaccurate impedance calculations.

The general procedure was to select an Impatt diode and carry out the VSWR measurements at selected values of reverse bias below breakdown. Then, this same Impatt would be transferred to the reflection coefficient measurement system and, at the same selected values of reverse bias voltage, the impedance would be measured.

A comparison of the VSWR and reflection coefficient measurements determined the values of the required constants. Then, the transient impedance measurements were carried out before the Impatt diode was removed from the reflection coefficient measuring system.

6.4 Experimental Measurements

The hermetically sealed package in which the semiconductor diode is mounted, serves to protect the delicate p-n junction and also to provide coupling from the diode chip to the external circuit. Consequently, the semiconductor diode terminals are not accessible for direct impedance measurements. In the process of arriving at a value of the semiconductor impedance (Z_e) two other impedances need to be considered. These associated impedances are the actual measured impedance (Z_m) and the impedance at the outer reference surface of the diode package (Z_p). The value of Z_m is transformed from its reference plane to the reference plane of Z_p by an equivalent [illegible] which is determined by the measurement circuitry used. The reference plane for Z_p is the outer surface of the diode package and the equivalent circuit of this package transforms Z_p to Z_e.

The use of the 50 ohm mounting system for the diode package, shown in Fig. 6.6, greatly simplifies the transformation of Z_m to Z_p (37,41,44). Since the impedance transformations involve the use of lumped element equivalent circuits to represent distributed effects, the simpler the transformations to be represented, the more representative the equivalent circuit. The mounting system used here has the dual advantage of simplifying the calculations as well as contributing to increased accuracy of the impedance transformations.

The Impatt diodes used in this work were commercially obtained, Hewlett-Packard model 5082-0437 diodes, encapsulated in the common pill with two prong package. (whose outline is illustrated in Fig. 6.8).

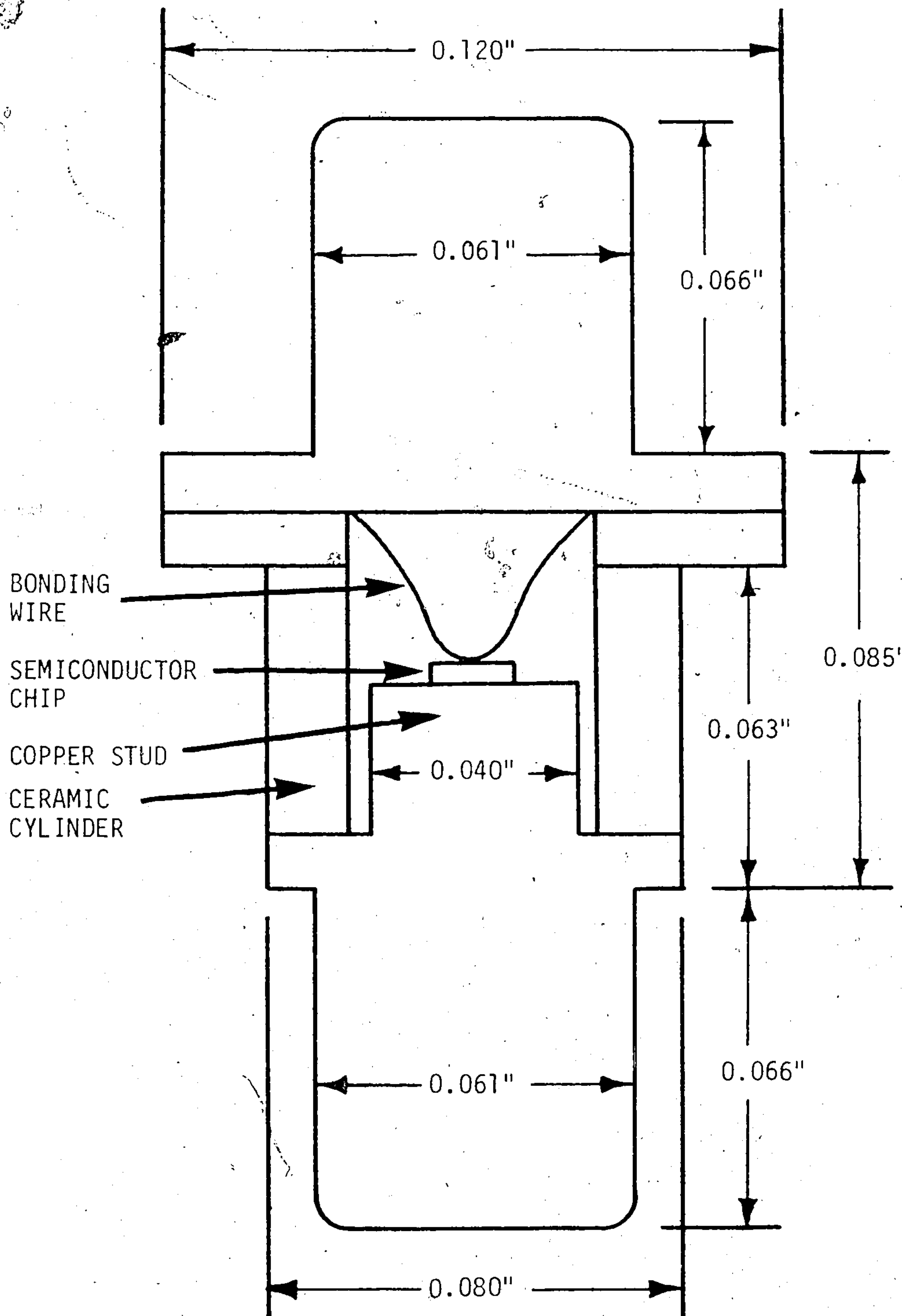

FIG. 6.8 CROSS SECTION OF HEWLETT PACKARD 5082-0437 IMPATT DIODE

All measurements were carried out at frequencies in the range of 5.7 to 8.3 GHz and hence were close to a common carrier microwave communications frequency band.

6.4.1 Derivation of the Diode Package Equivalent Circuit

As stated in sub-section 6.3.3, the reference plane selected for the impedance measurements was the large flange on the diode package shown in Fig. 6.6. This location of the reference plane was selected as it was also the reference plane of the electrical short used as a reference for both the reflection coefficient and the VSWR measurements. The equivalent circuit for representing the transformation of the impedance measured at the reference plane (Z_m) to the impedance at the outer surface of the diode package (Z_p) was arrived at by using a metal diode of the same physical dimensions as the real diode package. It was determined, by VSWR measurements, that the impedance of this dummy metal diode, at the reference plane, could be represented by a lumped inductor of 0.6 nH. This value of inductance was constant over the frequency range of 5 to 8 GHz.

The procedure of using a dummy metal diode to obtain the relation between Z_m and Z_p has been used in previous work[44] where reduced height waveguide mounting systems were employed. Although the higher order modes necessary to match the TEM mode electric and magnetic fields to the metal diode will be somewhat different from those required for the real diode package, this difference is considered to have a small effect on the impedance transformations. The principle of using a single, lumped- inductance, element for the transformation from Z_m to Z_p is the same as that used by Getsinger[37] for diodes mounted across

a waveguide, in shunt with coaxial conductors and at the end of a shorted coaxial line. Owen and Cawsey [45] also found that the single inductive element was sufficient to transform Z_m to Z_p.

Getsinger[37] also indicates that, as the outer diameter of the diode package approaches that of the coaxial inner conductor, the radial modes that require matching to the TEM fields vanish. Then, the value of the lumped-inductive element is that of a shorted transmission line whose characteristic impedance is formed by the diode package outer diameter and whose length is equal to the height of the ceramic sleeve of the diode package. In the package mount used here the diameter of the coaxial center conductor is 0.120" and the outer diameter of the package is 0.080", so very little radial mode matching should be required. This is also indicated experimentally, as the measured impedance of the metal diode is very nearly that of a short circuited section of transmission line whose inner conductor diameter and length are those presented by the dummy diode.

The above results are in good agreement with Owens and Cawsey's[45] work, who carried out very extensive measurements to characterize a diode package of very similar dimensions. The equivalent circuits used by Getsinger, Owen and Cawsey, along with the version derived for this work are shown in Fig. 6.9. Owens, introduced a capacitance (C_1) that was due to the ceramic cylinder in the diode package but found that this only had significance at frequencies above 12 GHz. If the value of C_1 is introduced at frequencies aroung [illegible] GHz, its only effect is to slightly reduce the magnitude of Z_m before it is transformed by

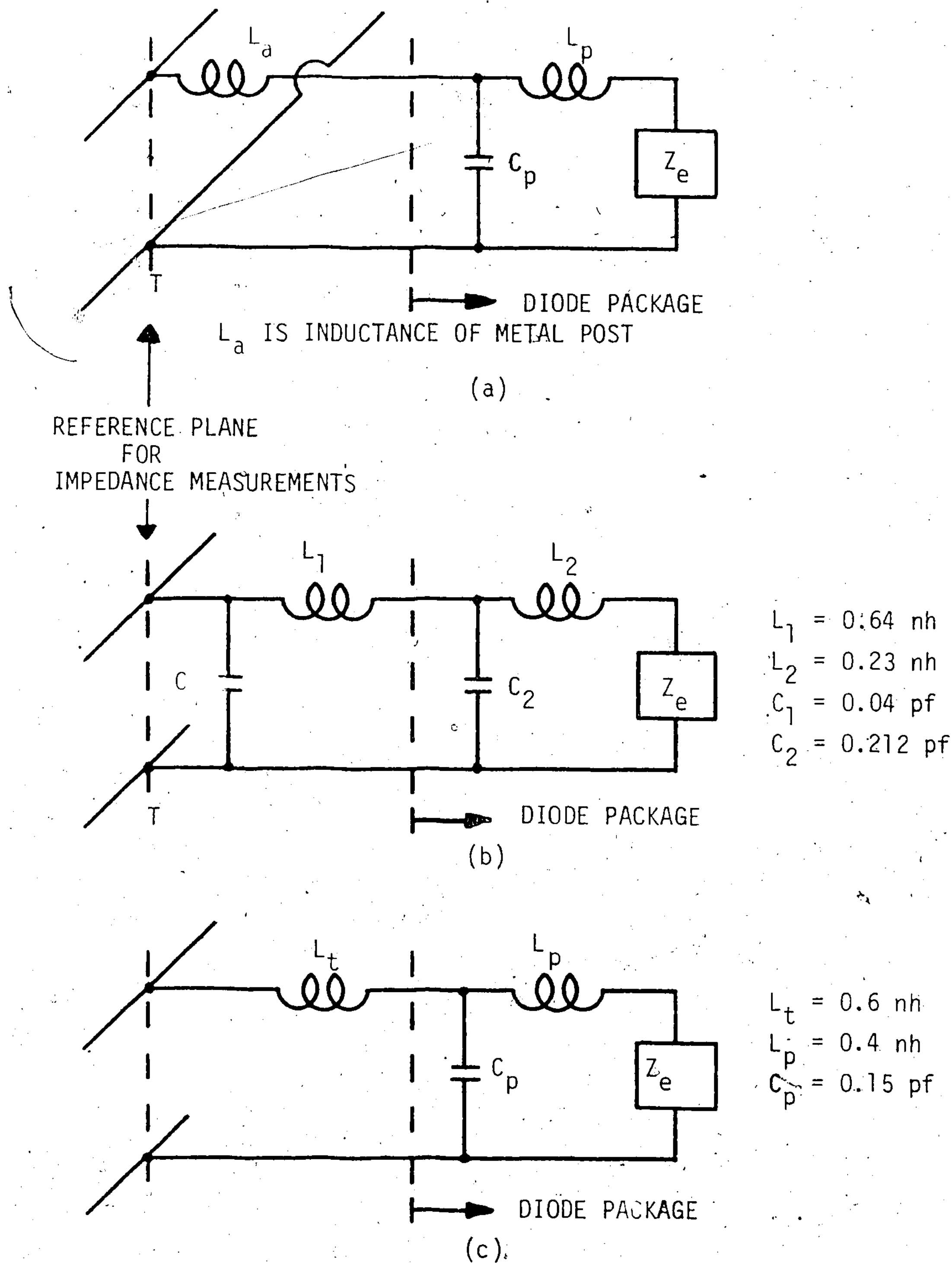

FIG. 6.9 EQUIVALENT CIRCUIT FOR PACKAGED IMPATT DIODE
(a) GETSINGER'S MODEL
(b) OWENS AND CAWSEY'S MODEL
(c) MODEL USED FOR THIS WORK

the transmission line inductance L_1 (L_t this work) to Z_p. Therefore, the value of C_1 was omitted for this work.

The values of C_p and L_p (Figure 6.9 (c)) are essentially those listed on the diode specification sheet as the package capacitance and inductance, respectively. In the diode package shown in Fig. 6.8, $_p$ represents the capacitance between the top of the post and the top cap of the package, while L_p is mainly the inductance of the lead wire(s). The value of L_p can be determined from the difference in the inductive impedance of a metal diode and that of an internally shorted diode package, when measured at the same impedance reference plane. The internally shorted diode package that was available had the same outer physical dimensions as the actual diode package but the internal structure was unknown and probably slightly different than that of the actual diode used. However, these measurements were carried out to obtain a representative value for L_p. A value for L_p of 0.35 - 0.4 nh was found in the frequency range of 5 to 8 GHz. The manufacturer's listed values of L_p and C_p were 0.5 nh and 0.2 pf, respectively. Thus, the values of L_p and C_p for the actual diode's package would be close to the above values. Using these magnitudes as a first approximation, the final values of L_p and C_p were arrived at by fitting the depletion layer capacitances, measured at 1 MHz on a Boonton Bridge, to those calculated from a transformation of Z_m to Z_e using the equivalent circuit given in Fig. 6.9(c). This matching was carried out for a range of reverse bias voltages below breakdown.

By choosing the values of L_p and C_p to be 0.4 nh and 0.15 pf respectively, the calculated capacitance was within 4% of the measured values at 1 MHz for bias voltages of 40 to 90 volts (breakdown voltage was 100 volts). This completed the determination of the necessary equivalent circuits required to transform Z_m to Z_e.

6.4.2 Experimental Results

In the experimental setup shown in Fig. 6.5, there are three monitor positions, each of which is designed to be connected to a 50 ohm impedance. The monitor position "A" was provided by a tee and this position was continuously loaded by one of the 50 ohm channels of the oscilloscope. The continuous loading served two purposes. One was to present a reasonable match to the 50 ohm output impedance of the bias voltage pulser, as the d.c. power supply was a large impedance mismatch; the other purpose served was to provide a reference bias voltage level so that the measurements would be reproducible. Monitor positions"B" and "C", alternately shared the remaining 50 ohm channel of the oscilloscope. Position "B" was a 50 ohm connector in parallel with the 1 ohm current-viewing resistor. This was used just prior to the calibration of the R.F. detector, to enable the current pulse through the diode to be obtained. The current pulse through the diode was necessary to serve as a reference for comparison between the theoretical calculations and the experimental results. Monitor position "C" is a 50 ohm tee that shared the output of the R.F. detector with the bias voltage supply for the R.F. detector. This provided a positive d.c. offset to the oscilloscope that tended to balance the negative output

voltage of the R.F. detector and permitted the use of the most sensitive range of the oscilloscope channel.

It was found that, when the diode package holder was loaded by the 50 ohm input impedance of the oscilloscope channel, in lieu of an avalanche diode, the waveform observed at the bias pulser (monitor A) was very similar to that observed at "A", when the diode holder held an avalanching diode. This effect is apparent when traces for "A" are compared in Figs.6.10(a) and (b). In this way, the rise time of the bias voltage pulse at the location of the Impatt diode was determined. Also apparent from this measurement was that the current pulse through the diode follows the voltage pulse across the diode very closely(Fig. 6.10a)).

To avoid instabilities in the monitoring oscilloscope traces when repetitive bias pulses are applied to the Impatt diode, a steady d.c. current of 1 ma was maintained in the Impatt diode. This ensures that the Impatt diode has an identical response for each pulse in the repetitive train of bias pulses and the oscilloscope traces are steady. This d.c. current level is sufficiently low that the temperature of the semiconductor junction is essentially that of the copper heat sink. The bias voltage pulses had a duration of about 30 nanoseconds and a repetitive frequency of 100 KHz, giving a duty cycle of 0.3%. Thus, it was assured that the semiconductor junction temperature closely approached that of the heat sink,in between bias voltage pulses.

The procedure followed for each set of measurements started with the determination of the Impatt diode current response for each specific value of bias voltage pulse to be used. Next, the current-viewing resistor was replaced with a copper disc and the reverse bias

Fig. 6.10 PHOTOGRAPHS OF TYPICAL WAVEFORMS OBSERVED ON THE OSCILLOSCOPE DURING ELECTRONIC IMPEDANCE MEASUREMENTS USING THE CARRIER REINSERTION METHOD.

In all photographs, the vertical scale for current and detected R.F. waveforms is 10 MV/cm. The voltage waveforms have a vertical scale of 500 MV/cm or 1V/cm as shown in the individual photographs. Also, all photographs have a horizontal scale of 5 nsec/cm.

Fig. 6.10(a) Voltage and current waveforms throughout the measuring system

trace #1 - bias voltage pulse at monitor position A in Fig. 6.5

trace #2 - bias voltage pulse at the diode holder

trace #3 - current pulse for avalanching diode taken at monitor position B in Fig. 6.5

trace #4 - detected waveform of the sum of the incident and reflected R.F. taken at monitor position C in Fig. 6.5

For traces #1 and 2, the 50 ohm impedance of the oscilloscope channel was connected to the diode holder in lieu of an avalanching Impatt diode.

For trace #3 the current pulse was taken as a voltage across a 1 ohm disc resistor in series with an avalanching Impatt diode in the diode holding unit.

Traces #2, 3 and 4 are for the bias voltage pulse at monitor position A, shown in trace #1.

Fig. 6.10(b) Voltage pulse at mónitor position A related to the resultant current through the diode measured at monitor position B.

The upper set of three traces are the voltage pulses at monitor position A, while the lower set of three traces are the current pulses at monitor position B.

Fig. 6.10(c) Typical measurement photograph

trace #1 - detected waveform of the sum of the incident and reflected R.F.

trace #2 - detected waveform of the reflected R.F. alone

trace #3 - the reference voltage pulse at monitor position A

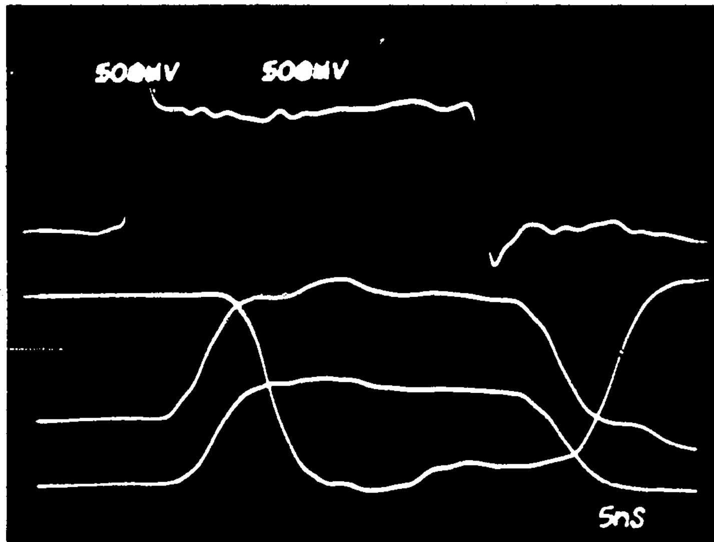

Fig. 6.10 (a)

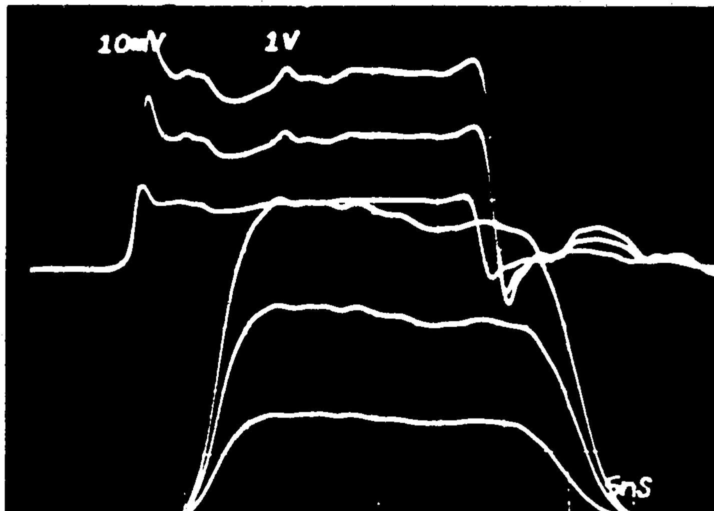

Fig. 6.10 (b)

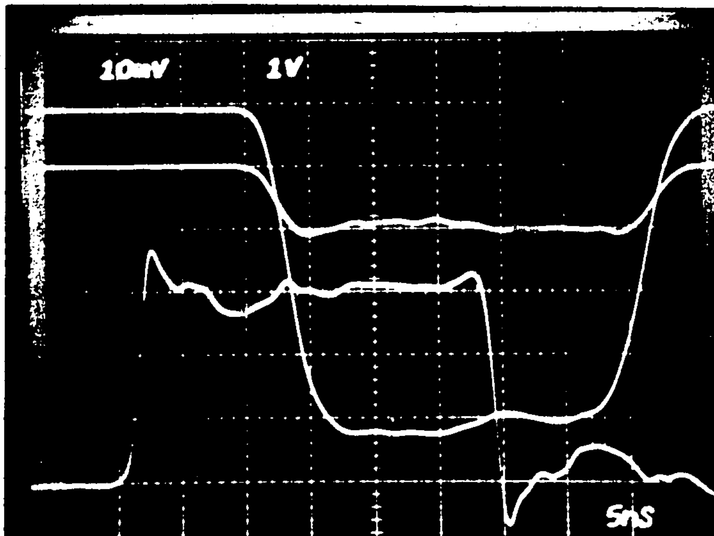

Fig. 6.10 (c)

applied to the Impatt diode was gradually increased until a d.c. current of 1 ma was reached. As the reverse bias voltage was increased, the R.F. detector was calibrated at several values of reverse bias below breakdown. Next, the bias voltage pulses were applied at the same levels for which the current response was taken earlier. The oscilloscope traces representing the output of the R.F. detector were photographed. In the photograph, the magnitude of both the reflected R.F. and the sum of the incident and reflected R.F. were recorded, along with the waveform at monitor position A. These three traces were recorded for each specific level of bias voltage pulse used. A typical photograph is shown in Fig. 6.10(c).

The experiments were carried out with two different Impatt diodes, whose characteristics are given in Table 6.1. These characteristics were determined from capacitance-voltage measurements taken at bias voltages below breakdown and at room temperature. The results of the experiments are shown in Figs. 6.11 to 6.23. In these plotted results, the measured impedance has been transformed via the equivalent circuit of Fig. 6.9(c), to obtain the electronic impedance of the semiconductor diode. Also shown in these figures are the associated

TABLE 6.1

CHARACTERISTICS OF H.P. 5082-0437 IMPATT DIODES

DIODE	BREAKDOWN VOLTAGE AT 1 MA	CAPACITANCE AT BREAKDOWN	AVERAGE DOPING LEVEL	DEPLETION REGION WIDTH
#1	101 V	0.34 pf	$1.0\times10^{16}cm^{-3}$	3.75 μ
#8	102.2 V	0.27 pf	$6.5\times10^{15}cm^{-3}$	4.7 μ

results from the computer model. These associated results are given here for ease of comparison in the following Chapter.

The measured current response and electronic impedance of diode #1 and #8 at room temperature, for various microwave frequencies and d.c. bias levels, are given in Fig. 6.11 to 6.23. A breakdown of these figures is as follows:

- Figs 6.11 to 6.14 - diode #1, 6.0 GHz, 3 and 4 volt bias pulses
- Figs 6.15 to 6.17 - diode #8, 6.0 GHz, 3 and 4 volt bias pulses
- Figs 6.18 to 6.20 - diode #1, 7.8 GHz, 3 and 6 volt bias pulses
- Figs 6.21 to 6.23 - diode #8, 7.8 GHz, 3 and 6 volt bias pulses

In all the results of the electronic impedance measurements, the plotted data displays very little scattering of points and the resulting curves are well behaved.

The series resistance due to contact losses, the resistance of the substrate and the undepleted region of the diode can be represented by R_s. The value of R_s can be taken from the experimental results[46] as the real part of the diodes electronic impedance when the bias voltage reaches the breakdown value. For the purpose of this work the value of R_s has been taken as the real part of the electronic impedance when 1 ma of d.c. current is maintained in the diode. This

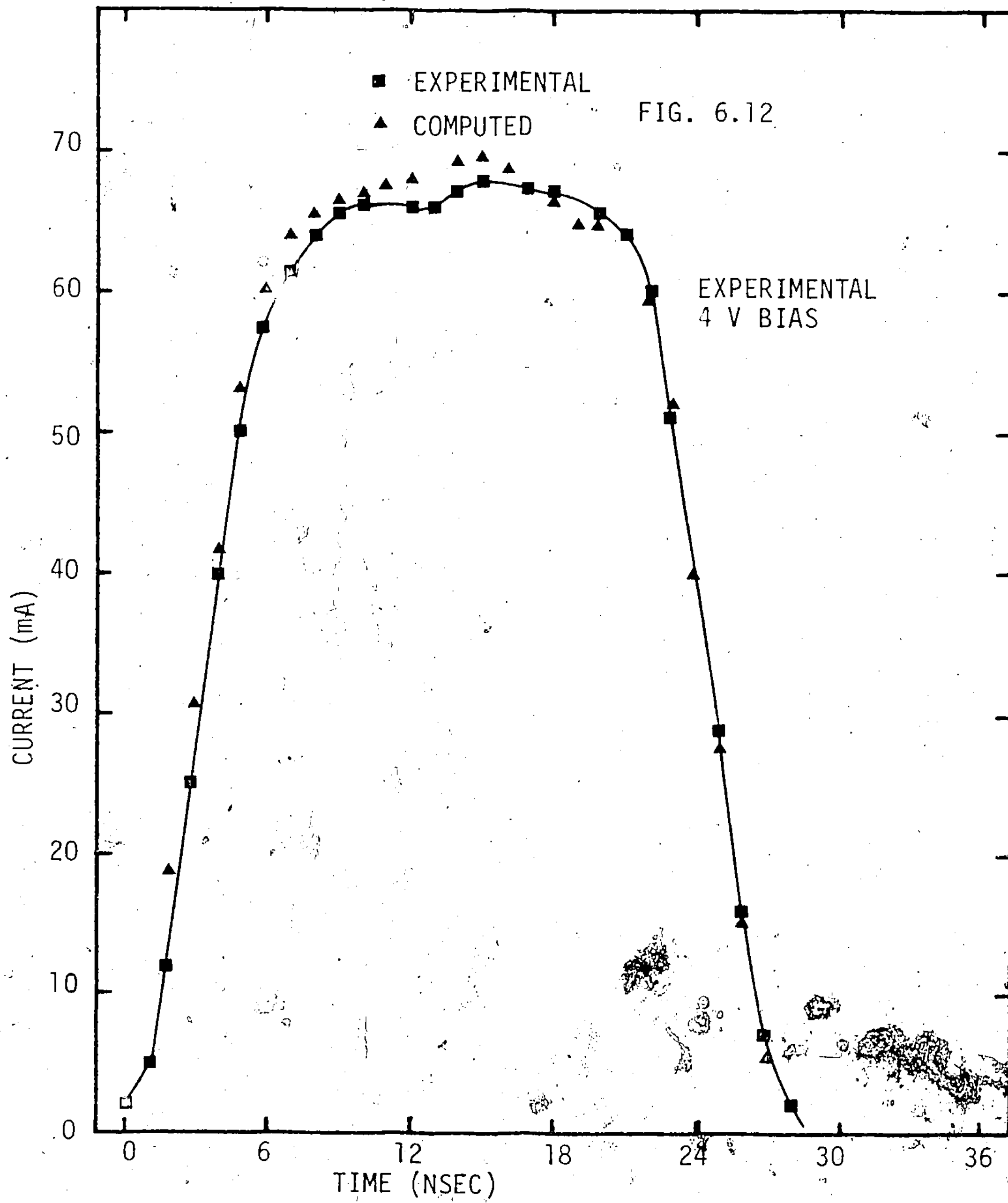

FIG. 6.11 PULSED D.C. CURRENT RESPONSE FOR IMPATT DIODE #1 AT 6.0 GHz

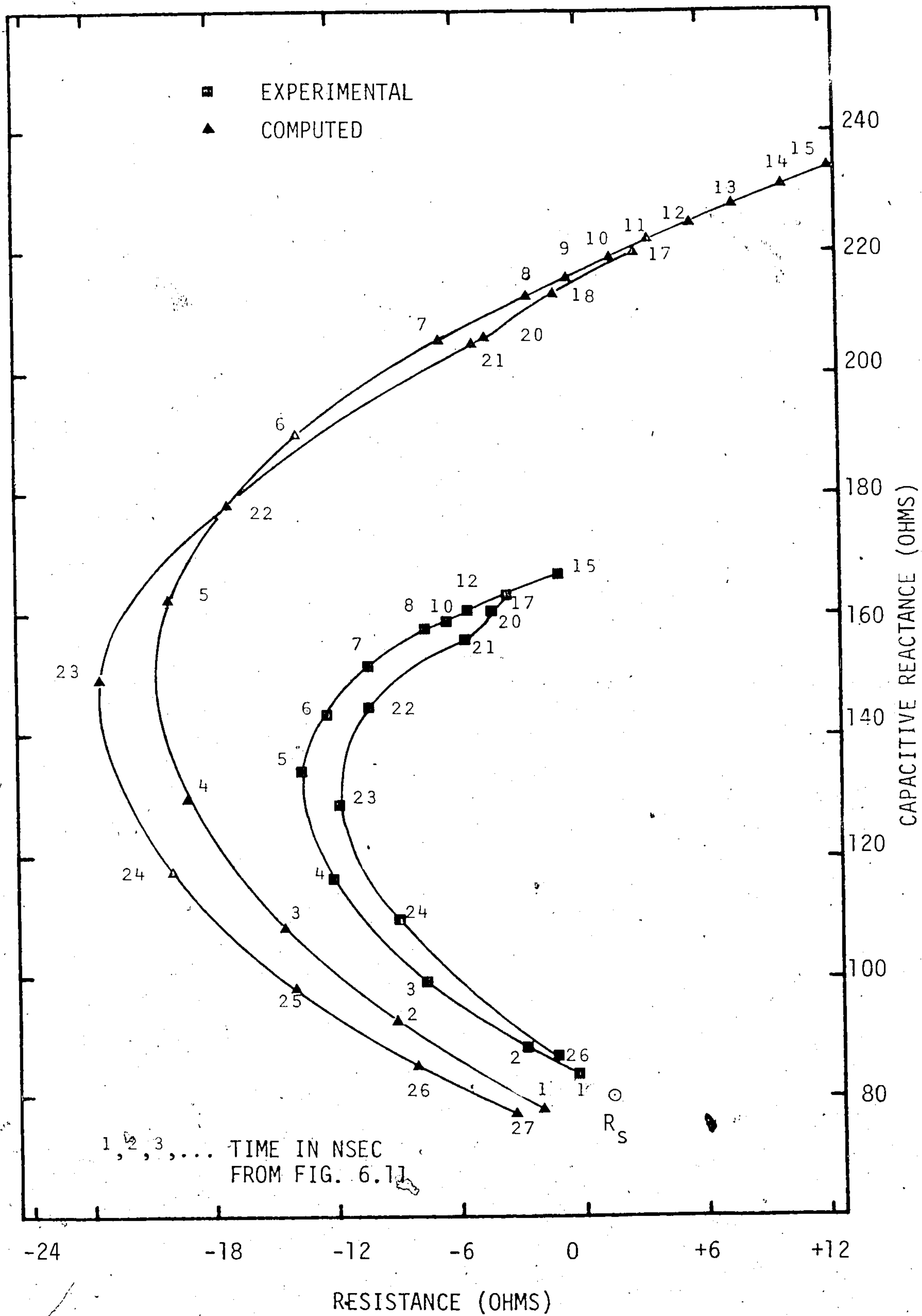

FIG. 6.12 COMPUTED AND MEASURED ELECTRONIC IMPEDANCE FOR DIODE #1 AT 6.0 GHz - 4 V EXPERIMENTAL BIAS

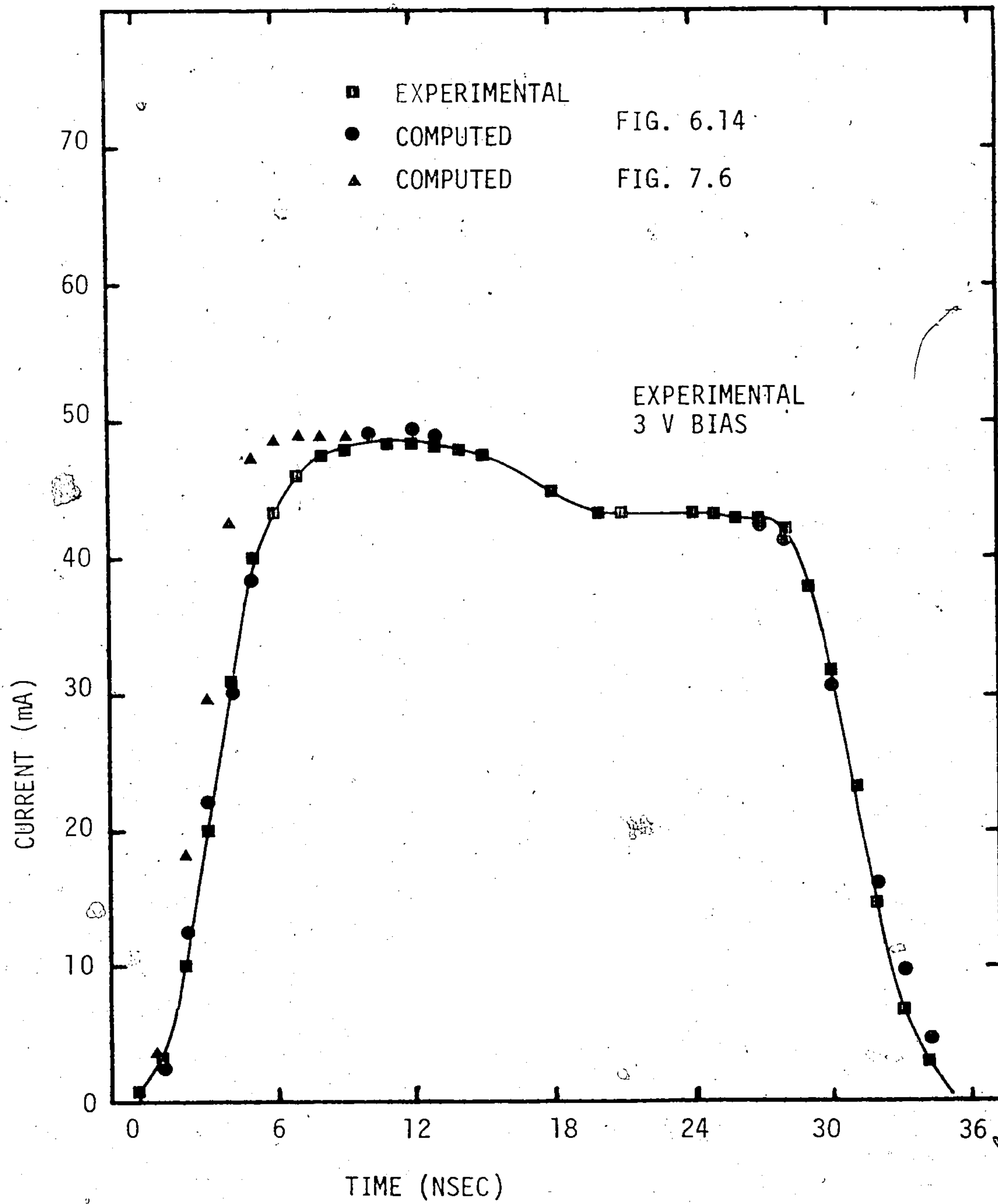

FIG. 6.13 PULSED D.C. CURRENT RESPONSE FOR IMPATT DIODE #1 AT 6.0 GHz

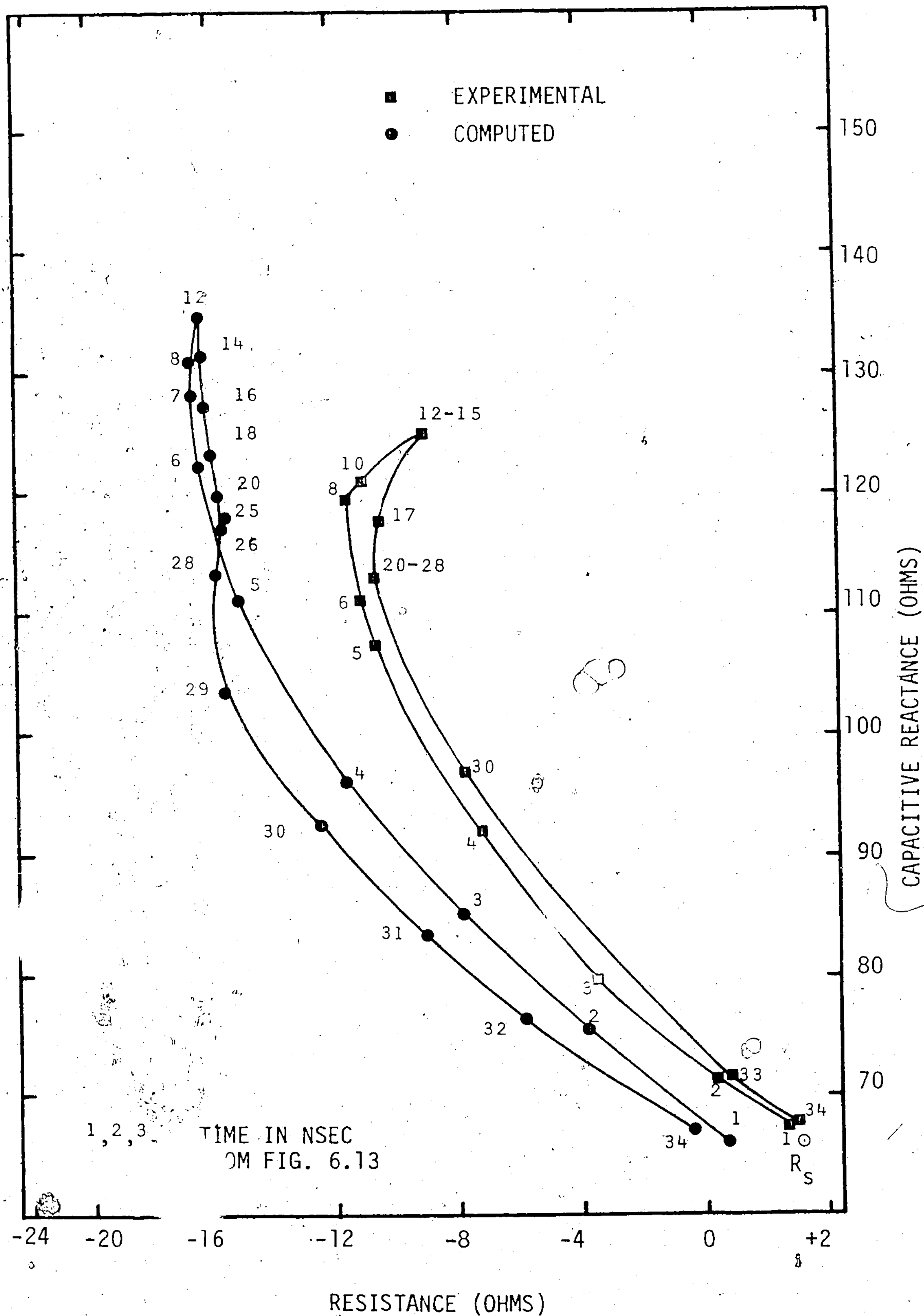

FIG. 6.14 COMPUTED AND MEASURED ELECTRONIC IMPEDANCE FOR DIODE #1 AT 6.0 GHz - 3V EXPERIMENTAL BIAS

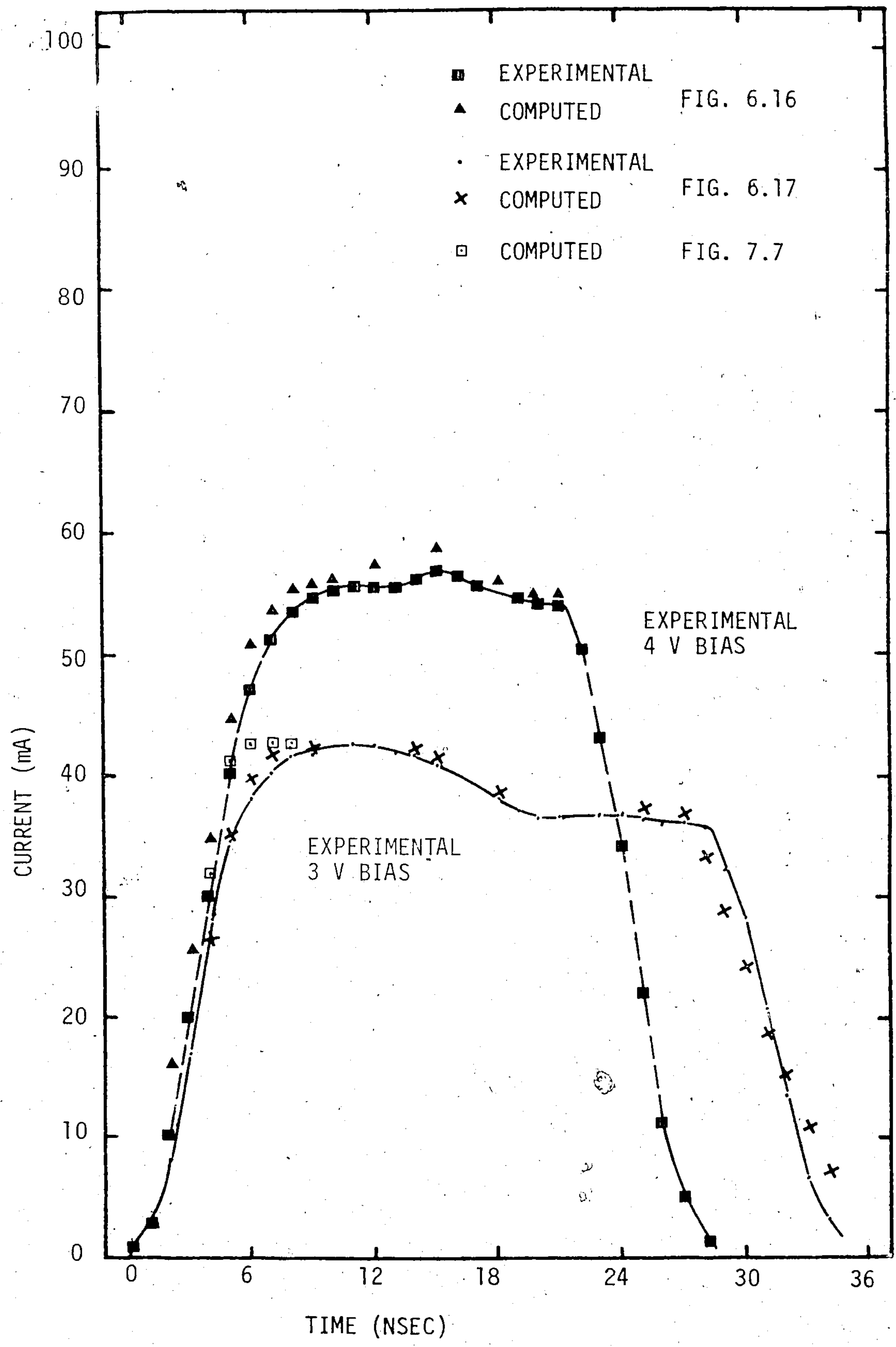

FIG. 6.15 PULSED D.C. CURRENT RESPONSE FOR IMPATT DIODE #8 AT 6.0 GHz

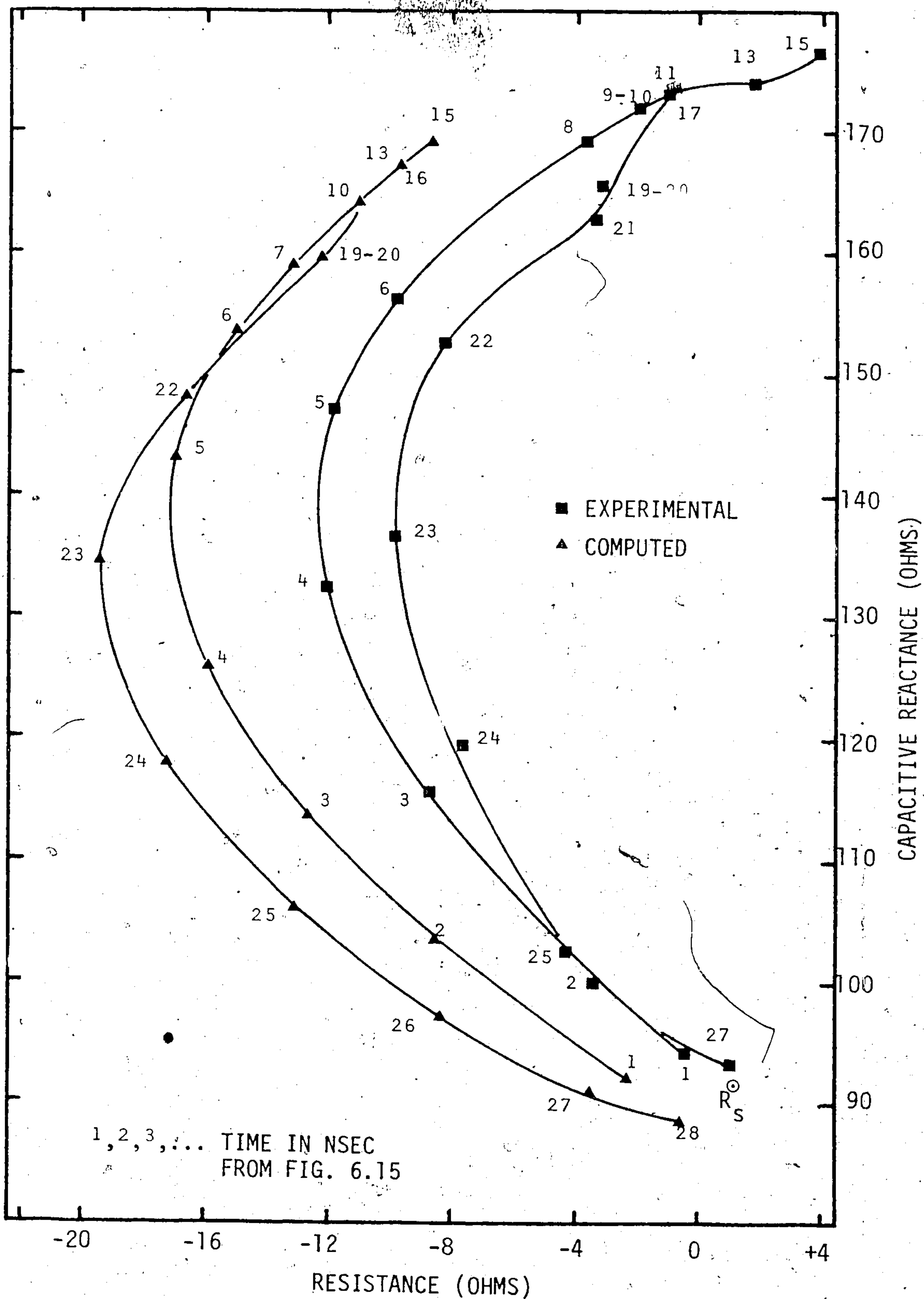

FIG. 6.16 COMPUTED AND MEASURED ELECTRONIC IMPEDANCE FOR DIODE #8 AT 6.0 GHz - 4 V EXPERIMENTAL BIAS

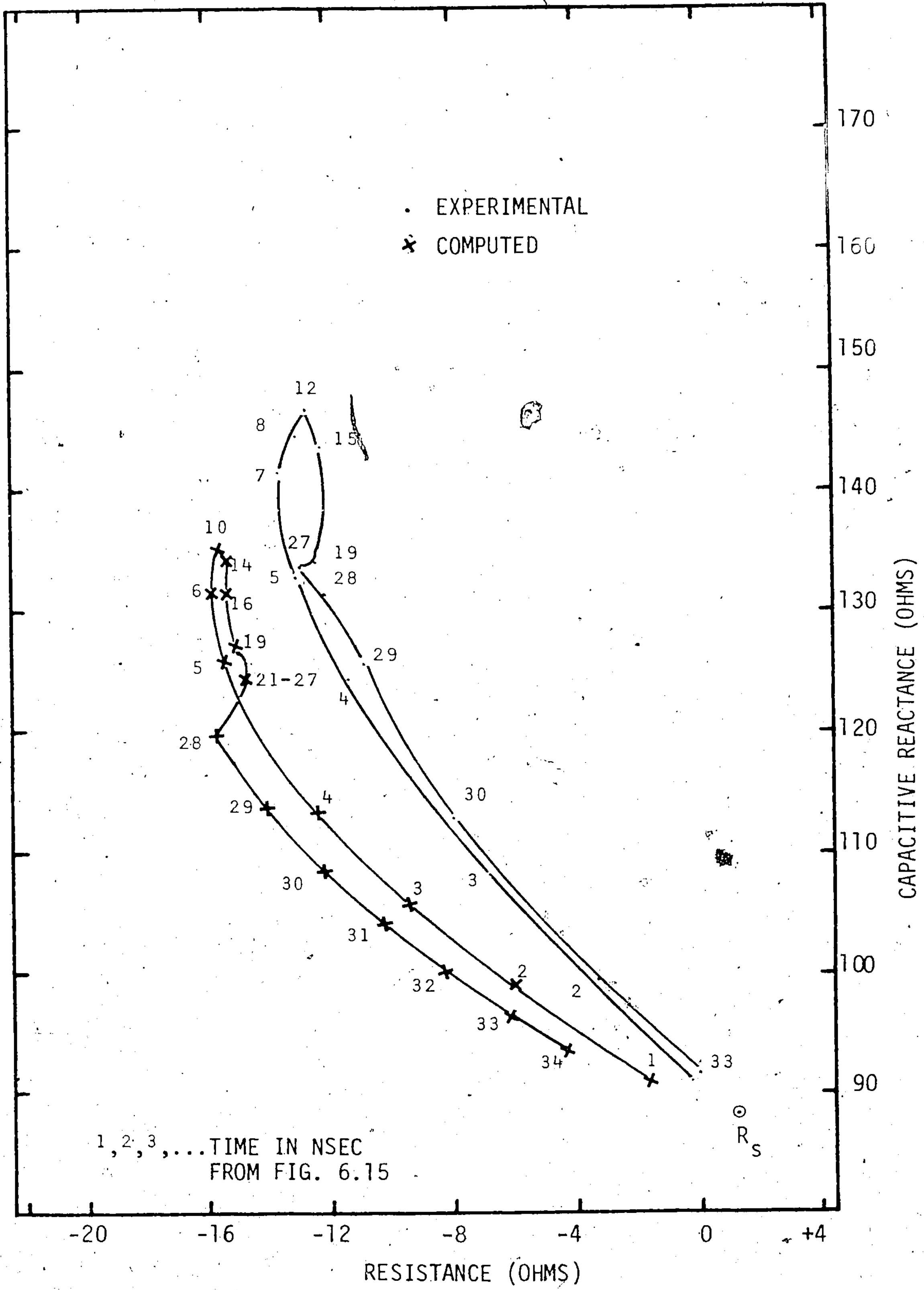

FIG. 6.17 COMPUTED AND MEASURED ELECTRONIC IMPEDANCE FOR DIODE #8 AT 6.0 GHz - 3V EXPERIMENTAL BIAS

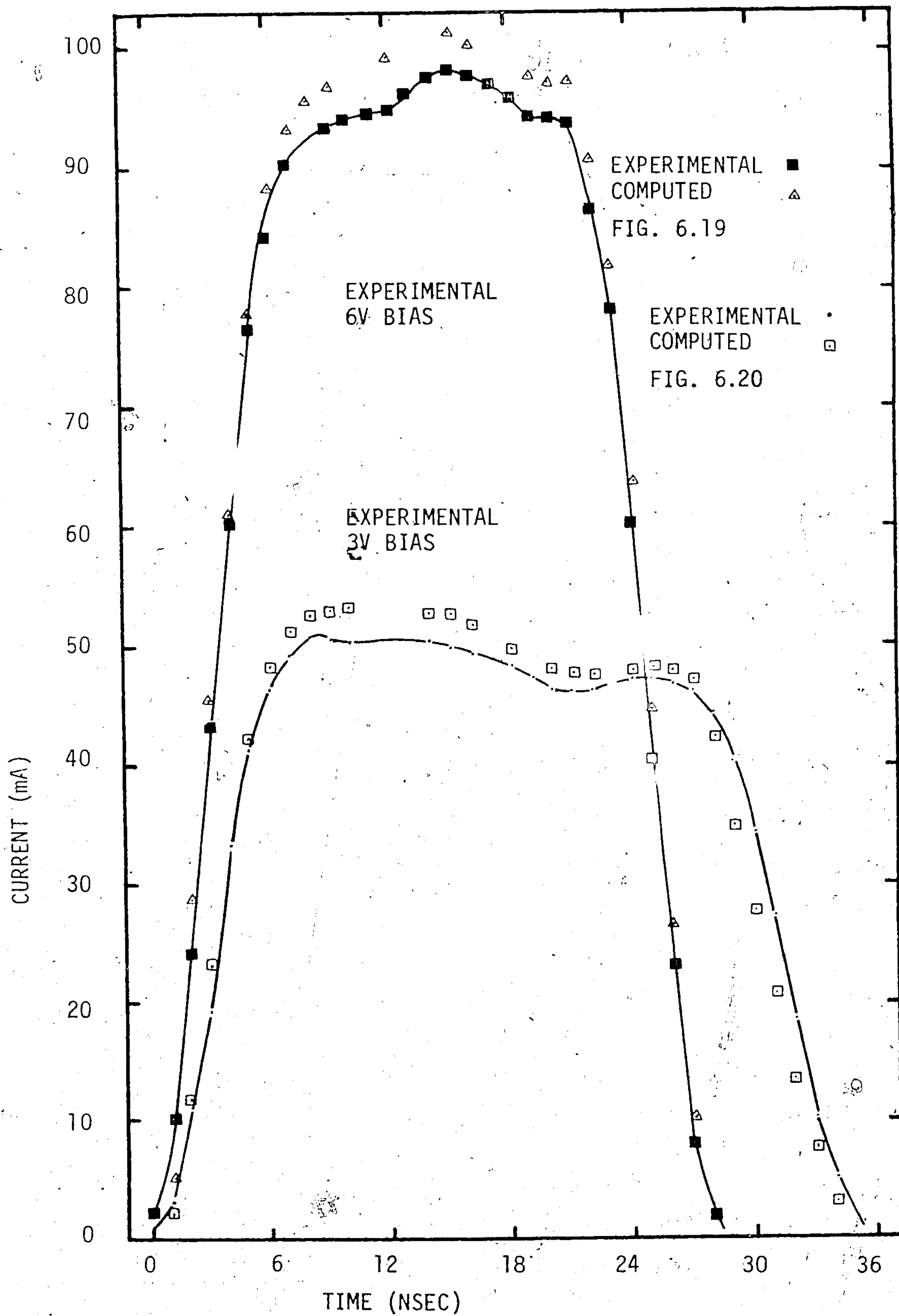

FIG. 6.18 PULSED D.C. CURRENT RESPONSE FOR IMPATT DIODE #1 AT 7.8 GHz

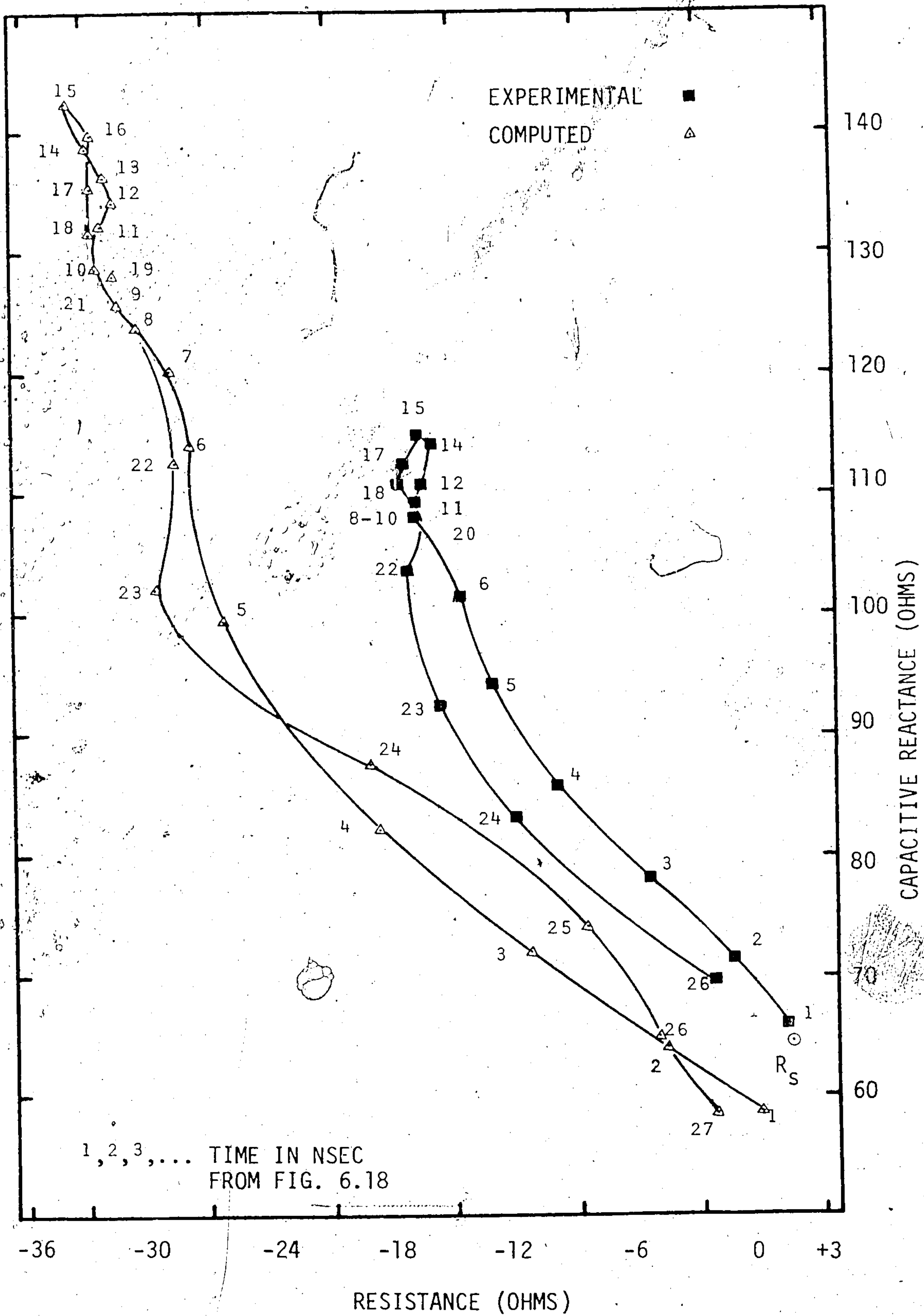

FIG. 6.19 COMPUTED AND MEASURED ELECTRONIC IMPEDANCE FOR DIODE #1 AT 7.8 GHz - 6 V EXPERIMENTAL BIAS

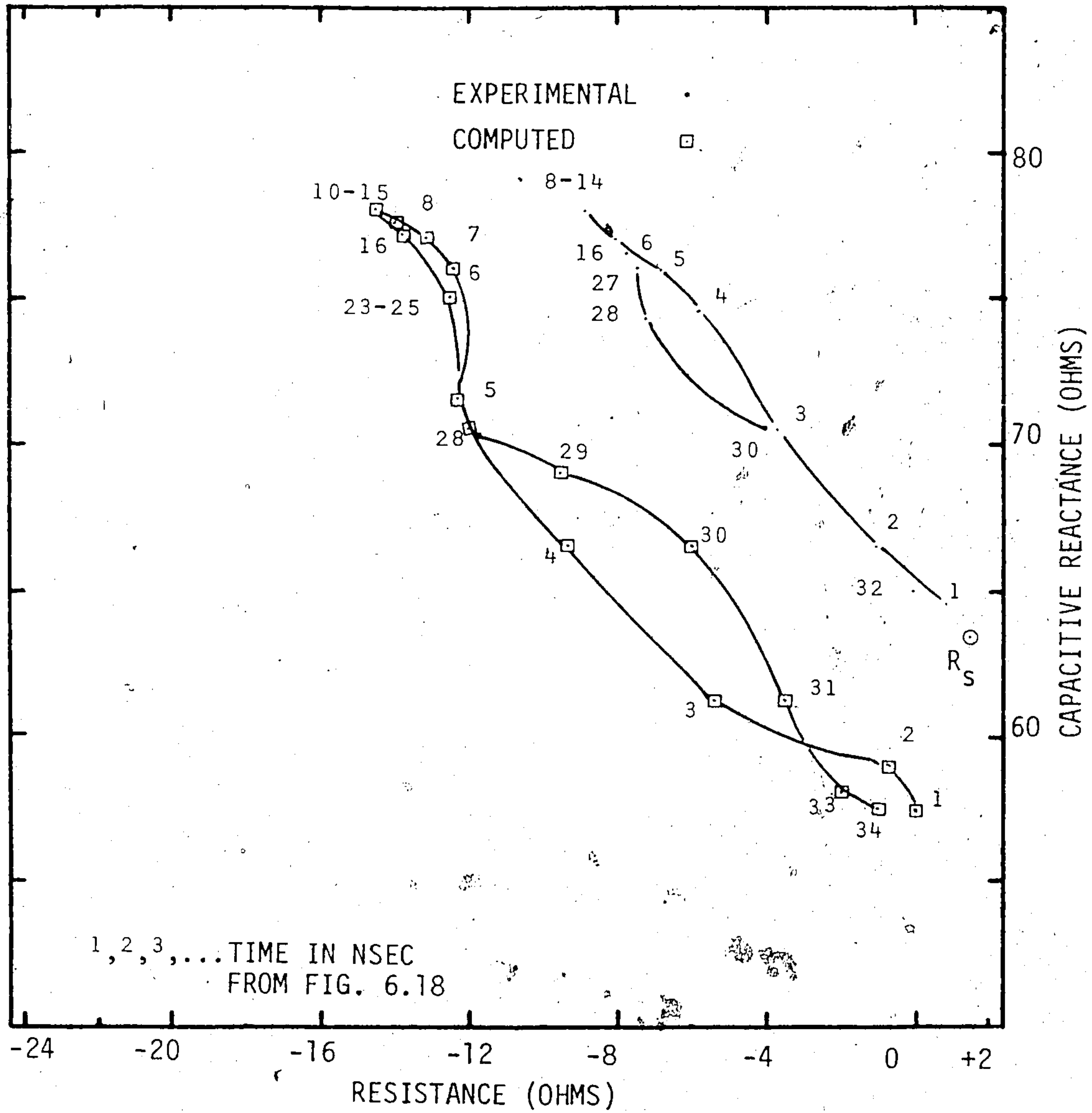

FIG. 6.20 COMPUTED AND MEASURED ELECTRONIC IMPEDANCE FOR DIODE #1 AT 7.8 GHz - 3 V EXPERIMENTAL BIAS

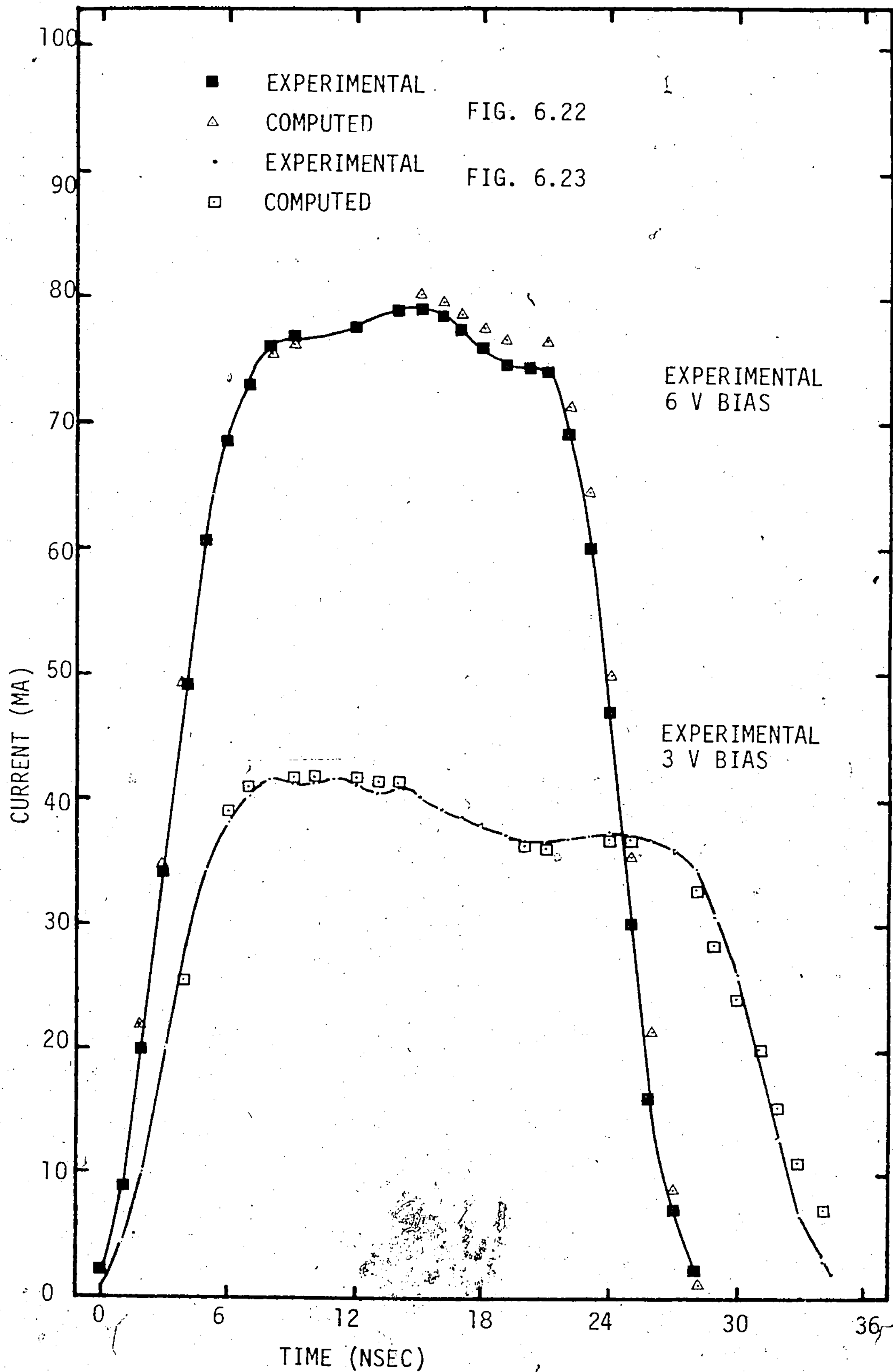

FIG. 6.21 PULSED D.C. CURRENT RESPONSE FOR IMPATT DIODE #8 AT 7.8 GHz

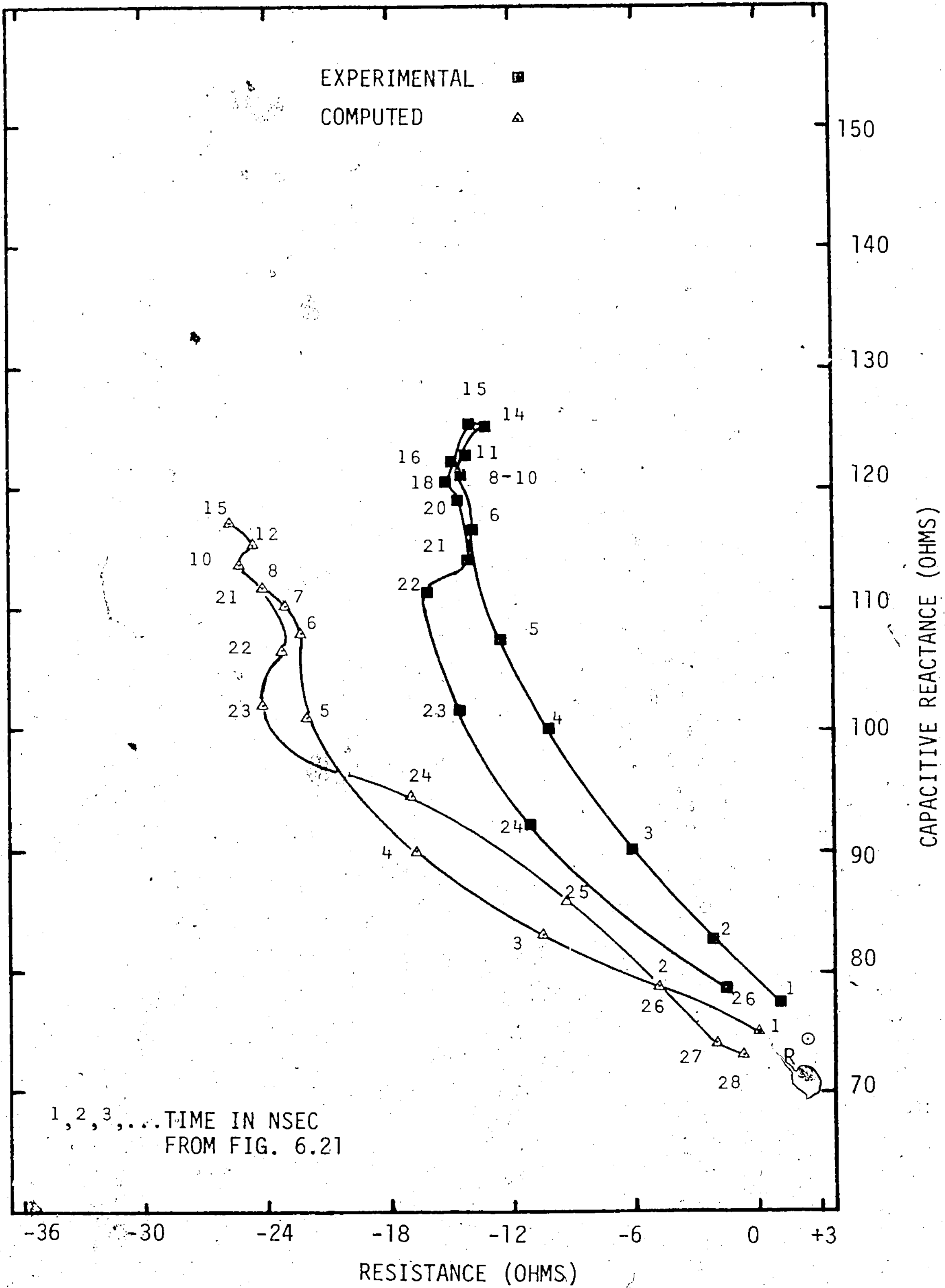

FIG. 6.22 COMPUTED AND MEASURED ELECTRONIC IMPEDANCE FOR DIODE #8 AT 7.8 GHz - 6 V EXPERIMENTAL BIAS

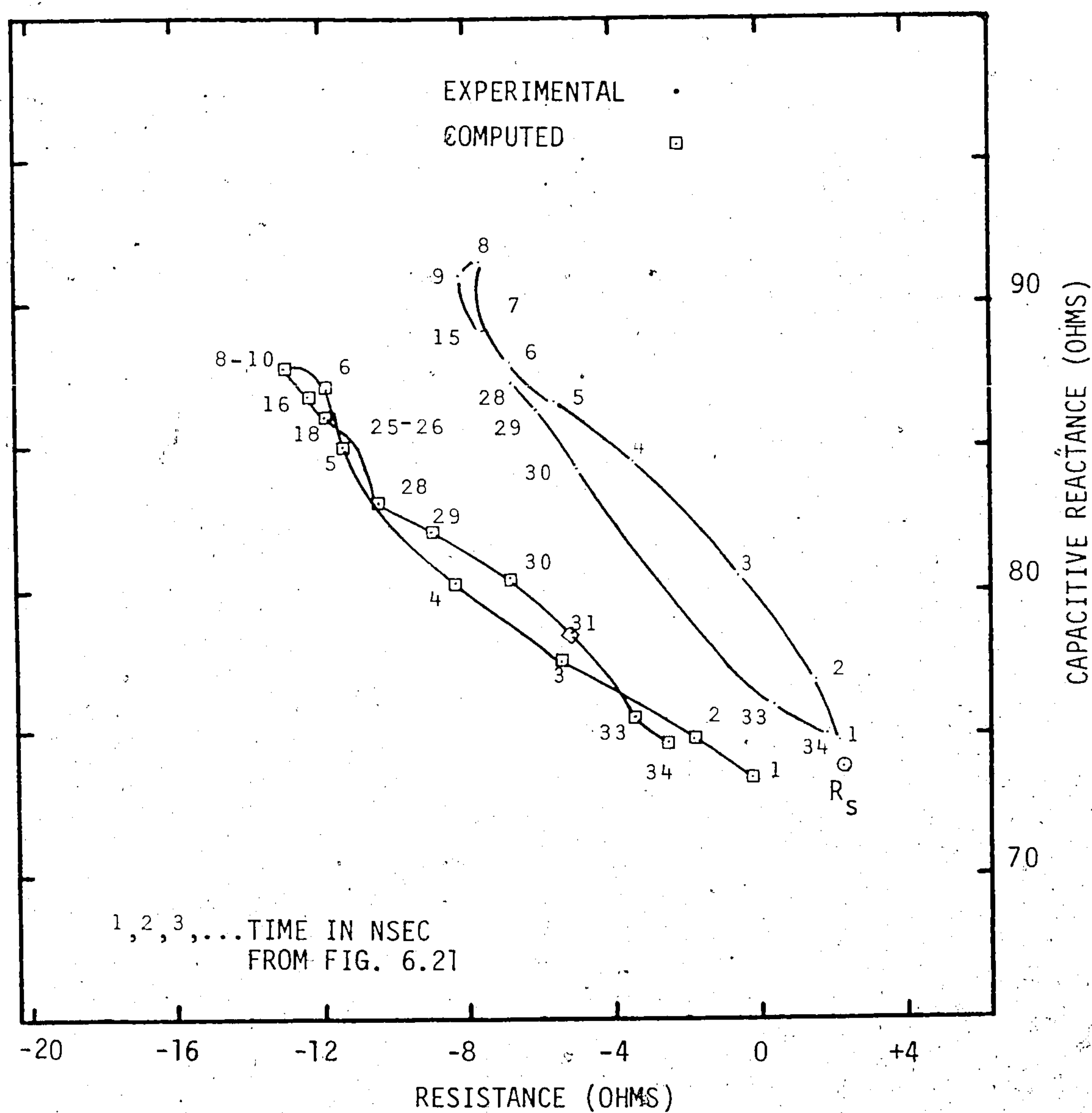

FIG. 6.23 COMPUTED AND MEASURED ELECTRONIC IMPEDANCE FOR DIODE #8 AT 7.8 GHz - 3 V EXPERIMENTAL BIAS

value is indicated on all the appropiate figures. For diode #1, the value of R_s was about 1.5 ohms from impedance measurements taken at both 6.0 and 7.8 GHz, while for diode #8 the value of R_s was 1.2 ohms from measurements at 6.0 GHz, and 2.4 ohms for measurements at 7.8 GHz.

The value of R_s was not included in the computer model consequently, when comparing the computed and experimental results, the value of R_s should be algebraically added to the computed results. This is readily accomplished as R_s only affects the real part of the calculations and the computed curves are simply shifted along the real axis an amount equal to the magnitude of R_s.

6.4.3 Accuracy of Measurement System

Because of the unknown influence of the second harmonic on the measurements and the absence of facilities to conduct highly accurate steady-state impedance measurements, it is difficult to arrive at a specific evaluation of the measurement accuracy for the method used here. Further, a detailed investigation of the inaccuracies in the measurement system would be overshadowed by the limitations inherent in the coaxial four-port circulator and R.F. detector used. However, a qualitative discussion should prove useful.

In the Carrier Reinsertion method there are three main areas which are subject to measurement errors. These sensitive areas are; the packaged diode mounting unit, the separation of the incident and reflected R.F. signals and the R.F. detector itself. To provide a means of calibrating the R.F. detector sub-system, the impedance of the packaged diode should be known for several values of reverse bias voltage

below breakdown. The diode mounting unit has to reproduce these diode package impedances as magnitude and phase in a reflected R.F. voltage. To minimize possible errors being introduced during this transformation, the packaged diode holding unit should be an integral part of the measurement of the packaged diode impedance, both external to and internal to, the Carrier Reinsertion Method. By designing the diode holder to be compatible with a standard APC-7 precision connector, this source of error was minimized for the work carried out here.

An important area closely associated with the diode holding unit, that may introduce some error in the impedance measurements, is the four-port circulator used to separate the incident and reflected R.F. signals. In the coaxial four-port circulator used for this work, the isolation between the paths followed by the incident and reflected R.F. signals was found to be 20 dB. Therefore, it would be possible to have up to 1% of the incident R.F. power, or 10% of the incident voltage, bypassing the diode holder and interfering with the reflected R.F. signal. As long as the magnitude of the reflected R.F. signal is not small with respect to the magnitude of the incident R.F. signal, 20 dB of isolation should therefore provide experimental results of sufficient accuracy.

Another possible source of measurement error lies in the operation of the R.F. detector sub-system. As discussed in the Appendix B, the actual detector diodes have R.F. - input- d.c. - output characteristics that vary appreciably when used over a wide range of incident R.F. signal powers. This necessitates a piece-wise linear approximation to these characteristics and the determination of the constants of

proportionality (to calculate the reflection coefficient) for each linear segment. To minimize the introduction of measurement error in this procedure, the R.F. detector unit should be selected, or tuned, for best linearity over the required range of operating levels. Also, there should be sufficient versatility in the measurement system to ensure that the range of detected output levels evident in the actual measurements, was covered by the calibration procedure carried out at reverse bias voltages below breakdown.

The error associated with the Carrier Reinsertion Method of impedance measurement should be small and will mainly be determined by the characteristics of the R.F. detector unit. Some error was inherent in this measurement method, as it was used here, but, this was essentially due to availability of equipment and is not believed to have significantly affected the overall accuracy of these measurements.

6.5 Summary

The measurement of microwave impedance under transient conditions requires that the measurement method be capable of following variations in the magnitude and phase of the impedances being measured, as a function of time. In this chapter, two distinct types of microwave impedance measurement methods have been evaluated, with regard to their suitability for the transient impedance measurements on Impatt diodes. These measurements of the complex impedance were carried out using a direct comparison of the voltage/current waveforms and also, by measuring the complex reflection coefficient.

In the measurement of the transient impedance by the direct

comparison of voltage and current waveforms, two methods were used. Both the Cavity Oscillator and the Air-line Tee Methods were tested. These methods were readily implemented, as a small amount of equipment was required, however, both these measurement methods proved to have serious limitations that restricted their usefulness.

The Carrier Reinsertion Method for the measurement of transient impedance actually measures the complex reflection coefficient, which is then converted to an impedance. This method requires more extensive use of test equipment but is free of the difficulties associated with the waveform comparison methods. To the best of this author's knowledge, the Carrier Reinsertion Method, as developed here, has not been used in any previous impedance measurements on Impatt diodes. This method is suitable for either steady-state or transient impedance measurements. The method, as utilized here, had some limitations due to availability of equipment but overall, the method appears to have good potential for future work in this field.

The electronic impedance of Impatt diodes, under transient conditions, has been measured by using the Carrier Reinsertion Method. The plotted data form well behaved curves that display very little scattering of the measured values. These measurements have been obtained by reverse biasing the Impatt diode to maintain a d.c. current of 1 ma and then modulating the d.c. bias voltage supply with low-voltage pulses. These bias pulses had rise times as short as 5 nanoseconds at the reference plane of the diode and it was determined that the d.c. current response of the packaged diode was at least equivalent to these

bias voltage pulse rise times. Therefore, short duration bias pulses, in the range of 30 nanoseconds, could be used. These short duration bias pulses enabled the use of very low duty cycles which minimized the effects of temperature changes in the diode's semiconductor junction. The measurement holding unit for the packaged diode was designed to give a simple transformation from the measured impedance values to the electronic impedance of the semiconductor chip itself, thus, simplifying the calculation and improving the accuracy of the measurements. Since these impedance measurements have been referenced to the d.c. current response of the diode, comparisons of these measured results with computer models of the Impatt diode are readily carried out. A detailed comparison will be given in the following chapter.

CHAPTER VII

Discussion of Theoretical and Experimental Results

7.1 Introduction

There have been several publications[4,24,25,47,48] describing theoretical models of the Impatt diode, but very few publications include a direct comparison between the theoretically-derived and the experimentally-measured electronic impedance. The work undertaken here has been carried out with the intent of substantiating the validity of the theoretical transient model with experimental results.

In the experiments, and hence in the theoretical model, the bias voltage pulses were of short duration (about 30 nanoseconds). For these short-durations bias pulses, temperature effects on Impatt diode operation are minimal. Further, the comparison between the computations and the measurements were made on the basis of similar d.c. current pulses and thus, changes in the temperature of the semiconductor junction are accounted for. Therefore, the discussion of the transient impedance characteristics will be carried on without any reference to the junction temperature.

7.2 Comparison of Computations and Measurements

The experiments were carried out on two separate diodes and at two frequencies that were sufficiently distinct that differences in the behaviour of the electronic impedance (z_e) could be observed. This procedure ensured a more valid comparison between the computed and the experimental results. As an indication of the type of comparison

to be expected, it was noted that Greiling and Haddad[25], in their comparison between theory and experiment, encountered differences in the real and imaginary part of z_e in the range of 15-60% and 5-10%, respectively. Further, Decker *et al*[49] claim that an accurate comparison between theory and measurements can only be obtained when the effects of injecting contacts are taken into account.

Generally, the computations and the measurements of the diode's electronic impedance exhibited the same type of behaviour. This agreement holds for both frequencies used and also at high and low bias levels. A comparison of the plotted results in Figs. 6.11 to 6.23 shows that the slopes and curvatures of the computed and experimental results are very similar. A significant indicator for the comparison of the results is in the behaviour of the electronic impedance when the bias pulse passes from its initial rapid rise to its relatively flat top. Here, the clockwise loop at 6.0 GHz, Figs. 6.14 and 6.17, and the counter clockwise loop at 7.8 GHz, Figs. 6.19 and 6.23, are displayed by both the computed and the experimental results. About the only significant discrepancy between the computed and the experimental results appears to be in the relative magnitudes of the real and imaginary parts of the electronic impedance, with the largest discrepancy occurring in the real part. The differences between the computations and the measurements are typically 20% for diode #8 and 40% for diode #1 in the real parts of z_e, with the differences in the imaginary parts of z_e being typically 8% for both diodes. When making these comparisons, it should be remembered that the plotted computed results have not taken the value of R_s into account. (Where R_s is the resistance

due to ohmic contacts, substrate resistance and undepleted portion of the drift region. R_s is in series with Z_e).

From a comparison of the plotted results, it is evident that the measurements, in some aspects, do not exhibit the same magnitude of variation in behaviour as do the computed results. This is probably due to a slower response in the measuring system, although part of the magnitude discrepance could be due to the influence of the second harmonic in the driving R.F. voltage waveform, as it appears across the diode.

7.2.1 Response of the Measuring System

From Figs. 6.12, 6.19, and 6.22, the experimental results appear to be a smoothed version of the theory. Part of this difference between the computations and the measurements could be due to the response in the R.F. detection subsystem. This detector response could account for the discrepancy between the computed and measured behaviour of the electronic impedance during the decay time of the bias voltage pulse. During the initial part of the decay time, both the computed and measured results show the same relative shift in the values of Z_e but, as the decay time progresses the computations show a recovery trend that is not apparent in the experimental results, until after a few nanoseconds have passed.

Equipment problems alone, do not account for all the differences between the computation and the measurements. This is evident in that the two diodes are affected differently, with the measured results for

diode #1 displaying a more restricted behaviour than those of diode #8. This is particularly evident at the higher current levels, Figs. 6.12 and 6.16. At the lower bias levels the behavior of the two diodes is much closer related.

7.2.2 Second Harmonic Effects

The current waveform of the diode computer model is Fourier-analyzed to obtain the d.c. component plus, the first, second and third harmonics. The ratio of the magnitude of the second harmonic to the magnitude of the fundamental frequency component ($\gamma_{2/1}$) is plotted in Figs. 7.1 and 7.2 for 6.0 and 7.8 GHz, respectively. Generally, there is an increase in the value of $\gamma_{2/1}$, with increasing d.c. current level in the diode and the overall behaviour of the $\gamma_{2/1}$ plot is similar to the waveform of the corresponding d.c. current pulse.

For diode #8, the value of $\gamma_{2/1}$ is relatively small and varies from 1 to 4%, with different frequencies and bias voltage levels. However, for diode #1, the value of $\gamma_{2/1}$ shows a significant change for different bias voltage levels, ranging as high as 14% for high d.c. current levels at 6.0 GHz. For both diodes the value of $\gamma_{2/1}$ is larger for 6.0 GHz than for 7.8 GHz with the biggest difference being exhibited for diode #1.

(25)

Greiling and Haddad have shown that it is possible for an appreciable second harmonic component to be present in the R.F. voltage waveform, generated by the second harmonic component in the R.F. current waveform of the diode. In the experiments carried out here, the driving R.F. voltage applied to the Impatt diode is initially of single frequency.

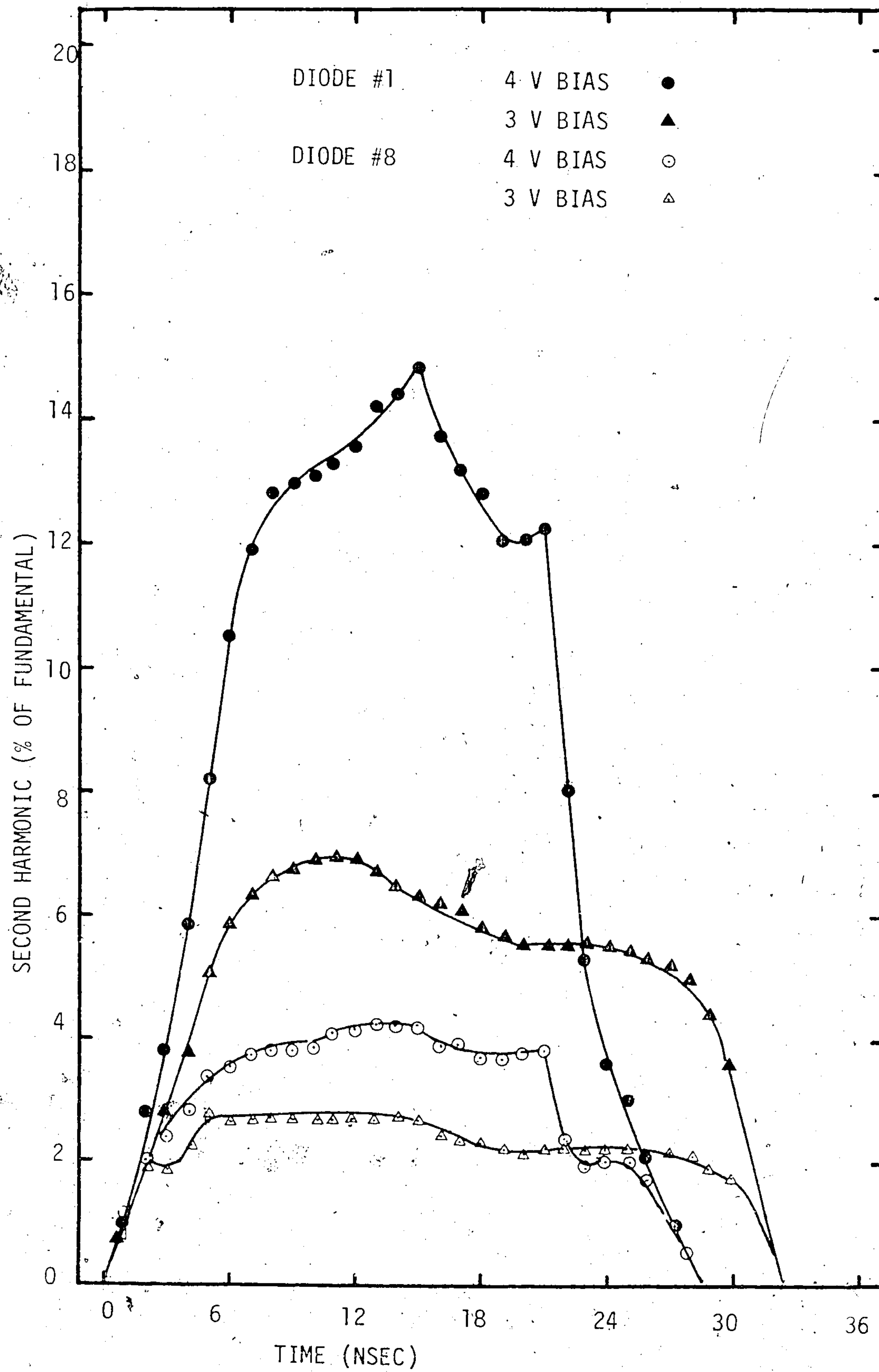

FIG. 7.1 COMPUTED RATIO OF SECOND HARMONIC TO FUNDAMENTAL R.F. COMPONENT OF IMPATT DIODE CURRENT AT 6.0 GHz

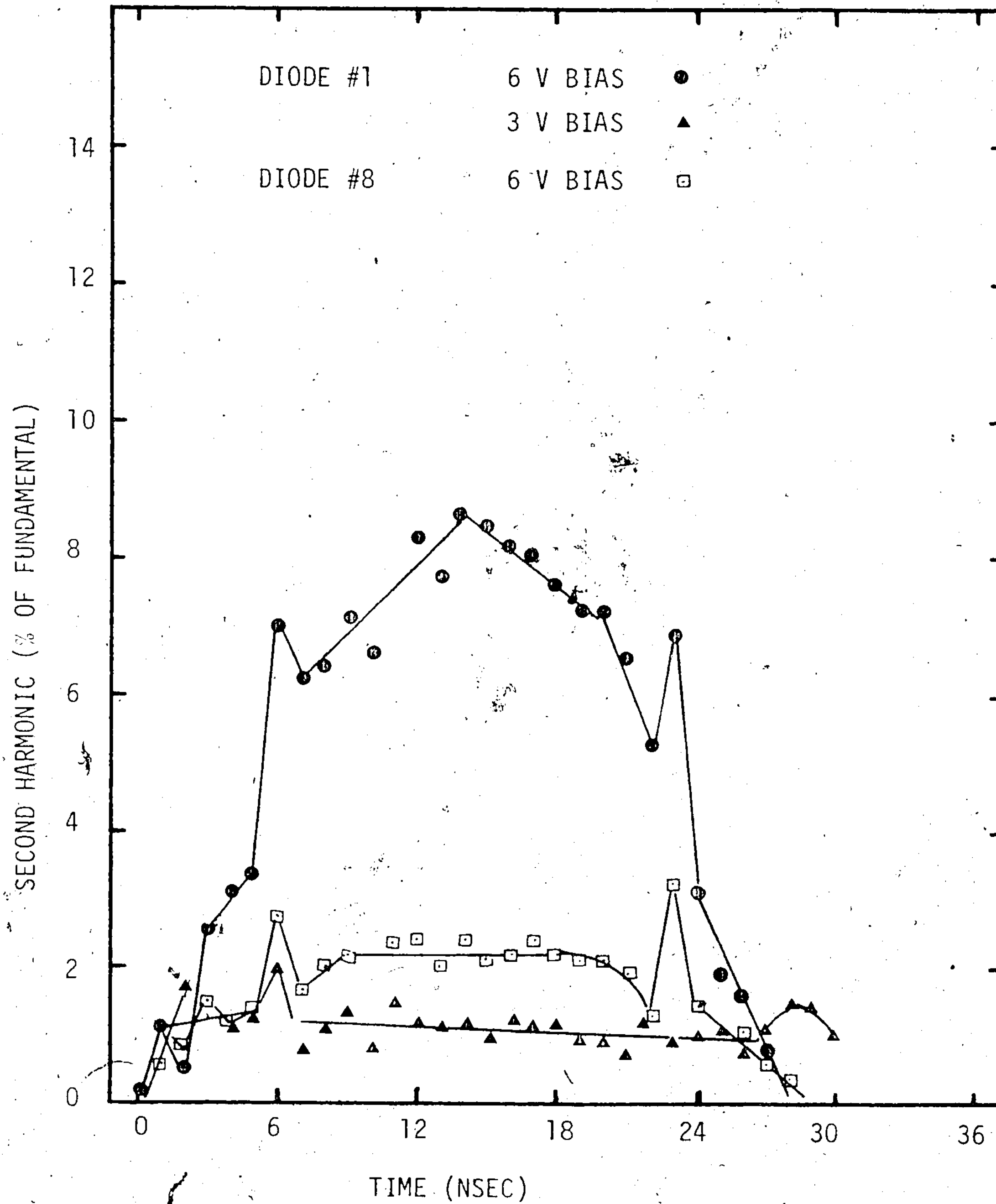

FIG. 7.2 COMPUTED RATIO OF SECOND HARMONIC TO FUNDAMENTAL R.F. COMPONENT OF IMPATT DIODE CURRENT AT 7.8 GHz

Then, since the second harmonic component of the R.F. voltage is not absorbed in the measuring system (coaxial four-port hybrid, Fig. 6.1), it is possible that a significant R.F. voltage at the second harmonic frequency could be developed in the diode holder, as the Impatt diode is biased to higher current levels. Consequently, another variable is introduced to modify the measured values of the electronic impedance.

A possible explanation of the significant differences in the magnitude of the electronic impedances, of diode #1, with respect to the computed results, at the higher current levels, could be the influence of a second harmonic component in the R.F. voltage. From Figs. 6.14 and 6.20, it is observed that the measured and computed values of the electronic impedance, for diode #1, display a close correspondence for oth 6.0 and 7.8 GHz. These results are for moderate current levels in the diode. For higher currents the results are as shown in Figs. 6.12 and 6.19, where there is significant differences between the computed and measured values of the electronic impedance. From Fig. 7.1 and 7.2, the value of $\gamma_{2/1}$ is much larger for the higher current levels. This discrepancy between the computed and measured values of the electronic impedance, at the higher current levels, is not evident for diode #8. Also, the value of $\gamma_{2/1}$, is relatively small for both moderate and high current levels in this diode. As it is well known[50] that the second harmonic in the R.F. voltage does have a significant influence on the behaviour of the Impatt diode, it is likely that the second harmonic is also influencing the measurements taken here .

7.2.3 Degree of Correspondence of Computed and Experimental Results

Because of the questions raised concerning the response of the measuring system and the extent of the effects of the second harmonic component of the R.F. voltage across the diode, it was thought that only a limited amount of curve fitting should be carried out. Therefore, efforts to fit the computations to the measurements were confined to small variations in the values of the parameters x_a, K, C_d and τ_d in the computer model. The effects of variations in these parameters are outlined in Chapter IV, sub-section 4.3.2, as are the final values chosen for the comparison between the experimental and computed results (Table 4.1). Consequently, only the significance of the changes from the theoretical values will be discussed here.

The value of the equivalent width of the avalanche region, x_a, was arrived at by considering the experimental and computed characteristics of diode #1. From Fig. 4.6, it is evident that the value of x_a is less than 1.55 microns while, from the characterization of Scharfetters model (Fig. 3.4), the value of x_a is at least 1.35 microns. Since the doping levels[23] of diode #1 were slightly less than those of Scharfetters model, a value of 1.45 microns for x_a, of diode #1, was selected. Diode #8 has a doping concentration that is less than that of diode #1 and therefore has a value of x_a greater than 1.45 microns. From information[23] given on the predicted widths of avalanche regions for different doping levels of Silicon, a value of 1.65 microns for x_a, in diode #8 was deemed to be appropiate. The values of x_a chosen for these diodes are in general agreement with those predicted by previously

published work and were in proportion to the values of K selected for the diodes.

It is difficult to correlate the sum of the avalanche and drift regions with the total depletion width of the diode. The value of x_a is an equivalent width, while the width of the drift region and its associated transit time are actual values. Therefore, the value of T_d was chosen as outlined in Chapter IV and then held constant.

Magnitude scaling was mainly accomplished by variations, in the values of the depletion layer capacitance (C_d'). The variations from the measured values of C_d at 1 MHz were a maximum of 0.03 pf and this is within the tolerance between capacitance values measured at 1 MHz and several GHz, when stray capacitances of the package are taken into account[45]. Therefore, the values of C_d used in the final comparison between computed and experimental results are quite accurate and within the tolerances found by other workers in this field.

As outlined in Chapter IV, the value of the coefficient for the space charge term associated with the width of the avalanche region (K), was selected to provide the best behavioural comparison between the computations and the measurements. Some magnitude scaling was also achieved by this selection but, this was not the main effect. From the constant field theory, the values of K should be 0.011 for diode #1 and 0.015 for diode #8. As shown in Table 4.1, the actual values of K used differed a little from these theoretical values and also displayed some frequency dependence. Some differences between the theoretical and actual values used are to be expected, as the constant field model

only gives an estimate of the true value of K. The different values of K for different frequencies would seem to indicate a functional dependence for K that is not evident in the constant field model. However, this frequency dependence is small and may have been accentuated by other characteristics of the measurement system.

7.3 Effects of the Bias Pulse on the Electronic Impedance.

As described in Chapter IV, a comparison between computed and experimental results must be made on the basis of the similar d.c. current pulses, which result from the simulated and applied bias voltage pulses, respectively. Both the computations and the measurements indicate that this resultant d.c. current pulse will be very similar to the bias voltage pulse, across the diode, in rise times and overall shape. As the general shape and rise time of the bias voltage pulse, across the diode, can be controlled by the circuit designer, advantage can be taken of the dependence of the electronic impedance upon the d.c. current pulse in the diode.

7.3.1 Magnitude of the Bias Voltage Pulse

Generally, as the magnitude of the d.c. current increases, the magnitude of the negative impedance of the diode increases as well. This increase contributes to an increase in the R.F. power output of the diode. However, from Figs. 6.12 and 6.16 it is observed that, once the level of d.c. current exceeds a certain value, the real part of the electronic impedance starts to decrease in magnitude. This is a result of the space charge effect of the mobile carriers modifying the total phase shift across the diode. The larger the space charge effect, the

shorter the time allowed for the avalanche current pulse to form. This results in a smaller phase shift being developed in the avalanche region, between the conduction current and the R.F. voltage. The change from increasing magnitude to decreasing magnitude, in the real part of the electronic impedance, is clearly evident at 6.0 GHz but, is not evident at 7.8 GHz, Figs. 6.19 and 6.22, even though the current levels at 7.8 GHz were much higher than those at 6.0 GHz, Figs. 6.11 and 6.18, respectively.

The reason for the reduced effects of the space charge at 7.8 GHz is that, at this higher frequency, the phase shift across the avalanche region is a smaller part of the total phase shift across the diode. Taking a mean length for the drift region as 3 microns for the diodes used here, at 6.0 GHz this length represents about 65° of phase shift, between conduction current and R.F. voltage, while at 7.8 GHz this same length represents about 86° of phase shift. Consequently, the reduction of the phase shift in the avalanche region, due to the space charge effect, is much less critical at 7.8 GHz than at 6.0 GHz.

7.3.2 Rise Times of the Bias Voltage Pulse

The effect upon the electronic impedance of the rise of the bias pulse can be obtained from the plotted results of the electronic impedance as a function of time and d.c. current levels. The plotted results were analyzed and salient features are summarized in Tables 7.1 and 7.2; the information was arrived at in the following manner: consider diode #1 at 6.0 GHz; selecting a current level of 30 ma in Figs. 6.11 and 6.13, the corresponding times are 3 nanoseconds and 4 nanoseconds in Figs. 6.12 and 6.14 respectively. The values of the

TABLE 7.1

TRANSIENT AND STEADY-STATE VALUES OF ELECTRONIC IMPEDANCE COMPUTED AND MEASURED AT 6.0 GHz

DIODE	FREQ (GHz)	METHOD	CURRENT LEVEL	3 VOLT BIAS	6 VOLT BIAS	STEADY STATE
#1	6.0	Computed	Fig.6.11	Fig.6.14	Fig.6.12	Fig.7.4
			30 ma	4 nsec -13.6-j106	3 nsec -14.5-j107.5	-12.8-j104
			Fig.6.13			
			48.5 ma	12 nsec -18.3-j144.5		-18.5-j146
			Fig.6.11			
			49 ma		4.7 nsec -20.8-j148	-18.5-j147
			64 ma		7 nsec -6.7-j205	-4.0-j205
			68 ma		12 nsec +5.5-j22.5	+6.4-j225
		Measured	25 ma	3.5 nsec -7.4-j96	3 nsec -7.5-j99	
#8	6.0	Computed	Fig.6.15	Fig.6.17	Fig.6.16	
			26 ma	4 nsec -12.6-j113	3 nsec -12.8-j113.5	-11.6-j112
			42 ma	12 nsec -15.4-j135	4.8 nsec -17.2-j1[illegible]	-15.4-j135
			53.5 ma		7 nsec -13.2-j159	-12.5-j158
			58.5 ma		15 nsec -8.5-j169	-8.4-j169.5
		Measured	25 ma	3.75 nsec -10.4-j120	3.5 nsec -10.8-j124	

TABLE 7.2

TRANSIENT AND STEADY-STATE VALUES OF ELECTRONIC IMPEDANCE

COMPUTED AND MEASURED AT 7.8 GHz

DIODE	FREQ (GHz)	METHOD	CURRENT LEVEL	3 VOLT BIAS	6 VOLT BIAS	STEADY STATE
#1	7.8	Computed	Fig.6.18	Fig.6.20	Fig.6.19	Fig.7.3
			33 ma	4 nsec -9.3-j64	2.3 nsec -7.0-j67.3	-8.2-j68.0
			48 ma	6 nsec -12.4-j76 23 nsec -12.6-j75		-12.6-j75
			53 ma	10 nsec -14.5-j78		-14.4-j78.5
			88 ma		6 nsec -27.8-j113	-28-j112
			99 ma		12 nsec -31.6-j134 17 nsec -32.6-j135	-32.2-j131
			101 ma		15 nsec -33.8-j142	-32.8-j137
		Measured	33 ma	4 nsec -5.8-j74.5	2.5 nsec -3.5-j74.5	
#8	7.8	Computed	Fig.6.21	Fig.6.23	Fig.6.22	
			34 ma	5 nsec -11.4-j85	3 nsec -10.6-j83	-10.2-j84.5
			41.5 ma	9 nsec -13.0-j87.8		-12.9-j87.5
			68.5 ma		6 nsec -22.5-j108	-22.4-j106
			76.8 ma		10 nsec -25.4-j113.5	-25.0-j113.5
			80 ma		15 nsec -26.0-j117.0	-26.0-j117
		Measured	38 ma	6 nsec -6.9-j88	3.25 nsec -7.0-j92.5	

electronic impedance are then taken from the appropiate graphs. Values of the computed steady-state electronic impedance are taken from Figs. 7.3, 7.4 and 7.5 for the appropiate d.c. current levels. These steady state values of electronic impedance were calculated using the same parameter values as those used for the final computations plotted in Figs. 6.12 to 6.23. Thus, a direct comparison is possible.

Effects of the mobile carrier space charge will place an upper limit on the magnitude of the real part of the electronic impedance (Z_e). Apart from this, the rise times of the bias voltage pulse can have a significant effect upon the characteristics of the diodes Z_e. Essentially, the effects of the rise times are confined to modifying the real part of Z_e with very little change in the imaginary part of Z_e.

From the data given in Tables 7.1 and 7.2, it is evident that the maximum negative value of the real part of Z_e can be increased beyond the equivalent (same d.c. current level) steady-state values for both diodes and at both frequencies used here. However, there is a limit beyond which a further decrease in the rise time of the bias voltage pulse produces little further increase in the negative real part of Z_e and may even reduce the magnitude of the real part of Z_e. This effect is well illustrated in Table 7.2 for 7.8 GHz and for 6.0 GHz in Table 7.1 and Figs. 7.6 and 7.7, with the corresponding current levels being given in Figs. 6.13 and 6.15, respectively. This minimum rise time appears to be about 5 nanoseconds for 7.8 GHz and 4 nanoseconds for 6.0 GHz. It would appear that by using the minimum rise time of the

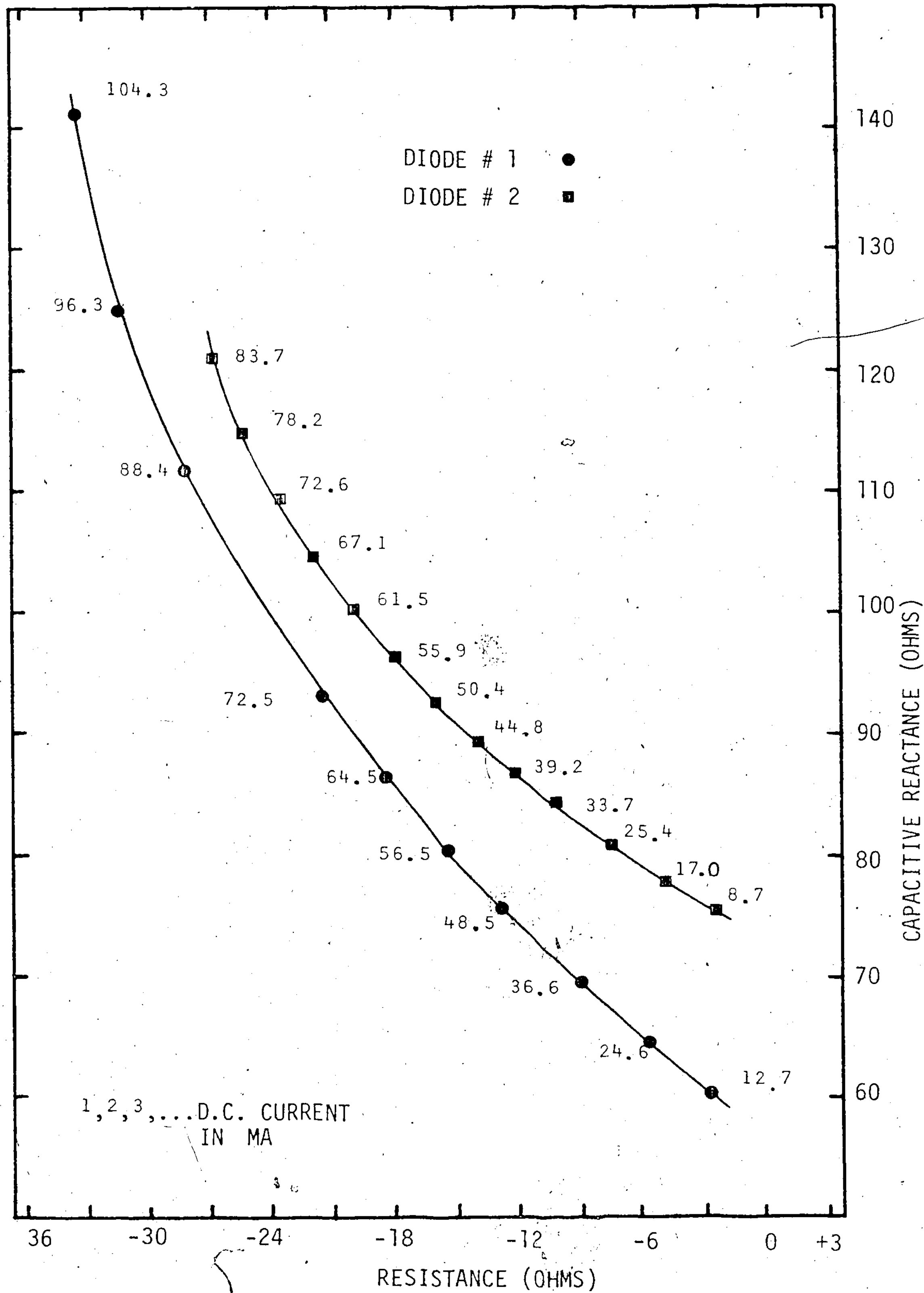

FIG. 7.3 COMPUTED STEADY-STATE VALUES OF ELECTRONIC IMPEDANCE AT 7.8 GHz AND 2 VOLTS R.F.

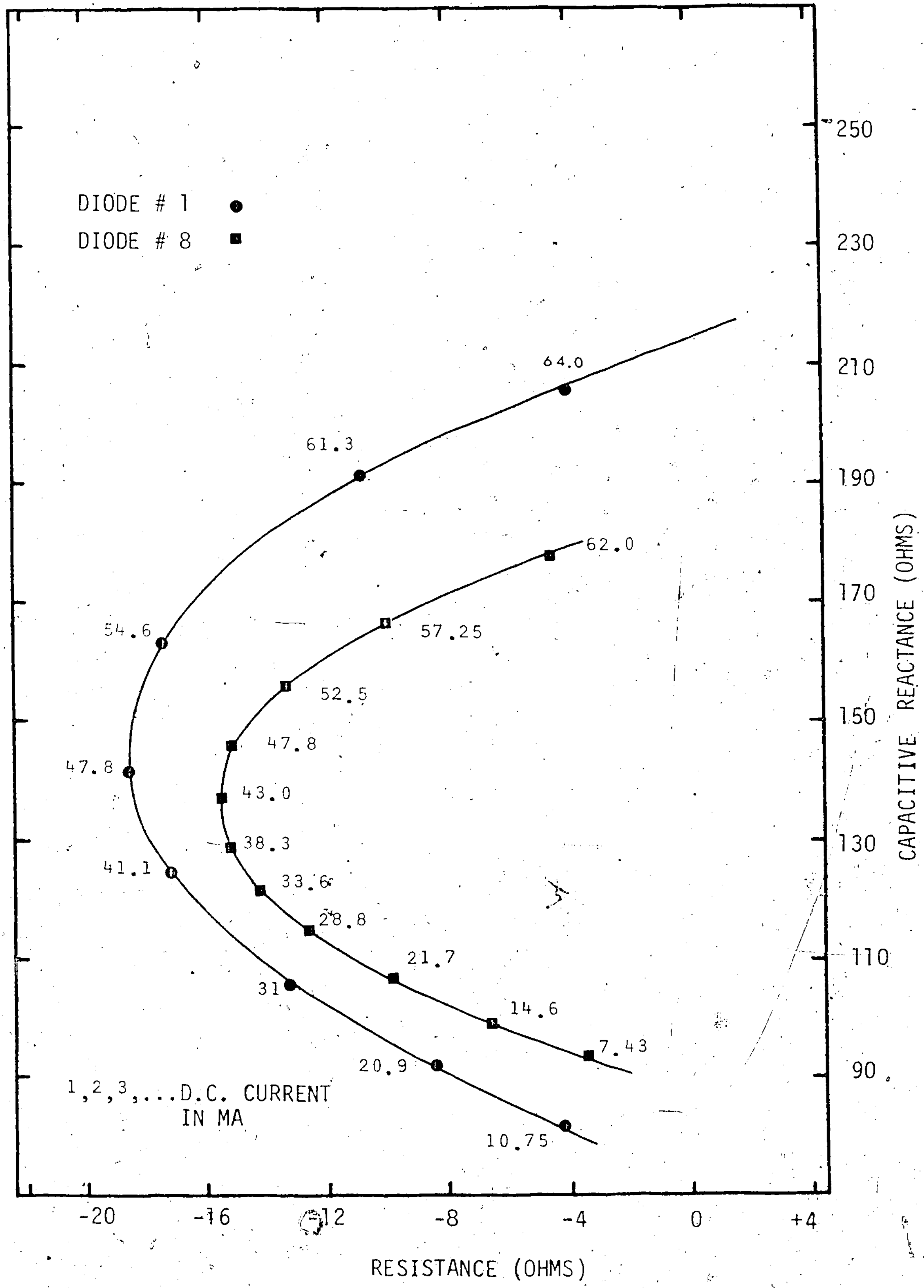

FIG. 7.4 COMPUTED STEADY-STATE VALUES OF ELECTRONIC IMPEDANCE AT 6.0 GHz AND 2 VOLTS R.F.

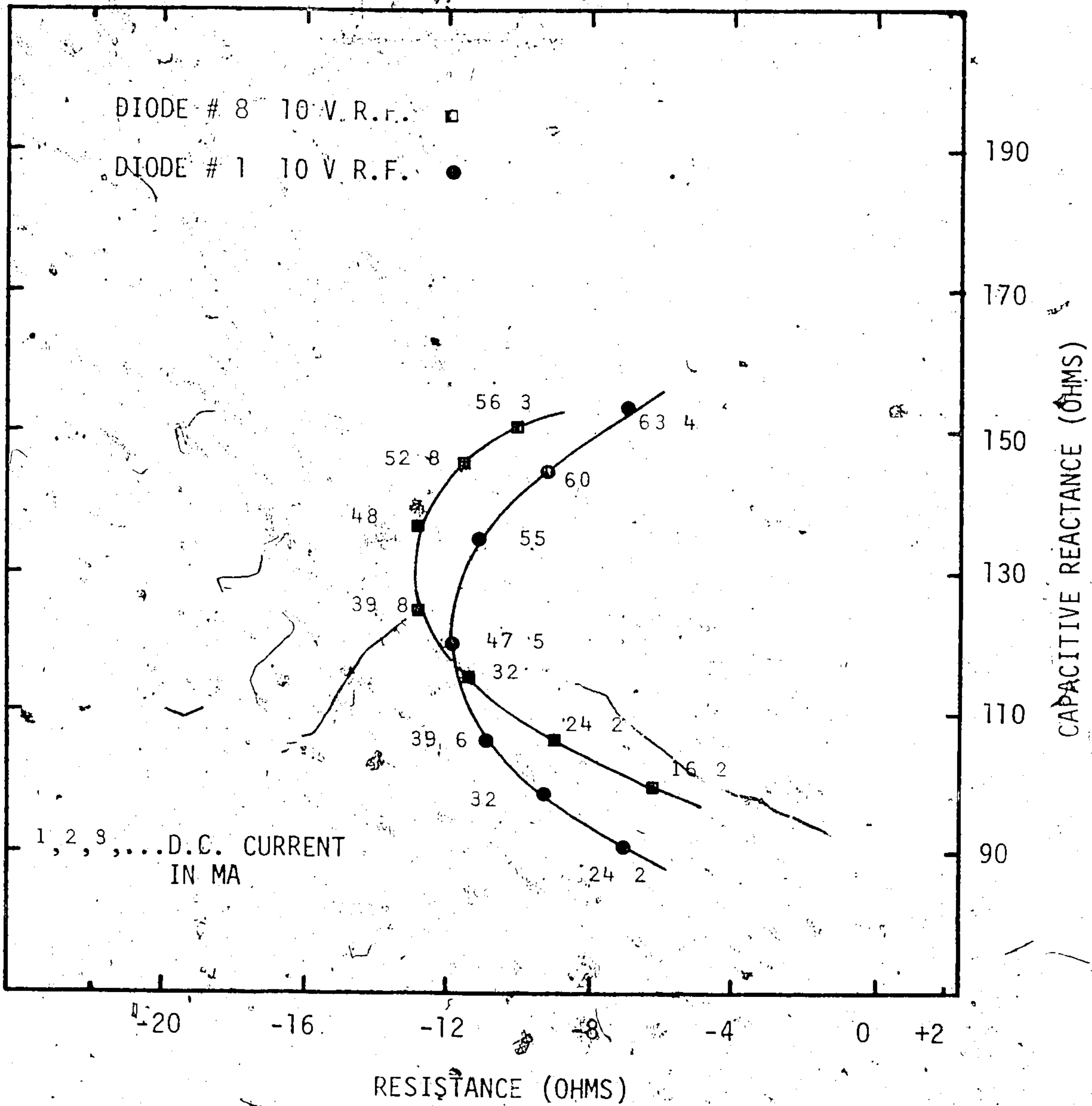

FIG. 7.5 COMPUTED STEADY-STATE VALUES OF ELECTRONIC IMPEDANCE AT 6.0 GHz AND 10 VOLTS R.F.

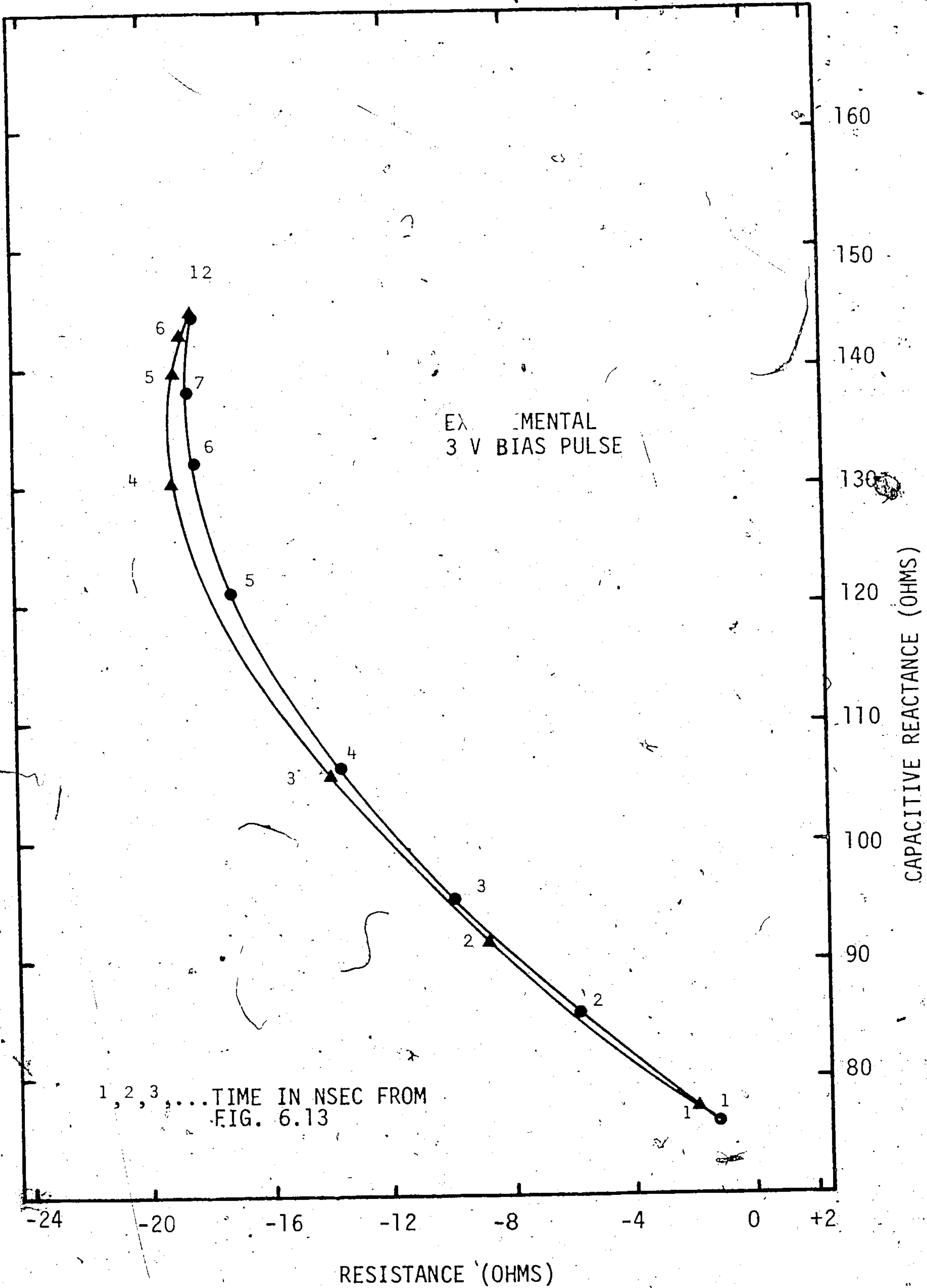

FIG. 7.6 COMPUTED VALUES OF ELECTRONIC IMPEDANCE FOR DIODE #1 AT 6.0 GHz FOR DIFFERENT BIAS VOLTAGE PULSE RISETIMES

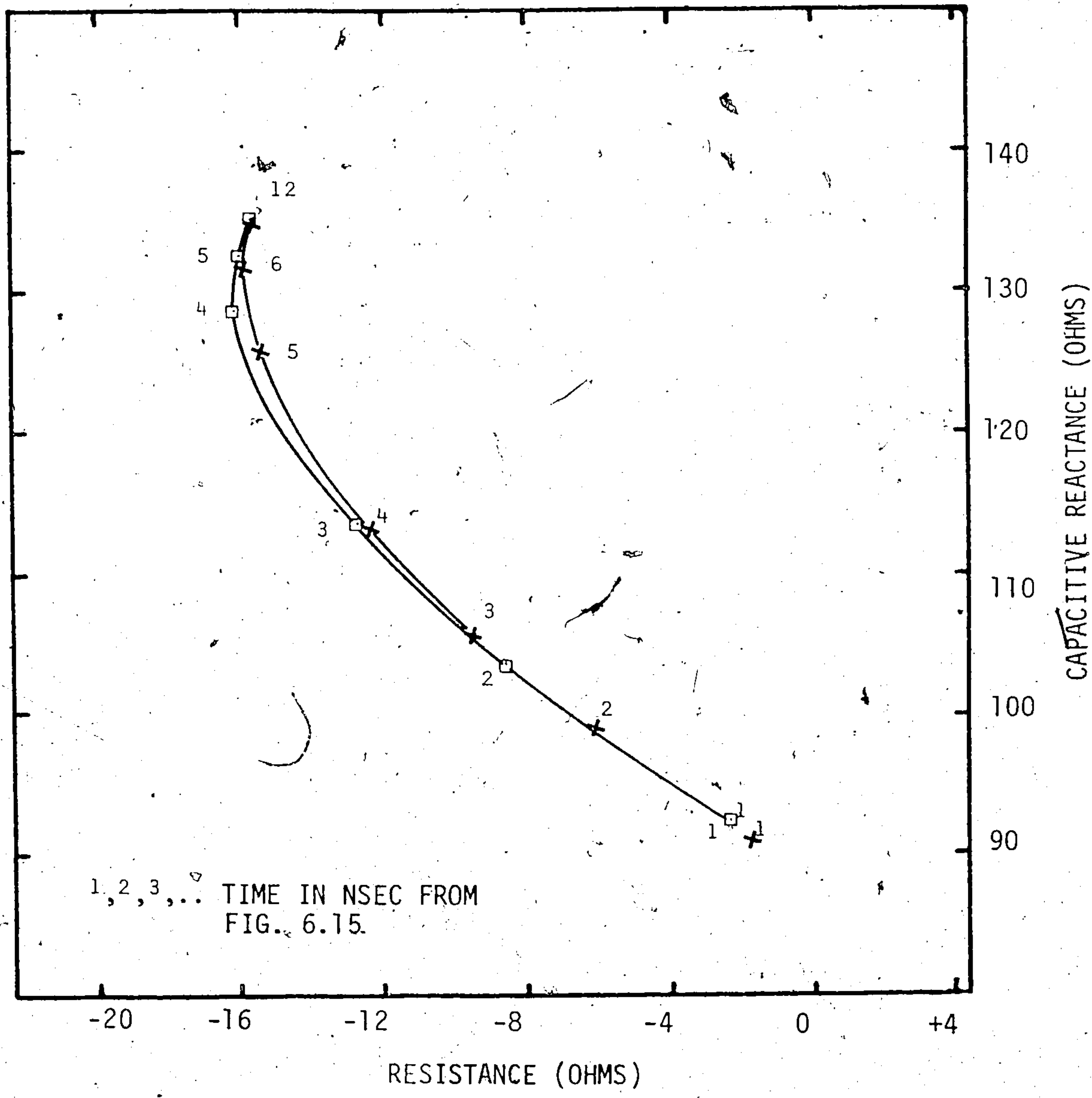

FIG. 7.7 COMPUTED VALUES OF ELECTRONIC IMPEDANCE FOR DIODE #8 AT 6.0 GHz FOR DIFFERENT BIAS VOLTAGE PULSE RISE TIMES

bias voltage pulse an increase in the magnitude of the real part of Z_e of about 10-15% can be expected during the rise time of the bias voltage pulse. This increase is not very large but may be useful in the start of oscillations in a coupled cavity.

7.4 Recovery Time from Transient to Steady-State Conditions

Overall, there are relatively small departures from the steady-state values of the electronic impedance during transient conditions. These departures occur mainly during the buildup and decay of the bias voltage pulse, with the transient behavior of Z_e during the decay, being more pronounced and of longer duration.

From the appropiate Figures and Tables 7.1 and 7.2, it is apparent that the effects of the rise times of the bias voltage pulse are somewhat different at 6.0 GHz from those at 7.8 GHz. This difference is probably due to the fact that the real part of Z_e reaches its maximum magnitude at relatively low current levels at 6.0 GHz, while at 7.8 GHz this maximum limit has not quite been reached at very high current levels. The clockwise loops at 6.0 GHz, (Figs. 6.14 and 6.17), and the counter-clockwise loop at 7.8 GHz, (Figs. 6.19 and 6.23), in the behavior of Z_e, are due to the transient values of Z_e returning to their steady-state values. At 6.0 GHz, during the transition interval of the d.c. current pulse from its rapid rise to its relatively slowly varying top, the more negative values of the real part of the transient Z_e monotonically approach their steady- state values; hence the clockwise loop. For 7.8 GHz, during the same transition of the d.c. current pulse, the transient Z_e appears to overcorrect, with the real part

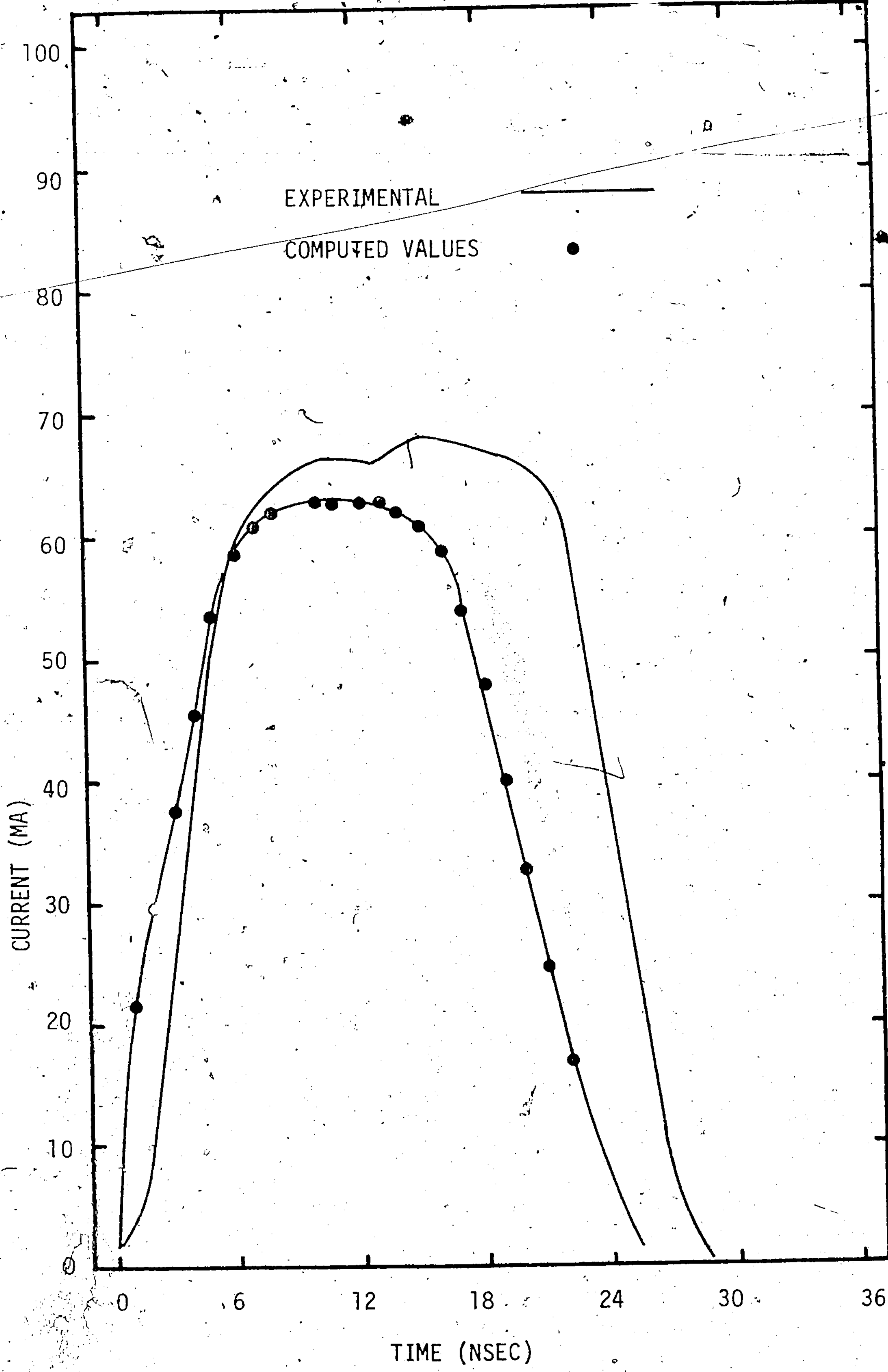

FIG. 7.8 COMPUTED CURRENT RESPONSE FOR DIODE #1 AT 6.0 GHz WITH 10 VOLTS R.F. AND 4 VOLTS EXPERIMENTAL BIAS

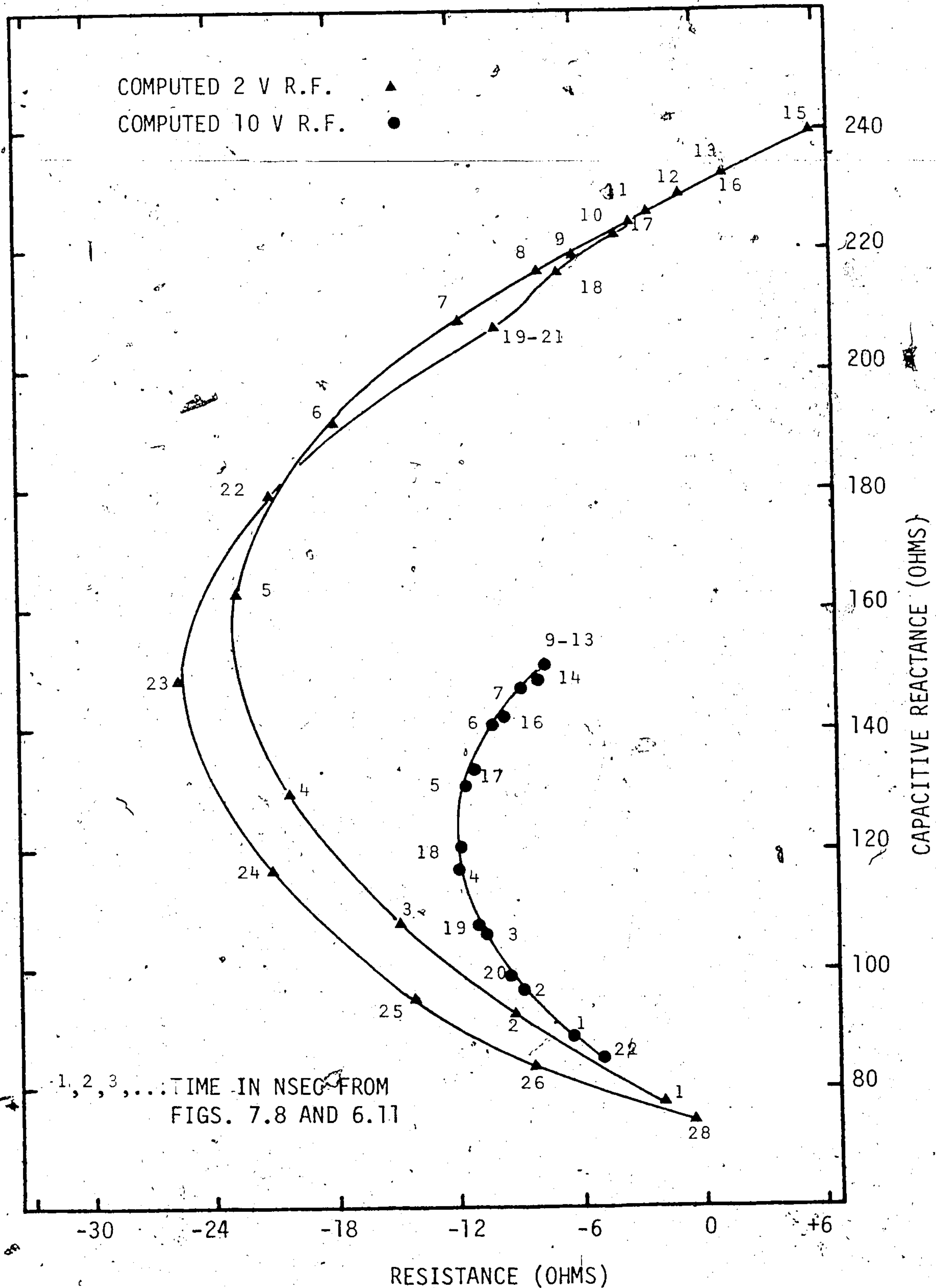

FIG. 7.9 COMPUTED VALUES OF ELECTRONIC IMPEDANCE FOR DIODE #1 AT 6.0 GHz AND 4 V EXPERIMENTAL BIAS

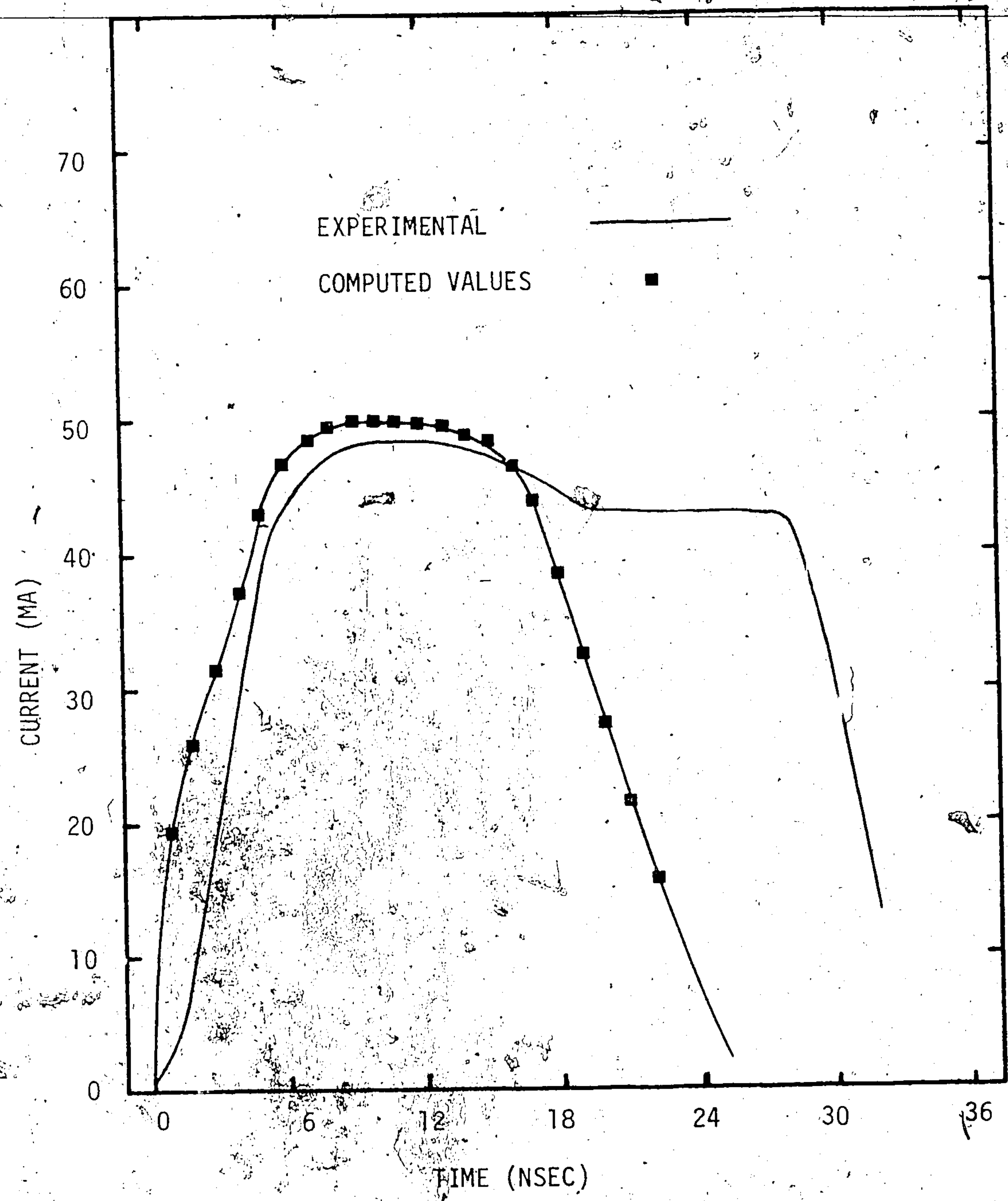

FIG. 7.10 COMPUTED CURRENT RESPONSE FOR DIODE #1 AT 6.0 GHz WITH 10 VOLTS R.F. AND 3 V EXPERIMENTAL BIAS

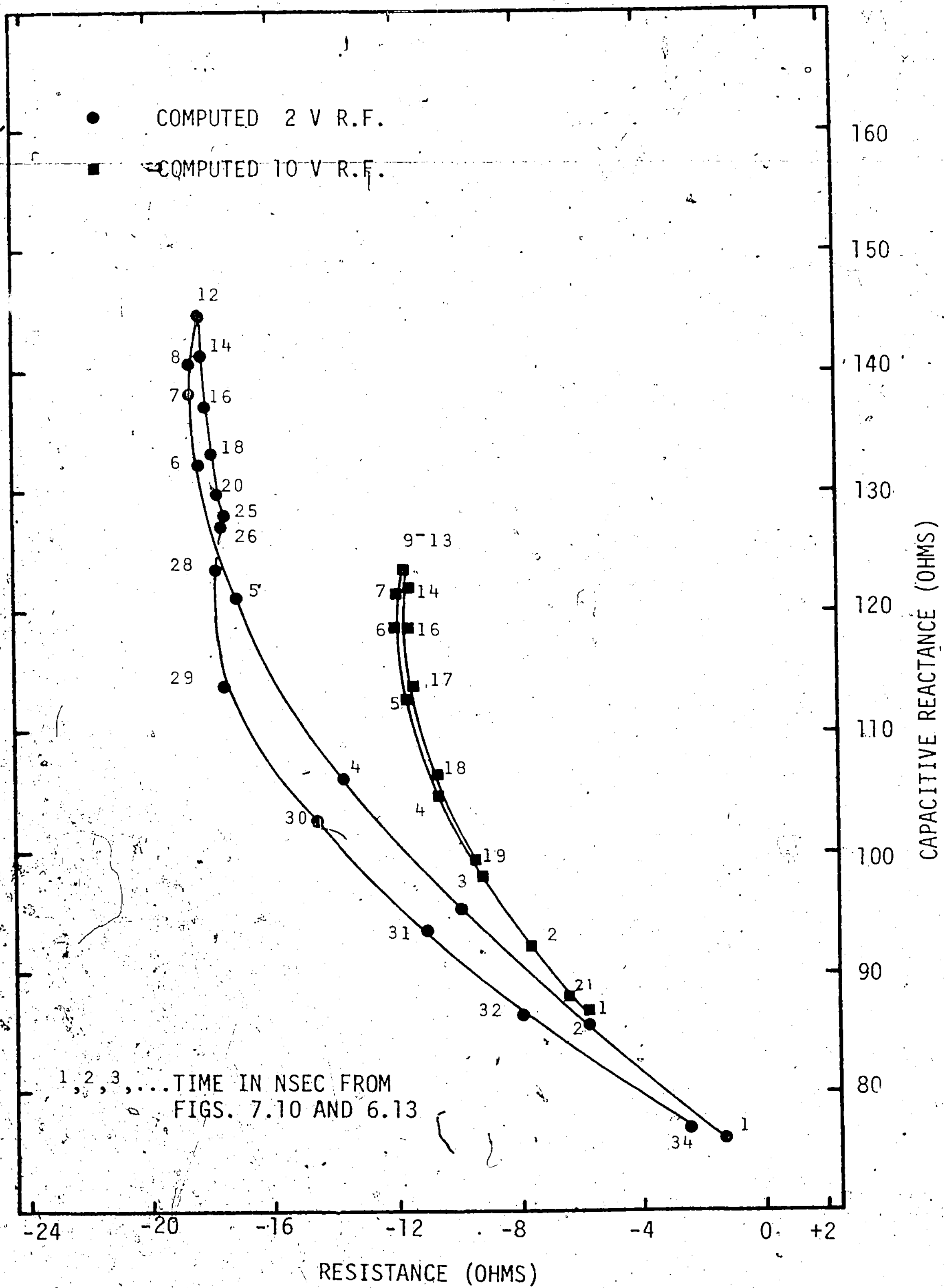

FIG. 7.11 COMPUTED VALUES OF ELECTRONIC IMPEDANCE FOR DIODE #1 AT 6.0 GHz AND 3 VOLTS EXPERIMENTAL BIAS

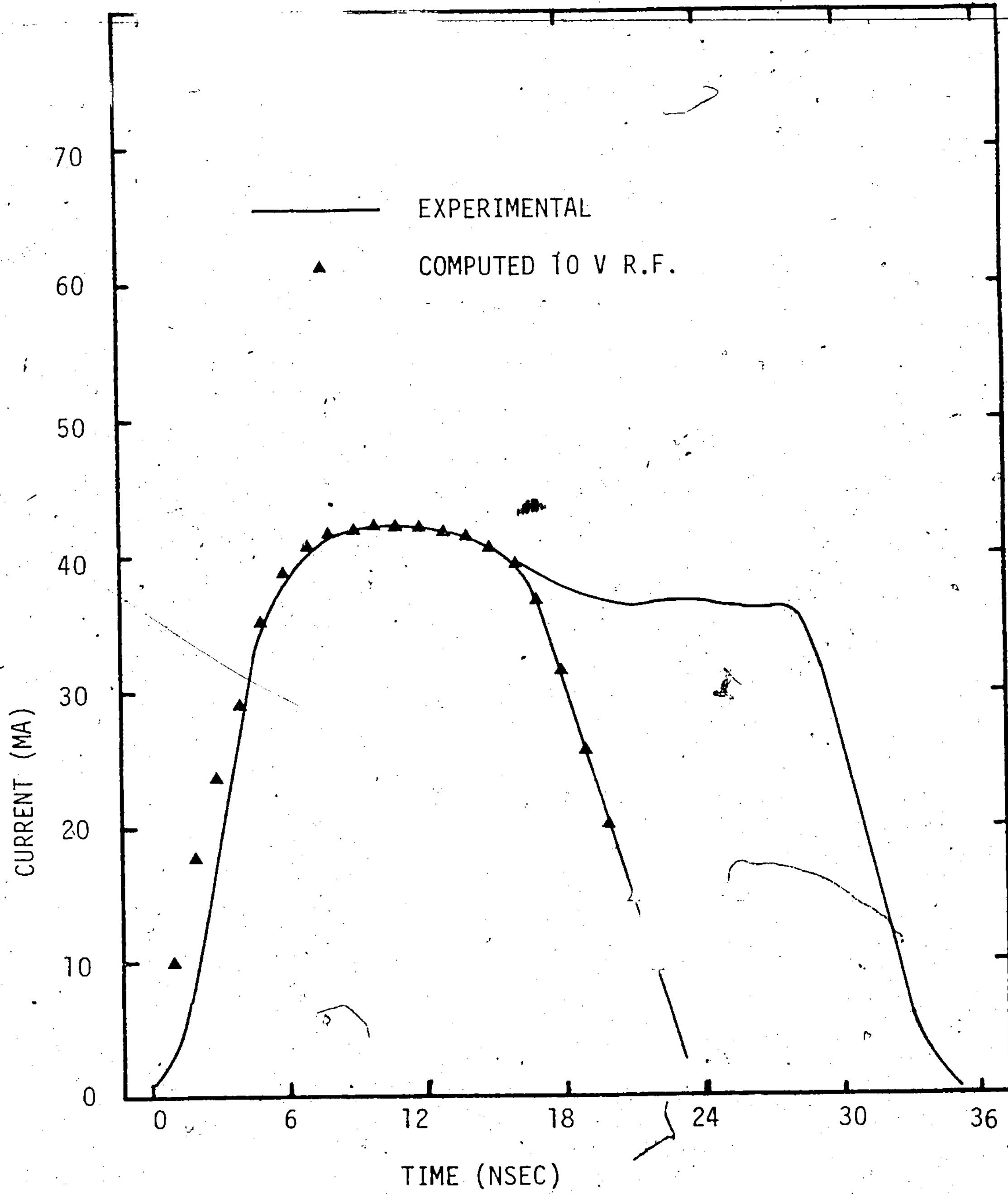

FIG. 7.12 COMPUTED CURRENT RESPONSE FOR DIODE #8 AT 6.0 GHz WITH 10 VOLTS R.F. AND 3 VOLTS EXPERIMENTAL BIAS

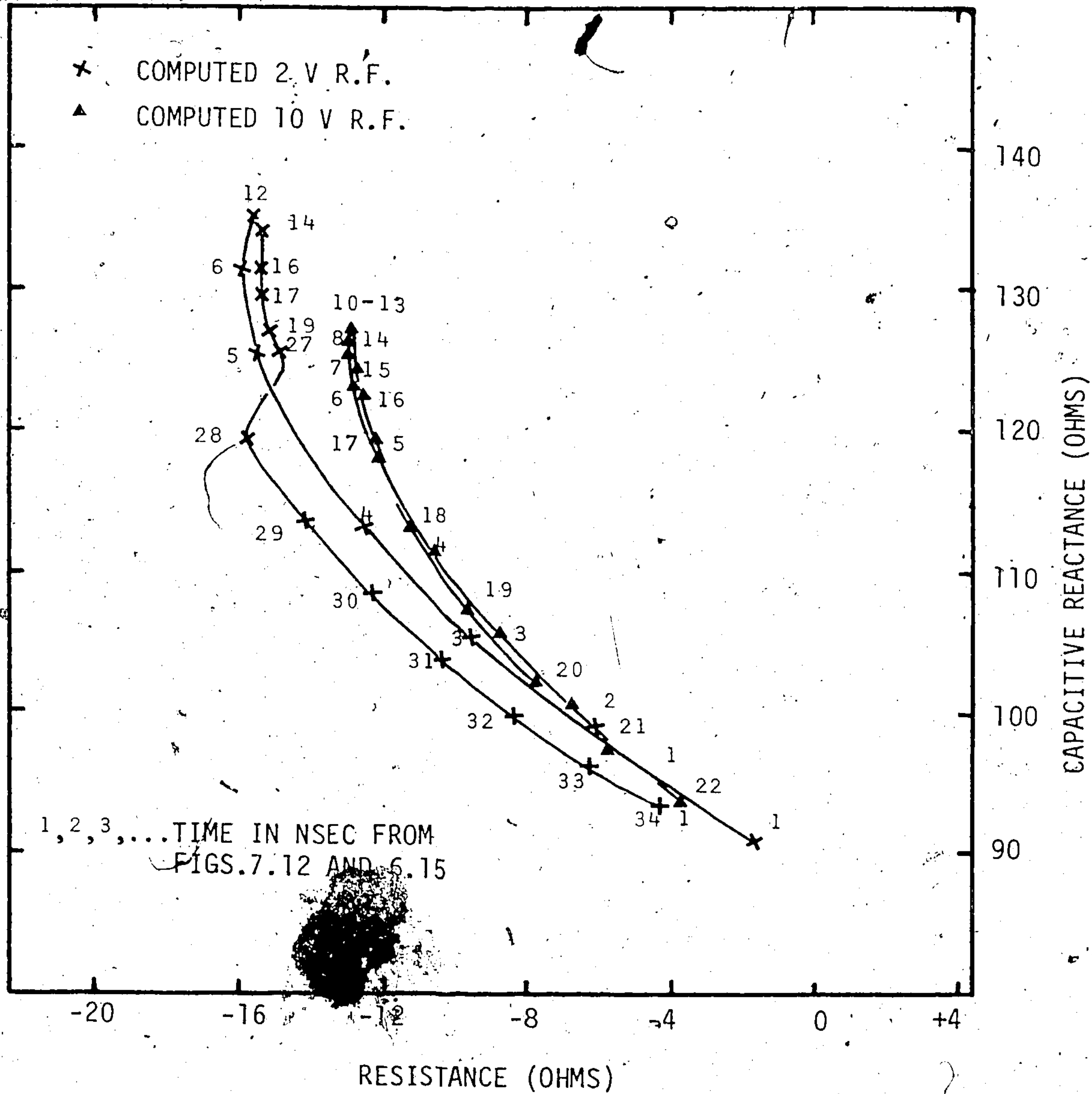

FIG. 7.13 COMPUTED VALUES OF ELECTRONIC IMPEDANCE FOR DIODE #8 AT 6.0 GHz AND 3 VOLTS EXPERIMENTAL BIAS

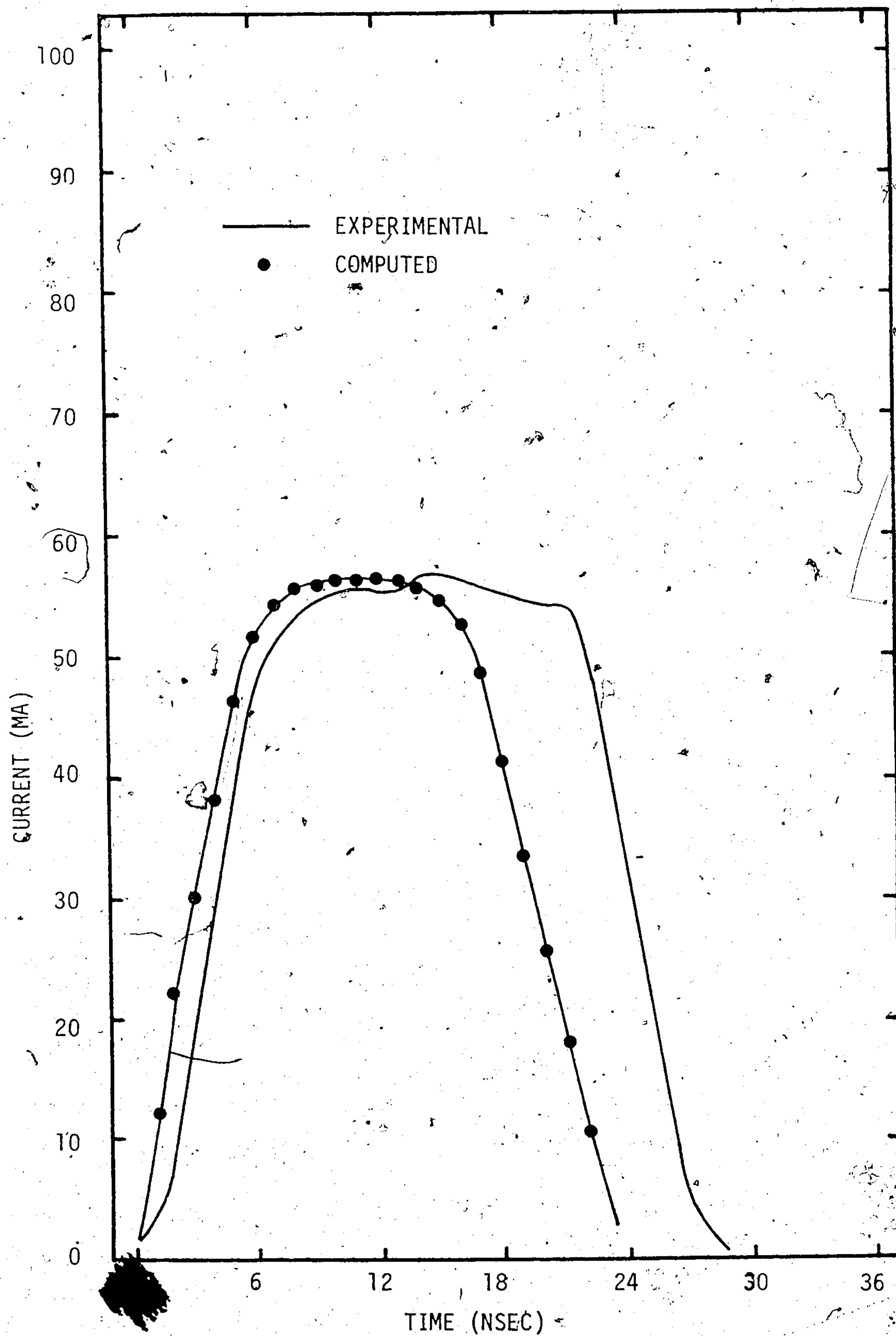

FIG. 7.14 COMPUTED CURRENT RESPONSE FOR DIODE #8 AT 6.0 GHz WITH 10 VOLTS R.F. AND 4 VOLTS EXPERIMENTAL BIAS

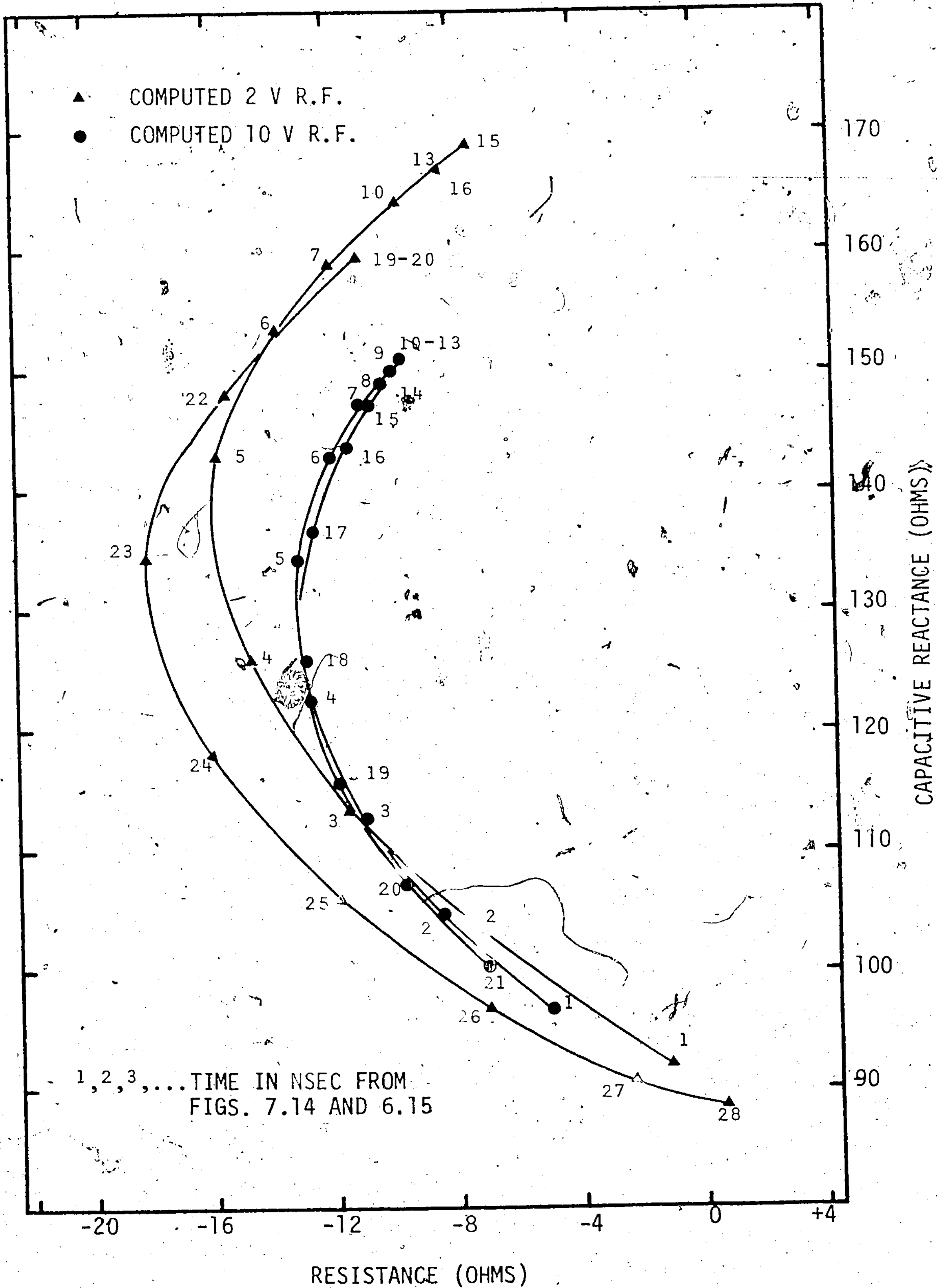

FIG. 7.15 COMPUTED VALUES OF ELECTRONIC IMPEDANCE FOR DIODE #8 AT 6.0 GHz AND 4 VOLTS EXPERIMENTAL BIAS

becoming less negative than its steady-state value and hence the counter-clockwise loop results. In both cases, the time required for the transient Z_e to settle to their steady-state values is about 5 nanoseconds.

The previous discussions have been for the case where the magnitude of the R.F. voltage has been one-or-two volts across the diode. To gain an insight into the behaviour of the electronic impedance at higher R.F. voltages, some computations were carried out using 10 volts as the magnitude of the driving R.F. voltage across the diode. These computations were restricted to 6.0 GHz as the bias levels used at this frequency give practically all the behavioural aspects of the electronic impedance for the diodes under study here. The results of these computations, for diode #1 and #8 are given in Figs. 7.8 to 7.15 inclusive. As expected, the magnitudes of Z_e calculated using ten volts R.F. are less than those using two volts R.F. However, a comparison of the transient and steady-state values of Z_e, under the influence of 10 volts R.F., shows very little difference between the two sets of computations. Therefore, a discussion of the recovery time from transient to steady-state conditions is somewhat unimportant and for practical purposes, it can be assumed that steady-state conditions prevail at all times for this higher magnitude of R.F. voltage.

7.5 Summary

Generally, there was found to be a close comparison in the behavioural aspects of the computed and measured values of the electronic impedance under transient conditions. Comparisons between the computations

and the measurements were carried out on the basis of similar d.c. current responses for the simulated and actual bias voltage pulses used. This, plus the short-duration bias pulses, ensured that the effects of changes in the temperature of the semiconductor junction could be ignored.

The main discrepancy between the computed and the measured results appears in the relative magnitude of Z_e. An important cause of this discrepancy is due to the influence of the second harmonic component of the R.F. voltage impressed upon the diode. The ratio of the magnitude of the second harmonic to the fundamental in the R.F. current waveform of the diode, increases with increasing d.c. current levels. A second harmonic component in the R.F. voltage is developed from this second harmonic in the R.F. current and as the measuring system will not absorb this second harmonic frequency, it is likely that a significant second harmonic component is present in the R.F. voltage in the diode holder. A detailed evaluation of this second harmonic effect was not carried out in this study.

In general, the significant differences between transient and steady-state values of the electronic impedance, occur during the initial buildup and decay of the bias voltage pulse across the diode. These differences are most prominent at the lower magnitudes of R.F. voltage. At R.F. voltages of one or two volts, the transient values of the electronic impedance can have real parts that are about 10-15% more negative than their steady-state counterparts. Under these conditions, there appears to be an optimum rise time of 4 to 5 nano-

seconds for the bias voltage pulse, with a recovery time of about 5 nanoseconds needed for the transient values of the electronic impedance to return to their steady-state values. At magnitudes of R [illegible] oltage in the range of 10 volts, there is negligible difference between the transient and steady-state values of the electronic impedance.

CHAPTER VIII

DISCUSSION AND CONCLUSIONS

This study has investigated the behaviour of the electronic impedance under transient conditions for a type of Impatt diode. The analysis and results are applicable to Read diodes and one-sided abrupt p-n junction diodes. In the course of this work, several aspects of the operation of these diodes have been investigated, with the following results:

— An improved analytical model of the diode, which applies to both steady-state and transient operating conditions, has been formulated and evaluated.

— A model for the transient heat flow in the diode's semiconductor junction has been developed which has been verified by experimental results and incorporated into a computer model of the diode.

— A method for the measurement of the diode microwave impedance has been developed which allows the measurements to be conducted under steady-state or transient conditions.

All of these aspects have been incorporated into a computer model of the Impatt diode which has been programmed on a large digital computer.

The analytical equations developed here describe the behaviour of the Impatt diode under d.c., small-signal and large-signal conditions for both steady-state and transient operation. These equations are

relatively simple in form and make use of a minimum number of approximations, while still maintaining an efficient computer solution. The equations are sufficiently versatile to describe either p^+n or n^+p one-sided abrupt junctions in a variety of semiconductor materials. The structure of the equations is such that the effects of the several pertinent parameters are readily apparent, thus facilitating the simulation of the experimentally obtained results with the computer model. This leads to a more rapid understanding of the problem under study.

The describing equations and the computer model for the Impatt diode have been shown to be valid from comparisons with other published works and from experimental results obtained for the transient behaviour of the electronic impedance of the diode. These equations have been used to accurately model the steady-state and transient thermal response of the p-n junction along with the d.c. and a.c. operation of the diode under steady-state and transient operating conditions. An empirical representation for the current profiles in the avalanche region of the diode, under dynamic operating conditions, has allowed the equations to include the individual ionization rates and scattering limited drift velocities for the carriers and also has allowed the inclusion of the space charge term for the avalanche region.

The effects of injecting contacts and the spreading of the avalanche and drift regions under conditions of high R.F. signal levels have not been taken into account. Similarly, the associated effects of non-scattering-limited drift velocities, unswept epitaxial layer

and dispersion of the pulse of carriers in the drift region have been omitted from this analysis. For the model of the Impatt diode under study here, all of these factors are of somewhat secondary importance, except for the effects of injecting contacts, which may influence the degree of correspondence between the magnitude of the computed and measured values of the diode electronic impedance.

In studies concerning the transient impedance of Impatt diodes for applications in oscillators or amplifiers, the behaviour of the junction temperature as a function of the duration of the bias voltage pulse is important. Both the steady-state and transient thermal properties of a type of Impatt diode were investigated. A study of the time dependence of the junction temperature was carried out over an ambient temperature range of 20°C to 150°C and over time interval of from 5 to 200 nanoseconds after the onset of the bias voltage pulse. These studies have related the experimental results to a theoretical model for heat flow in a semiconductor junction. Good agreement has been obtained between the two types of results.

A theoretical model of the time dependence of the junction temperature was arrived at by considering a one-dimensional analysis of a semi-infinite semiconductor wit' a region of heat generation at one end. This model is sufficient for pulsed operation of the diode with pulse widths and repetition rates such that the high thermal resistance of the bonding wire does not influence the heat flow in the substrate. Incorporating the time dependence of the junction temperature into the computer model, for the Impatt diode, was readily carried out by adding a time varying term to the simulated d.c. bias voltage pulse.

This computer model produced very good agreement with the experimental results.

It has been found that the relative change in junction temperature during the application of the bias voltage pulse, was essentially the same for the entire range of heat sink temperatures used here. Thus, the thermal behaviour of the Impatt diode will remain essentially the same for average junction temperatures from 20°C to 150°C. Consequently, the junction temperature does not have to closely approach the heat sink temperature between each bias pulse, as only the average junction temperature is important and higher pulse repetition rates can be used without altering the transient thermal response of the diode.

The junction temperature mainly alters the d.c. current level in the diode, therefore, as long as the computed and experimental results are compared on the basis of similar d.c. currents in the diode, the effects of junction temperature changes on this comparison are minimized. If the bias voltage pulses are of short duration (around 40 nanoseconds), the effects of junction temperature changes are significantly reduced and may even be able to be ignored in certain circumstances.

A method has been developed for impedance measurements under transient conditions. In this method, the reinsertion of the R.F. Carrier allows the measurement of the complex reflection coefficient as a function of time. This Carrier Reinsertion Method is suitable ~~for either steady-state or transient impedance measurements. Under~~

transient conditions the response time of the measuring system was found to be as low as 5 nanoseconds utilizing standard, commercially available, coaxial and waveguide components. This response time can be further reduced by modifying the manner in which the bias voltage pulses are applied to the packaged diode. The accuracy of this measuring system should be at least equivalent to that of conventional VSWR techniques used for steady-state impedance measurements, although a detailed investigation of the relative accuracy was not carried out. Overall, the Carrier Reinsertion Method appears to have good potential in the measurement of microwave impedances that are a function of time.

It has been found that the significant differences between transient and steady-state values of the Impatt diode electronic impedance (Z_e), are of relatively short duration and are confined to the initial buildup and decay of the bias voltage pulses applied to the diode. These differences are most prominent at the lower R.F. voltages and are largely confined to the real part of Z_e, with the imaginary part of Z_e being relatively unaffected. At R.F. voltages of one or two volts, the transient values of the real part of Z_e can be about 15% more negative than their steady-state counterparts. Under these conditions, there appeared to be an optimum rise time of 4 to 5 nanoseconds for the bias voltage pulse across the diode, with a recovery time of about 5 nanoseconds needed for the transient values of Z_e to return to their steady-state values. At the higher R.F. voltages, such as 10 volts, there appeared to be a negligible difference between the

transient and steady-state values of Z_e.

These variations in the real part of Z_e are of significance when the Impatt diode is employed in R.F. oscillators. By utilizing fast rise time bias voltage pulses, the initial growth of oscillations in a coupled cavity will be enhanced by the more negative real part of Z_e. Further, it appears that this enhancement is readily attainable, as rise times of the bias voltage pulse across the diode of about 4 to 5 nanoseconds, can be obtained with commonly available microwave circuit components. The relatively short duration of the transient effects ensures that the steady-state values of Z_e can be used for most design purposes. In self-deviating Impatt oscillators, used in frequency modulated carrier systems, the information is placed on the carrier by modulating the bias supply of the Impatt diode. When pulse code modulation is employed some additional amplitude distortion may be introduced due to the transient behaviour of the real part of Z_e. However, the magnitude of the frequency deviation will not be affected by the transient conditions.

An interesting result of this investigation of transient conditions on the electronic impedance of Impatt diodes is that the real part of Z_e may become positive under certain conditions of bias voltage and diode design. It appears, for Impatt diodes which have a drift region transit time that is less then 1/5 the period of the R.F. frequency of operation, that the real part of Z_e will become positive for moderate, pulsed, d.c. current levels. Under these conditions, the maximum negative value of the real part of Z_e is reached for

relatively low d.c. current levels for pulsed operation. When the R.F. frequency is increased such that the drift region transit time is about 1/4 of the R.F. period, the maximum negative value of the real part of Z_e is not reached until relatively high levels of pulsed d.c. current are applied.

This "peaking" characteristic of the real part of Z_e, with increasing d.c. current levels, may be used to advantage in self-deviating Impatt oscillators. When the bias circuit of the Impatt is modulated, the R.F. output of the oscillator varies in frequency and magnitude due to the changes in the imaginary and real parts, respectively, of the diode Z_e. The magnitude variations in the R.F. are undesirable and can be minimized by biasing the Impatt diode such that the average value of the real part of Z_e is at its peak or maximum negative value. This minimizes the variations in the real part of Z_e and maximizes the variations in the imaginary part of Z_e.

This peaking of the real part of the Impatt diode's Z_e is detrimental to the operation of R.F. amplifiers and pulsed R.F. oscillators. As the magnitude of the R.F. voltage across the diode increases, less d.c. bias voltage is required for a given level of d.c. current. In large-signal amplifiers, the high magnitude of R.F. signals may drive the real part of the diode's Z_e past its maximum negative value, which will result in less gain and may further complicate the associated compensation circuitry. For Impatt oscillators that provide pulsed R.F., this peaking effect of the real part of Z_e will place limitations on the permissible magnitudes of d.c. bias voltage and the

resulting R.F. signal levels.

The overall effect of this peaking of the real part of the Impatt diode's electronic impedance will be to place more stringent limitations on the design of the diode for its specific task, as it is the width of the drift region which determines the lower frequency and level of d.c. bias current for which the peaking takes place.

During the course of this work, certain aspects of the study arose which merit further investigation: One important topic is the influence of the second harmonic of the R.F. voltage across the diode. This second harmonic effect limits the validity of the experimental results to those obtained with low values of the fundamental R.F. voltage.

Another topic that warrants further investigation is the effect of injecting contacts. It has been shown that injecting contacts can influence the comparison of computed and measured results of the diode's electronic impedance but, the extent of this influence has not been established.

The results of the suggested investigations, combined with those of previously published work and the results reported here, should enable an analytical model of the Impatt diode to be constructed which will produce much closer correspondence between calculated and measured values of the electronic impedance.

REFERENCES

1. W.E. Wilson, "Pulsed LSA and TRAPATT Sources for Microwave Systems", Microwave Journal, Vol. 14, pp. 33-41, August, 1971.

2. V.J. Higgins, J.J. Baranowski, "The Utility and Performance of Avalanche Transit Time Diodes and Transferred Electron Oscillators in Microwave Systems", Microwave Journal, Vol. 13, pp. 37-42E, July, 1970.

3. S.M. Sze, "Microwave Avalanche Diodes", Proc. IEEE, Vol. 59, pp. 1140-1154, August, 1971.

4. W.T. Read, "A Proposed High Frequency Negative Resistance Diode", Bell Sys. Tech. J., Vol. 37, pp. 401-446, March, 1958.

5. R.L. Johnston, D.L. Scharfetter, D.J. Bartelink, "High Efficiency Oscillations in Germanium Avalanche Diodes Below the Transit Time Frequency", Proc. IEEE (lett.), Vol. 56, pp. 1611-1613, September, 1968.

6. B.C. DeLoach Jr., "Modes of Avalanche Diodes and their Associated Circuits", IEEE J. Solid-State Circuits, Vol. SC-4, pp. 376-384, December, 1969.

7. E.F. Scherer, "Large-Signal Operation of Avalanche Diode Amplifiers", IEEE Trans. Microwave Theory Tech., Vol. MTT-18, pp. 921-932, November, 1970.

8. Y. Takayama, "Power Amplification with Impatt Diodes in Stable and Injection Locked Modes", IEEE Trans. Microwave Theory Tech., Vol. MTT-20, pp. 266-272, April, 1972.

9. T.P. Lee, R.D. Standley, "Frequency Modulation of a Millimeter-Wave Impatt Diode Oscillator and Related Harmonic Generation Effects", Bell Sys. Tech. J. Vol. 48, pp. 143-161, January, 1969.

10. A.M. Rybczynski, "Digital Bias Modulation of Impatt Diode Oscillators", M.Sc. Thesis, Department of Electrical Engineering, University of Alberta, Edmonton, Canada, 1972.

11. R.H. Haitz, "Nonuniform Thermal Conductance in Avalanche Microwave Oscillators", IEEE Trans. ELectron Devices, Vol. ED-15, pp. 350-361, June, 1968.

12. G.I. Haddad, P.T. Greiling, W.E. Schroeder, "Basic Principles and Properties of Avalanche Transit Time Devices", IEEE Trans. Microwave Theory Tech., Vol. MTT-18, pp. 752-772, November, 1970.

13. S.M. Sze, R.M. Ryder, "Microwave Avalanche Diodes", Proc. IEEE, Vol. 59, pp. 1140-1154, August, 1971.

14. S.M. Sze, Physics of Semiconductor Devices, Chapters 2-3-5, John Wiley and Sons, Inc., New York, 1959.

15. R.K. Willardson and A.C. Beer, Semiconductors and Semimetals, Vol. 7, Chapter 7, Academic Press, New York.

16. J.L. Moll, Physics of Semiconductors, Chapter 4, McGraw-Hill, Inc., New York, 1964.

17. A. Javed, "Computer Aided Study of the Electrical Behaviour of Microwave Varactors", Ph.D. Thesis, Department of Electrical Engineering, University of Alberta, Edmonton, Canada, 1970.

18. W. Schockley, Electron and Holes in Semiconductors, Van Nostrand, New York, 1950.

19. E.J. Ryder, "Mobility of Holes and Electrons in High Electric Fields", Phys. Rev., Vol. 90, pp. 766-769, June, 1953.

20. A.G. Chenoweth, K.G. McKay, "Photon Emission from Avalanche Breakdown in Silicon", Phys. Rev. Vol. 102, pp. 369-376, April, 1956.

21. W.G. Oldham, R.R. Samuelson, P. Antognetti, "Triggering Phenomenon in Avalanche Diodes", IEEE Trans. Electron Devices, Vol. ED-18, pp. 1056-1060, September, 1972.

22. W.E. Schroeder, G.I. Haddad, "Avalanche Region Width in Various Structures of Impatt Diodes", Proc. IEEE, Vol. 59, pp. 1245-1248, August, 1971.

23. G. Gibbons, S.M. Sze, "Avalanche Breakdown in Read Diodes and PIN Diodes", Solid-State Electronics, Vol. 11, pp. 225-232, February, 1968.

24. D.L. Scharfetter, H.K. Gummel, "Large Signal Analysis of a Read Diode Oscillator", IEEE Trans. Electron Devices, Vol. ED-16, pp. 64-77, January, 1969.

25. P.T. Greiling, G.I. Haddad, "Large Signal Equivalent Circuits for Avalanche Transit Time Devices", IEEE Trans. Microwave Theory Tech., Vol. MTT-18, pp. 842-853, November, 1970.

26. H.K. Gummel, D.L. Scharfetter, "Avalanche Region of Impatt Diodes", Bell Sys. Tech. J., Vol. 45, pp. 1797-1827, December, 1966.

27. C.B. Norris, J.F. Gibbons, "Measurement of High Field Carrier Drift Velocities in Silicon by a Time of Flight Method", IEEE Trans. Electron Devices, Vol. ED-14, pp. 38-43, January, 1967.

28. M. Classen , W. Harth, "Analog Computer Model for an Avalanche-Diode Oscillator", Electron Lett., Vol. 5, pp. 218, 15 May, 1969.

29. A.S. Jackson, Analog Computation, McGraw-Hill, New York, 1960.

30. System/360 Scientific Subroutine Package (360 A-CM-03) Version III, Programers Manual (H20-0205-3).

31. S.D. Conte, Elementary Numerical Analysis, Chapter 6, McGraw-Hill, New York, 1965.

32. J. Nigrin, "Double Pulse Measurements of Avalanching p-n Junctions Submicrosecond Transient Thermal Response", Review of Scientific Instruments, Vol. 43, pp. 264-268, February, 1972.

33. E. Mosekilde, P.A. Lebwohl, D.G. Carlson, "Transient Heat Flow from an Epitaxial Layer into the Substrate", Proc. IEEE., Vol. 59 , pp. 1030-1032, June, 1971.

34. R.H. Haitz, "Model for the Electrical Behaviour of a Microplasma", J. Appl. Phys., Vol. 35, pp. 1370-1376, May, 1964.

35. H.S. Carslaw, J.C. Jaeger, Conduction of Heat in Solids, Second Edition, Oxford University Press, London, 1959.

36. ITT, Reference Data for Radio Engineers, Howard W. Sams and Co., Inc., Indianapolis/Kansas City/New York, 1969.

37. W.J. Getsinger, "The Packaged and Mounted Diode as a Microwave Circuit", IEEE Trans. Microwave Theory Tech., Vol. MTT-14, pp. 58-69, February, 1966.

38. B.C. De Loach, "A New Microwave Measurement Technique to Characterize Diodes and an 800 GHz cutoff Frequency Varactor at Zero Volts Bias", IEEE Trans. Microwave Theory Tech., Vol. MTT-12, pp. 15-20, January, 1964.

39. C.N. Dunn, J.E. Dalley, "Computer Aided Small-Signal Characterization of Impatt Diodes", IEEE Trans. Microwave Theory Tech., Vol. MTT-17, pp. 691-695, September, 1969.

40. J.W. Gewartoswki, J.E. Morris, "Active Impatt Diode Parameters Obtained by Computer Reduction of Experimental Data", IEEE Trans. Microwave Theory Tech., Vol. MTT-18, pp. 157-161, March, 1970.

41. B.B. Van Iperen, H.J. Tjassens, "Novel and Accurate Methods for Measuring Small-Signal and Large-Signal Impedances of Impatt Diodes", Philips Res. Rpts., Vol. 27, pp. 38-75, 1972.

42. R.L. Johnston, D.F. Ciccolella, B.C. De Loach, "The Transient Microwave Impedance of PIN Diodes", International Solid State Circuits Conference, University of Pennsylvania, pp. 102-103, February 19, 1965.

43. ———, "Frequency Multiplication With Step Recovery Diodes", Hewlett Packard Application Note #908, 15 February, 1966.

44. J.M. Roe, F.J. Rosenbaum, "Characterization of Packaged Microwave Diodes in Reduced Height Waveguide", IEEE Trans. Microwave Theory Tech., Vol. MTT-18, pp. 638-642, September, 1970.

45. R.P. Owens, D. Cawsey, "Microwave Equivalent Circuit Parameters of Gunn-Effect-Device Packages", IEEE Trans. Microwave Theory Tech., Vol. MTT-18, pp. 790-798, November, 1970.

46. J.J. Goedbloed, "Determination of the Intrinsic Response Time of Semiconductor Avalanches from Microwave Measurements", Solid State Electronics, Vol. 15, pp. 635-647, June, 1972.

47. T. Misawa, "Negative Resistance in P-N Junctions Under Avalanche Breakdown Conditions, Pts. I and II", IEEE Trans. Electron Devices, Vol. ED-13, pp. 137-151, January, 1966.

48. J.A.C. Stewart, D.R. Conn, H.R. Mitchell, "State Space Analysis of General Impatt Diode Small Signal Lumped Models", IEEE Trans. Microwave Theory Tech., Vol. MTT-18, pp. 835-842, November, 1970.

49. D.R. Decker, C.N. Dunn, H.B. Frost, "The Effect of Injecting Contacts on Avalanche Diode Performance", IEEE Trans. Electron Devices, Vol. ED-18, pp. 141-147, March, 1971.

50. W.E. Schroeder, G.I. Haddad, "Effect of Harmonic and Subharmonic Signals on Avalance-Diode Oscillator Performance", IEEE Trans. Microwave Theory Tech., Vol. MTT-18, June, 1970.

APPENDIX A

FOURIER ANALYSIS AND COMPLEX IMPEDANCE

A series of the form

$$f(x) = \frac{1}{2} A_o + \sum_{n=1}^{\infty} [A_n \cos(nx) + B_n \sin(nx)] \quad (1)$$

is called a trigonometric series. It is called a Fourier series if all the coefficients A_n, B_n can be obtained in the following manner

$$A_n = \frac{1}{\pi} \int_o^{2\pi} f(x) \cos(nx)\, dx \qquad n=o,1,2,... \quad (2)$$

$$B_n = \frac{1}{\pi} \int_o^{2\pi} f(x) \sin(nx)\, dx \qquad n=1,2,3,... \quad (3)$$

By using a change of variables

$$x = \frac{\pi}{L} t$$

the series is now written in a more convenient form as

$$f(t) = A_o/2 + \sum_{n=1}^{\infty} [A_n \cos (\frac{n\pi}{L} t) + B_n \sin (\frac{n\pi}{L} t)] \quad (4)$$

where the coefficients are given by

$$A_n = \frac{1}{L} \int_o^{2L} f(t) \cos (\frac{n\pi}{L} t) dx \qquad n=o,1,2,... \quad (5)$$

$$B_n = \frac{1}{L} \int_o^{2L} f(t) \sin (\frac{n\pi}{L} t) dx \qquad n=1,2,3,... \quad (6)$$

and 2L is the period over which the integration takes place.

From Section 4.2 Eq. (18), the total current in the external circuit of the Impatt diode can be written as

$$\overline{I}_T(\tau) = \overline{I}_{ex}(\tau) + \overline{C}_d \frac{\partial V(\tau)}{\partial \tau} \tag{7}$$

The external conduction current is a well behaved function and both integrable and differentiable over any one period. Therefore, it may be assumed that this function has a Fourier series. Similarly, the R.F. voltage may be assumed to have a Fourier series also.

To arrive at the electronic impedance of the semiconductor diode, the complex ratio of the fundamental components of Eq. (7) and $V(\tau)$ must be taken. The fundamental component of current may be obtained by Fourier analysis of Eq. (7) and written as

$$I_T(\tau)_f = A \cos\left(\frac{\pi}{L} t\right) + B \sin\left(\frac{\pi}{L} t\right) \tag{8}$$

This equation is now rewritten in a more convenient form by using Euler's formula

$$\exp\left(j \frac{\pi}{L} \tau\right) = \cos\left(\frac{\pi}{L} t\right) + j \sin\left(\frac{\pi}{L} t\right) \tag{9}$$

After some rewriting, Eq. (8) becomes

$$\overline{I}_T(\tau)_f = \sqrt{A^2 + B^2} \sin\left(\frac{\pi}{L} \tau + \sigma\right) \tag{10}$$

where

$$\sigma = \tan^{-1} (A/B) \tag{11}$$

Similarly, the fundamental component of the R.F. voltage may be written as

$$V(\tau)_f = \sqrt{C^2 + D^2} \quad \sin\left(\frac{\pi}{L}\tau + \phi \right) \tag{12}$$

where

$$\phi = \tan^{-1} (C/D) \tag{13}$$

Letting the electronic impedance (z_e) be defined as

$$z_e = V(\tau)_f/\overline{I_T}(\tau)_f \tag{14}$$

then, upon using the relations given in Eqs. (10) to (13), the real and imaginary parts of z_e are,

$$\text{Real } (z_e) = \left| V(\tau)_f/\overline{I_T}(\tau)f \right| \cos(\phi-\sigma) \tag{15}$$

$$\text{Imaginary } (z_e) = \left| V(\tau)_f/\overline{I_T}(\tau)f \right| \sin(\phi-\sigma) \tag{16}$$

In the computer program, Fourier analysis was carried out using over one hundred points for each period analyzed. As a check on the accuracy of the results, the waveform for the R.F. voltage was analyzed for the d.c. component and the harmonic components along with the fundamental. As the relation for [illegible]) was a cosine series, the analysis was considered accurate as long as the magnitudes of the d.c. and harmonic components were very small with respect to the magnitude of the fundamental component.

APPENDIX B

DERIVATION OF REFLECTION COEFFICIENT FROM CARRIER REINSERTION

The relationships between Voltage Standing Wave Ratio (VSWR), voltage reflection coefficient (Γ), transmission line characteristic impedance (Z_o) and the load impedance (Z) are the following:

$$\Gamma = \frac{Z-Z_o}{Z+Z_o} \quad ; \quad VSWR = \frac{1+|\Gamma|}{1-|\Gamma|} \quad ; \quad Z = Z_o\left(\frac{1+\Gamma}{1-\Gamma}\right) \tag{1}$$

The magnitude of the voltage reflection coefficient is $|\Gamma|$ where

$$|\Gamma| = \frac{|V_r|}{|V_i|} \tag{2}$$

and V_r, V_i are the reflected and incident voltage waves respectively. A further useful relationship is

$$\frac{|V_i + V_r|}{|V_i|} = \frac{|V_i\,(1+\Gamma)|}{|V_i|} = |1+\Gamma| \tag{3}$$

Defining the complex reflection coefficient as

$$\Gamma = A + j\,B$$

then

$$|\Gamma| = \sqrt{A^2 + B^2} \quad ; \quad |\Gamma|^2 = A^2 + B^2 \tag{4}$$

and

$$|1+\Gamma| = \sqrt{(1+A)^2 + B^2} \quad ; \quad |1+\Gamma|^2 = (1+A)^2 + B^2 \tag{5}$$

from which

$$A = \frac{|1+\Gamma|^2 - (1+|\Gamma|^2)}{2} \tag{6}$$

and

$$B = \sqrt{|\Gamma|^2 - A^2} \tag{7}$$

Once the values of $|1+\Gamma|^2$ and $|\Gamma|^2$ are known, the values of A and B can be calculated. Both the magnitude and sign of A can be calculated however, only the magnitude of B can be calculated. The sign of B is arrived at by knowing the sign and magnitude of B at some time and then monitoring the value of $|1+\Gamma|^2$. For B to change sign the value of $|1+\Gamma|^2$ has to decrease to a minimum and then increase again.

Both the relations $|1+\Gamma|^2$ and $|\Gamma|^2$ are a direct measure of the values of $|V_i|^2$ and $|V_r|^2$ and therefore a direct measure of the incident and reflected powers. An R.F. detector operating in the square law region will give, as an output, a d.c. voltage that is directly proportional to the R.F. power incident upon it. Ideally then, an R.F. detector can be used to obtain the values of $|1+\Gamma|^2$ and $|\Gamma|^2$ as follows:

$$\left| \frac{V_i+V_r}{V_i} \right|^2 = \frac{|V_i+V_r|_d^2}{|V_i|_d^2} = |1+\Gamma|_d^2 \tag{8}$$

$$\left| \frac{V_r}{V_i} \right|^2 = \frac{|V_r|_d^2}{|V_i|_d^2} = |\Gamma|_d^2 \tag{9}$$

where the subscript "d" refers to a quantity an R.F. detector can measure. Since the R.F. detector is not ideal, some proportionality constants will be required and the relations for the complex reflection coefficient will be

$$A = [\, U|1+\Gamma|_d^2 - (1 + S\,|\Gamma|_d^2\,)]/2 \qquad (10)$$

and

$$B = \sqrt{S\,|\Gamma|_d^2 - A^2} \qquad (11)$$

where U and S are arbitrary constants to be determined for each specific R.F. detector.

In practice, the R.F. detectors used have characteristics that display appreciable variation when monitored over a wide range of incident R.F. signals. To account for a possible change in the values of the constants U and S, in Eqs. (10) and (11), the R.F. input/d.c. output characteristics of the detector used, were measured over the range of R.F. signal levels of interest. These characteristics are shown in Fig. B.1 for various detector bias voltages. By making a piecewise linear approximation to these curves values of U and S can be obtained for each individual linear approximation segment.

The constants, U and S, are determined by measuring a load whose complex reflection coefficient is known. The general procedure is to take the d.c. output level of the R.F. detector in millivolts and find the equivalent R.F. power in milliwatts from Fig. B.1. This equivalent R.F. power is then the subscripted value ("d") in Eqs. (10) and (11). The values of U and S are those for the appropiate piecewise linear approximation that applies to that particular range of R.F. detected levels. This procedure is followed for the range of R.F. levels of interest. The complex reflection coefficient of an unknown load can be found by following a similar procedure of converting the detected d.c. levels to equivalent R.F. powers, from Fig. B.1, and substituting these values into Eqs. (10) and (11).

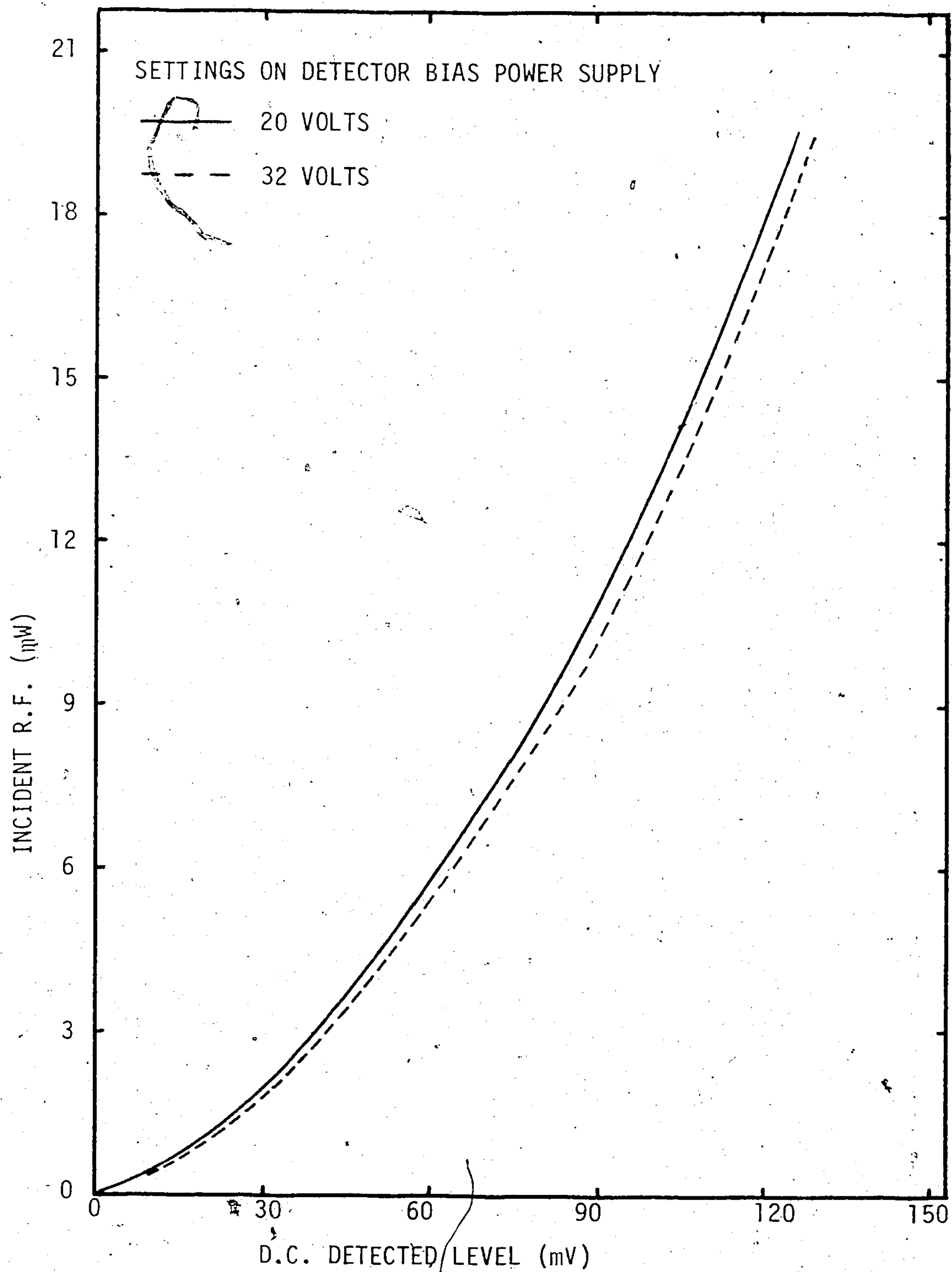

FIG. B.1 CALIBRATION CHART FOR R.F. DETECTOR

APPENDIX C

R.F. DETECTION

The R.F. detector unit used in the work reported here was a commercially available Hewlett-Packard Crystal Detector Model J424A. The waveguide mount has a bandwidth of 5.3 - 8.2 GHz, with the detector diode itself having a much broader frequency range. Schematic diagrams of the physical and electrical properties of this R.F. detector unit are shown in Fig. C.1.

The crystal diode may be considered as a voltage generator with an internal resistance of 3K to 20K ohms shunted by approximately 10 picofarads of capacitance. This gives the detector an R.C. time constant of from 30 to 200 nanoseconds. The equivalent internal resistance can be reduced to around 200 ohms by forward biasing the crystal diode; this places the value of the R C time constant in the range of 2 nanoseconds. Thus, the response time of the R.F. detector unit can be controlled by adjusting the forward bias of the crystal diode.

This forward bias was applied in series with a 10K ohm resistor as shown in Fig. 6.5. As only a few hundred millivolts are required to forward bias the detector diode, a 10K ohm resistor was placed in series with the detector and the biasing d.c. power supply. This allowed the use of a commonly available power supply and also protected the delicate crystal diode from transients in the operation of the biasing power supply. The series 10K resistor was placed in the center conductor of a RG58 A/U coaxial cable and located inside

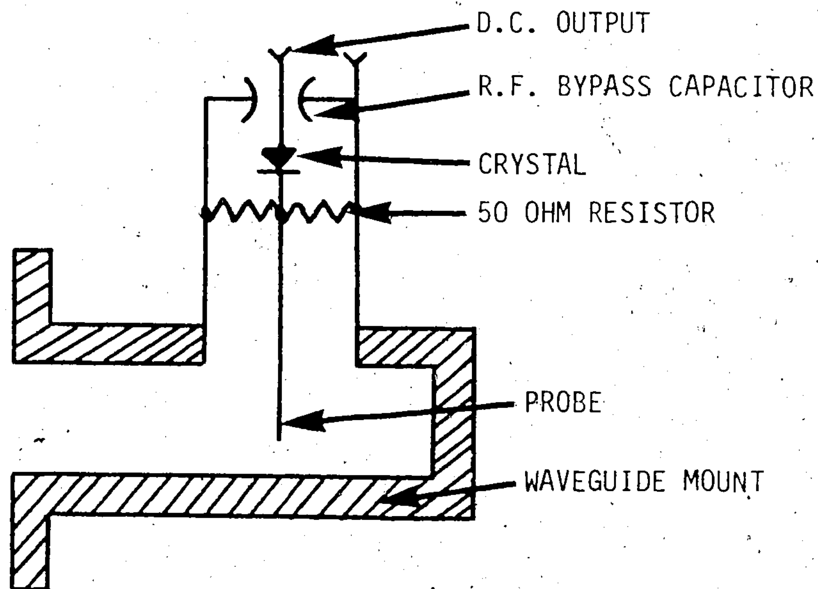

(a)

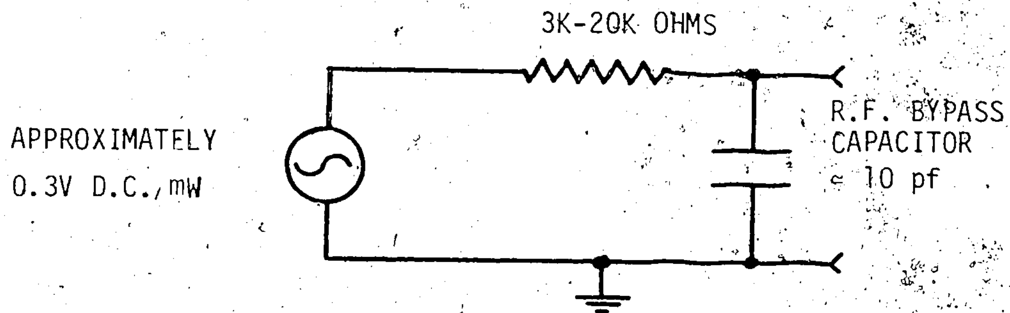

(b)

FIG. C.1 HEWLETT PACKARD CRYSTAL DETECTOR MODEL J424A
(a) SCHEMATIC OF WAVEGUIDE MOUNT
(b) SCHEMATIC OF EQUIVALENT CIRCUIT

the BNC connector at the detector end of the cable. In this way parasitic effects were reduced while still providing a convenient method of applying the bias voltage to the detector unit.

To ensure adequate response time in the detector system, the output of the detector was connected directly to the 50 ohm oscilloscope channel. This constituted a heavy loading of the R.F. detector unit which decreased the sensitivity of the unit and necessitated the use of the most sensitive range of the oscilloscope channel (10 mv/cm). By connecting the positive biasing voltage and the oscilloscope channel to the R.F. detector unit with a BNC tee, two advantages were realized. One advantage was that the actual forward bias across the detector could be monitored on the oscilloscope and also, this positive bias voltage offset the negative d.c. level that is the normal output of the detector unit, thus making it easier to use the most sensitive scale on the oscilloscope channel.